Study of MBE growth and characterization of Gallium Nitride films and nanostructures

A Thesis submitted in partial fulfilment

of the requirements of the degree of

Doctor of Philosophy

by

Manoj Kesaria

Chemistry and Physics of Materials Unit

Jawaharlal Nehru Centre for Advanced Scientific Research

Bangalore-560064

April, 2012.

Declaration

I hereby declare that this thesis entitled "**Study of MBE growth and characterization of Gallium Nitride films and nanostructures**" is an authentic record of research work carried out by me under the supervision of Prof. S. M. Shivaprasad at the Chemistry and Physics of Materials Unit, Jawaharlal Nehru Centre for Advanced Scientific Research, Bangalore, India, and it has not been submitted elsewhere for the award of any degree or diploma. In keeping with the general practice of reporting scientific observations, due acknowledgement has been made whenever work described here has been based on the findings of other investigators. Any omission that might have occurred due to oversight or error in judgement is regretted.

Date: 04th, June, 2012

Manoj Kesaria

Place: Bangalore, India

Certificate

Certified that the work described in this thesis entitled "**Study of MBE growth and characterization of Gallium Nitride films and nanostructures**" has been carried out by Manoj Kesaria, under my supervision at the Chemistry and Physics of Materials Unit, Jawaharlal Nehru Centre for Advanced Scientific Research, Bangalore, India.

Date: 04th, June, 2012 Prof. S. M. Shivaprasad

Place: Bangalore, India (Research Supervisor)

Acknowledgements

I express my heartfelt gratitude to my research supervisor, Prof. S.M. Shivaprasad for his invaluable guidance and constant encouragement. I am extremely grateful to him for suggesting the research projects as well as propelling it in the right direction. His optimistic and imaginative approach in scientific research is awe-inspiring. I am indebted to him for the acquired skills in several instrumental techniques. His methodical approaches with the instruments and his creative ideas have helped in the efficient use of them. I thank Mrs. Anupama Shivaprasad for her warmth and hospitality.

I am grateful to the present Chairmen of CPMU, Prof Balasubramanian and ex-Chairmen Prof C.N.R. Rao and Prof. G.U.Kulkarni, for their constant support and encouragement in various ways. I am grateful to Prof C.N.R Rao for being a source of inspiration to all of us with his boundless enthusiasm, up-to date knowledge, dedication and commitment to science. I express my sincere thanks to various collaborators during my research work, Prof. P.I.Cohen, Prof Chandrabhas Narayan, Dr Ranjan Datta, and Prof Umesh Waghmare, and I thank all the faculty members of CPMU for their cordiality, especially my teachers, Prof. S. Ranganathan, Prof. Sobhana Narshiman, and Prof G.U Kulkarni for the courses they taught.

I would like to thank all my teachers, who have guided me till now, especially Professors of Bipin Bihari College, Gandhi sir, Sunandana madam, Rudrakant sir, Prof. Shiv Govind, Prof. T. K. Sharma and Professors of Bundelkhand College, especially H. C. Agarwal sir who prompted me to take up research as a career. I take this opportunity to thank my NPL lab seniors Dr Amish G Joshi, Dr Govind, and Dr. Mahesh Kumar for introducing me to the various aspects of the surface science lab and equipment and their helpful and friendly attitude.

I am grateful to my present labmates, Satish, Praveen, Jithesh, Malli, Shreedhar, Varun, Darshna and Arpan for discussions and cheerful atmosphere. Special note of thanks to

Mrs Selvi, Dr Kartik, Mr. Mahesh, Mr. Kishore, for help with SEM measurements and Shireesha for TEM measurements. Timely and ready assistance and also friendly attitude from technical staff, Mr. Srinath, Mr. Somashekar and Mr. Karmarkarji is acknowledged. I am very thankful to Mr. Anil (XRD), Mr. Vasu (UV, PL), Mrs. Usha (TEM), for their invaluable technical assistance.

I thank the staff of academic and administrative section in JNC for their assistance. I also thank the library and computer lab staff for their help. Financial assistance from Council of Scientific and Industrial Research (CSIR), JNCASR is acknowledged.

I thank all JNC colleagues for a memorable and joyous JNC life. I also thank my friends at JNCASR, and there are no words to express my gratitude to my family members. This thesis is dedicated to them.

Preface

The potential performance of group III nitrides optoelectronic devices has been limited due to a high density of threading dislocations (~ $10^{10}cm^{-2}$) arising due to the relaxation of strain induced by the lattice mismatch between GaN film and c-plane sapphire substrates. Thereby, defect free semiconductor nanostructures have been envisaged as new paradigm for devices and fundamental studies due to the absence of residual strain, exclusion of most extended defects, long photoluminescence life time, low surface recombination velocity and high mechanical quality factors in nanostructures. Molecular Beam Epitaxy (MBE) grown nanostructures are driven by a competition between the thermodynamics and kinetics including factors such as surface energies, sticking coefficients, diffusion coefficients on different crystal planes and supersaturation. This thesis is a study of the formation of thin films and nanostructures of GaN on Al_2O_3(0001), Si(001) and Si(111) surface by Plasma Assited MBE (PA-MBE). The work involves synthesis in the growth parametric space followed by complementary characterization. The work done is reported in the following Chapters:

Chapter 1 introduces issues related to GaN film growth, including the misfit induced dislocation formation, and highlights the motivation for the present work of kinetically controlling GaN growth of 2D thin film and nanostructures.

Chapter 2 presents the status of current research of single crystalline nanostructure growth on single crystal surfaces of Al_2O_3 and Silicon substrates, elucidating the various growth mechanisms ascribed in literature.

Chapter 3 describes the growth and characterization techniques employed in this study and their calibration. The practical details of the MBE growth and the *in situ* and *ex situ* characterization methods are presented.

Chapter 4 presents the results of the growth and characterization of doped and undoped 2D-GaN films and HEMT structure grown by PA-MBE. The high quality of the films is manifested by a narrow FWHM of ≈108 arc sec of the (0002) reflection, threading dislocation density by AFM of ~10^8 cm^{-2}, mobility ≈500 cm^2/Vs and 1cm^2/Vs carrier concentration of ~10^{17} cm^{-3} and 10^{19} cm^{-3} for Si doped and Mg doped films, respectively. High performance AlGaN/GaN high electron mobility transistor (HEMT) structure is realized, with mobility of ≈1500 and ≈5000 cm^2/Vs at 300K and 77K and a sheet carrier concentrations of ~10^{12} cm^{-2}.

Chapter 5 presents the results of the formation and characterization of GaN nanostructures in a nitrogen rich growth condition with N/Ga Beam Equivalent Pressure (BEP) ratio of 100. In the relatively low temperature growth regime (480−630°C) we observe the formation of dense wedge-shaped GaN nanowall hexagonal network, around open screw dislocations. At high temperatures (730−880°C) flat morphology films with a dislocation density of ~$10^{10}/cm^2$ are formed, which transform into faceted mounds beyond 830°C. The formation of c-oriented epitaxial GaN nanocolumns on bare sapphire at 680°C are presented and effect of growth kinetics on nanowall and nanocolumn formation and their structural and optoelectronic properties are discussed. A narrow parametric window is identified by varying Ga flux (2.86×10^{14} to 4.84×$10^{14}$$cm^{-2}s^{-1}$), Nitrogen flow rate (2.0 to 8.0 sccm) and temperature (480 to 880°C) where 1-D nanocolumns of GaN with high density (1×$10^8$$cm^{-2}$) are observed. Epitaxy, assembly and shape of the nanocolumns suggest that such spontaneous formations can reduce process steps for high performance device structures.

Chapter 6 presents a coverage dependence study at different substrate temperatures that enables us to understand the mechanism of nanostructure formation. The various forms of nanostructures such as nanowall network, self-organised nanocolumns and Frank-Read structures are discussed and the probable mechanisms that govern their formation under kinetically controlled growth is discussed.

We provide direct evidence for observation of formation of GaN nanocolumns at screw dislocations and Frank Read mills as nucleation centres.

Chapter 7 provides an insight of the effect of substrate type, and on GaN epitaxy and nanostructure formation. We also demonstrate the spontaneous formation of nanorods on silicon surfaces, such as (111) and (100), which are discussed in terms of Frank spiral growth. We also demonstrated a novel way of formation of single crystalline, c-oriented defect free GaN nanowires of diameter $\approx$10nm by a 4-stage growth process. The nanowall network is used as a template to initially grow a low temperature (400^{o}C) 2D layer which upon annealing dewets into defect free single crystalline, c-oriented nanowires in a single growth process which is characterized by complementary techniques, including ultra high resolution TEM.

Chapter 8: lists the highlights of this work, provides a summary of the thesis. The conclusions arrived at from the experimental observations, and the prospects and directions the future scope of the work undertaken in this study are also provided.

Contents

Acronyms

LED	Light Emitting Diode
MBE	Molecular Beam Epitaxy
PAMBE	Plasma Assisted Molecular Beam Epitaxy
LD	Laser Diode
DVD	Digital Video Disc
LCD	Liquid Crystal Display
CD	Compact Discs
TD	Threading dislocation
QW	Quantum Well
TEM	Transmission Electron Microscope
IC	Integrated circuit
CMOS	Complementary Metal Oxide Semiconductor
QCSE	Quantum Confined Stark Effect
VCSEL	Vertical Cavity Surface Emitting Laser
RCLED	Resonant Cavity Light Emitting Diode
BEC	Bose Einstein Condensate
HEMT	High Electron Mobility Transistor
2DEG	Two Dimensional Electron Gas
1D/2D/3D	One Dimension/ Two Dimensions/Three Dimensions
FM	Frank van der Merwe
VW	Volmer Weber
ES	Ehrlich Schwoebel
III-N	Group Third Nitride
III-As	Group Third Arsenide
III-V	Group Third and Fifth
VLS	Vapour Liquid Solid
SLS	Solution Liquid Solid
VSS	Vapour Solid Solid
CVD	Chemical Vapour Deposition
MOCVD	Metal Organic Chemical Vapour Deposition
MOMBE	Metal Organic Molecular Beam Epitaxy
SNAP	Superlattice Nanowire Pattern
EQE	External Quantum Efficiency
EL	Electroluminescence
NW, NR, NC	Nanowire, Nanorods, Nanocolumns
AM	Air Mass

HVPE	Hydride Vapour Phase Epitaxy
RFMBE	Radio Frequency Molecular Beam Epitaxy
HRTEM	High Resolution Transmission Electron Microscope
SPM	Scanning Probe Microscope
STM	Scanning Tunnelling Microscope
DFT	Density Functional Theory
ELOG	Epitaxial Lateral Overlayer Growth
BEP	Beam Equivalent Pressure
QC	Quartz Crystal
FESEM	Field Emission Scanning Electron Microscope
CL	Cathodoluminescence
CCD	Charged Coupled Device
FFT	Fast Fourier Transform
RHEED	Reflection High Energy Electron Diffraction
FWHM	Full Width Half Maximum
XRD	X-ray Diffraction
BEL	Band Edge Luminescence
YL	Yellow Luminescence
PL	Photoluminescence
GPa	Giga Pascal
XPS	X-ray Photoelectron Spectroscopy
TO	Transverse Optical
LO	Longitudinal Optical
RMS	Root Mean Square
SEM	Scanning Electron Microscope
P-V	Peak to Valley
AFM	Atomic Force Microscope
SFM	Scanning Force Microscope
UID	Un-intentional doped
UV-VIS	Ultra Violet-Visible
LPP	Longitudinal Optical Phonon Plasmon Mode
DI	Diffusion Induced
LBL	Layer By Layer
BCF	Burton Cabrera Frank
FR	Frank Read
UHV	Ultra High Vacuum
LEED	Low Energy Electron Diffraction
AES	Auger Electron Spectroscopy
MOVPE	Metal Organic Vapour Phase Epitaxy

ML	Monolayer
RF	Radio Frequency
PID	Proportional Integral Derivative
PBN	Pyrolitic Boron Nitride
HCL	Hollow Cathode Lamp
UV LED	Ultra Violet Light Emitting Diode
SCCM	Square Cubic Centimetre
OES	Optical Emission Analysis
PMT	Photomultiplier Tube
RGA	Residual Gas Analyzer
PXRD	Powder X-ray Diffractometer
BSE	Back Scattering Electrons
SE	Secondary Electrons
SC	Specimen Current
AE	Auger Electrons
TE	Transmitted Electrons
EDS	Energy Dispersive Spectroscopy
PIPS	Precision Polishing System
SAD	Selected Area Diffraction
FE	Free Exciton
BE	Bound Exciton
XRC	X-ray Rocking Curve
RSM	Reciprocal Space Mapping

Chapter 1

Introduction and motivation

1. Introduction (motivation)

The group III-Nitride solid state devices, which have permeated our daily life, are light emitting diodes (LEDs) and laser diodes (LDs). In fact, they have been overshadowed only by the transistor. The power efficiency, ruggedness and compactness of these light emitting devices are unbeatable and have greatly contributed to their dissemination. LEDs are seen on electronic billboards at airports, subways and train stations indicating important information, and are extensively used as back-lighting and indicators in all electronic applications that requires a human interface. More recently, 3D displays based on LEDs are posing challenge to LCD displays and are overtaking other devices. Since the 1980's, LDs and LEDs led to the creation of a whole new branch of consumer electronics in the form of CD and DVD players/writers, laser printers and fibre-optics. The potential of High Brightness LEDs which can replace all Solid State Lighting, and the possibilities for forming full-spectrum Solar Cells, make these materials the most sought after by researchers and industries.

The first infrared compound semiconductor GaAs laser was formed in September 1962 at General Electric from the work of Hall et al[1]. In October the same year Holonyak and Bevacqua, also at General Electric, demonstrated the first red semiconductor laser and red LED based on $GaAs_{1-x}P_x$,and were commercially available by December 1962[2]. Because of the low electrical-to-optical power efficiency (12 lm/W), these devices were initially used only for indoor indicator applications replacing electromechanical meters and nixie tubes. However, because of the use of $GaAs_{1-x}P_x$ the emission spectrum was limited to colours from infrared to yellow, where as blue, violet and UV were still unreachable, which has prompted an intense research effort in this direction. For years, researchers were mainly focused on group II-VI semiconductors such as ZnSe, which did not converge to any usable device. The only commercially available blue-emitting LED was based on SiC, which had a very low efficiency and very low brightness but has been commercialized despite its severe shortcomings, since no alternatives existed. Another material considered for blue light emission was GaN. **Figure 1.1** shows bandgap engineering possible with GaN and related InN & AlN, collectively known as III-nitrides. These materials do not exist in nature, and the creation of this semiconductor family that

emits light over such a huge range of important wavelengths is a major breakthrough in materials science. On alloying InN (bandgap 0.7eV) that emits in the IR range with GaN (bandgap 3.4 eV) that emits in the near-UV, the entire spectrum range from 0.7−3.4 eV can be spanned, which includes the visible region. Similarly, on alloying AlN (bandgap 6.2eV) with GaN spans near-UV to deep-UV (i.e. 3.4eV to 6.2eV).

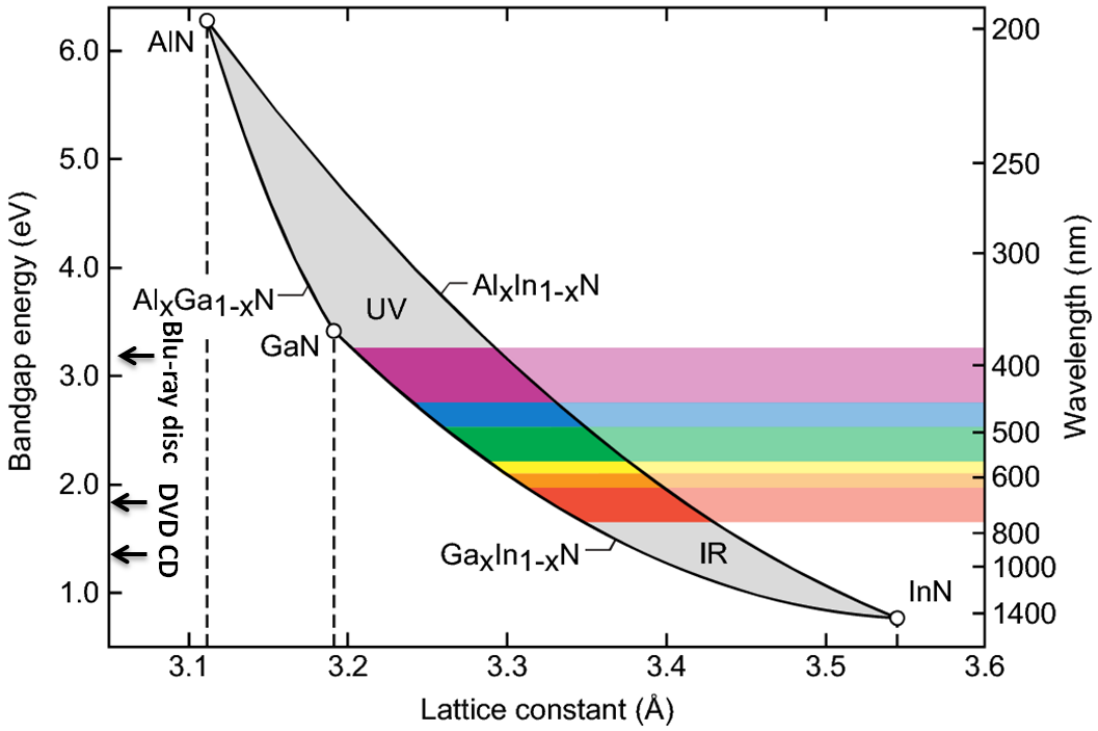

Figure 1.1 *bandgap versus lattice constant for III-Nitride and laser energies for reading/writing compact discs (CD), Digital video discs (DVD) and Blu-ray discs and visible spectrum*[3] .

Blue, green, yellow and red electroluminescence from a GaN metal-insulator-semiconductor diode was demonstrated by Pankove et al. (RCA Princeton Laboratory) in 1972[4-5]. However, the device efficiency was very low and it was not possible to achieve p-type doping. The layers also exhibited a very large unintentional background doping and were having very poor quality epitaxial layers and consequently received very little attention during the 1970's and 1980's. The groundbreaking work of the group of Akasaki propelled GaN to a level where it could be considered as a potential candidate for blue light emission. In 1986 Amano et al. showed that high quality GaN epitaxial films could be obtained using buffer layers[6]. During 1988, Akasaki et al. achieved p-type

doped GaN layers for the first time using Mg[7]. Despite these key discoveries, GaN was still not considered as a serious candidate for blue LEDs and LDs. This situation was changed by persistent work on investigating GaN by Shuji Nakamura, of Nichia Chemicals (Japan) which was a small company specialized in phosphors. In 1993 Nakamura developed the first efficient blue-emitting high-brightness GaN-based LED and in 1996 the first GaN edge-emitting blue-violet or UV continuous-wave LD[8]. Since these devices were introduced commercially, the range of applications for LEDs and LDs has been greatly extended. Most notable is the UV-emitting LEDs that can be combined with phosphors to create white-light solid-state emitters with an efficiency that is potentially much higher (250 Lumens/Watt) than that of incandescent and fluorescent lamps (90 Lumens/Watt)[9]. The power saving capabilities of solid-state white-light emitters will become increasingly important since there is an exponential increase in energy consumption.

The progress in solid state lighting primarily involves development of visible nitride-based light emitting diodes (LEDs). This progress is impeded because of the presence of a high dislocation density caused by large lattice mismatch with available substrates and lack of low cost GaN substrates[10-12]. At present the most suitable substrate has been c-plane sapphire [Al_2O_3(0001)], which has a lattice parameter of 0.47 nm, while GaN has 0.32 nm[13]. According to the theory of strained epitaxial layer predictions, epilayer will maintain the lattice constant of the underlying substrate while its strain energy increases with thickness, *h*, for system under thermodynamic equilibrium[14]. A point will be reached when it is energetically favourable to relive strain through misfit dislocation generation. Due to the lattice mismatch between GaN film and c-plane sapphire substrate, the growth of heteroepitaxial overlayer leads to in-plane strainσ,

$$\sigma = \frac{a_f - a_s}{a_s} = \varepsilon + \delta \quad \text{.....(1.1)}$$

where a_f and a_s are lattice parameters of film and substrate, respectively. If substrate is assumed rigid then the strain will be accommodated in the overlayer, then the epitaxy will be under elastic strain (psuedomorphic), ε, or some of the strain can be accommodated by misfit dislocation formation, δ. The large mismatches in lattice constant (+33%) and thermal expansion coefficient (36%) of GaN and Al_2O_3 (0001) substrates cause strain in

the overlayers, the GaN films grown have the epitaxial orientation $[0001]_{Al_2O_3}$// $[0001)]_{GaN}$, $[10\bar{1}0]_{Al_2O_3}$// $[11\bar{2}0]_{GaN}$ shown in **Figure 1.2**. This 30° rotation about [0001] leads to the mismatch reduction from 33% (compressive) to -14.6 % (tensile), for the basal plane growth of GaN over $Al_2O_3(0001)$[15].

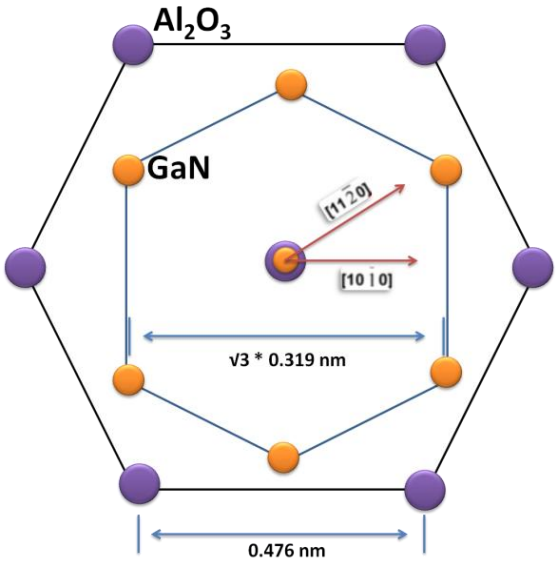

Figure 1.2 *orientations between GaN and Al_2O_3 in-plane directions.*

Figure 1.3a shows GaN film (in top panel) with $a_f = \frac{\sqrt{3}}{2} a_{GaN}$ = 0.276nm, $c_f = \frac{1}{2} c_{GaN}$= 0.259 and Al_2O_3 substrate (in bottom panel) with $a_s = \frac{1}{2} a_{sapphire}$ = 0.238nm, $c_s = \frac{1}{6} a_{sapphire}$ = 0.217. Lattice constants of the unstrained or relaxed GaN layers are a_{GaN} = 0.3186nm and c_{GaN} = 0.5178nm and for c-plane sapphire are $a_{sapphire}$ = 0.478nm and $c_{sapphire}$ = 1.299nm. The biaxial strain in the (0001) plane for GaN film on sapphire substrate can be evaluated by relations,

$$\varepsilon_{xx} = \varepsilon_{yy} = \frac{a_x - a_0}{a_0} \quad \text{.....(1.2)}$$

$$\varepsilon_{zz} = -\frac{a_y - c_0}{c_0} = -\frac{2C_{13}}{C_{33}} \varepsilon_{xx} \quad \text{.....(1.3)}$$

The subscript "0" denoted the lattice constant of the unstrained GaN film, a_x and a_y are the lattice constants of the strained GaN film in the parallel and perpendicular to the

(0001) plane while C_{ij} are the elastic constants[16]. In pseudomorphic condition (**Figure 1.3b**), $a_x = a_s$, GaN layer gets strained which gets relaxed by generation of misfit dislocations as shown in **Figure 1.3c**. The in-plane strain, σ can be relaxed partially through the formation of misfit dislocation at the interface. If a sufficiently large quantity of misfit dislocation is formed, the film will be completely relaxed, but the remnant microscopic strain field will still exist around the dislocation[17].

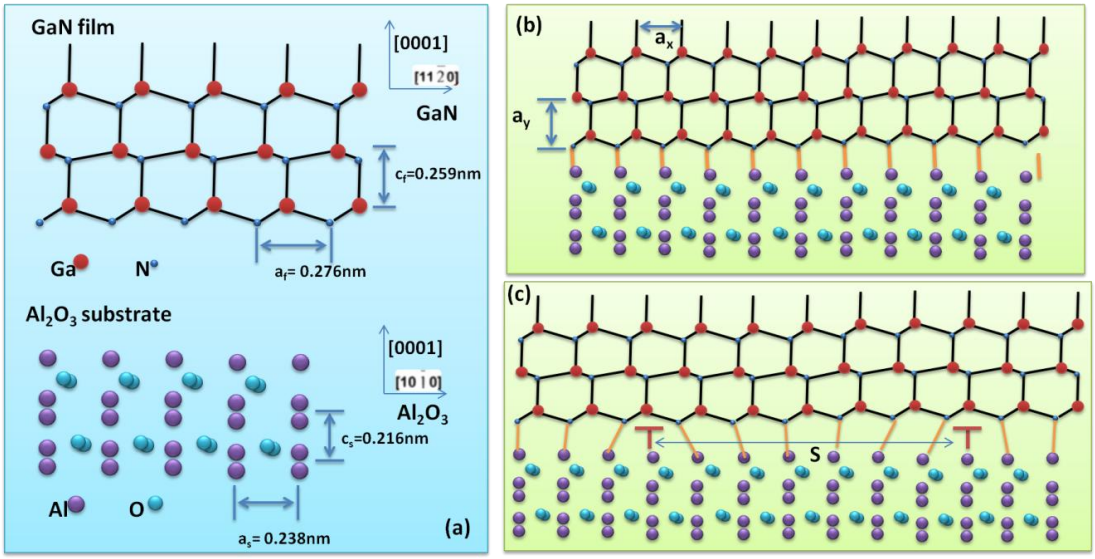

Figure 1.3 *ball and stick model of* ***(a)*** *GaN film in top panel and Al_2O_3 substrate in bottom panel, GaN film grown on Al_2O_3 substrate in epitaxial orientation* $[0001]_{Al_2O_3}$// $[0001)_{GaN}$, $[10\bar{1}0]_{Al_2O_3}$// $[11\bar{2}0]_{GaN}$ *, under biaxial compression* ***(b)*** *with strain accommodation for thin pseudomorphic GaN film and* ***(c)*** *subsequent strain relaxation with misfit dislocation generation.*

In case of GaN grown on sapphire the projection of the wurtzite GaN lies in a horizontal direction parallel to the (0001) substrate surface. The large mismatch gives $h=h_c$ which is less than a monolayer and the strain is quickly relieved with misfit dislocation generation. Compete relaxation required misfit dislocation at an average spacing S≈2nm, can be calculated form equation 1.4

$$S = \frac{b}{\sigma} = \frac{ba_s}{a_f - a_s} \quad \text{.....(1.4)}$$

where *b* is the magnitude of Burgers vector and is dependent on the type of dislocations. The array of geometrically misfit dislocations is confined to the GaN/sapphire interface

approximately 20nm from the interface. However, they do not contribute to the threading dislocations (TDs) in GaN film. It is generally assumed that the TDs evolved from the coalescence of tilted and twisted islands formed during the initial stage of GaN nucleation. These dislocations tend to cluster together leaving the large volume of the epilayer free from defects. The threading dislocation density in GaN grown on sapphire is $10^{8}-10^{10}$ cm^{-2} giving an average spacing S≈100 nm for the later.

The majority of the threading dislocations (**Figure 1.4**) are in the [0001] direction. They can be categorized into a-type (pure edge dislocation **Figure 1.4a1**) with Burgers vector **b** = 1/3<11$\bar{2}$0>, c-type (pure screw dislocation **Figure 1.4a3**) with Burgers vector **b** = [0001] and a+c type (mixed dislocation) with Burgers vector **b** = 1/3<11$\bar{2}$3>. Threading dislocation are defined by two orthogonal vectors: the Burgers vector ***b*** and the dislocation line vector ***l***. The a-type threading dislocation is defined by vector **b** (along a-axis) orthogonal to ***l*** (along c-axis), which is a planar defect consisting of an extra partial plane of atoms resulting from the coalescence of misoriented islands about the [0001] axis. In case of c-type threading dislocation **b** (along c-axis) vector parallel to ***l*** (along c-axis), and for c+a type dislocation both vector **b** and ***l*** are inclined off c-axis**.**

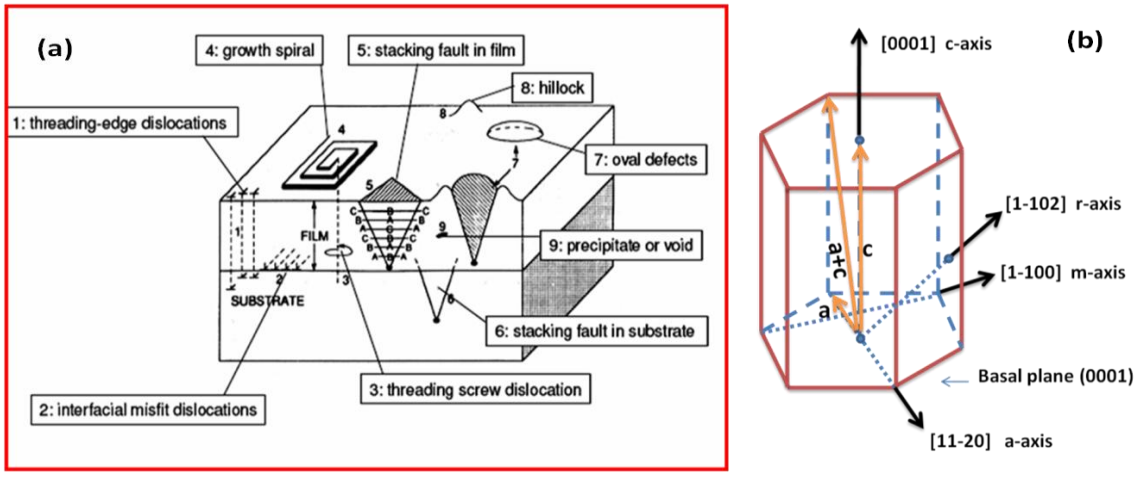

Figure 1.4 (**a)** *shows type of defect and dislocation formed observed in heteroepitaxial growth of thin films,* ***(b)*** *shows GaN crystallography with Burgers vector of edge dislocation* ***a****, screw dislocation* ***c*** *and mixed dislocation* ***a+c****.*

Dislocations with different Burgers vectors can also interact (via recombination, annihilation processes) with each other and bunch together to generate a new dislocation. However, dislocation propagation will not be terminated unless its strain energy is

released though V-defect formations, at grain boundaries or other linear of planar defects. Other defects such as stacking faults (**Figure 1.4a5,6)** which had the stacking sequences of ABABACAC and ABABCACA are generally observed in GaN films. **Figure 1.5** shows TEM micrograph of threading dislocations observed in GaN film grown on bare c-plane sapphire.

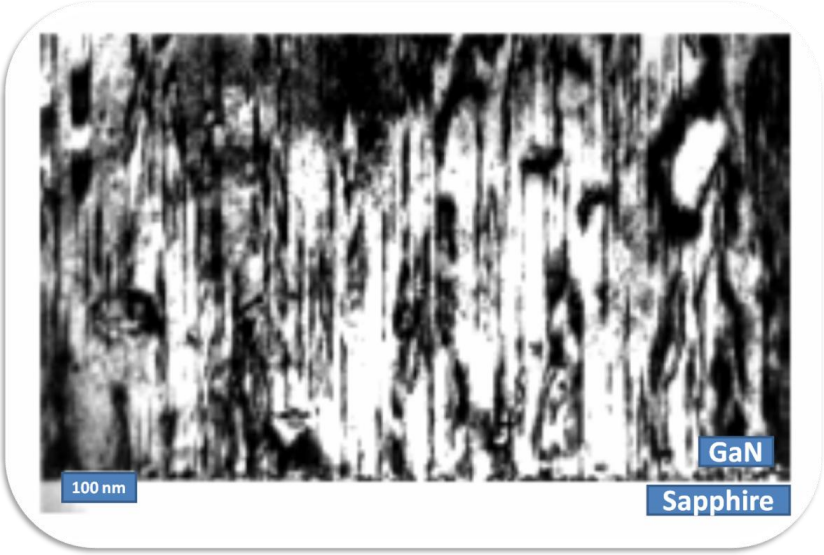

Figure 1.5 *is a TEM micrograph of GaN film grown over c-plane sapphire.*

Figure 1.6 shows a light-emitting diode (LED) structure, and the schematic of a high resolution image of an active region, which is a repeat of thin InGaN quantum wells (QW) of thickness ≈2nm, sandwiched between GaN layer of thickness ≈7nm (barrier layer). This important active region is sandwiched between thick n-type and p-type GaN and is formed on typically a c-plane sapphire $\{Al_2O_3(0001)\}$. When voltage is applied to this structure, electrons are injected into the active region from n-type GaN and holes from the p-type GaN. These electron and holes exist in active layers at different energy levels, separated by an energy bandgap. On recombination of electron and holes in the active region, light energy of wavelength equivalent to the bandgap energy is released, and the colour of this emitted light can be tuned by varying the bandgap of this active region.

Figure 1.6 also has transmission electron micrograph (TEM) that shows the high density of threading dislocations ~ 5×10^{9} cm^{-2} which results from the large lattice

mismatch between GaN on c-plane sapphire. Dislocations generated in the thick base layer, threads through the active layer of LEDs and causes direct or indirect deleterious effects on LED efficiency, hence causing a significant drop in LED efficiency (**Figure 1.7**). The major issues such as "efficiency droop" which is caused due to high injection current and "green gap" which is due to poor efficiency of green-emitting LEDs, are reasons which hamper solid state lighting progress along with poor chromaticity and low efficiency of exiting phosphor coated white LED. GaN based Blue LDs have made strides in the DVD player market as blue-ray Laser Disk players and are expanding the data storage capacity. Even though the use of LDs is widespread, the device still has several drawbacks like, it is not possible to integrate with other electronic components on a single wafer.

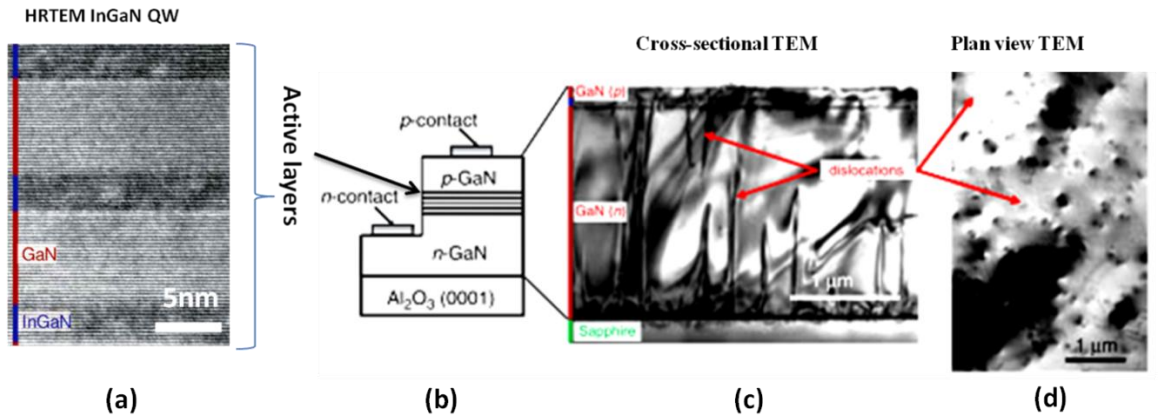

Figure 1.6 *Light-emitting diode (LED) structure (b) together with transmission electron micrographs (TEM) showing (c and d) the high density of threading dislocations resulting from the growth of GaN on sapphire and (a)is the high resolution image of active layer (InGaN quantum wells separated by GaN barriers) on the left of the schematic* [18].

Figure 1.6 also has transmission electron micrograph (TEM) that shows the high density of threading dislocations ~ 5× 10^9 cm^{-2} which results from the large lattice mismatch between GaN on c-plane sapphire. Dislocations generated in the thick base layer, threads through the active layer of LEDs and causes direct or indirect deleterious effects on LED efficiency, hence causing a significant drop in LED efficiency (**Figure 1.7**). The major issues such as "efficiency droop" which is caused due to high injection current and "green gap" which is due to poor efficiency of green-emitting LEDs, are reasons which hamper solid state lighting progress along with poor chromaticity and low

efficiency of exiting phosphor coated white LED. GaN based Blue LDs have made strides in the DVD player market as blue-ray Laser Disk players and are expanding the data storage capacity. Even though the use of LDs is widespread, the device still has several drawbacks like, it is not possible to integrate with other electronic components on a single wafer.

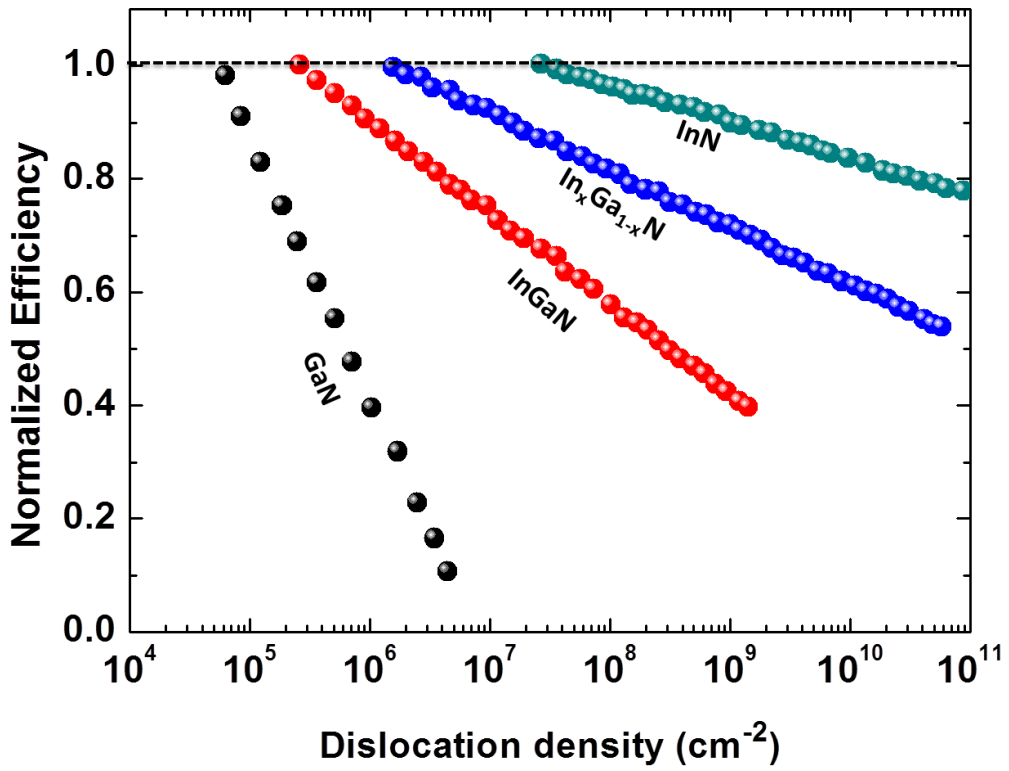

Figure 1.7 *Emission efficiency versus dislocation density for III-Nitrides films*[19].

Integrated Circuits and role of nanostructures

According to the popular 'Moore's Law', by Intel co-founder Gordon Moore, a visionary, predicted that the "number of transistors incorporated in integrated circuit (IC) chip will approximately double every 24 months" (**Figure 1.8a**). Moore's also meant that by decreasing the costs per transistor, more transistors can be built on the same silicon wafer. Silicon technology is gaining ground in our daily lives due to steady rise in processing power of silicon based device (measured in millions of instructions per second (MIPS)) and increased density coupled with improved multiple core processor

microarchitecture. For continuous evolution of Moore's Law innovations are necessary not only in dimension and scaling but also in integrated circuit materials and structure, since the physical limits of atomic structure would be reached by 2015 (**Figure 1.8b**), mainly due to the limitation of standard photolithography technique. Alternate possibility is to develop transistor structures on self assembled nanowires with existing technology. As of now, nanowire based vertical and planar transistors have been fabricated.

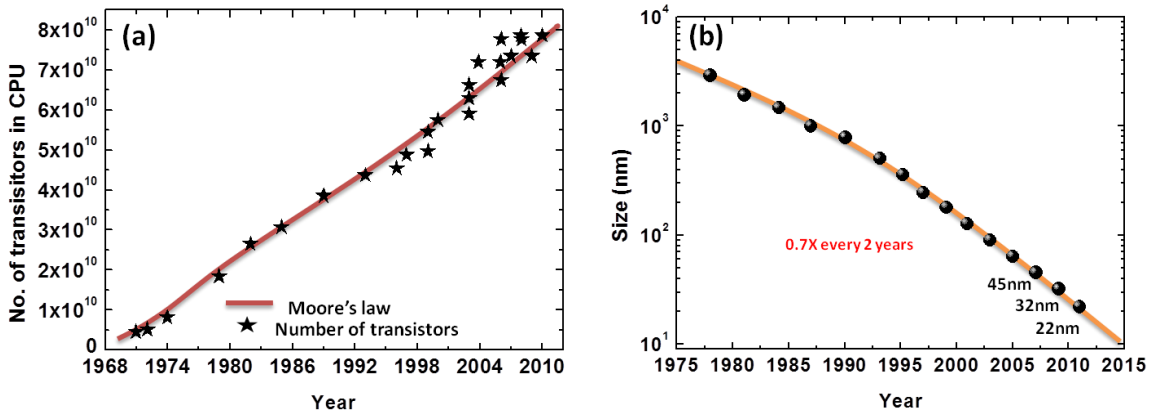

Figure 1.8*(a) Moore's Law (Intel Corporation) showing the correlation between 1970 and 2010, (b) Evolution of Moore's Law: transistors dimensions scale to improve performance, reduce power and cost per transistor. (Source: Intel Corporation 2011).*

Among many existing compound semiconductors, III-nitrides might pioneer nanowire devices or their integration with well established silicon technology by fabricating nanowire based circuitry, as nanostructure formation allows reduction in lattice mismatch effect. Next generation self assembled nanostructures could be used for interlinking vertical nanowire based transistors, ultra bright and high resolution LED, high efficient tandem solar cell etc., by forming micro-structural array of self assembled millions of nanowire (schematic shown in **Figure 1.9**[20]) on a single block. Other applications such as gas sensors require increased surface area to volume ratio which can be achieved by nanostructures. There are recent reports on the growth of GaN and InGaN nanowires on bare silicon substrate and on buffer layers sapphire substrate[21-24]. The advantages of nanowires over high defect density 2D layers are: reduced defect density, large surface-to-volume ratio, large light extraction efficiency, compatibility with low cost large area silicon substrate and reduced strain distribution which weaken

piezoelectric polarization filed. Recent work in III-N nanowires is focussed on growth, material aspect and optically pumped devices. There are reports[25-26] on electrically injected single nanowire LEDs on foreign substrates, LEDs with single ensembles grown on Si(111) substrates, but these involve complicated nanowires transfer and low yield and also Si(111) is not compatible with complementary metal oxide (CMOS) technology.

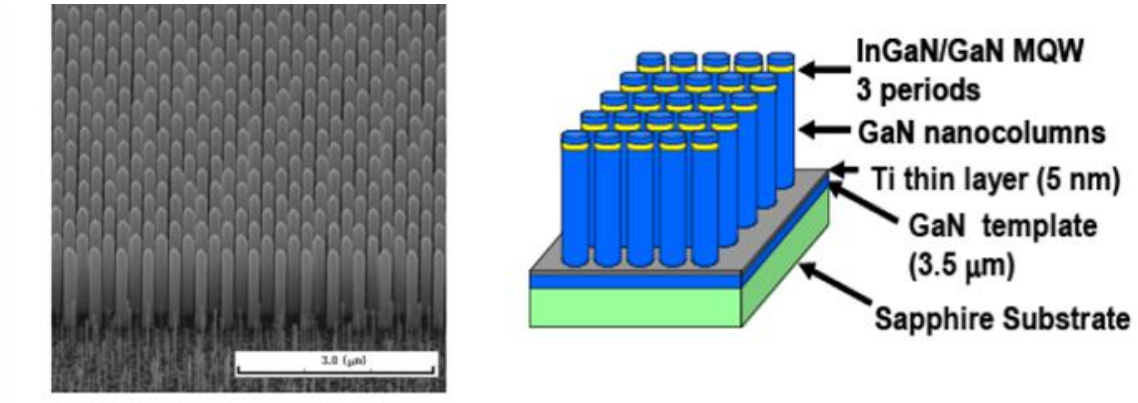

Figure 1.9 *SEM image and schematic of phosphor free MBE grown white nanoLED along with different emission from different diameter LED structure* [33].

There is a need to develop phosphor-free solid state white light sources. This can be achieved by nitride-based LEDs in which InGaN/GaN quantum wells in the active region are tuned to obtain either broad emission or emission of dual or multiple wavelengths, which can integrate to produce white light. A shortcoming associated with the use of quantum wells is the large quantum confined Stark effect (QCSE)[27-28] in the wells and the resulting blue shift in emission wavelength with applied bias and light absorption and emission frequencies. As a consequence, electron states shift to lower energies while the hole states shift to higher energy. Thus, electrons and holes are spatially shifted to the opposite sides of the potential barrier of the QW, which preserves excitions in the system, reducing the recombination efficiency (or fluorescence quantum yield) of device. It has been shown that the wavelength shift due to QCSE[29], arising from large polarization field in quantum wells, is absent is nanorod LEDs due to absence of such fields. Because of the high aspect ratio (e.g. length≈10μm and diameter≈20nm) of nanorods, external field influence remains confined to the base of nanorods and causes no influence to QW in the nanorods LED. As a result, electron and holes within the quantum

well may occupy states within a discrete set of energy subbands and consequently, only a discrete set of frequencies of light may be absorbed or emitted.

The use of nanowires in the design of white LEDs is important and advantageous due to many reasons, such as Ga (In) N nanowires can be grown directly, using Ga as a self-catalyst on Si (001) which is technologically important. Extensive structural characterization by several groups [30-31] have indicated that nanowires are free of extended defects such as dislocations, stacking faults, and twins and thus the surface recombination velocity of nanowires are two orders of magnitude smaller than that on the free surface of GaAs. The Auger coefficients measured in In(Ga)N nanowires and InGaN/GaN disk-in-nanowire are $2-3$ orders of magnitude smaller than those measured in heteroepitaxial bulk materials with defects present[32]. The composition of the disks has been tuned to obtain multi-wavelength luminescence and white light emission.

The most prevalent of the suggested laser structures is the Vertical Cavity Surface Emitting Laser (VCSEL) where the laser light is extracted perpendicular to the surface of the structure in contrast to conventional edge-emitting semiconductor lasers which emit light parallel to the surface[34]. Large scale integration and device testing on the wafer level are both allowed by the VCSEL scheme[35]. In addition, VCSELs allow unique applications, single mode lasers desirable for coupling into optical fibers and optical neural networks. The first modern continuous-wave VCSEL operating at room temperature was demonstrated in 1989 by the group of Iga at Tokyo Institute of Technology [36]. This device was based on (Ga,Al)As and was emitting in the infrared range. A cheaper alternative to the VCSEL is offered in the form of a resonant-cavity light emitting diode (RCLED)[37-38], which improves the light extraction. So far electrically driven nitride-based RCLEDs or VCSELs have not been realized. A very exciting and extraordinary phenomenon in the form of cavity polaritons is offered by high-quality nitride-based microcavities, where the quasi-particle is created by the strong coupling between an excitons and a photon-mode of the cavity[39]. This strong coupling effect has been observed in GaAs microcavities at cryogenic temperatures. However, the large GaN exciton binding energy of 26 meV opens up the study of cavity polaritons at room temperature[40], as Bose-Einstein condensate (BEC) may be formed at room temperature

according to Tawara[41] with a gain as a result of certain scattering processes and then coherent light will be emitted from the polaritons in that state, that might create a new type of lasers without threshold.

The other III-nitride devices which are worth noting are deep-UV radiation structures which have many important applications including water purification, air purification, and the detection of biological agents. The large energy band gap differences (E_G(GaN):3.4eV and E_G(AlN):6.2eV), high electron velocities (~10^7 cms^{-1}) and high thermal and chemical stability makes III-Nitrides system attractive for fabricating Gallium Nitride (GaN) based devices for high-power, high-frequency space applications. GaN based devices have superior material properties such as high breakdown field (5MV/cm), high thermal conductivity (1.3$Wcm^{-1}C^{-1}$), high peak velocity (> $3x10^7cm^{-1}s$), high saturation velocity (>$1.5x10^7cm^{-1}s$), and high sheet charge density ($1x10^{13}cm^{-2}$) in comparison to GaAs, Si, Ge etc[42-46]. GaN/AlGaN High Electron Mobility Transistor (HEMT) is the fastest transistor which is suitable for microwave and millimetre wave applications[43] and is based on the unique two dimensional electron gas (2DEG) that is formed at heterointerface as a result of bandgap engineering.[44] Steep spike-shaped quantumwells at the heterojuntion cause large conduction-band offsets as well as large discontinuity in the piezoelectric and spontaneous polarization[45]. However fundamental issues of thin film growth, strain control, defects engineering and formation of nanostructures need to be understood well to tailor make systems that can lead to futuristic devices that III-nitrides are capable of. The effort in this work are towards understanding the role of kinetics of growth and substrate effects on formation of 2D-films and nanostructures of GaN, grown mainly on c-plane sapphire on Silicon.

Chapter 2

Research status of GaN single crystalline film and nanowires by MBE

2. Research status of GaN single crystalline films and nanowires by MBE

This Chapter is a literature survey of the work done in this field, to set-up conditions which formulated the need to do the present work. The Chapter describes the kinetics of growth by the MBE technique and also reviews the mechanism based on the work done on 2D-films and nanostructure (especially nanowire) formation.

2.1 Fundamental thin film growth process

The principle of MBE is the crystallization of thin films with a rate of typically 1monolayer/s in UHV via reactions between thermal-energy beams of constituent elements and a crystalline substrate surface maintained at an elevated temperature in order to enhance surface diffusion. An important aspect of this growth technique is that the atoms or the molecules in the beams do not interact with each other before they reach the substrate. Typically, MBE is used to grow epitaxial films i.e. the crystal structure and orientations of the films are determined by the crystalline substrate.

The individual atomic processes which determine the film growth in its initial stages[47] are illustrated in **Figure 2.1**.The molecules or atoms impinging on the substrate are adsorbed through physisorption (Van der Waals forces type) or chemisorption (chemical reaction with electron transfer). The adsorbed atoms or molecules may then migrate on the substrate surface with a diffusivity determined by the substrate temperature and the surface conditions. When they find a lower-energy site at ledges, kinks or defects they may incorporate into the substrate lattice. Additionally, an adsorbed atom or molecule may interact with others and form a stable or critical nucleus that might grow into a film for further incorporation. The unincorporated species re-evaporate due to thermal desorption. All these processes are related to activation energies to be overcome and their temperature-dependent rate constant **k** obeys Arrhenius law[48]:

$\mathbf{k} \propto e^{\frac{E_a}{K_B T}}$, ... (2.1)

where E_a is the activation energy, k_B the Boltzmann constant and T the temperature.

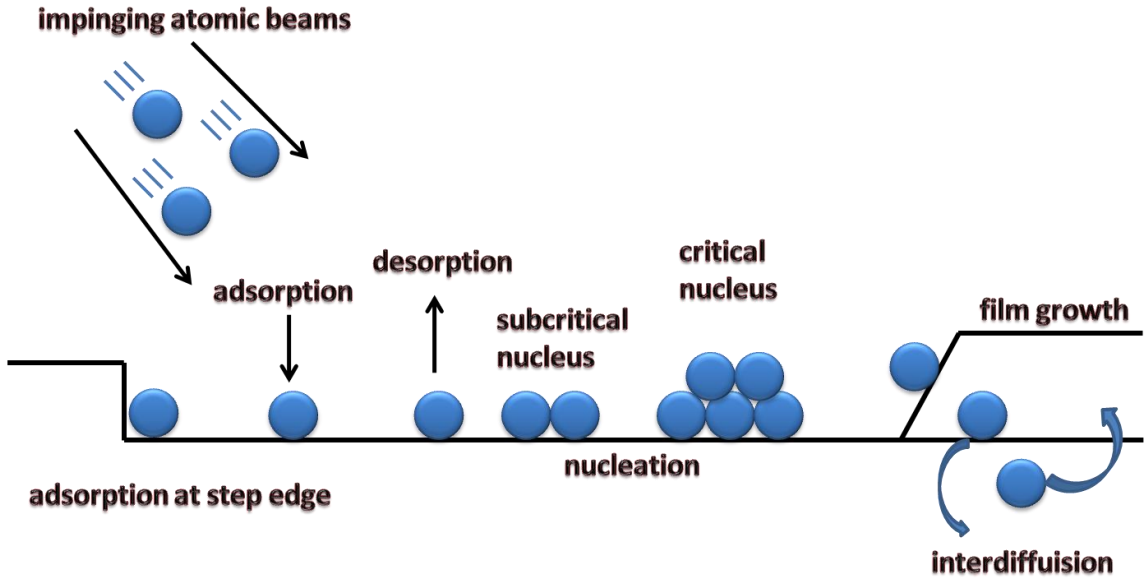

Figure 2.1 *schematics of the surface processes occurring during film growth by MBE.*

At the substrate surface, growth occurs far from thermodynamic equilibrium and is governed mainly by the kinetics of the reaction between the topmost layers and the impinging species. On a mesoscopic scale, the film morphology develops according to one of the three possible growth modes sketched in **Figure 2.2**. The growth modes depend on many factors like surface free energies, difference in lattice parameters and forces between atoms of the deposited material and temperature. In the **Frank-van der Merwe** or layer-by-layer growth mode, atoms in the film are more strongly bound to the substrate than to each other and the energy is minimized when the substrate is entirely covered by the planar (2D) film. In the **Volmer-Weber (VW) mode**, the substrate is not wetted by the film, and three-dimensional (3D) islands grow directly on the substrate surface. Atoms in the film are more strongly bound to each other than to the substrate. The **Stranski-Krastanov (SK) mode** often appears for heteroepitaxial growth due to the lattice mismatch between the substrate and the deposited layer inducing strain in the latter. In this case growth occurs first in a layer-by-layer fashion before strain is elastically relaxed by the formation of 3D islands. The transition 2D-3D occurs once the

elastic energy counterbalances the surface energy required to form facets[49]. For further material deposition, depending on the lattice mismatch plastic relaxation can also occur leading to the formation of dislocations.

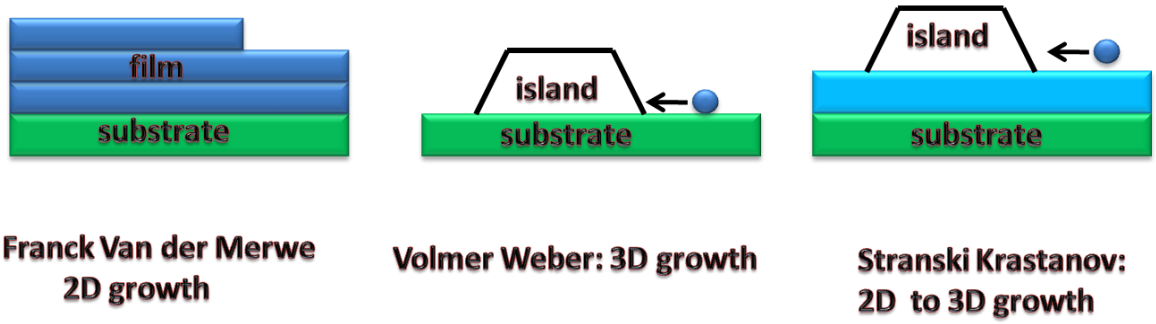

Figure 2.2: *Schematics of the three crystal growth modes: layer by layer (Frank-van der Merwe), island (Volmer-Weber) and layer plus island (Stranski-Krastanov).*

In the case of homoepitaxy, thermodynamics predicts a layer by layer growth mode. However, under conditions far from equilibrium, kinetic limitations associated with finite rates of mass transport processes can greatly affect the growth mode. For a vicinal surface consisting of terraces and atomic steps, adatom transport implies not only transport across terraces (intralayer) but also across steps (interlayer). Each transport is related to different activation barriers and their difference constitutes the **Ehrlich-Schwoebel (ES) barrier**[50] and corresponds to the reduction of the coordination of an adatom while crossing the step-edge as illustrated in **Figure 2.3**.

Thus, the probability for an atom to diffuse onto the lower terrace depends on the ES barrier that can be negligible or insurmountable. Depending on this barrier, three possible growth modes are observed leading to different morphologies[51]. The **step-flow mode** occurs when the adatom intralayer mobility is high so that all adatoms reach the step before nucleation sets in and the step advances. In the case where the adatom migration is shorter than the terrace width, **layer-by-layer or multilayer growth** takes place depending on the rate of the interlayer mass transport. In the extreme case where this transport is zero, the adatom cannot escape from the top of the **island and 3D growth** is promoted. Because the adatom mobility depends greatly on the growth parameters, the

growth mode can thus be altered by changing the deposition rate and the temperature. Lastly, surfactants also affect the growth mode by modifying the surface energies, the intralayer diffusion and the intralayer diffusion barriers[52].

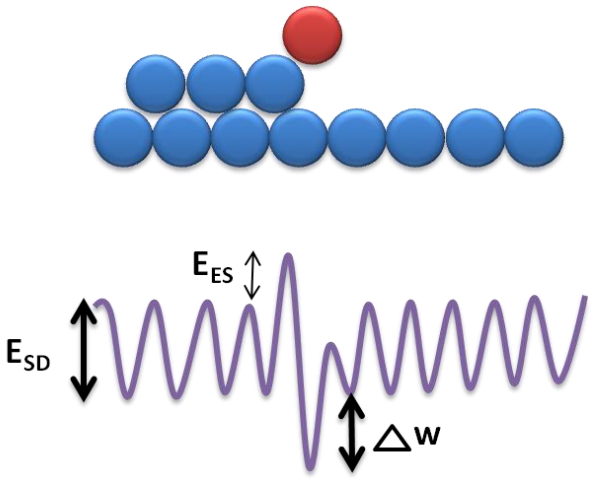

Figure 2.3: *Schematic drawing of the potential for an atom moving toward a step edge with an ES barrier E_{ES}, ΔW is the binding energy to a step site and E_{SD} the activation energy for the terrace diffusion.*

2.1.1 Adatom kinetics in GaN thin film growth in Ga rich condition

In PAMBE growth of GaN film Ga atoms and the excited N_2* plasma molecules in the beams do not interact with each other before they reach the substrate. In epitaxial GaN thin film growth the crystal structure and orientations is determined by the crystalline substrate. Typically in Ga rich condition, growth of GaN film on c-plane sapphire substrate grow along [0001] as a stable wurtzite crystal. The atomistic processes involved in the initial stages of GaN film growth are shown schematically in **Figure 2.4**.

The impinging Ga and N_2* molecules or atoms on the substrate are adsorbed either through physisorption or chemisorption. The adsorbed Ga and N_2* atoms or molecules migrate on the substrate surface with a diffusivity determined by the substrate temperature and the surface conditions. An adsorbed Ga and N_2* atom or molecule may interact with others to form a stable or critical GaN nucleus which evolve into a film on

further incorporation. The unincorporated Ga re-evaporate or get desorbed due to thermal desorption. On c-plane sapphire substrate surface, GaN thin film growth occurs far from thermodynamic equilibrium and is governed mainly by the kinetics of the reaction between the topmost layers and the impinging species.

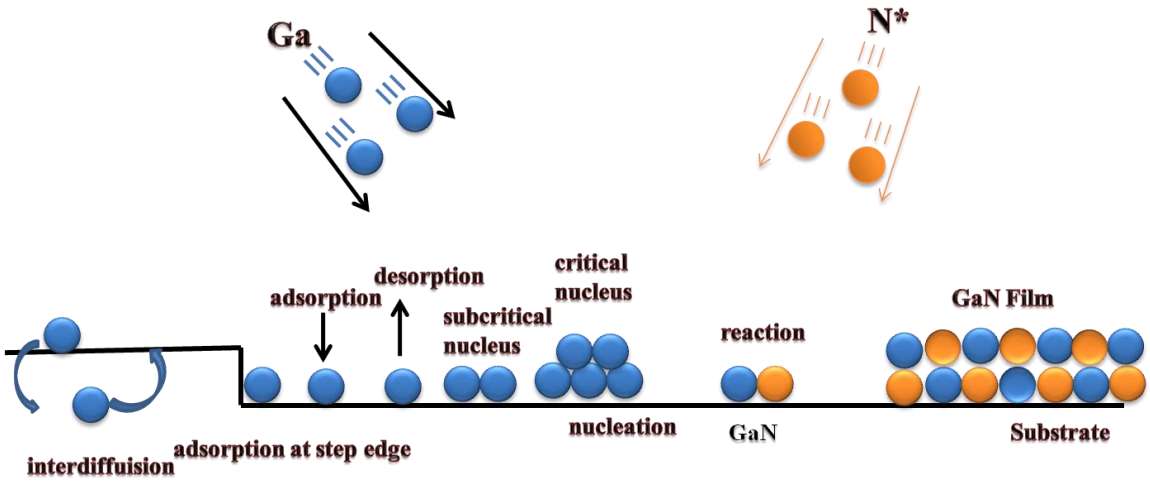

Figure 2.4: *Schematics of the surface processes occurring during GaN film growth in Ga rich condition by PAMBE.*

Among the kinetic processes adsorption, desorption and adatom diffusion are considered to be a key parameters which controls the growth rate, the material quality, and the surface morphology. Zywietz et al[53] have calculated the potential energy surface (PES) for Ga and N adatoms over GaN (0001) and (000$\bar{1}$) surfaces. The proposed model for (0001) surface is a Ga-terminated bilayer and for (000$\bar{1}$) surface is a Ga-adlayer structure. The diffusion barriers of Ga adatoms for (000$\bar{1}$) surface is 0.2 eV and for (0001) surface 0.7 eV, while for N adatoms diffusion barriers for (000$\bar{1}$) surface if 1.1 eV and for (0001) surface 1.3 eV. An important consequence of these results is that Ga adatoms will be orders of magnitude more mobile than N atoms at typical growth temperatures (~730°C) [54-55]. The low diffusion barrier is a direct consequence of the fact, that GaN equilibrium surfaces are Ga-stabilized (discussed in Chapter 4). For Ga atoms the adsorbate-surface interaction is realized by Ga-Ga bonds. The melting point of Ga is

slightly above room temperature (T_{melt}=30℃) and the Ga–Ga bonds are weak and the adatoms behave almost like a liquid film on the surface. The N adatoms have large diffusion barrier in comparison to Ga adatoms. On equilibrium surfaces N adatoms are unstable against evaporation as N_2 molecules and can be kinetically stabilized at surface during film growth. The migration of N adatoms is a highly activated process under higher N-rich growth conditions the nitrogen desorption rate become smaller than the absorption rate.

As a consequence, extended regions which has surface covered by N atoms may be formed. These N adatoms influences the migration path and the diffusion barrier of Ga adatoms. The diffusion of Ga adatoms on N-terminated (0001) and $(000\bar{1})$ surfaces is considered only for Ga adatoms since N adatoms on N-terminated surfaces results in the formation of weakly bound N_2 molecules desorbing at typical growth temperatures. For both surface orientations the diffusion barrier of Ga adatoms is strongly affected. At (0001) the migration barrier increases from 0.6 to 1.8 eV while at $(000\bar{1})$ it increases from 0.2 to 1.0 eV. N adatoms can be incorporated on the surface although they are thermodynamically unstable. The different mobilities of Ga and N adatoms and the formation of excess N have important consequences on the growth of GaN. In the Ga-rich regime where the amount of N on the surface is small, the Ga adatoms are highly mobile and a step-flow mode resulting in 2D growth is expected. As a consequence, the surface morphology should be improved and a low density of defects is expected. Further, if excess Ga adatoms are present on the surface (as expected for Ga-rich growth conditions), N adatoms can be efficiently incorporated. The probability that fast moving Ga adatoms capture N atoms is much higher than the other process where N atoms form molecules and desorbs from the surface. To grow GaN the incoming N-flux must be larger than the N-desorption rate which is mainly governed by the N adatom diffusion barrier. This excess of N at the surface (which can be formed under N-rich conditions) significantly reduces the mobility of Ga adatoms. The reason is the formation of strong Ga–N bonds, which have to be broken during the migration of the adatoms. The reduction in surface diffusivity when going towards more N-rich conditions is consistent with a recent MBE

growth study by Tarsa et al[56]. Under Ga-rich conditions step flow is observed (implying low diffusion barriers) while under more N-rich conditions island formation is found.

2.2 Nanowire growth mechanisms

The conventional thin film technology encounter interfacial lattice mismatch issue that often result in highly defective thin film structures. In this regard, nanowire growth provides a natural mechanism for relaxing the lattice strain at the interface and enables dislocation-free semiconductor growth on lattice mismatched substrates, for example, III-As, III-N on silicon and Al_2O_3. The traditional semiconductor industry has to be integrated with the material morphology and size dependent properties of low dimensional structures, which are the result of strong photon, phonon, and electron confinement effects within the semiconductor nanostructures. The study of nanostructures is driven by a need to improve upon present devices. Nanostructures allow devices with different functionality due to quantum effects, as their sizes approach the Bohr radius. Moreover, nanostructures have increased surface to volume ratio compared to thin films, with a correspondingly enhanced sensitivity to external agents and light detection so that novel nanodevices can be produced which can be used in harvesting mechanical, electrical, light and heat energies. Among various nanostructures possible, quantum dots and nanowires have received most attention while nanowalls also have great potential. There are now many different growth methods for semiconductor nanostructure formation which can be commonly placed into two categories, namely, the bottom-up and top-down approaches. The bottom-up approach starts with individual atoms and molecules and builds the desired nanostructures. It has been shown that atoms can be manipulated using a scanning tunnelling microscope to produce atomic scale structures (Eigler et al)[57].

2.2.1 Nanowire growth methods and integration

These early works on nanowhiskers and nanorods were popularized as semiconductor nanowires in the following decade. In the late 1990s, the field of semiconductor nanowires underwent a significant expansion and became one of the most

active research areas within the materials science community[58-60], and has now developed into a relatively mature research area with exciting and new research opportunities. This can be seen from the number of papers (Inset of **Figure 2.5**) published on nanowires, which has increased exponentially in last ten years. The nanowire field is now understanding new fundamental science as well as developing potential applications. Both discovery-based and hypothesis-driven research have led to emergence of subfields such as nano-electronics, nano-photonics, nano for energy conversion and storage, and interfacing nanowires with living cells[61]. The unique one-dimensionality inherent in nanowires has already solved some of the long-standing technical problems that have plagued the thin film community. For example, integration of optically active semiconductors (e.g., III-V's) onto silicon is critical for the next generation of computing tools that will merge photonics with electronics on a single platform.

A faster and more conventional bottom–up process for nanowire formation is the vapour-liquid-solid (VLS) approach, where a metal catalyst is used to initiate growth of nanowire using typical semiconductor growth techniques. In 1964 when R. S. Wagner proposed VLS mechanism[62] for whisker growth which is governed by equation (2.2):

$$R_{min} = \frac{2V_l}{RTlnS}\sigma_{lv} \quad \text{..... (2.2)}$$

where R_{min} is the minimum wire radius, V_l is the molar volume of the metal droplet, σ_{lv} is the liquid-vapor surface energy, and S is the degree of supersaturation of the vapour[63], which has played a significant role in research of semiconductor whiskers at nanoscale dimensions. **Figure 2.5** shows the number of times the Wagner and Ellis paper[64] on VLS growth has been cited and shows it is a commonly used method for nanowire growth with essentially exponentially increasing interest.

In the early 1990s, Hitachi scientists applied VLS technique to the growth of III-V nanowhiskers[65-66]. At this time, good positional and orientational control was achieved as well as the first p-n junctions based on heterostructured nanowhiskers was demonstrated[67]. This was followed by important studies in two separate research laboratories in the mid 1990s. A new whisker growth mechanism was proposed by William Buhro's group at Washington University, where they synthesized III-V

nanowhiskers using a solution-liquid-solid (SLS) process[68]. Meanwhile, the Charles Lieber group at Harvard initiated a research program in the area of inorganic nanorods. Carbide[69] and oxide nanorods[70] were produced through vapour phase conversion and transport processes in several of these early studies. The VLS process was introduced for actual nanoscale growth by Charles Lieber's group around 1998, as a proof of concept that the VLS process is useful for nanowire growth. There are several problems with using the VLS process for growing III-V nanostructures. For Si nanowires the phase diagram is typically based on only two elements: silicon and gold[71].

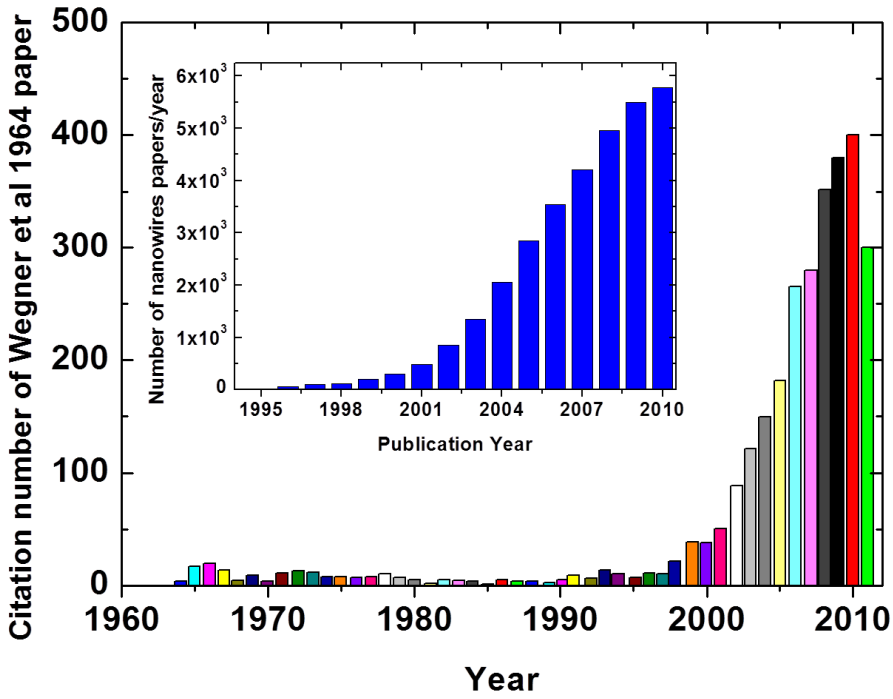

Figure 2.5: *Wagner and Ellis 1964 paper has been cited 1386 times and is plotted as a function of publication year (Web of Science, http://isiknowledge.com/, accessed 2011). Inset shows a survey of an increase in the number of publications on nanowire related topics from year 1993-2010. Total research papers are (36343) published from 1993 to 2010 (Source, ISI Web of Knowledge; keyword, nanowires).*

For the growth of III-V nanostructures using the VLS process the catalyst is not the group III or group V material, so a third element is introduced as the catalyst, making the phase diagram more complex as it is a ternary system. It has been reported that for III-As nanowires the group III element alloys with the typically catalyst gold, forms the

liquid phase, while the As diffuses into the solid-liquid interface to grow the III-As nanowire[72]. In contrast, Persson et al. suggests that the catalyst is actually solid in the case of III-V nanowire growth and the presence of the catalyst is enough to confine the growth; this is known as vapour-solid-solid (VSS) growth[73]. The exact growth mechanism is not yet clear but seems to be dependent on the semiconductor of interest, growth temperature, and the catalyst used.

The preparation of nanowires in a controllable way is a challenging task that can be achieved by using a large range of approaches and fabrication techniques[72,74-75]. Two general approaches which are employed in nanowires synthesis are referred to as bottom-up and top-down. Beside MBE, the major nanowire fabrication/synthesis technique in use is chemical vapour deposition (CVD) which is composed of several subclasses like the hydride vapour phase epitaxy (HVPE) and metal-organic CVD (MOCVD). In this case, instead of the physical deposition of elements, chemical precursors decompose and react at the substrate surface to produce the desired substance. The sticking coefficients are much lower than in the case of physical deposition unless enhanced by a catalyst. Metal-organic-MBE (MOMBE) or chemical beam epitaxy (CBE) is a hybrid technique which combines the advantages of UHV like MBE with the versatility of MOCVD. The top-down approach relies on dimensional reduction through selective etching, lithography and various nanoimprinting techniques. Similarly, for the integration of nanowires building blocks, there are also two such general approaches, such as Langmuir-Blodgett techniques, the other being lithographical processes. In the current scenario we need both approaches for many of the applications related to semiconductor nanowires. Synthesis based on bottom-up approaches can be used to generate structures with dimensions ranging from angstroms to hundreds of nanometers. On the other hand, while the fabrication based top-down processes which still have difficulty in creating structures below 30 nm, have a great advantage for integration and addressability. There are a couple of good examples that illustrate the value of both strategies. The thermoelectric performance of silicon nanowires has been examined in both synthetic and fabricated nanowires. The Yang group has focused on VLS grown and chemically etched nanowires[76] while the Heath group has provided their Superlattice Nanowire Pattern

Transfer (SNAP) process to produce very thin silicon nanowires[77] The concept of nanowire based solar cells has attracted enormous attention because of their potential advantage in carrier transport, charge separation, and light absorption. The Lieber group has developed a fairly sophisticated core-sheath growth and contact strategy for their silicon p-i-n nanowire solar cells with efficiencies up to 3.5%[78] On the other hand, etching and overgrowth processes have also been developed to fabricate high density silicon core-shell solar cells. Efficiencies up to 6% have been demonstrated in this type of top-down fabricated nanowire core-shell arrays[79]. Here, both synthetic and fabricated nanowires offer similar core-shell solar cell designs, but with differences in interface sharpness and carrier recombination kinetics, and are found useful for sensor and laser research. On the basis of chemically synthesized nanowires, chemical/biological sensors[80] and nanolasers[81] have been developed and fully integrated nanowire chemical sensors[82] and nanopillar lasers[83] have been fabricated and tested using all top-down processes. The top-down approach typically has the advantage of having high throughput and more amenable for large scale integration. As for the integration of ultrahigh density nanowires circuitry, this has been one of the major challenges for nanowires prepared by either method.

2.2.2 Nanowire and thin film based optoelectronics

The high efficiency and long durability of semiconductor light emitting diodes (LED) based on thin film technology makes them ideal for displays and solid state lighting[84]. However, further miniaturization of electrically driven multicolour light sources is crucial to a variety of fields including integrated nano-photonic and optoelectronic systems, high-resolution microdisplays, ultrahigh density optical information storage, and multiplexed chemical/biological analysis. This is where nanoscale LEDs comes into play and semiconductor nanowires (III-V and nitrides) have been widely considered as good candidates for such applications. Since the demonstration of first nanowire LED using vertical GaAs pn-junction arrays by Hitachi[67], nanowire-based LEDs have been successfully realized in a variety of cross-nanowire junctions[85-86],

longitudinal[87] and coaxial heterostructures[88] with electroluminescence (EL) emission spanning the entire visible spectrum, and the near-infrared and ultraviolet[86]. In most of these cases, quantum efficiency of the light emitting devices was not reported, and it is difficult to quantitatively compare with the existing thin film technologies. The highest external quantum efficiency (EQE) reported for nanowires LEDs is in core/multishell nanowires that consist of n-GaN core and $In_xGa_{1-x}N$/GaN/p-AlGaN/p-GaN shells. The estimated EQE for these nanowire LEDs was 5.8% at 440 nm and 3.9% at 540 nm[88] This result is comparable to InGaN-based single quantum well thin film LEDs in the blue and green wavelength range[89], and thus better results are expected by optimizing collection efficiency and interface control to minimize undesired nonradiative recombination.

A similar comparison can be made between nanowires and conventional thin-film solar cells. It remains a challenge to make inexpensive, high-efficiency photovoltaic devices for large scale energy conversion. Semiconductor nanowires have been proposed to be fundamentally advantageous for photovoltaic applications due to their unique properties[90] like, long absorption path lengths while maintaining short distances for carrier collection/transport, interpenetrating heterojunction interfaces, allowing efficient carrier extraction following light absorption, strong light trapping in high-density nanowire arrays and modification of material properties and cell efficiencies through size and composition variation of the nanostructures. Dye-sensitized solar cells using dense arrays of oriented, crystalline ZnO nanowires as the anode have been designed to improve charge collection efficiency. Since direct electrical pathways provided by the nanowires ensure the rapid collection of carriers generated throughout the device, and an efficiency of 2.5%[91] under AM 1.5 illumination has been demonstrated. Coaxial silicon nanowires (p-type/intrinsic/n-type (p-i-n)) have achieved energy conversion efficiency of up to 3.4% under AM 1.5 illumination and are able to drive functional nanoelectronic sensors and logic devices[92] Strong light-trapping effects were observed in high-density silicon coreshell nanowire array solar cells with efficiencies up to 6%[79] Integrated with ultralow power nanosystems, these nanowire-based photovoltaic devices may serve as clean and sustainable miniature power sources. However, it remains a scientific challenge to design heterostructures with performances exceeding that of the existing silicon photovoltaic

technology, which has a commercial efficiency larger than 20% and theoretical limiting efficiency of 29%[93] Issues to be considered include surface recombination problems associated with the high surface area of the nanowires.

2.2.3 Catalyst-assisted nanowire growth and mechanism

The most commonly employed bottom-up method as discussed earlier is the VLS technique. In this technique nanometer-sized metallic particles form a low-temperature eutectic alloy with the nanowire (NW) material and act as a preferential sink for arriving atoms or in the case of precursor molecules as a catalyst for the necessary chemical process leading to the reactant incorporation [**Figure 2.6 (a)**]. These particles act as a collector for the deposited material[94] and the chemical potential[95] of the particle increases until supersaturation is reached. At this point, the NW material precipitates under the particle at the liquid-solid interface. Crystal growth proceeds thus unidirectionally by lifting of the particle. More recently it is observed that these particles could also be solid[96-98], growth occurring then through the vapour-solid-solid (VSS) mechanism. Several models were developed to account for the NW morphology dependence on the different experimental growth parameters. Givargizov studied the growth rate of Si whiskers grown by CVD using Au as a catalyst in dependence of their diameters and showed that the growth was strongly affected by the Gibbs-Thomson effect causing faster growth of the wider whiskers and the cessation of growth for whiskers of diameter smaller than a critical value[99]. However, for growth by MBE, the opposite trend was ascertained by Schubert et al[100], while Kodambaka et al[101] observed no dependence. The apparent contradiction can be attributed to the very different growth conditions. The generally accepted growth mechanism implies the incorporation of atoms not only by direct impingement onto the NW tip but also by diffusion on the substrate and along the side-facets of the NW. In consequence, it is to expect that for growth techniques inducing different surface reaction and diffusivity, different dependences are obtained. From the observation of longer tilted thin whiskers nucleated at substrate steps, Givargizov concluded that the rate-limitation of whisker growth was the incorporation of the whisker

material into the crystal lattice under the seed. Indeed, the nucleation barrier was expected to be strongly reduced at the step interface with the seed. Bootsma and Gassen[102] earlier reported that the chemical decomposition at the liquid-solid interface should be the rate-controlling process **[Figure 2.6 (a)]**, dependent on the NW synthesis technique since different physical/chemical surface reactions occur. In the catalyst-assisted approach offers the NW location and size are defined by the particle ones. Thus, in combination with lithography, it is possible to precisely position NWs of desired dimension[103-104]. However, the catalyst may also incorporate into the NW material, thus degrading its physical properties[105-107]. Hence there are constant efforts to develop other approaches not relying on any external catalyst.

2.2.4 Catalyst free nanowire growth and mechanism

This approach is preferred in order to grow NWs of high material purity, since no foreign catalyst material is required. Already in 1921, Volmer and Estermann tried to explain the different growth rates on different crystal facets observed for the growth of Hg[108] since the molecules diffuse on the surface of adsorption. In the early 1950s Sears proposed a growth mechanism based on the presence of a built-in screw dislocation to account for the growth of Hg whiskers[109]. The screw dislocation introduces an additional step that would catalyse the formation of a new monolayer in agreement with the Frank model[110], by the incorporation of atoms impinging at the whisker tip and diffusing along the sidewall toward an active sink, as sketched in **Figure 2.6 (b)**.

More generally, Sears[111] noted that uniform surface nucleation plays no role in the growth of whiskers and that the supersaturation required for whisker growth is much lower than the one to nucleate an atomic layer. Therefore, since this supersaturation is below the critical value for two dimensional nucleation, radial growth is hindered. However, this diffusion-dislocation model has been contested on the basis that only a few whiskers embody dislocations, and because stepped whisker side facets still grow slower than the flat top one. However, the recent observation of screw dislocations in PbS NWs [112]and in GaN NWs[113], make the debate interesting. The diffusion model postulated by

Sears is very important for NW growth and was further developed[114] and also extended to the catalyst-assisted growth by Givargizov[115] who postulated that the active sink could also be a catalyst particle instead of a screw dislocation. According to this the axial growth rate V is given by equation (2.3):

$$V = \frac{dl}{dt} = I + \frac{4I\lambda s}{d} \tanh \frac{l}{\lambda_s} \quad \text{..... (2.3)}$$

with *l* the whisker length, *d* the whisker diameter, *t* the time, I the impingement current at the whisker tip and λ_s the root mean square diffusion distance on the whisker surface.

The first term accounts for the growth by direct impingement of atoms at the tip while the second one is related to the surface diffusion on the surface of the substrate and on the side-facets of the NW. This model was experimentally verified for catalyst-free NW[116] growth as well as for the catalyst-assisted one[117-118] for different material systems and different growth techniques, the adsorption-desorption processes on the NW tip surface, the effects of growth on the substrate surface and the growth parameters (supersaturation, temperature)[119] and explains the divergence observed for the NW length-diameter dependence[94,101].

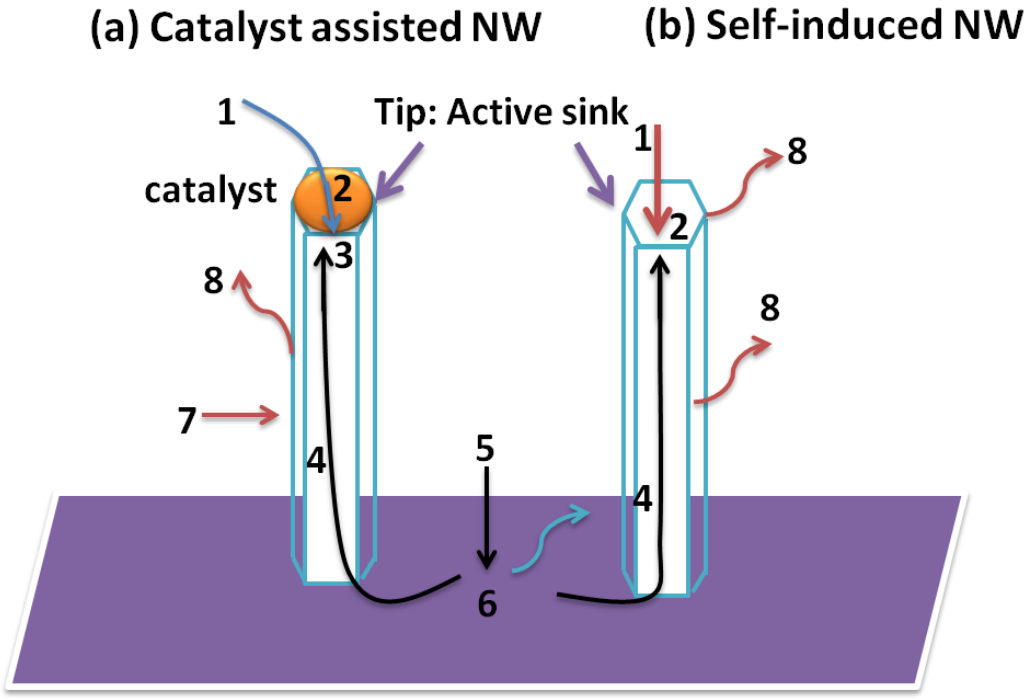

Figure 2.6 *Schematic of the processes involved (a) in the catalyst-assisted and (b) in the catalyst-free growth. (1) Adsorption on the NW tip. (2) Incorporation. (3) Diffusion through the particle and precipitation. (4) Surface diffusion. (5) Adsorption on the substrate. (6) Film growth. (7) Adsorption on the NW side facets. (8) Desorption from the different surfaces.*

A simple model proposed in 1967 by Schwoebel[120] where starting from a surface covered by circular concentric steps, this model assumes different adatom mobilities on top and side-facets and different capture rates at steps for atoms approaching either from the upper or the lower terrace of the step as a consequence of the Ehrlich-Schwoebel barrier. This analysis predicted that for certain capture ratios a "filamentary crystal" with atomically flat sidewalls could be formed. However, all these models always consider the diffusion and impingement of only a single species, even for compound materials. In particular, for the III-V semiconductors the group III atoms are considered as the surface-diffusing, rate-limiting species assuming that the group V atoms are always in excess[121]. But as reported by several experimental results on NW growth by MBE[122-124] (which will be discussed in next section), the axial growth rate of the NWs was evidenced to be group V limited. Also, it is clear that these different species exhibit different adsorption; desorption and diffusion behaviours that are dependent on their ratio[125-126] (different sticking coefficient, different diffusion length, different residence time).

2.2.5 Growth of catalyst free GaN nanowires by MBE

Several studies based on the catalyst-free approach were carried out for the III-V system, but the understanding of the growth mechanisms has been more challenging than that of catalyst-assisted growth. Park et al[127] have studied the formation of InAs NWs on SiO_x in a quartz tube, and concluded that at high temperature the decomposition of SiO_x forms nanometer-sized Si clusters that enhance In attachment rate. This group also compared the nucleation of catalyst-free Ge and InAs NWs and In nanoparticle-catalysed InAs NWs on porous Si[128], and suggested that the NW growth starts from solid nuclei. They observed a correlation between the degree of porosity and the InAs NW formation, suggesting that the pits could act as energetically favourable nucleation sites.

More specifically concerning the III-nitride system and growth by MBE, nucleation studies have been intensively carried out, without a general consensus. At first, the model based on the formation of GaN islands formed upon nitridation of Ga droplets on patterned Si/SiO_2 substrates has been proposed by Guha et al[129] to explain the selective growth of GaN NWs by MOMBE. Similarly, Calleja et al[130] proposed that a self-catalytic growth mechanism for the GaN NW formation on unpatterned Si substrates by solid-source RFMBE. In this model liquid Ga clusters formed by the restriction of the Ga surface mobility imposed by N-excess could act as a catalyst. In addition, a similar self-catalytic VLS process from Ga droplets was suggested for the nucleation of GaN NWs on top of a low temperature GaN buffer grown on Si(111) under N-excess[131-132]. In this case NWs are formed inside V-shaped craters whose concave geometry in the broken GaN buffer favours Ga nanocapillary condensation. In turn, NW crystal seeds would grow inside these openings. Upon variation of the V/III ratio, control on the NW density and diameter could be obtained. More specifically, Ga droplets formed from the thermal decomposition of HVPE GaN films heated in situ in TEM at 1050°C were observed to promote the growth of GaN NWs[133]. In this way, the VLS growth of GaN NWs was evidenced to occur by the redissolution of the decomposition products into the Ga droplets. *Ex-situ* TEM investigation revealed that GaN NWs grown from a similar separate experiment grew along the [0001]GaN directly from GaN pellets and presented a smooth tip free of any Ga droplet[132]. Thus, the absence of metal droplets at the tip of the NWs is not a sufficient argument to invalidate the Ga self-catalytic VLS model. However, this model has been later largely refuted for RFMBE growth[125,134-135], Calleja et al[135] investigated in detail the effect of Ga droplets pre-deposited on Si(111) substrates on the nucleation of GaN NWs. They observed that the NW size and density was independent of those of the Ga droplets, and that large droplets even hinder NW growth. Instead of the Ga self-catalytic VLS mechanism, a model based on the formation of 3D islands acting as a seed for subsequent NW growth is now generally accepted[123,125,136], but the mode of formation of these islands are not elucidated.

Generally, NWs forms under N-excess and their density and size can be tuned by changing the V/III ratio and temperature[123,135,137-139]. However, it has been observed in a

few cases that Ga-excess could also lead to NW growth if the growth temperature is high enough to desorb the excess Ga atoms[140]. For GaN NW growth on Si, Ristic et al. proposed that critical nuclei are formed by a Volmer-Weber (VW) mode driven by the important lattice mismatch with the substrate, where island coalescence is blocked by the preferential incorporation of Ga on the island top side[125]. This idea was based on the experimental result that a wetting layer was not observed by HRTEM[125,139]. However, the group of Calarco et al. reported[136] the presence of a thin and rough wetting layer connecting GaN NWs and small GaN clusters. In this case, the critical diameter for nucleation was deduced from the smallest of those clusters and amounts to 7 nm. On Si(111), this GaN wetting layer forms on top of an interfacial silicon nitride one that is partly amorphous. In contrast to the GaN wetting layer, the silicon nitride one has been invariably observed during GaN NW growth on Si[123,135-136,141]. It was suggested to form prior to GaN growth due to the strong affinity of N to bind to Si atoms[135-136], its 2–3 nm thickness is usually not uniform. Therefore, locally tilted surface appears at Si_xN_y irregularity or at step bunches on the Si surface tilting the NWs [135-136]. However, almost epitaxial contact with the substrate could still remain for the NWs formed at the very early stage of the deposition[136]. Nitridation at 790°C of Si(111) substrates prior to GaN NW growth results in the attainment of a more homogeneous Si_3N_4 layer and in turn reduces the NW tilting angles. In this case, EELS measurement at the Si/GaN interface revealed that Si out diffuses from the substrate within the NWs whereas no Ga was found within the intentionally formed SiN interfacial layer. Thus, it was also concluded that the local accumulation of strain resulting from N penetration into Si or the local enrichment of Si could induce the nucleation of GaN NWs[139]. It is commonly observed that for thick Si_xN_y layer the NWs are growing with random orientation but along the c-direction[123,135-136,139]. From SEM measurements of the NW density before and after the nucleation completion, Calarco et al[142] evaluated the nucleation duration of GaN NWs grown directly on Si(111) was observed to be completed when coalescence of the NWs started but the nucleation duration was very long (60 min at 785°C), and no new NW nucleation was reported following the coalescence. The NW density decreased after a sudden

increase at the early stage of the nucleation. A linear dependence of the mean values of the NW length and the NW diameter on time implied the lateral growth of the NWs[139,142].

For GaN NW growth on AlN buffer, a Stranski-Krastanov (SK) or even a Frank-van der Merwe (FM) (Layer by layer) growth mode of the GaN islands was suggested to be promoted by the lattice mismatch reduction[123,125]. It has been shown that the presence of this AlN buffer on top of Si(111) improves the NW orientation in comparison to nucleation directly on top of the Si substrate,[123,135] and the thickness of such buffer has a strong influence on the NW diameter and density. For AlN buffer layers thinner than 10 nm, this result was attributed to the growth of NWs at the edge of AlN grains[143]. In addition, by a post-growth SEM investigation similar to the one carried out by Calarco et al[144], two nucleation regimes could be identified [123]. In the first one, the lateral and vertical growth rate of the islands, which are initially similar, rapidly drops and increases, respectively, and there is a rapid increase of the island density. In the second regime, the NW density and growth rates become constant. For AlN buffer thicker than 30 nm, a mixture of a faceted matrix and NWs is obtained due to the more favourable island coalescence[135]. In this case, it was observed that NWs nucleate in the centre of hexagonal pits with $(\bar{1}102)$ facets and that atomic N has a stronger influence on the nucleation density than Ga[145]. It was concluded that NW nucleation and growth originate from the formation of specific planes that have different sticking coefficients for Ga, the one of the c-plane being the highest[145]. The nucleation mechanisms of GaN NWs epitaxially grown by plasma-assisted MBE on a crystalline AlN buffer layer are deeply related to the relaxation process of the lattice-mismatch-induced (i.e., epitaxial) strain. An initial process of elastic relaxation proceeds through several successive shape transitions and is followed by a complete plastic relaxation within full pyramids, which results in the formation of the very first NWs. This nucleation mechanism can account for the self-induced formation of epitaxial nitrides NWs, for which a strong epitaxial relation with the substrate operates. It is well known that GaN NWs can also be grown by plasma-assisted MBE on a thin amorphous silicon dioxide or silicon nitride layer. If self-induced GaN NWs are directly grown on silicon without an AlN buffer layer, such an amorphous interlayer inevitably forms owing to the use of an active nitrogen flux leading to a

nitridation process. In this case, the previous relaxation process cannot be involved since it is expected that the epitaxial relation with the substrate is much weaker. It has been suggested that GaN clusters are formed in the very early stages of the nucleation process and could act as a seed for the self-induced formation of NWs. Cheze et al[146] have also pointed out the interplay between the processes of silicon substrate nitridation and NW self-induced formation but the exact nucleation mechanism is still unresolved.

Lymperakis et al[147]. recently showed by first-principles calculations a strong in-plane anisotropy of the diffusion barriers on nonpolar GaN surfaces for gallium adatoms, revealing that the single diffusion-induced mechanism operates but is not enough to completely account for the self-induced NW growth, and Foxon et al[148] suggested that geometric effects in the MBE chamber could play a non-negligible role. The recent mechanisms are based on the prerequisite that the very first NWs have already nucleated and cannot account for their formation. For the self-induced approach, a clear distinction between the nucleation phase, which defines the position and radius of NWs, and the subsequent growth phase, results in a lengthening of the NW nuclei. Songmuang et al[123] mentioned that GaN three-dimensional [3D] islands are formed according to an assumed initial Stranski-Krastanov mechanism and could act as a seed for the subsequent growth of GaN NWs at their top. Calarco et al[144] also stressed the fact that the nucleation process is kinetically slow and could be defined as the process during which the GaN NW density increases before reaching a maximum. The experimental growth of GaN nanowires by MBE using the VLS process has involved the use of a nickel catalyst and N-rich growth, which sees the nickel particle riding the tip of the nanowires. Another reported method of growing GaN nanowires by MBE uses only the N-rich growth regime and Si or AlN substrates. The N-rich growth regime promotes the growth of three dimensional crystal growth and, in the long term, nanostructures due to the reduced adatom diffusion length[135]. The N-rich growth also means that the growth rates are restricted by the gallium flux and the N-rich growth process is also a valid way of growing other III-nitride nanowires. Even with the issues faced with growing GaN nanowires, devices have already been fabricated as both p-type and n-type nanowires[149]. For example as-grown GaN nanowires with two contacts have been used for photodetectors[150]. Also, GaN

nanowire Schottky diodes have been fabricated using a two step metallisation, and by using a scanning probe microscope (SPM) to contact one end of the nanowire to form the Schottky contact[151]. Due to good optical confinement properties, Pauzauskie et al[152] have used GaN nanowires as waveguides, and with the addition of a wrap around contact the optical intensity can be electrically modulated. Researchers have also shown that optical pumping of GaN nanowires can lead to lasing[153]. One of the most well developed devices is the nanowire field effect transistor (FET), which allows for determination of the carrier concentration and mobility of individual nanowires[154]. To produce a p-n junction p-type GaN substrates have been substituted, LEDs have been fabricated and tested. Improvements to the p-n junction have involved Mg-doping of GaN nanowires and junction fabrication by n-type and p-type nanowires crossing over each other or by a junction in one nanowire. Also, the incorporation of quantum wells has been achieved[155]. Presently the focus has been on recreating present devices using nanowires as the active region, although nanowires may offer more unique devices in future[27]. It has been shown that the growth of GaN can also be conducted under Ga-rich conditions, thereby improving growth rates. Moreover, the Ga-rich growth allows for self-seeding growth and the possibility of hierarchical nanowires for unique devices[31]. To study these, both in situ and ex-situ, PA-MBE has been the most appropriate technique due to non-involvement of any complex precursor, and being an ultra high vacuum technique with possibility of monitoring growth in the sub-monolayer regime and fine control of the deposition parameters. Excellent results have been published in literature showing a high density of high aspect ratio nanowires, which have been attributed to the presence of special buffer layers and high Nitrogen to Gallium ratio [N]/[Ga]. Excess nitrogen[156] for the formation of nanowires, and substrate temperature determines the nature of the nanostructures formed[157], and can enable the convergence of the speculation conjectured for the formation of nanostructures. Being a difficult and expensive technique the results from PA-MBE have been sparse and there is a lack of systematic deposition parametric controlled experiments and thus has led to controversial inferences that did not seem to converge. Motivated by this, our attempt here is to present our substrate temperature controlled PA-MBE GaN growth studies on c-plane sapphire (0001) surface, probed by

sophisticated *in-situ* and *ex-situ* techniques. Our results demonstrate the criticality of growth parameters [158] in the formation of GaN nanostructures such as GaN nanowall matrix, faceted nanowires, and nanotubes[159]. We provide direct evidence to the dependence on the GaN matrix layer characteristics and the role of screw dislocations at the interface as the nucleation sites involved in low-dimensional structure formation and we demonstrate that there is no need for buffer layers.

Chapter 3

Measurements and Experiments

3. Measurements and experiments

This chapter is an overview of the experimental techniques and methods employed to obtain results presented in this thesis. First, a description of the fundamental concepts of MBE growth is proposed and then experimental details of film formation and its *in-situ* monitoring techniques are provided. After this a description of the basis of the *ex-situ* characterization techniques employed in this work are given.

3.1 Need for ultra high vacuum (UHV)

If surface of an ideal, clean reconstructed or relaxed surfaces of solid is exposed to atmosphere, atoms and molecules will adsorb and destroy well-ordered surface structure, and the presence of contaminated layers will prohibit controlled, systematic investigation of the surface properties. UHV is required for two principal reasons; one is to enable atomically clean surface required to maintain a contamination-free state for the duration of experiment and other is to permit the use of low energy electron and ion-based experimental techniques without interference from gas phase scattering. To use probes such as RHEED, LEED, XPS, AES etc, for surface studies the mean free path of probe and detected particles (electrons, atoms, ions) in the vacuum environment must be greater than the dimensions of the apparatus so that these particles can travel to and fro from the surface to detector without undergoing any interaction with residual gas phase molecule. This requires pressure better than ~10^{-10} Torr. UHV conditions are generally regarded as being in the region below $10^{-9}-10^{-11}$ Torr. The required pressure depends on the nature of the surface, but for highly reactive surfaces the necessity of UHV is mandatory. **Table 3.I** shows variation in parameters with pressure depending on temperature and molecular mass. Since atmospheric pressure is ≈760Torr, which implies that the number of gaseous atoms in a UHV chamber is ~10^{-12} that of air per unit volume. Thus, for collision free pressure should be <10^{-4} Torr and for maintaining atomic clean surface pressure should

be $<10^{-9}$. Hence, we must work at very low pressures (i.e. ultra high vacuum (UHV)) to maintain clean surfaces for any length of time.

To obtain UHV conditions, initially the vacuum chamber will be pumped down to $10-10^{-2}$ Torr, using a rotary pump/diaphragm/sorption pump, then the chamber will be pumped down to $10^{-2}-10^{-6}$ Torr using a Turbomolecular pump. At this stage, the vacuum chamber is baked to temperature ~150℃ for ~48 hours and once chamber cools down to room temperature, the chamber pressure reaches UHV region. Baking process removes gas atoms adsorbed to the wall of chamber, which otherwise will take months to desorb form the wall surfaces. For large vacuum chamber with large pumping load, cryogenic pumps of large pumping capacity (2000*l*/s) are employed, and to maintain clean environment for longer time at $\sim 10^{11}$Torr, combination of ion-getter and titanium sublimation pumps are also employed.

Degree of Vacuum	Pressure (Torr)	Gas Density (molecules m^{-3})	Mean Free Path (m)	Time/ML (s)
Atmospheric	760	$\sim 10^{25}$	$\sim 10^{-8}$	$\sim 10^{-9}$
Low	1	$\sim 10^{22}$	$\sim 10^{-5}$	$\sim 10^{-6}$
Medium	$\sim 10^{-3}$	$\sim 10^{19}$	$\sim 10^{-2}$	$\sim 10^{-3}$
High	$\sim 10^{-6}$	$\sim 10^{16}$	$\sim 10^{2}$	1
Ultra High	$\sim 10^{-10}$	$\sim 10^{12}$	$\sim 10^{5}$	$\sim 10^{4}$

Table 3I. *approximate variation in parameters with pressure depending on temperature and molecular mass.*

3.2 Molecular beam epitaxy (MBE)

Developed at the end of the 1960's in Bell Laboratories[160], MBE contributed largely to the nanoscience and nanotechnology development by enabling fabrication of tailored compound semiconductor structures with atomic layer precision. The demonstration of a blue violet laser diode fabricated by MBE in Sharp Laboratories in 2004 [161] definitely

showed the potential of MBE to rival MOVPE technique also for commercial applications. However, MOVPE stays the workhorse for industrial III-V epitaxy due to its versatility for the gas sources, its large range of controllable growth rates, and its high productivity with high uniformity achieved during deposition on large surface areas. In contrast, advantages of MBE over the other important growth techniques are the ultra-high vacuum (UHV) environment favourable to *in-situ* growth analytics, the reduced consumption of the source materials, its ability for accurate control on deposition rate that makes it successful as a research tool, and its non-dependence on precursors and their dynamics. The growth temperature of MBE is usually low due to non-dependent on precursor cracking.

The growth experiments presented in this work were carried out in a SVTA Nitride MBE system (**Figure 3.1**) equipped with two Ga, one Al, one In, one Si and one Mg cells. The beam sources were kept at temperatures higher than the melting point of the evaporant (29.8℃ for Ga, 660.4℃ for Al, 156.6℃ for In) in order to prevent the possible cracking of the crucible during solidification. A radio-frequency (RF) plasma source (SVTA RF 4.50) was mounted on a standard port for effusion cells to dissociate molecular nitrogen with purity. The RF generator was operated at the frequency of 13.56 MHz and with maximum output forward power of 500 W in order to produce neutral atomic nitrogen (N). Reflection High Energy Electron Diffraction (RHEED) by Staib, Ellipsometer by Sentech, Optical reflectometer by SVTA, Atomic Mass Absorption Spectrometer (AccuFlux) by SVTA are integrated. A low background pressure ~10^{-11}Torr was maintained in our MBE system by a turbomolecular pump, an ion pump and a cryogenic pump, along with a liquid-nitrogen-filled cryoshroud used to trap impurities and condense unused beam flux. The preparation and load lock chambers are also equipped with ion pump and a turbo molecular pump. The UHV environment preserves the beam nature of the molecules directed toward the substrate by preventing the scattering of the latter with the eventual residual gas molecules. The maximum admissible value of the residual nitrogen gas pressure was estimated to be $p_{max}=10^{-4}$ Torr in order to insure a mean free path of Ga atoms large enough (approximately 20 cm) to reach the substrate surface [162], a condition easily fulfilled in UHV.

On the other hand, the contamination concentration of the growing surface has to remain as low as possible, and therefore the limitation on the maximum admissible value of the residual gas pressure imposed by the very low growth rates. The concentration of each incorporated element depends also on its sticking coefficient, because the typical deposition rate used during the growth of GaN films is even lower than 1 ML/s. For oxygen, a sticking coefficient of 0.12± 0.08 at 300 K on clean GaN(0001)1×1 surfaces has been reported by Janzen et al, and this coefficient could be reduced a hundred times in the presence of an additional monolayer of gallium. In this case, a background pressure higher than 10^{-11} Torr would be acceptable, even considering the already low sticking efficiency of atomic N of 0.36 at 600°C (the one of group III elements is assumed to be unity at moderate temperature) suggested by Osaka et al[163]. Additionally, contamination might have a strong effect on the nucleation phenomena, especially under the unusual conditions for GaN NWs growth, i.e. N-rich and at a low growth Ga-rate. Hydrogen, for instance, is known to enhance the diffusion length of adatoms[164]. Disregarding the sticking coefficient, this is one order of magnitude more than the incorporated flux of Ga atoms corresponding to about $2.86-4.84\times10^{14}$ atoms $cm^{-2}s^{-1}$, so that H-adsorption is negligible under standard growth conditions.

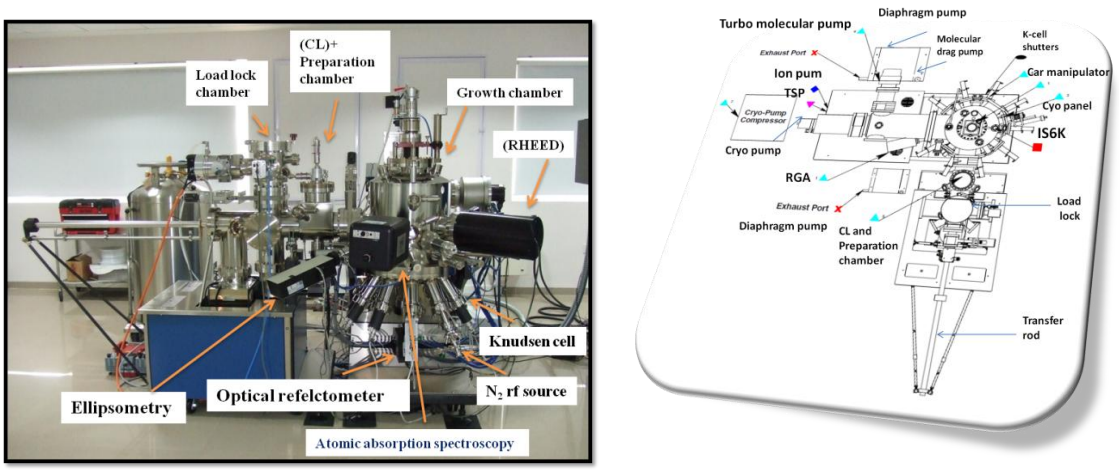

Figure 3.1 *SVTA Nitride Molecular Beam Epitaxy System along with its schematic*.

Group III source (Knudsen cell)

The SVT Associates Effusion Cells, whose schematic is shown in **Figure 3.2**, Models SVTA-275/450/458 with 5, 16, 20, 22, 40 and 50cc capacities, are designed for operation in a UHV environment. The K-cells of Ga and In are designed with hot lip and Al with cold lip style filament heaters. The effusion cells have a PBN crucible, controlled by PID temperature controller and a heater power supply to be fully operable.

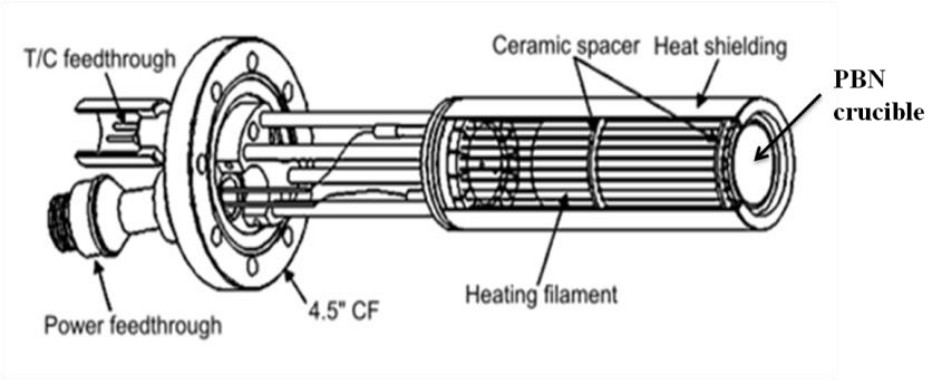

Figure 3.2 *Schematic of Knudsen cell, Models SVTA-275/450/458.*

During growth, the constituent elements to be deposited are evaporated from the aperture of effusion cells containing Knudsen-type crucibles. The maximum evaporation rate Γ_e is given by the Knudsen effusion **equation (3.1)**:

$$d\Gamma_e = \frac{dN_e}{A_e dt} = p_{eq}\sqrt{\frac{N_A}{2\pi M K_B T}} \quad [m^{-2}\,s^{-1}] \text{..... (3.1)}$$

with N_e the number of molecules evaporating from the surface A_e, N_A the Avogadro constant, T the temperature, p_{eq} the equilibrium evaporant pressure, k_B the Boltzmann constant and M the molecular weight of the evaporated material. The conventional crucibles are of conical shape, made of pyrolitic boron nitride (PBN) and their aperture gives rise to a $\cos^2$ intensity distribution. The stability of the deposition rate is guaranteed by the accurate control of the cell temperature as seen in **equation 3.1**, achieved by proportional-integral derivative (PID) controllers. In addition, mechanical shutters in

front of each cell allow the very rapid interruption of the molecular beams in order to switch from a component to another and get abrupt heterostructure interfaces. We have calibrated our metal sources (Ga, Al, and In) by a line of sight ion gauge and atomic absorption spectroscopy (AccuFlux, SVTA, Inc). Since Gallium source is used extensively than other metals in this work, details of calibration of Ga flux is provided.

Atomic absorption spectroscopy

Figure 3.3 shows AccuFlux process monitor by SVTA, USA (Atomic Absorption Spectroscopy) is a non-intrusive optical, highly sensitive and selective technique for determining concentrations of atoms in vapour phase. A light beam with wavelength corresponding to the absorption line of the atomic species of interest is directed across the deposition chamber in front of the substrate where a portion of the beam is absorbed by the atomic flux. The exciting beam is detected and the absorption coefficient is used to compute the flux. The instrumentation is located outside of the vacuum chamber. The AccuFlux Process Monitor utilizes Hollow Cathode Lamp (HCL) technology for generation of material selective and ultra bright radiation. Gallium, Aluminium and Indium HCLs with highly selective UV filters are used to tune the system to the absorption line of interest for the respective material. A UV LED (light emitting diode) signal serves as a reference to compensate for the loss of optical signal due to window coating during deposition. The ultraviolet light is allowed to travel through the vapour flux twice by adding a retro-reflector on a viewport on the opposite side of the vacuum chamber, regardless of its incident angle. A photomultiplier (PMT) accurately detects the radiation even at low light levels. PID temperayture control of the PMT module ensures reduced drift and noise. The optical design includes a modulator ("chopper") that alternately exposes the photo detector to a reference beam of the lamp and the sensing beam. The ratio of these two signals is then digitally processed with a lock-in technique that provides high noise rejection of stray light. Let $\mathbf{I_0^{chamber}}$ be the light intensity of this signal (no flux), detected by PMT. Let $\mathbf{I_0^{ref}}$ be the reference signal (coming from the chopper) and $\mathbf{I_0^{noise}}$ be the noise signal detected by PMT (when all the lamps are off). Note, that $\mathbf{I_0^{ref}}$ and $\mathbf{I_0^{noise}}$ do not depend on presence or intensity of the flux. Then,

$I_0^{norm} = (I_0^{ref} - I_0^{noise})/(I_0^{chamber} - I_0^{noise})$ ..... (3.2)

is the normalized intensity of the light going through the chamber when there is no evaporation. Let $I_f^{chamber}$ be the intensity of the signal, when evaporation of the material occurs and the light goes through the **f**lux.

$I_f^{norm} = (I_0^{ref} - I_0^{noise}) / (I_f^{chamber} - I_0^{noise})$ .....(3.3)

Transmission of the light through the flux can be calculated as:

$T = I_0^{norm} / I_f^{norm}$ ..... (3.4)

Selection of the reference signal in our case is such that I_0^{norm} is always <1.

Absorption $A = 1 - T$ ..... (3.5)

Deposition Rate (DR) is proportional to Absorption for small Absorption values (AA<<1):

$DR = SF \times A$ .....(3.6)

where SF is a scaling factor .

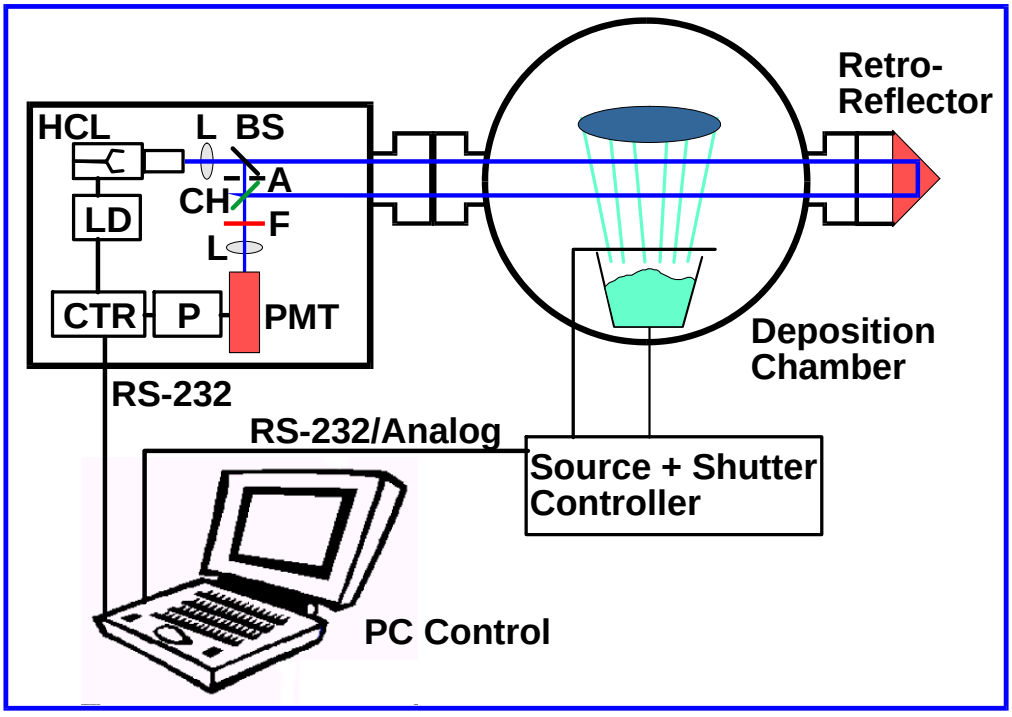

Figure 3.3 *Atomic Absorption Monitoring Technique: HCL= Material Specific Hollow Cathode Lamp, L=Lens, BS=Beam Splitter, A=Aperture, CH=Chopper, F=Filter, PMT=Detector, P=Lock-in-Amplifier, LD= Light Source Drive, CTR=Digital Signal Processor.*

Nitrogen Source (R.F plasma source)

An RF plasma ion source, from SVT associates, is UHV Compatible for MBE Systems. It has an operation power range from 200 to 500 RF Watts, with a built-in manually tuned RF matching network with type N connector and 50 Ohm input impedance, and standard operating frequency 13.56 MHz. Inside the ion source, there is a built-in RF shield. Water cooling is enough to dissipate the heat during the run. The typical gas flow rates are 2 to 8 SCCM for N_2 and O_2. PBN tube is used as the plasma discharge chambers with an interchangeable aperture. This whole source system is mounted in a standard 4.5" CF flange, and the in-vacuum diameter is 2.35", and the total custom length is about 12". The image of the RF plasma ion source is shown in **Figure 3.4a**.

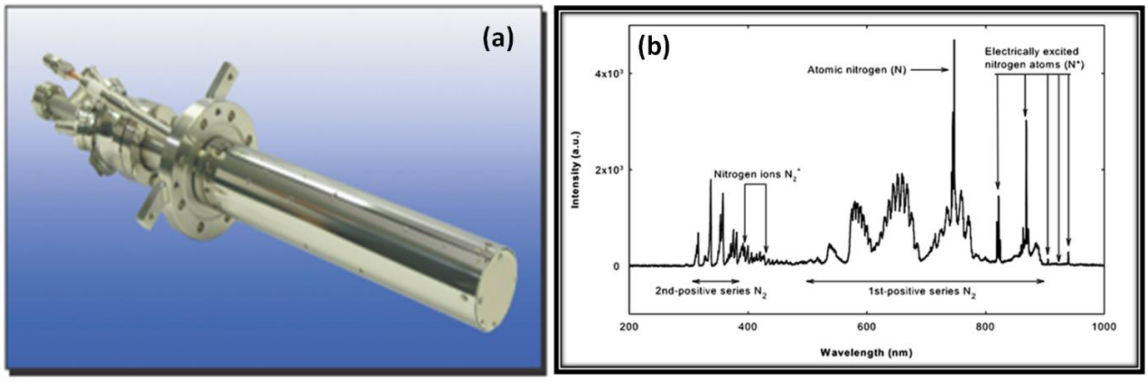

Figure 3.4 (a) *SVTA RF plasma source, (b) is an OES spectrum taken at 200 W RF and a nitrogen chamber pressure of* 1×10^{-5} *Torr.*

The RF plasma ion source has a viewport for monitoring the glow of the running plasma and a plug-in spark igniter to assist plasma ignition. Also, the ion source has three mini ports for a shutter, a high voltage energy controller (a set of grids), and high voltage ion beam deflection plate electrodes. To ignite and stabilize the plasma, an RF matching box for the RF plasma source is mounted directly on the ion source flange. To make the impedance stable, the hot part of the matching box is water and forced air cooled. To remove the ions from the beam, a high voltage plate electrode is used. The ion energy is controlled by three grids, made from UHP (ultra-high purity) graphite. Nitrogen is

produced by creation of plasma, where RF power is used to excite pure nitrogen gas into active species. As the plasma source efficiency is independent of the substrate temperature, this allows for high growth rates at the growth temperatures required for GaN. The energetic nitrogen species that are produced from the plasma source include molecular nitrogen, atomic nitrogen and ionised nitrogen[165]. Each species has its own optical signature and through optical emission analysis (OES) quantitative information regarding nitrogen species can be determined[166]. Collection of the optical spectrum is done through the view port provided on the backside of the plasma source, as it looks directly into the PBN cavity.

A typical optical spectrum from the SVTA-4.5 plasma source is shown in **Figure 3.4b.** The atomic nitrogen (N) species is seen at 745 nm and the electrically excited nitrogen atoms (**N***) appear in the spectral lines of 821, 868, 906, 920 and 940 nm. Compared to the atomic species, the nitrogen molecules are represented by a band due to the accumulation of vibrational and rotational energy in molecular species. The first negative series of nitrogen ions ($\mathbf{N_2^+}$) forms the 391 and 428 nm features. The first positive series of the N_2 band is the main feature in the 600 nm region, while the second positive series of the N_2 band is represented by the features at 316, 337, 357, and 380 nm. From the OES of our SVTA 4.5 plasma source, the plasma appears to be dominated by the atomic nitrogen species at 745 nm. The composition of the nitrogen species can be manipulated by varying the RF power or the nitrogen chamber pressure. With increasing RF power the N_2:N ratio decreases mainly due to the atomic N increasing, determined by peak intensity comparison of the first positive series of the N_2 band at 660 nm and the electrically excited nitrogen atoms (N*) at 869 nm.

Residual Gas Analyzer (RGA)

Residual Gas Analyzers are also known as Mass Spectrum Analyzers. These can sometimes be upgraded to also include energy analysis – in which case they are known as Mass and Energy analyzers. Under UHV conditions the mean free path of the desorbing species is long enough to reach the ionizer. There, they are transformed into positive ions

and separated according to their mass to charge ratio (m/Z) in the electric field of four electrode rods. At the exit of the quadruple an ion detector measures either the ion current directly (Faraday Cup) or the electron current proportional to the ion current and converts the measured current into an equivalent partial pressure. A conventional state-of-the-art quadruple mass spectrometer (Residual Gas Analyzer SRS 200) was also installed in MBE chamber. The schematic of basic RGA system is shown in **Figure 3.5.** This RGA allows the detection of ions in a mass range of 1 to 200 atomic mass units (amu) with a resolution better than 0.5 amu at 10% peak height. The device was equipped with an electron multiplier in order to detect partial pressures not down to 5×10^{-14} Torr with a maximum time resolution of 2 sec. During the present studies, the considered desorbing species are the isotopes 69Ga and 71Ga with occurrence 60.1% and 39.9%, respectively. The RGA is used to evaluate quality of vacuum and leak detection.

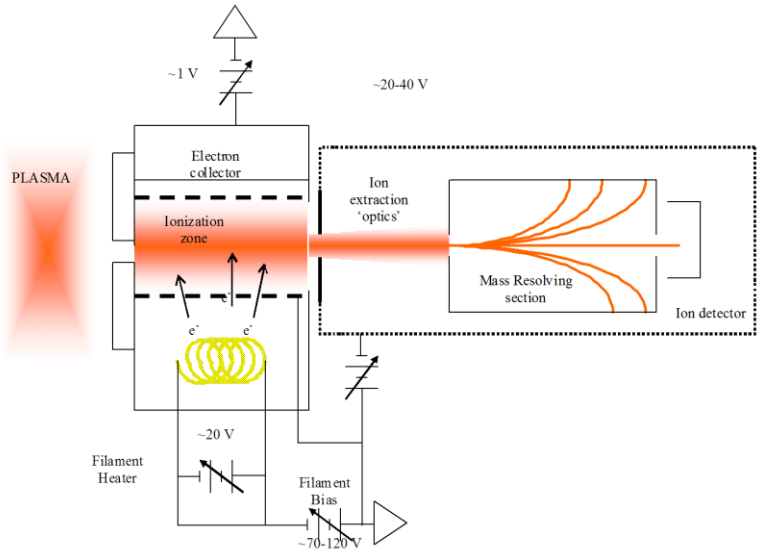

Figure 3.5 *schematic diagram showing major components of Residual gas analyzer (RGA) and typical ion motion.*

3.3 Structure and morphology characterization techniques

3.3.1 Reflection High-Energy Electron Diffraction (RHEED)

Reflection high energy electron diffraction (RHEED) allows us to obtain real-time information about the film surface quality, strain relaxation and growth rate, and the

possibility to determine *in-situ* the evolution of the morphology and the crystal structure of the growth front [167]. The geometry of this technique is illustrated in **Figure 3.6**. The electron source was typically operated at 10 kV and 1.5 A. This high-energy electron beam is directed in grazing incidence (1-3°) onto the sample surface in order to limit the penetration depth and to get sensitivity only to the few outermost atomic layers. The diffracted beams are observed at similar angles on a phosphorous-coated screen that is mounted perpendicularly to the sample surface. The diffraction pattern observed on the screen correspond to the intersection of the reciprocal lattice of the sample with the Ewald sphere of radius $k_i = 2\pi/\lambda$ where k is the wave number and λ the wavelength.

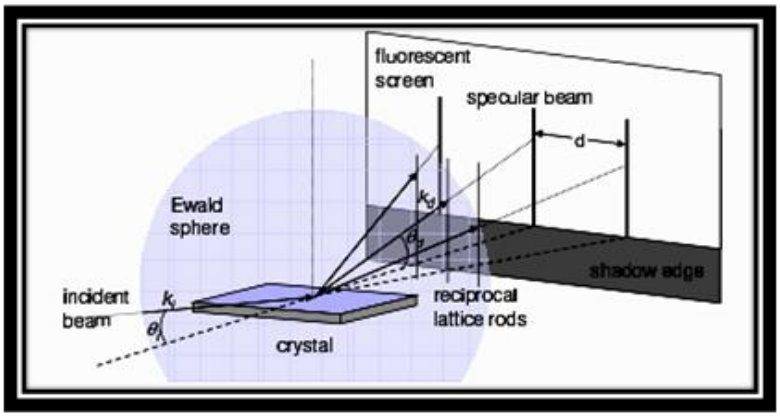

Figure 3.6 *Geometry of RHEED set-up*.

The RHEED pattern is composed of three features: a direct beam which is seen due to the low grazing angle used, the shadow edge of the substrate and also the reciprocal lattice pattern. The grazing electrons only penetrate a few atomic layers, so the information gained can be assumed to originate from a nearly 2D surface lattice; in reciprocal space the distance between the streaks (they are streaks due in part to the lack of atomic-scale flatness over the sampling area) are the inverse distance of the lattice spacing being probed. The surface can be treated as a 2D surface lattice gives a partial understanding, as often in real epitaxy the surface experiences 3D island growth. In the case of an atomically smooth and single-crystalline sample surface, the reciprocal lattice corresponds to a lattice of rods perpendicular to the surface in real space. The Ewald sphere intersection with this lattice should ideally form spots as seen in **Figure 3.7(a)**, but

due to instrumental divergence and crystal imperfections a streaky pattern is obtained[168]. Amorphous layers correspond to a halo without any structure and polycrystalline layers display ring patterns [**Figure 3.7 (b)**]. If the surface is rough, the diffraction is obtained in transmission through the asperities and the diffraction pattern is spotty [**Figure 3.7(d)**]. From the RHEED pattern, it is also possible to gather information on the crystal lattice. Indeed, the distance d between the streaks provides the lattice parameter in the surface plane. For rough surfaces the distance between the planes perpendicular to the growth direction can also be measured.

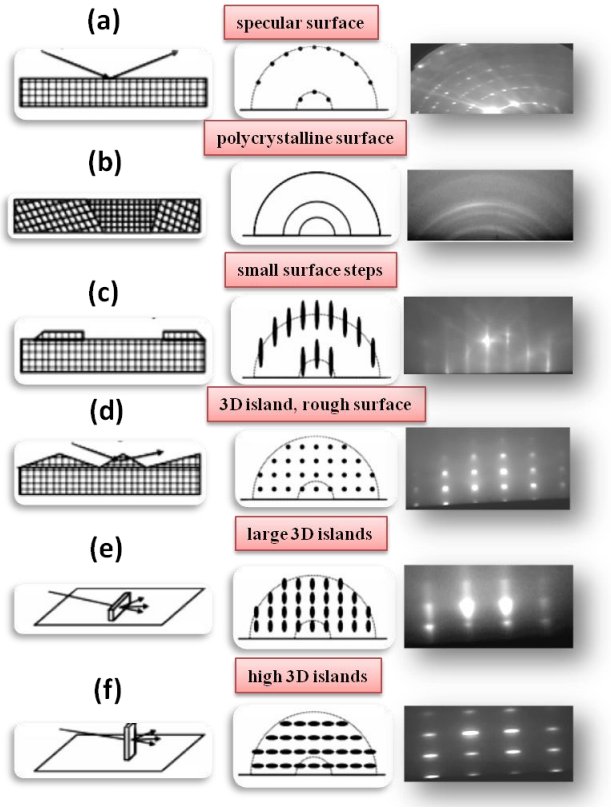

Figure 3.7 *Surface morphologies deduced from corresponding RHEED patterns*.

Determination of c/a ratio from spotty RHEED pattern

To determine c/a ratio from typical spotty RHEED pattern recorded along two orthogonal azimuths <$2\bar{1}\bar{1}0$> and <$1\bar{1}\,00$>. This method is used in this work to examine both in-plane and axial atomic orderings along <0001> of nanostructures. **Figure 3.8**

shows RHEED pattern along azimuths <2$\bar{1}\bar{1}$0> and <1$\bar{1}$00> and the schematic representation of the wurtzite crystal structure. The wurtzite structure is formed from two interpenetrating hcp sublattices, each filled with one type of atom. The paired sublattices are stacked in an ABAB. . . . . sequence along the c axis. Viewing from the <2$\bar{1}\bar{1}$0> and <1$\bar{1}$00> projections, the observed lattice periodicities detected by RHEED are c and c/2, respectively which is in agreement with the axial ordering of RHEED shown on the left and right side of **Figure 3.8** [169].

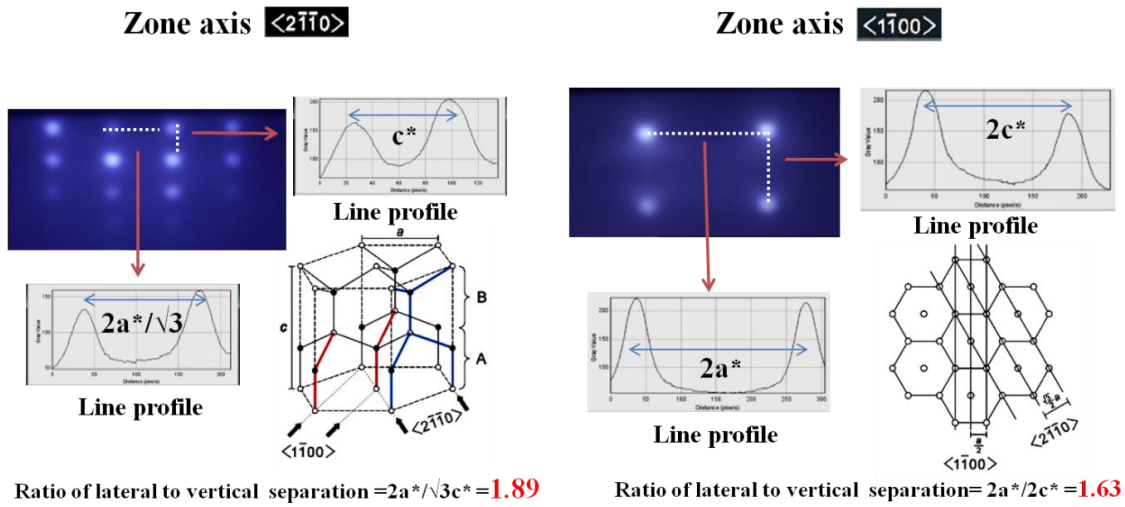

Figure 3.8 *Determination of c/a ratio from spotty transmission RHEED patterns acquired along azimuths <2$\bar{1}\bar{1}$0> and <1$\bar{1}$00>, along with line profiles in both lateral and vertical directions and the schematic representation of the wurtzite crystal structure in each case.*

In addition, the ratio of in-plane RHEED spot periodicities can be obtained from these two electron azimuths. In the growth plane, the measured value is $1/\sqrt{3}$, confirming a hexagonal basal plane. In case of <2$\bar{1}\bar{1}$0> azimuth, ratio of distances between the RHEED spots in lateral and vertical direction is 1.89 which is equal to $2a^*/\sqrt{3}c^*$ ($a^*=2\Pi/a$, $c^*=2\Pi/c$) this implies that the c/a ratio is 1.63, simillary for <1$\bar{1}$00> azimuth, distance between the RHEED spots in lateral and vertical direction is 1.63 which is equal to $2a^*/2c^*$, implies c/a ratio of 1.63. Thus in both azimuths c/a ratio is identical and similar to the thick wurtzite bulk GaN.

3.3.2 High Resolution X-ray Diffraction (HR-XRD)

XRD measurement is non-destructive and does not require any sample preparation prior to measuring. According to Bragg's law, incident X-rays get scattered by an electron cloud surrounding each atom in the crystal and interfere constructively, such that the path difference AB (nλ) between the incident and scattered ray become equivalent to 2d sin θ, where d is the spacing between the atomic planes and θ is the angle between the incident monochromatic beam and the atomic plane. **Figure 3.9** show schematic of X-ray diffraction, where x-ray radiation having a wavelength λ close to the crystal lattice spacing probes a crystal**.** When Bragg's condition is satisfied, each set of crystal planes will produce diffraction spot, with the positions and shapes of the diffraction spots being inversely related to the spacing of the crystal planes and size of the crystallites. These crystal planes are associated with the real space and the diffraction spots with the reciprocal space, spots collectively form a 3D reciprocal lattice. The crystal in general acts as a 3D diffraction grating and the 3D array of diffraction maxima can be investigated when either the sample or detector is moved[170].

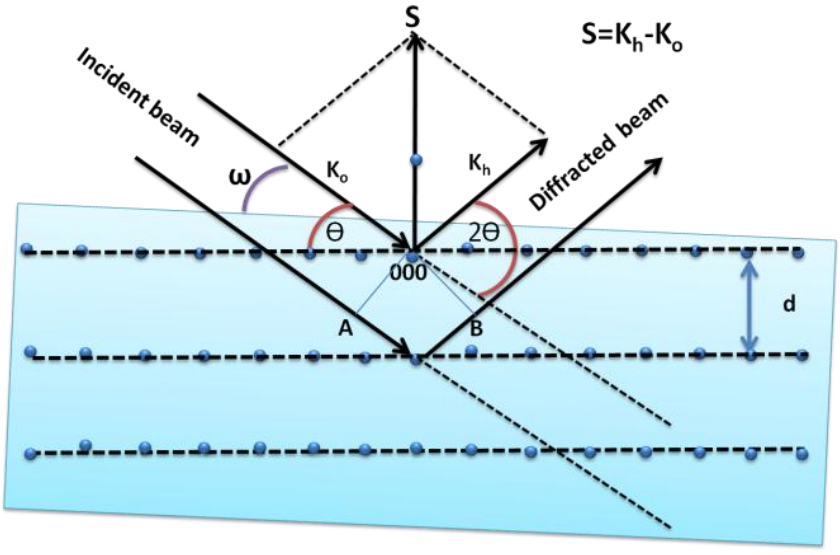

Figure 3.9 *Schematic illustrates x-ray diffraction conditions necessary for Bragg diffraction to occur and relationship of the incident (**k**$_0$), diffracted (**k**$_h$) and scattering (**S**) vectors with respect to the crystal. Planes of atoms are indicated by dotted lines, ω is the angle at which the incident beam meets a crystal plane, when the planes are not parallel to the sample surface***.**

Reciprocal lattice can be constructed by drawing a vector away from the origin in the direction of the normal to a particular set of crystal planes. The magnitude of this vector is 1/d, where d is the interplanar spacing. A point is plotted at the endpoint of the vector and a periodic array of points can be constructed by repeating it for each set of planes. As a result, directions remain the same in both real and reciprocal space, but distances are inverted. Any factor that alters the interplanar spacings will change the positions of the diffraction spots. In context of reciprocal lattice, diffraction can be illustrated as follows: the incident ($\mathbf{k_0}$) and diffracted ($\mathbf{k_h}$) beam vectors make an appropriate angles with respect to the crystal, the scattering vector ($\mathbf{S} = \mathbf{k_h} - \mathbf{k_0}$) will end at a reciprocal lattice point. The scattering vector **S** is the used as probe to investigate the reciprocal lattice and its length can be altered by changing the angle 2θ. The direction, or orientation, of **S** is scanned by changing **ω**, angle which incident beam make with the sample surface.

If we imagine reciprocal lattice being stuck to the crystal then the reciprocal lattice can be moved by moving the crystal with respect to the incident beam. Thus investigation of reciprocal space can be done either by altering the crystal orientation or by changing the length of the probe **S** by changing the angles ω and 2θ. This is illustrated in **Figure 3.10** by using Ewald sphere construction. The same vectors are shown along with a sphere of radius 1/λ (centred at the start of the incident beam vector $\mathbf{k_0}$). This sphere shows part of reciprocal space which can be explored with **S**, given a particular wavelength λ and angle θ. As θ increases, the length of the scattering vector **S** increases, up to a maximum possible length of 2/λ (twice the length of the incident vector $\mathbf{k_0}$). Where the sphere touches a spot, diffraction occurs. Not all diffraction spots can be accessed. The large diffractometer circle in **Figure 3.10** shows the outer limit which can be reached with **S** for a given λ and maximum θ. An offset in ω can be applied (**offset** = θ ± ω), the grey shaded areas (**Torus**) show regions where the sample would block either the incoming or the outgoing beam[171].

In practice, a crystal will rarely give very sharp diffraction spots. Instead, the spots are broadened in reciprocal space by micro structural defects, by the instrumental resolution and the macroscopic size and shape of the sample (such as wafer bending).

Broadening in reciprocal space (as measured in XRD scans) can be defined as **Δs**, where the scattering vector s = 1/d = 2(sinθ)/λ. Features in the real sample can cause broadening in reciprocal space according to the following relationships

$$\mathbf{L}=\frac{1}{\Delta s}\ ,\ \boldsymbol{\alpha}=\frac{\Delta s}{s}\ ,\ \boldsymbol{\varepsilon}=\frac{\Delta s}{2s} \quad \text{..... (3.7)}$$

Whereas broadening due to the limited size (L) does not vary with the distance from the origin (it is independent of s), the broadening due to lattice tilt and twist (α), microstrain (ε, defined as Δd/d) or composition/strain gradients will increase with the increase in the distance from the origin (it is dependent on s), as illustrated in **Figure 3.11**.

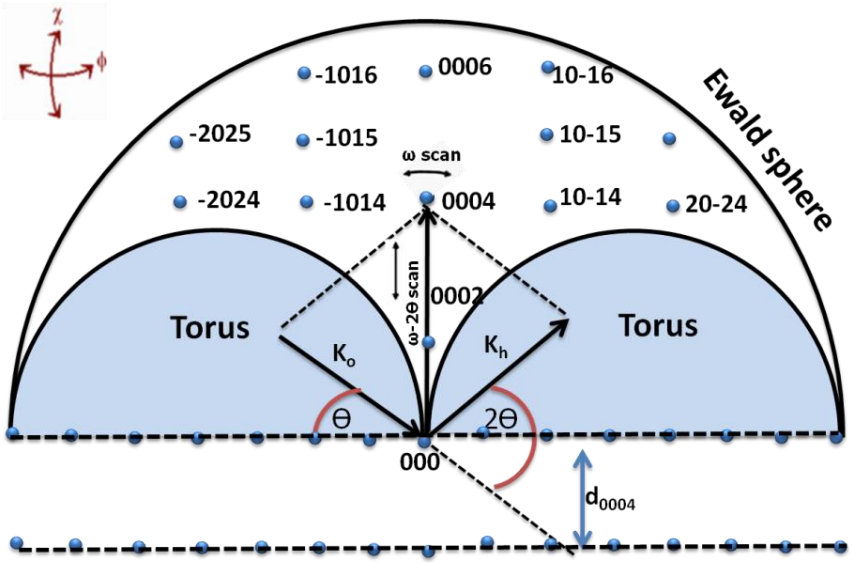

Figure 3.10 *A section through reciprocal space for an [0 0 0 1]-oriented GaN film. Regions of reciprocal space where the sample blocks a beam are shown in grey (inaccessible torus). Here, the vectors* $\mathbf{k_0}$ *and* $\mathbf{k_h}$ *have the length 1/λ (where λ = 1.54 Å); the vector S has a length of* $1/d_{0\,0\,0\,4}$ *and is perpendicular to the (0 0 0 4) plane. The Ewald sphere is shown here as a circle, cutting the 0 0 0 4 reciprocal lattice spot. Some spots are absent as they have an intensity of zero*[16].

Limited size (L) is due to a short x-ray correlation length produced due to a small crystallite size, short average distance between dislocations or limited film thickness (a small feature in real space corresponding to a large feature in reciprocal space). **Microstrain (ε)** is due to small-scale strain variations such as dislocations. Dislocations, stacking faults and point defects can contribute to weak diffuse scattering surrounding

each spot. Lateral microstrain broadening does not affect symmetric reflections, as the planes from which these arise have no lateral component. Wafer curvature will also broaden spots along a solid arc centred about the origin. Reciprocal space can be investigated by rotating the detector or sample in a diffractometer. Diffractometers generally contain an x-ray source, detector, incident and diffracted beam conditioners (such as slits to limit the beam divergence and a monochromator to filter out extraneous wavelengths). For lattice parameter measurements a monochromatic beam having a low angular divergence is needed to perform measurements at high 2θ angles [172]:

$$\frac{\Delta d}{d} = \frac{\Delta \lambda}{\lambda} + \frac{\delta}{\tan \theta} \quad \text{..... (3.8)}$$

where Δd is the precision of the interplanar spacing d, Δλ is the wavelength spread of the radiation, δ is the incident beam divergence and 2θ is the diffraction angle. A low δ is also needed when investigating broadening in the reciprocal space.

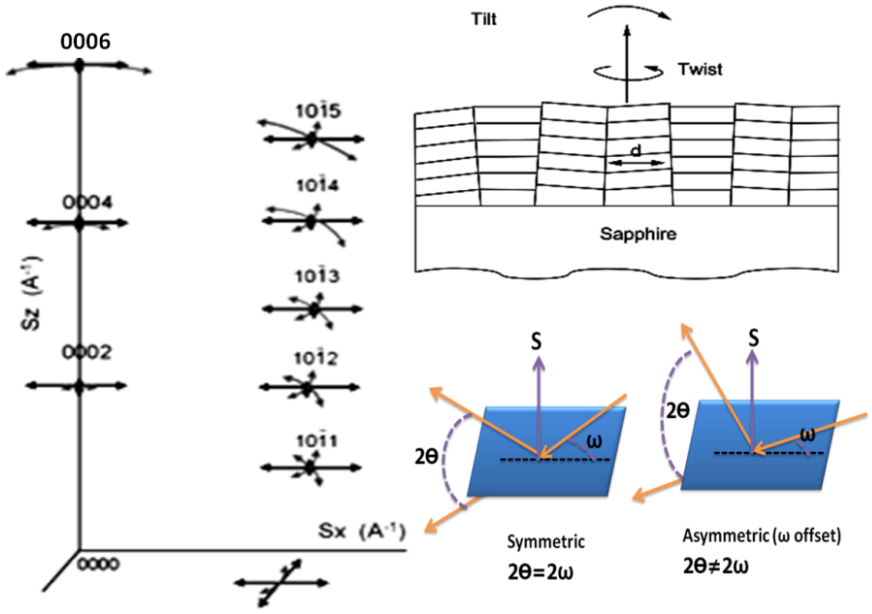

Figure 3.11 *Broadening in reciprocal space due to threading dislocations, tilt, twist and limited size. This can be measured in asymmetric and symmetric geometry.*

Diffractometer capable of providing a low δ and a low Δλ is required. Standard powder diffractometers (**PXRD**) have a divergent beam (δ typically~0.5°) with a

considerable Δλ, along with extra $K_{\alpha 2}$, K_{β} and W lines, reducing the resolution and making it difficult to measure weak peaks near a substrate peak (**Figure 3.12a**). It is optimized to give high-intensity data for non-oriented samples and does not allow reciprocal space mapping as the beam loses focus when the sample is tilted. For oriented samples a parabolic bent graded multilayer mirror can be used to convert the divergent beam to a nearly parallel beam (δ ~ 0.03°) thus reducing the broadening in ω and increasing the intensity (typically by a factor of 10)[173]. For most GaN work high resolution (HR) diffractometers is required (**Figure 3.12b**). These have a primary monochromator to eliminate unwanted wavelengths, reduce Δλ and reduce δ to as low as 0.003◦. Same HRXRD instrument can be used as double axis instrument with an open detector and triple-axis instrument with an addition of analyser crystal before the detector which define the direction of 2θ and gives a with good resolution in 2θ, although with lower intensity. The sample axes of rotation in a typical four-circle diffractometer are shown in **Figure 3.13a**, with different scan types are shown in **Figure 3.13b**.

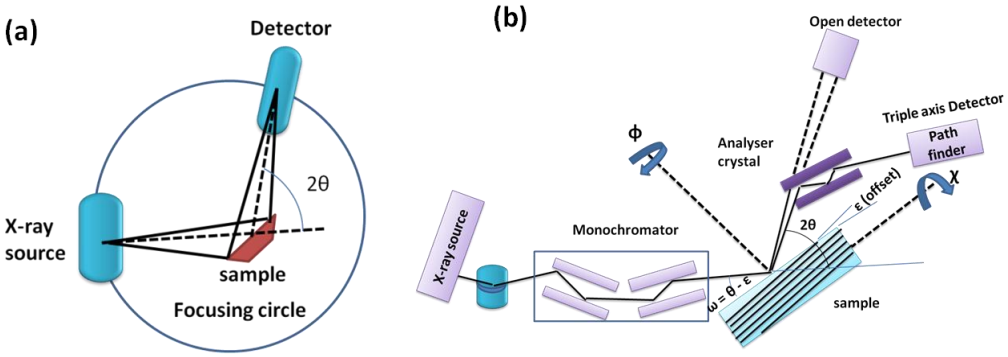

Figure 3.12 *Schematic of geometries for (a) powder diffraction (no incident beam monochromator) and (b) high-resolution diffraction (incident beam monochromator and precision goniometer present, analyser crystal optional)* [174].

ω-scans measure the film quality by scanning the diffraction spot in an arc, detecting broadening by dislocations and wafer curvature. ω–2θ or 2θ–ω scans probe the diffraction spot along a direction that generally has less broadening, and these scans (with an increasing scattering vector) are required for lattice parameter determination. Both ω andω–2θ scans can be called 'rocking curves', as both involve 'rocking' the sample about

the ω-axis (this can sometimes cause confusion). Both types can be performed with or without an analyser, but different volumes of reciprocal space will be sampled. **ω** refers to the angle between the incident beam and the sample surface, **2θ** refers to the angle between the incident and diffracted beams. **2θ–ω scan:** The sample (or the x-ray source) is rotated by ω and the detector is rotated by 2θ with an angular ratio of 1 : 2. In reciprocal space, S moves outwards from the origin. The length of **S** changes, but its direction remains the same and depends on the offset. For 2θ–ω scans, the x-axis is in units of 2θ, whereas for ω–2θ scans, the x-axis is in units of ω. When there is no offset and ω = θ this is a symmetrical scan (θ–2θ) which is vertical in reciprocal space (standard scan type for powder diffraction). **ω–2θ scan,** a simple 2θ–ω scan, but with ω on the x-axis.

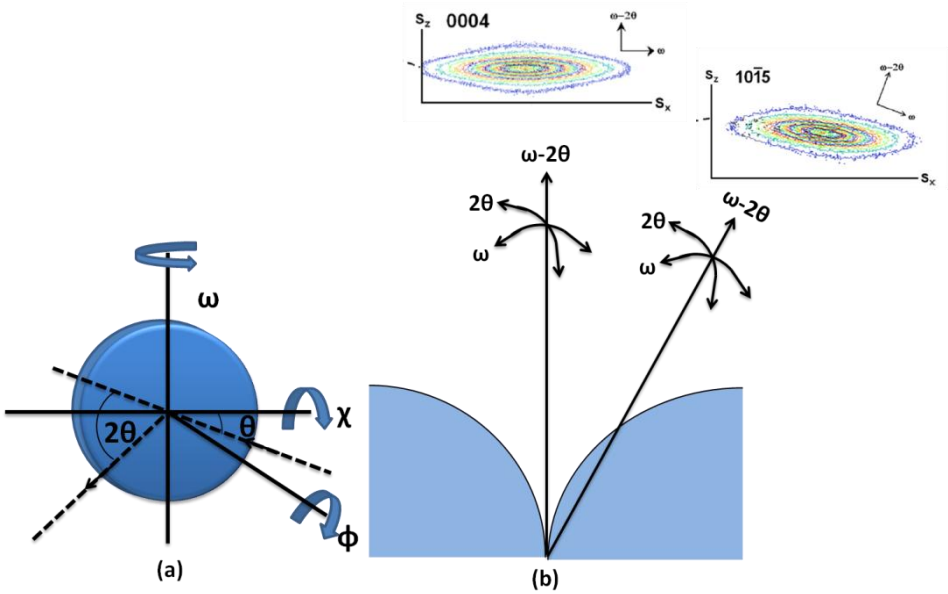

Figure 3.13 ***(a)*** *reference frame of sample with axes of rotation, axis* ***φ*** *is out of plane of page,* ***ω*** *and* ***χ*** *lie in plane of page (arrow inward is direction of incidence and outward for diffracted beam), (b) shows directions taken by different scan types (ω, 2θ and ω–2θ) in reciprocal space. Insets show reciprocal space maps (RSM) of the 0004 and* 10$\bar{1}$5 *reflections.*

3.3.3 Atomic Force Microscope (AFM)

Atomic force microscopy (AFM) is used to acquire profile of the surface of thin films at a nanometre scale. A cantilever with a fine tip is raster scanned over the thin film, when

the tip comes into contact with the thin film surface the cantilever deflects. A laser is used to measure the magnitude of deflection, therefore determining the height in relation to a set point. There are two modes of operation, tapping and contact. Tapping mode vibrates the cantilever, and reduces both the lateral forces on the tip (and the possibility of breakage) as well as collection of impurities on the tip. Contact mode is often an order of magnitude faster (30 sec per scan) and allows for atomic scale resolution, although it suffers from tip wear due to direct contact. AFM does have issues imaging rough samples or samples where the spacing between features is smaller than the size of the AFM tip, as this leads to improper imaging of the sidewalls of the features as shown in **Figure 3.14**. The AFM scans were performed under ambient conditions with a Veeco/Bruker Innova SPM (Scanning Probe Microscope). The instrument was operated in tapping mode with a Si cantilever, with tip radius 10 nm (model RSTEA) and scanning rate 1Hz. The average surface roughness is defined as the root mean square (rms) of the deviation from the mean height in the scanned area. The technique is especially used to measure surface roughness and the density, morphology and size of threading dislocations on GaN surfaces.

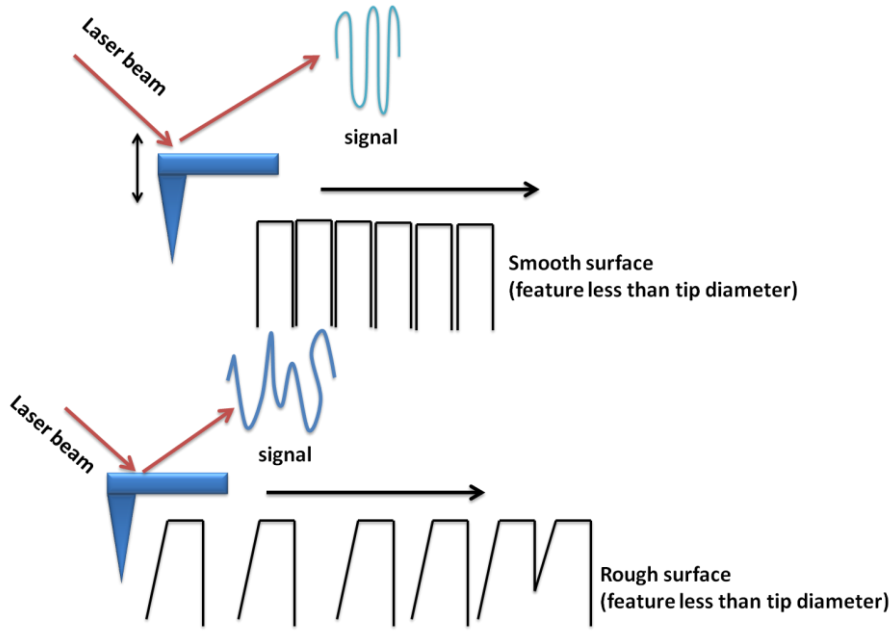

Figure 3.14 *AFM imaging issues due to feature size relative to tip geometry is shown schematically. The top image shows the smooth surface and the bottom represents rough surface along with their expected line scan.*

3.3.4 Scanning and Transmission Electron Microscope

Scanning Electron Microscope (SEM)

The scanning electron microscope (SEM) is a an electron microscope that builds up the images of the sample surface point by point in a time sequence by scanning it with a high energy beam of electrons in a raster scan pattern. The electrons interact with the atoms that make up the sample producing signals that contain information about the sample's surface topography, composition and other properties such as electrical conductivity. A field emission SEM (FESEM) is a type of SEM where a field-emission cathode in the electron gun of a SEM provides narrower probing beams at low currents as well as high electron energy, resulting in both improved spatial resolution and minimized sample charging, and damage. It is used for applications which demand the highest magnification possible. The types of signals produced by a SEM as shown in **Figure 3.15** include, secondary electrons (SEs), back-scattered electrons (BSEs), characteristic X-rays, light (CL), specimen current (SC), transmitted electrons (TEs) and Auger electrons (AE).

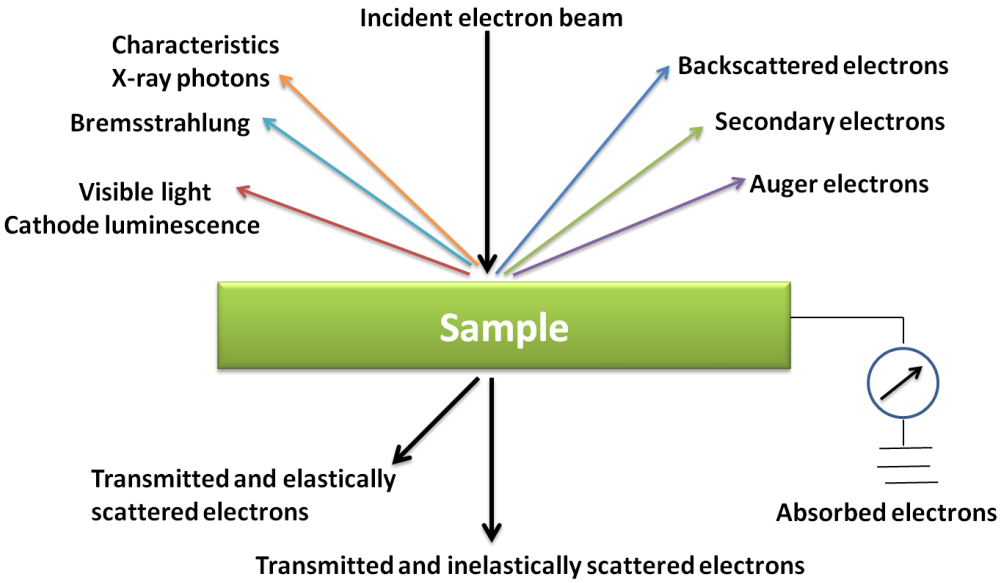

Figure 3.15 *Types of emission from a specimen surface excited by the primary incident electrons in a SEM instrument.*

SEs are sample electrons excited from the top surface layer of the specimen (0-10 nm). They are defined as having energy range 0-50 eV with the majority having energy of 3 to 15 eV. They produce the image of the surface of the sample and give information on sample topography. The emission of secondary electrons from each point on the specimen surface is dependent on its shape. BSEs are scattered beam electrons that emerge from greater depths in the sample. They are defined as electrons those having energy greater than 50 eV with the majority having energy approximately ¾ of the incident electron beam (probe energy). The number of BSEs that are emitted is strongly dependent on the mean atomic number of the specimen at the point of impact of the beam. So as the atomic number increases, the greater the number of electrons that are backscattered. BSEs give depth information and atomic number contrast within the image. Thus BSE images can provide information about the distribution of different elements in the sample. Characteristic X-rays are emitted when the electron beam removes an inner shell electron from the sample, causing a higher energy electron to fill the shell, and release energy as an X-ray with characteristic energy. These characteristic X-rays are used to identify the atomic composition, and measure the abundance of elements in the sample by Energy Dispersive Spectroscopy (EDS). CL light is generated by some specimens that contain electroluminescent materials. CL will be described in more detail in the next section of this chapter. SC is the electron flow out of the specimen to earth, and if an amplifier is placed in the return path of electrons to earth its value can be measured, and can be also be used for imaging. TEs can be detected provided the sample is exceptionally thin, will be discussed in detail in next section. AE are unscattered electrons produced via ionization of sample atoms, and have energies characteristic of the atoms. The most common or standard detection mode, secondary electron imaging (SEI) is used to produce two dimensional scan with topographical feature information about the specimen. The signals result from interactions of the electron beam with atoms at or near the surface of the sample. SEM can produce very high resolution image at or near the sample surface revealing details at nm scales due to the small wavelengths of higher energy electrons which allows better microscopic resolution. In case of field emission this resolution is much better and produces clearer, less electrostatically distorted images. Also high

quality, low voltage images are obtained with negligible electrical charging of samples. A focused beam of electrons is exposed to the sample and secondary electrons are emitted from the surface which are attracted to and collected by a detector. From the density of electrons a map of the surface can be obtained.

To overcome the imaging difficulties faced by AFM for a rough and/or nanostructured surfaces FESEM can be used. The electron wavelength is dependent on the acceleration voltage; in this study the voltage was typically 10 keV. This relates to a wavelength of 0.012 nm, which is significantly below the wavelength of 400 to 700 nm used in a conventional optical microscope, therefore leading to higher resolution images. The SEM imaging is performed with FEI Quant & Nova SEM with a maximum acceleration voltage of 10-30 kV and a typical beam current of 0.1–0.5 nA was used to measure the sample layer thicknesses through secondary electron imaging. Cross-sectional scanning electron microscopy was employed when a higher accuracy of the thickness determination was needed. It should be noted that SEM (and SE) was used primarily for thickness measurement for thick layers. In Scanning Electron Microscopy (SEM), the electron beam is not projected through the whole sample area. Instead, it is raster-scanned across the surface, and the secondary electrons, or x-rays, emit from the surface are recorded. Schematic of Scanning Electron Microscope (SEM) is shown in **Figure 3.16** This generates a lower-resolution image, but allows the direct mapping of surface features, and can even be used for elemental analysis (by study of the x-rays).

Transmission Electron Microscopy (TEM)

TEM (Transmission Electron Microscopy) allows the visualization of thin slices of material with a nanometre resolution. A TEM operates much like a light microscope, but uses electrons instead of visible light, since the wavelength of electrons is much smaller than visible light. Since electrons are used instead of light, glass lenses are no longer suitable. Instead, a TEM uses magnetic lenses to deflect electrons. Beyond this, a TEM is very similar to a conventional microscope, complete with condenser lenses, objective lenses, and projector lenses. Electrons are collimated from the source, passed

through the sample, and the resulting pattern of electron transmission and absorption is magnified onto a viewing screen (the image is typically recorded with a CCD camera). The image which is generated is a 2D map of the material's density (which can be used to map topography in thin samples as well). Schematic of transmission electron microscope is shown in **Figure 3.16**. Aberration corrected TEM can have sub-nanometre resolution and can almost resolve the electron density of individual atoms. A transmission electron microscopy (TEM) study was performed to investigate the defect structures. Cross-section TEM samples were produced by mechanical grinding, polishing, dimpling and ion milling with the Gatan Precision Polishing System (PIPS). Initial milling beam energy of 4keV at 8.0° was used until a tiny hole formed near the central area, and then low energy beam at 3keV at 4.0° was used to remove any ion beam damage. The samples were examined using two-beam conditions in the Technai F20 and high resolution TEM imaging in the Titan FEI. Techniques such as selected area diffraction (SAD) pattern, bright field (BF) image and dark field (DF) image, two-beam condition, high-resolution transmission electron microscopy (HRTEM) are used for **g.b** analysis of defects for investigating the edge, screw and mixed dislocations, stacking faults and grain boundary.

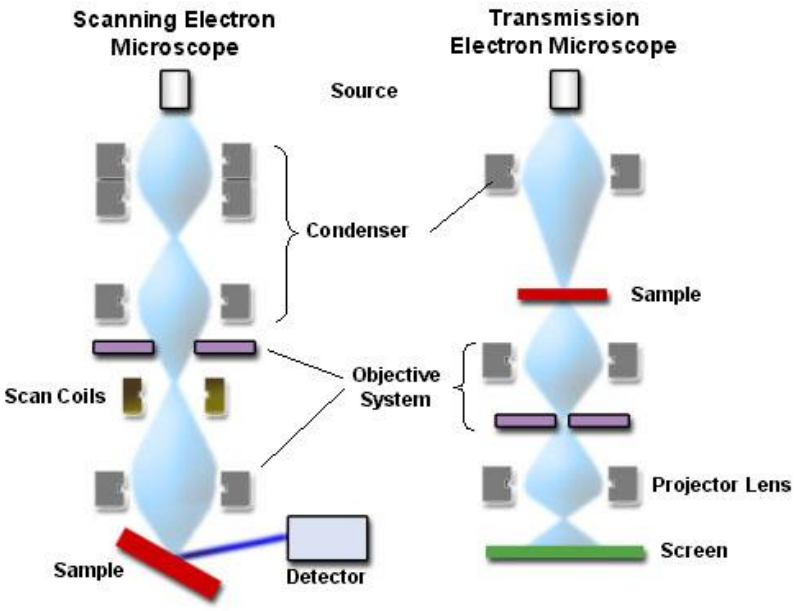

Figure 3.16 *Schematics of scanning electron microscope and transmission electron microscope.*

3.4 Optical Characterization:

3.4.1 Photoluminescence (PL)

Luminescence is generally defined as emitted light from cold objects (due to non-equilibrium excitation levels), in contrast to incandescence, which is the light emitted by hot bodies. There are various types of luminescence, named according to the type of excitation causing the light emission. In this work PL and CL techniques are used for understanding the optical properties of grown films. In Photoluminescence (PL) exciting source is electromagnetic radiation, with typical photon energy just greater than the material bandgap. In Cathodoluminescence (CL) exciting source is high energy (in KeV) electron beam. Optical characterization is a very precise technique for identifying the slightest impurities in a thin films. Photoluminescence (PL) is one of the most commonly used optical techniques, with a photon source used to excite a valence electron into the conduction band, after which the electron then relaxes to the bottom of the conduction band and then to a lower state by emitting a photon. Three processes which are involved in the luminescence as shown in **Figure 3.17** are (a) excitation, (b) energy transfer and thermalisation and (c) radiative transition of the carriers.

In a semiconductor, absorption of photons of energy higher than the bandgap results in the creation of free electrons and holes, which is a nonequilibrium distribution of electron-hole (e-h) pairs. The electrons and holes, respectively, thermalize quickly (~5 ps) to reach thermal equilibrium amongst themselves, and thus reach a quasi-thermal equilibrium described by quasi-Fermi levels in a short time compared to the time it takes for e-h recombination (typically > 200 ps). This thermalisation creates a population of electrons and holes close to the conduction and valence band edges, respectively. In pure materials (where stray electric field effects are small) and at low temperatures, the Coulomb attraction between the electron and hole causes their motion to be correlated, and the resultant Coulombically bound e-h pair is known as an **exciton**. In a pure material without any defect or impurities (intrinsic semiconductor) the exciton centre of mass is

perfectly free to move throughout the material, and thus such a particle is called a **free exciton (FE)**[175].

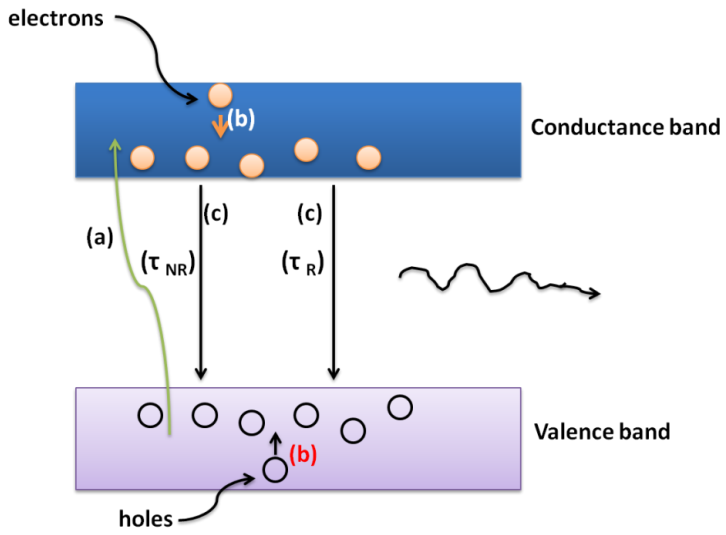

Figure 3.17 *Schematic diagram of the general process of luminescence (a) Excitation by an external source (b) thermalisation and relaxation to create metastable e-h pairs denoted as exciton (c) recombination which can be of two types; radiative (τ_R) and non-radiative(τ_{NR}). The emission of photon due to radiative recombination detected as luminescence.*

In most materials, there are finite concentrations of impurities or defects, and these disruptions of the periodicity of a lattice (impurities, vacancies, dislocations and even large scale defects such as surfaces) may either destroy an exciton or localize it. Impurities can trap a FE, and bind the exciton to the defect location with a certain impurity specific localization energy. These trapped excitons are called **bound exciton (BE)**. The localization energy is dependent on the nature of the defect (e.g. the chemical identity, symmetry, defect charge state etc.). At low temperatures, most of the free exciton in real materials are trapped and bound at defects due to thermalisation effects. As the temperature is raised, these are gradually released to form free exciton. In an impure material (as in the usual case), e.g. a doped material or one with lattice defects, new states can occur in the forbidden gap. Carriers can relax or be trapped in these states and recombination from these states can dominate the luminescence spectra at low temperatures. In the event of radiative recombination from such levels, one photon with an energy equal to the difference in energy between the initial and final state is emitted.

The emitted photon in radiative recombination is detected as PL light, and can be of many types depending on the defect nature. The optical emission may involve other states, so that features may correspond to conduction to valence band transitions (C-V), free exciton (FX), exciton bound to neutral donors or acceptors (A^oX), conduction band to acceptor transitions (CA), or donor to acceptor transitions (DA) as illustrated schematically in **Figure 3.18**

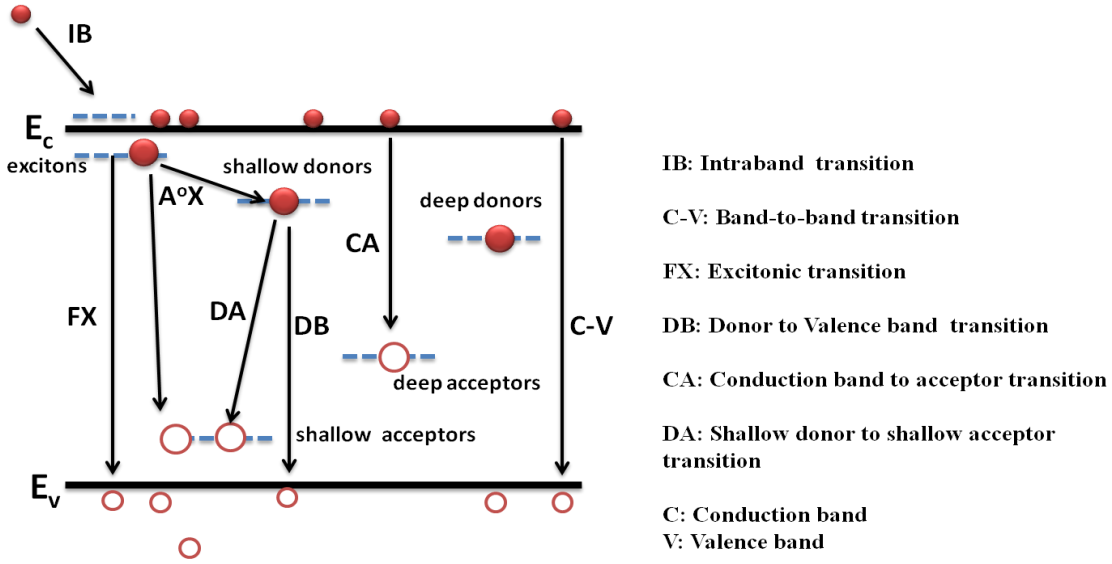

Figure 3.18 *Schematic representation of donor- or acceptor- related and direct radiative recombination's.*

Different radiative recombination paths are shown in **Figure 3.19**. The balance between intrinsic (i.e. free electron to free hole and/or FE) recombination and defect related recombination is dependent both on temperature and defect concentrations. At higher temperatures exciton or carriers trapped at defects tend to be thermally released (with a Boltzmann-factor dependence $\propto e^{-\Delta E_{localisation}}$) and intrinsic (bandedge) emission dominates, whereas at lower temperatures the carriers/exciton remain localized (trapped) at defects and defect-related emission dominates. In addition to the radiative recombination process there is another possible recombination process for excited carriers in semiconductors known as **nonradiative (NR)** recombination. In NR recombination, the excited state energy is converted to e.g. vibrational energy of lattice atoms i.e. phonons. Thus, the electron energy is converted into energy forms other than light at the

desired photon energy and are unwanted in photonic applications. There are several physical mechanisms by which NR recombination can occur. Defects in the crystal structure and multi-phonon emission are two common causes for this type of recombination as they form one or several energy levels within the forbidden gap of semiconductor. These energy levels can be efficient NR recombination centers, in particular if the level is close to the middle of the gap. These deep levels or traps kill or quench the luminescence[176].

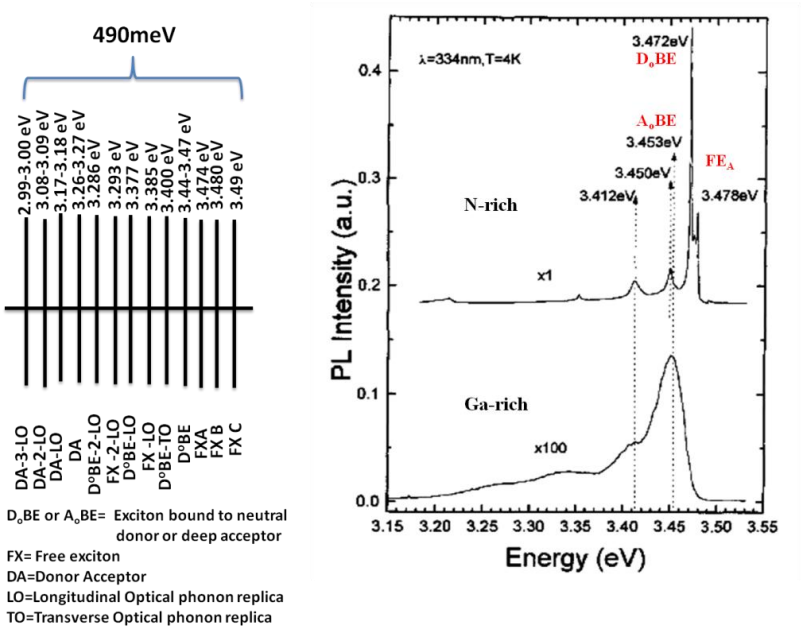

Figure 3.19 *A typical PL spectra at 4K for GaN films grown in N- and Ga- rich conditions. On the left all possible PL transitions in 490 meV spread are shown with their corresponding energy.*

At higher temperatures, as trapped carriers/exciton are thermally released from defects and become mobile they can diffuse through the crystal and encounter various defects which increase the probability of NR recombination at such defects. Thus, at higher temperature the fraction of NR recombination increases and the material's optical emission efficiency generally reduces. The PL photon energy produced in most materials is typically close to the bandgap energy (called near bandedge PL). In the case of recombination of FE in a direct bandgap material, the emitted photon energy equals the

bandgap minus the free exciton binding energy. In the case of recombination of BE in a direct bandgap material, the emitted photon energy equals the bandgap minus the FE binding energy minus the defect localization energy. Thus, as stated above the BE emission spectrum is slightly lower in energy than the FE emission energy, and each different species of defect leads to BE emission at specific photon energies, which enables one to use this emission to identify and study certain specific defects[177].

3.4.2 Cathodoluminescence (CL)

CL is a highly sensitive, noncontact and non-destructive technique used to asses electronic and optical properties of semiconductors with high spatial and spectral resolution. Semiconductors film is excited by an electron beam in a CL plus preparation chamber shown in **Figure 3.20** and luminescence emissions are analyzed. The excitation process in CL is described schematically in FESEM section and the other steps are same as described in PL section. Highly focused beam of electrons is directed onto a sample and light is emitted due to recombination of generated e-h pairs. This process (shown as inset of **Figure 3.21)** is termed Cathodoluminescence. The CL emissions are collected, analyzed and results are a direct measure of the electronic and optical properties. The CL emissions are strongly dependent on many factors such as material properties, electron beam energy and defect centers. Photoluminescence probes an area the size of the laser spot, typically on the order of 500 μm, which is too large for probing individual nanostructures. To obtain better information about individual nanostructure cathodoluminescence (CL) can be used, which is based on the emission of light from electron beam excitation using a SEM. With the enhanced resolution achieved with the SEM, spatial variation in the optical properties can be directly mapped to physical features, as has been seen in nanowires where there is a distinctive difference in the luminescence observed from the wetting layer and the nanowires.

CL spectra of Standard TDI GaN template acquired at ambient temperature (~ 300K), in a scan rage 300-900nm is shown in **Figure 3.21.** Spectra shows strong band edge luminescence (BEL) at ≈3.4eV(364nm) of FWHM≈10nm and defect-related

broadband yellow emission in range (450-700nm). According to Kanaya-Okayama model (**Table 3.II**), acceleration electron beam voltage of 5KV corresponds to penetration depth ≈ 200nm.

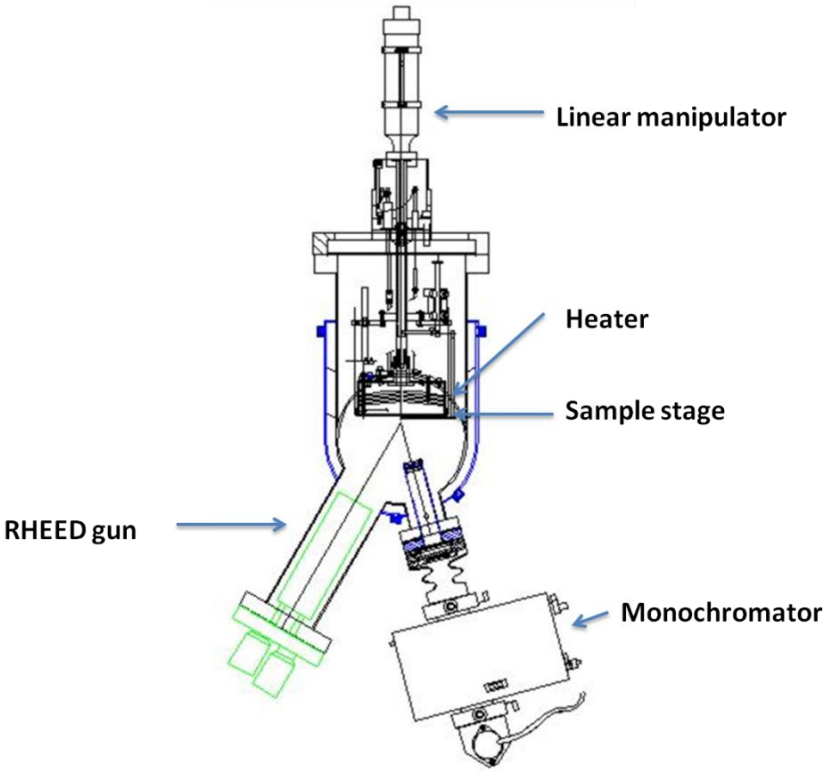

Figure 3.20 *Cathodoluminescence set up in preparation chamber*

V_b (KeV)	5	10	15	20	25
R_e (µm)	0.22	0.70	1.38	2.24	3.25
I_b (nA)	0.22	0.24	0.28	0.38	0.42
I_b $V_{b/}$ R_e (µW/µm)	5	3.4	3.0	3.4	3.2

Table 3.II: *Penetration depth R_e calculated by Kanaya-Okayama model*[178] *for electron beam parameters, accelerating voltage V_b, beam current I_b, spot diameter 0.26nm for wurtzite GaN.*

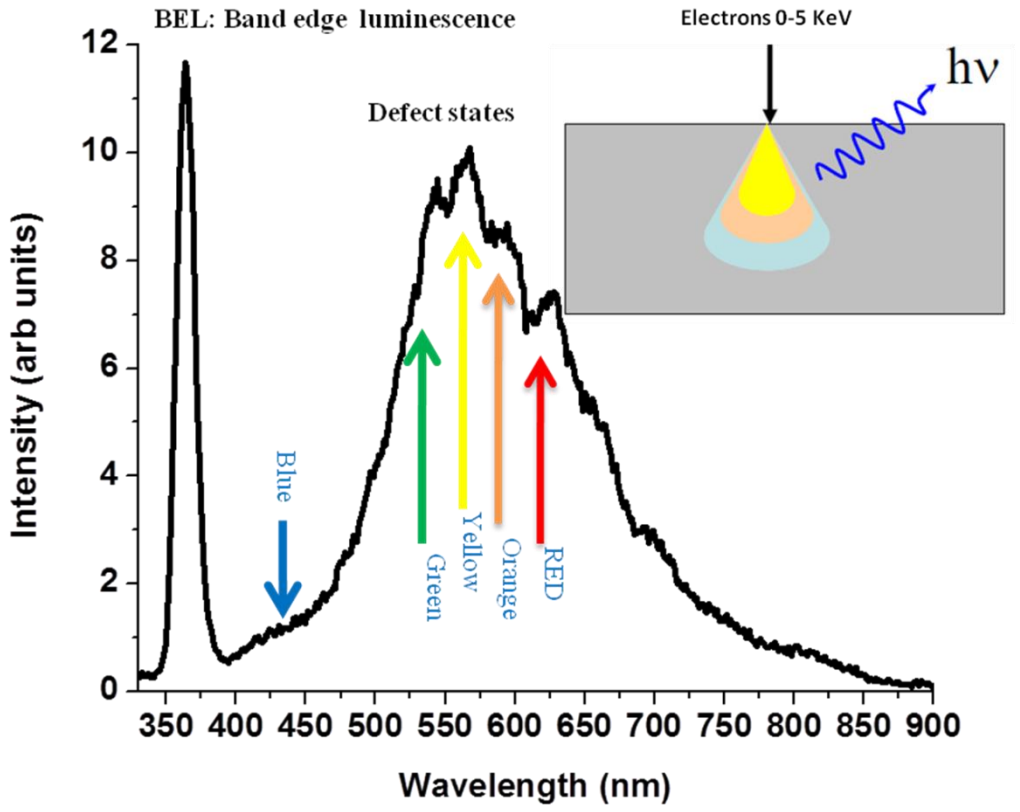

Figure 3.21 *CL spectra of standard 2µm thick TDI GaN template and inset shows schematic of Cathodoluminescence.*

3.4.3 Raman Spectroscopy (RS)

The Raman effect was first observed in 1928 by the distinguished Indian physicist Sir Chandrasekher Venkata Raman who studied scattering in liquids[179]. In that same year the effect was also observed in quartz crystal by Landsberg and Mandelstam. Raman received the Nobel prize in 1930 for his discovery of the effect which by then already bore his name[180]. Elastic scattering is termed Rayleigh scattering (after Lord Rayleigh) and this provides a starting point for the derivation of Raman scattering. Raman scattering is a general term for the inelastic scattering of light by a molecule, an essentially independent collection of molecules (in a gas or a liquid), or by a solid material. In solids the excitations studied are most commonly phonons (quantised lattice vibrations) but other

excitations can give rise to Raman scattering such as molecular rotational excitations (rotons), free-carrier excitations (plasmons) or magnetic excitations (magnons). Dynamic (time-dependent) fluctuations give rise to the inelastic scattering which can be explained by a modulation of the polarisibility. The term Brillouin scattering is usually reserved for inelastic scattering by acoustic phonons in materials. Raman scattering is a standard optical characterization technique for studying various aspects of solids such as lattice properties, electronic properties, and magnetic properties. Raman scattering has many advantages when compared with other spectroscopic techniques: it is in principle non-destructive, contactless, and requires no special sample preparation. Furthermore, when a standard Raman microscope is used with a visible laser for excitation, we can obtain lateral resolution of ~1 μm or less, which is determined by the beam waist of the probe laser at the sample surface. Raman scattering occurs essentially as a result of modulation of the electronic polarizability induced by various elementary excitations in solids such as phonons and plasmons. In the case of Raman scattering by phonons, the scattering efficiency is higher in covalent crystals than in ionic crystals, because the valence electrons are less localized and larger fluctuation of the polarizability can be induced by lattice vibration. From this viewpoint, nitride semiconductors are suitable for Raman scattering studies, since the chemical bonding is a mixture of covalent and ionic bonding. Furthermore, nitride semiconductors are generally robust and stand up well to laser irradiation, which is another advantage of Raman scattering studies.

In our study indigenously assembled Raman spectrometer over an optical bench is used for Raman measurement Water-cooled Spectra-Physics Series 2000 argon-ion laser operated at 488 nm (2.54 eV). Occasionally the visible system was operated at 457 nm (2.71 eV) and 514.5 nm (2.41 eV) excitation. The monochromatic, linear polarised parallel laser beam is first passed through one of several selectable neutral-density filters. Measurements requiring reduced laser power at the sample are quickly achieved by selection of a more optically dense filter. The laser beam is then focussed with a microscope objective and passed through a small pin-hole (diameter ≈20 μm) which provides spatial filtering (reducing non-uniformities in the beam from stray reflections or scattering from dust particles, for example). The beam is then brought back to a parallel

configuration and expanded in diameter by a converging lens. Laser plasma-line filters (band-pass filters) are usually placed in the beam path at this point to remove the laser plasma-lines. The laser beam is directed onto the first of two holographic notch filters (dielectric edge filters in the case of the UV system) which are designed to strongly reflect at the laser wavelength and to transmit with low attenuation at other wavelengths (typically a notch of width 10 nm). The reflected laser beam is then directed onto the sample via a conventional optical microscope typically using a × 50 magnification objective. This gives an effective laser excitation sphere of radius ~ 1 μm for transparent samples. Long working distance objectives are used when the sample is required to be placed further from the objective with an approximate 50% reduction in light collection (and hence detected Raman signal). In some cases × 40 and × 20 objectives are used for measurements at lower excitation density over a larger volume. Lower magnification objectives are used to find areas of interest on samples whilst using the microscope in a conventional manner, i.e., viewing samples through the eyepiece with white light illumination. A camera mounted at the top of the microscope allows electronic storage of these white light images. Reflected and Rayleigh elastically scattered light from the sample together with the inelastically scattered Raman signals are collected by the microscope and are directed onto the notch filters. After the second notch filter the intensity of the elastically scattered light is severely attenuated whilst the inelastically scattered light suffers little attenuation. The light is then focussed through a slit of variable width and dispersed by a motorised diffraction grating (blazed reflection type) onto a CCD camera via a shutter.

The CCD camera is electrically cooled to − 70 ℃ by the Peltier effect to improve the signal to noise ratio. The response of the diffraction grating strongly favours one linear light polarisation such that the response of the visible systems is essentially crossed polarisation detection with respect to the exciting laser light polarisation. Light rays emanating farther out from the centre of the excitation volume (and out of focus rays) are cut out by reduction of the slit width. The CCD (charge coupled device) camera has a rectangular two-dimensional array of pixels. Light falling on each pixel in the array is

converted to a charge proportional to the integrated light intensity. Upon read-out the charges are sequentially shifted across the array and are read electronically at one end of the array. The Raman scattered light is dispersed along the longer dimension of the CCD array. Pixels along the shorter dimension record signals of equivalent frequency (i.e., the same dispersion) but these signals are from points at the sample displaced (from the excitation centre) in a direction perpendicular to the front of the microscope stage (signals from points displaced parallel to the microscope stage would appear along the longer dimension of the CCD array and arecut out by the slit). A Raman spectrum is obtained by read-out of the exposed CCD. Pixels along the shorter dimension are summed together (known as binning). By closing the slit and reducing the number of the binned pixels the system can be operated in a confocal manner. This means that the recorded spectrum is generated from light emanating from a smaller volume in the sample. A personal computer system running software controls the data acquisition aspects of the spectrometer. Via computer software the user can set the spectral range for the spectrum (determined by the angle of the diffraction grating), the exposure time of the CCD (controlled by the shutter) and the pixels used on the CCD for data collection. After exposure of the CCD and read-out the spectrum appears on the computer screen which can then be stored and manipulated.

3.5 Electrical Characterization

3.5.1 Hall Measurement

A very quick and simple analysis tool for determining the electrical properties of semiconductors is the Hall effect. This measurement is performed by ECOPIA Hall effect measurement system, with external permanent magnet of 0.58 T field. The Hall effect measurement gives the resistivity, the carrier density and the mobility of the semiconductor. Using four ohmic contacts in the Van der Pauw layout (corner contacts on a square sample) the sheet resistance (RS) of the sample is determined by measuring the resistance across the horizontal and vertical sides. With the use of a magnetic field

perpendicular to the current flow, the electrons accumulate on one side of the sample. This then can be used to determine the carrier density and mobility. The force due to the magnetic field is known as the Lorentz force and is given by,

$$\mathbf{F} = \mathbf{qV} \times \mathbf{B} = q_x V_x \times B_x \text{ ----------(3.10)}$$

where q is the electrical charge of an electron, B the magnetic field and *v* is the drift velocity. The accumulation of electrons at the bottom of the sample (-y direction) from the downward deflected current and accumulation of holes at the top (y-direction) gives rise to a upward-directed electric field (+y direction) shown in **Figure 3.22**, ε, which balances the Lorentz force to give the Hall field,

$$\varepsilon_y = - v_x B_z \text{ ----------(3.11)}$$

The creation of the electric field ε_y is known as the Hall effect, and the terminal voltage $V_H = \varepsilon_y W$ (W is the film thickness) is the Hall voltage. The drift velocity is defined as,

$$v = \frac{j}{qn} = \frac{1}{Aqn} \text{ ----------(3.12)}$$

where *J* is the current density, n is the number of electrons traversing the cross sectional area A, and I is the electrical current. Substituting equation (3.12) into equation (3.11) to yield

$$\varepsilon_y = - (\frac{j_n}{qn}) B_z \equiv R_H J_n B_z \text{ -----(3.13)}$$

where R_H is the Hall coefficient and is expressed as,

$$R_H = - \frac{1}{qn} \text{ ----------(3.14)}$$

for electrons. Therefore by measuring the Hall voltage for a known current and magnetic field the carrier concentration and carrier type can be determined by rearranging equation (3.14), and assuming a homogeneous structure,

$$n = -\frac{1}{q\,R_H} = \frac{J_n\,B_z}{q\varepsilon_y} = \frac{I\,B_z W}{q\,A\,V_H} \text{ ----(3.15)}$$

where all the right hand terms are known. The equation for sample resistivity can be written in terms of the mobility of the carriers as,

$$\rho = \frac{1}{q\,(n\mu_n + p\mu_p)} \text{ ----------(3.16)}$$

where μ_n , μ_p are the electron and hole mobility, respectively. Assuming an n-type semiconductor such that $\mu_n\, n >> \mu_p\, p$, we may write

$$\rho = \frac{1}{q\,n_n\mu_n} \text{ ----------(3.17)}$$

$$R_s = \frac{1}{q\,n_{ns}\mu_n} \text{ ----------(3.18)}$$

$$\mu_n = \frac{1}{q\,n_{ns}R_n} \text{ ----------(3.19)}$$

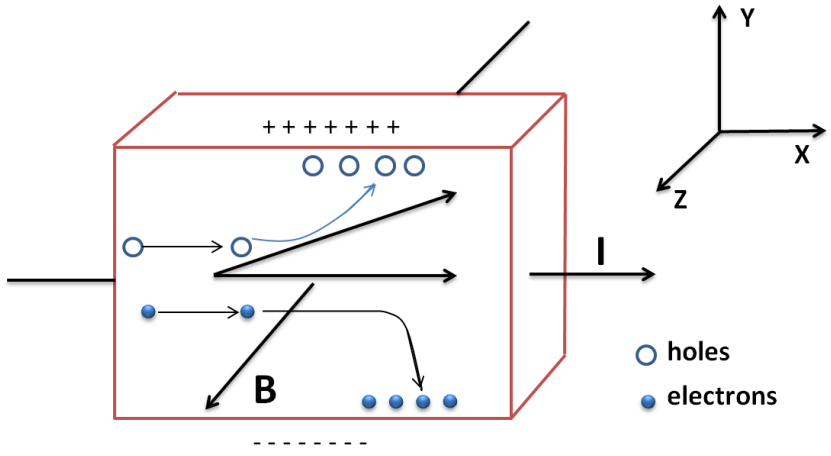

Figure 3.22: *Schematic illustrating the Hall Effect in n-type sample.*

Implicitly assumed in the analysis is that the sample is homogeneous. To determine the mobility and carrier concentration the Van der Pauw method is typically used. The technique is broken up into two measurements, determination of the resistivity

and a Hall measurement. For the resistivity measurement Van der Pauw determined that for an arbitrary shape one only needs to measure the resistance along the horizontal and vertical directions to be able to resolve the sheet resistance. This is done by applying a voltage across one edge of the sample and measuring the current flowing along the opposing edge. Further improvements can be made to the measurement by swapping the sides that the current and voltage is measured from and also by changing the current polarity, and taking appropriate averages. By changing the polarity the influence of the thermoelectric Seebeck effect can be reduced. From the averaged (a total of four resistance measurements per direction) resistance measurements the sheet resistance can be resolved using equation (3.20) by a suitable iteration method [181].

$$e^{-\pi R_{vertical}/R_s} + e^{-\pi R_{horizontal}/R_s} = 1 \text{ ---------- (3.20)}$$

For the Hall measurements a known magnetic field is applied perpendicular to the sample, while a known current is passed across the in-plane diagonal of the sample and the resulting voltage (Hall voltage) is measured along the opposite in-plane diagonal. From the Hall voltage the carrier concentration can be resolved using equation (3.15) and therefore the mobility can be calculated using equation (3.19).

3.6 Calibration

Ga flux calibration by a line of sight ion gauge

Initial base pressure of the growth chamber was ~1 × 10^{-10} Torr when Ga K-cell temperature was maintained at 100℃ (base pressure is considered as a reference for Ga flux calibration). Ga K-cell was throughly degassed prior to calibration upto 1100℃ to discount any error, due to source degassing. For calibrating Ga flux Ion gauge is brought in line of sight of Ga source and substrate. Then Ga K-cell temperature is ramped up to 600℃ in steps of 100℃, during this temperature variation no change in ion gauge reading is observed. K-cell temperature is ramped up in steps of 50℃ from 600-1000℃, and

beyond 1000℃ in steps of 10℃. At each temperature as shown in **Figure 3.23(a)**, Ga K-cell shutter is opened for 10 sec and the difference in ion gauge pressure is plotted on the vertical axis. We have used this pressure difference as Beam Equivalent Pressure (BEP), and considered it as a measure of Ga flux in this entire study[182].

Ga flux caibration by AccuFlux

The deposition rate can be computed based on above equations. Initial reference for absorption and desorption rate for Ga was 0.04Å, which corresponds to zero Ga flux. In **Figure 3.23(b)** Ga absorption and deposition rates are plotted after subtracting reference rate.

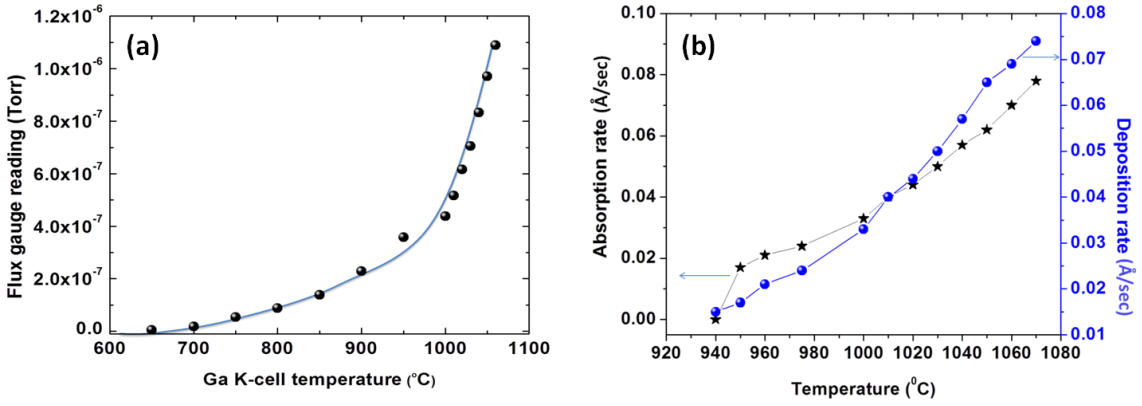

Figure 3.23(a) *Plot of difference in Ion gauge reading on 10 sec exposure to Ga flux versus Ga k-cell temperature,(b)absorption and desorption rate of Ga versus temperature.*

Nitrogen RF source calibration

We have observed that optical emission analysis (OES) spectra may not only differs due to make, type, aperture size, geometry etc., of the nitrogen plasma but it can also varies with nitrogen flow rate which depend on the combination of pumps used during growth. **Figure 3.24**, show variation in ion gauge reading versus nitrogen flow rate with different pumping combinations. For nitrogen flow rate of 3 sccm, growth

chamber pressure is 1.45 × 10^{-5} Torr, 1.91 × 10^{-5} Torr, and 3.91 × 10^{-5} Torr with both Cryo and Turbomolecular pump, only Cryopump and only Turbomolecular pump, respectively. This suggests that the nitrogen pressure can be different for same nitrogen flow rate with pumping combinations which can vary from one system to other. This nitrogen flow rate variation with pumping configuration leads to another variable parameter in nitrogen flux rate calibration. Thus there is a need for an extra parameter to make N/Ga ratio calculation more accurate this may standardize proposed growth diagrams in literature. **Figure 3.25** shows intensity of dominance 745 peak in OES spectrum measured in our system under test conditions at SVTA. On the basis of this calibration be have preferred 375W forward power for entire study.

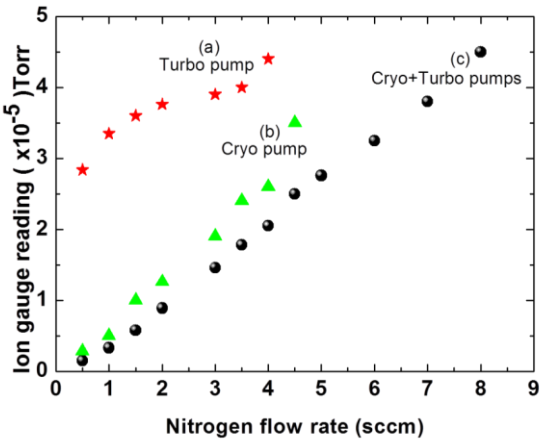

Figure 3.24, *show plots of variation in ion gauge reading versus nitrogen flow rate with different pumping combinations*

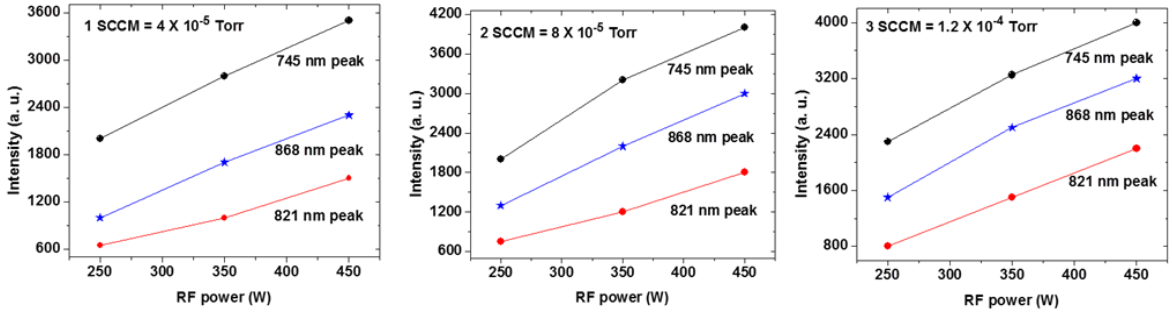

Figure 3.25 *Intensity of 745, 868 and 821 nm peak in OES spectra for different nitrogen flow rate is plotted for different rf power*.

XRD measurement and calibration

The XRD measurements were performed with a Bruker's D 8 Advance four-circle triple-axis diffractometer equipped with a $CuK_{\alpha 1}$ ($CuK_{\alpha 1}$ =0.1540562 nm) source in the focus of a multilayer x-ray mirror and a Ge(022) hybrid monochromator. The instrumental broadening amounts to 0.0033 ° or 11.88 arcsec. The strain state is probed by performing ω-2θ scans with a three-bounce Ge(022) analyzer for the GaN(0002) reflection, which allows to determine the peak positions with a very high accuracy. XRC scans are performed with a wide open detector at fixed position θ_B, leading to an angular acceptance of 1° for our diffractometer. A very quick estimate of the polar orientational spread or tilt can be obtained by carrying out symmetric ω-scans for the GaN(0002) reflection, thus the symmetric XRC scans are a good measure of the tilt. The full-width-at-half maximum (FWHM) or width, for short, of this XRC gives information that is a combination of the tilt and the lateral correlation length. X-ray rocking curves (XRC) in asymmetric coplanar geometry for the $(10\bar{1}5)$ reflections are generally recorded to determine the a and c lattice constants. More time-consuming reciprocal space maps (RSM) are needed to completely decouple the tilt and the lateral correlation length. It should be noted that the symmetric and asymmetric XRC of the c-plane sapphire substrate reflections were found to have a width close to the instrumental resolution, which shows that substrate mosaicity as well as strain-induced bending, which is significant for very thick films, can be neglected in the context of this work. In addition, because of the high intensity and narrow width of the sapphire substrate peak essentially all measurements were optimized using the Al_2O_3(0006) reflection, which was also used as a reference peak.

Chapter 4

Heteroepitaxial growth of 2D films and HEMT structures

4 Heteroepitaxial growth of 2D-films and HEMT structure

In this chapter the results of growth and characterization of doped and undoped 2D-GaN films grown by PAMBE are presented. The objective of work done in this chapter is to obtain a HEMT structure, by growing epitaxial 2D GaN layers of high structural, electrical and optical quality on c-plane sapphire, so as to form sharp interface of GaN and AlGaN heterostructure. The structure needs to consist of transparent and homogeneous layers with a smooth surface morphology and abrupt interfaces. The growth of planar AlGaN/GaN device structure by using Fe doped high quality semi-insulating base layer with improved stability is shown. Effect of n and p type doping on the structural and electrical properties of GaN film is also accomplished.

GaN films are usually grown on foreign substrates, such as sapphire, silicon or silicon carbide, because a large, low-cost, commercial-grade native substrate is still not available. The quality of the GaN film is therefore critically dependent on the ability of the transition layer (or buffer layer) used to accommodate the stress generated from large mismatches in the lattice constant and thermal expansion coefficient. Initially GaN films grown using metal organic chemical vapour deposition (MOCVD) had higher crystalline quality than those grown by the molecular beam epitaxy (MBE). In the MOCVD growth, the transition from a three-dimensional low-temperature (525–600°C) GaN nucleation layer to a two-dimensional GaN growth on a sapphire substrate takes place during the substrate temperate ramp-up to a higher process temperature (1060–1080°C), which effectively reduces the stress and improves the crystalline quality of a GaN film. On the other hand, the PAMBE growth process cannot achieve this transition due to the much lower growth temperature (700–800°C) used for the growth of a GaN layer. Therefore, a high dislocation density is generated as a result of a mismatch in lattice constant between the GaN film and the substrate, which propagates throughout the active GaN layer. However, of-late some of the best GaN devices have been grown by MBE on high-quality GaN templates. Those results have proven the ability of an MBE growth process to achieve GaN films and device structures suitable for high-performance devices if an

intermediate buffer layer is employed. MBE provides several advantages, such as real-time monitoring of material growth using reflection high-energy electron diffraction (RHEED), a carbon- and hydrogen-free growth environment, a smooth surface and sharp hetero-interfaces. Furthermore, GaN films can also be grown under a wide growth regime using MBE, through the careful control of growth parameters, i.e., temperature and Ga/N flux ratios. High quality GaN films are presently grown on AlN buffer layers on c-plane sapphire. Obtaining high quality GaN relies crucially on the pre-deposition of a very smooth and low defect density AlN buffer layers. The ability to meet these requirements is, in general, determined thermodynamically by the growth mode, i.e., two-dimensional (2D) versus three-dimensional (3D) growth, as well as by the growth kinetics. For a given material atomically smooth surfaces are achieved via two-dimensional or step-flow growth when adatom mobilities and surface diffusion lengths are sufficiently high**.** In this section, growth and characterization of high quality undoped GaN layer on AlN buffer layer by PAMBE by optimizing the growth parameters, based on the growth diagrams of Koblmueller and Heying et al[183-184], is attempted. AlN which is an essential material for deep-UV optoelectronic and high-power electronic applications due to its large bandgap and high breakdown field [185], also serves as a template for the growth of high-quality III nitrides, that can avoid internal absorption[186]. Moreover, an AlN buffer template is helpful for reducing current leakage in electronic devices[187]. Therefore, the high quality of GaN layer depends on the quality of AlN buffer layer, which makes MBE the preferred technique for the growth of high quality III-nitride films.

4.1 Growth of GaN over AlN buffer layer on c-plane sapphire

Growth of epitaxial high quality GaN film on sapphire is initiated by growing a thin AlN nucleation layer followed by a thick GaN layer in order to obtain film with reduced defect density. Sapphire substrates are first de-greased for 5 mins in acetone and methanol, respectively, and rinsed thoroughly in deionised water and dried with N_2. In order to get rid of the substrate surface of oxides thermal cleaning is done *in-situ* by heating the substrate at ≈500℃ in the MBE preparation chamber for 1 hour and then again at 800℃ in the growth chamber to remove the surface oxides. Growth diagram

proposed by Koblmueller et al [183] to obtain smooth AlN films of high structural, optical and electrical quality is shown in **Figure 4.1**. It is divided into three regimes, developed by varying Al/N ratio (Al flux is varied under constant nitrogen flux) and growth temperature for a large number of AlN layers grown on sapphire. Growth of AlN in N-rich or Al-deficient (Al/N<1) regime leads to rough surfaces (spotty RHEED pattern **C**), Al-rich or intermediate regime (Al/N>1) at high temperature leads to atomically smooth terraces (truncated streaky RHEED pattern **B**), and Al-rich conditions (Al/N≫1) lead to large Al droplet formation on AlN film surface, manifested as very low intensity streaky RHEED pattern **A**. The boundary line between the N-rich and Al-rich intermediate regimes is typically defined by the transition from a spotty to a streaky RHEED pattern at the limit where the Al flux equals the N flux, in the substrate temperature range of 775–820°C. The Al-droplet regime is separated from the intermediate regime by a boundary line [183]. We have used the intermediate Al-rich growth condition (marked as star in **Figure 4.1**) to obtain flatter surface morphology with good crystal quality of AlN layer.

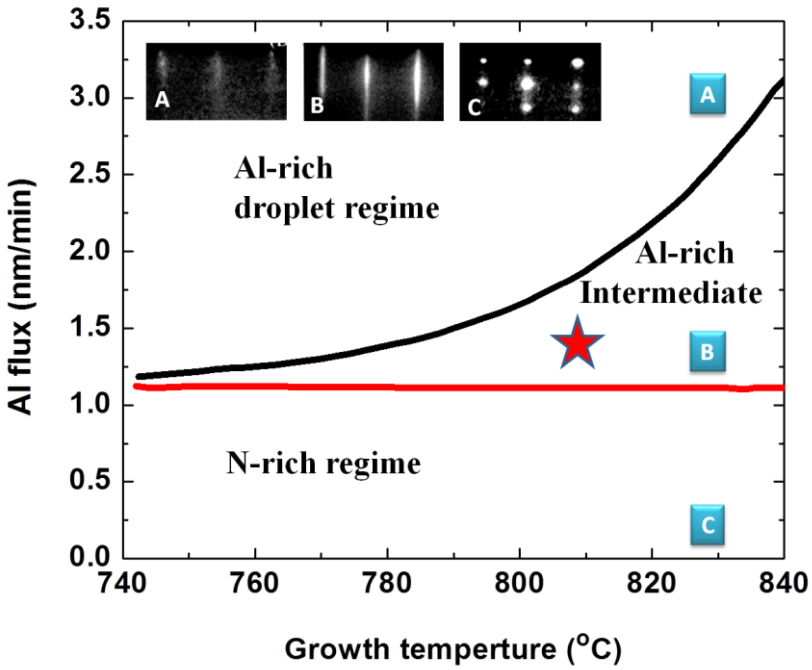

Figure 4.1 *Shows the plot of Al flux (active N-flux is kept constant) versus AlN growth temperature (rescaled from Ref [183]), star mark in figure shows growth conditions used to grow AlN buffer layer over c-plane sapphire. Inset shows RHEED pattern corresponding to each growth regime*

Growth diagram proposed by Heying et al [184] to obtain smooth GaN films (similar to **Figure 4.1** for AlN) of high structural, optical and electrical quality is shown in **Figure 4.2**. The plot has three regimes, observed by varying both the Ga/N ratio as a function of growth temperature. The Ga-flux is normalized to a constant active N-flux and the growth of GaN film in N-rich (Ga/N<1) regime leads to a rough surface with smooth plateau and very steep valley with root-mean-square (RMS) roughness ≈5−40nm (intense streaky RHEED pattern **B**), whereas nanocolumnar growth is favoured at temperature <760℃ under extremely N-rich conditions, as will be discussed in subsequent Chapters. Under N-rich conditions Ga desorption rate is higher than the arrival rate thus possibility of Ga bilayer formation is negligible. Heying et. al. [184] have determined a wide growth window at nominal growth temperature of 760℃. Since the wide range of Ga-fluxes (N-flux being constant) can be used to achieve Ga-stable growth conditions. Under Ga-stable regime (Ga/N>1) growth at high temperature leads to atomically smooth terraces (truncated streaky RHEED pattern).

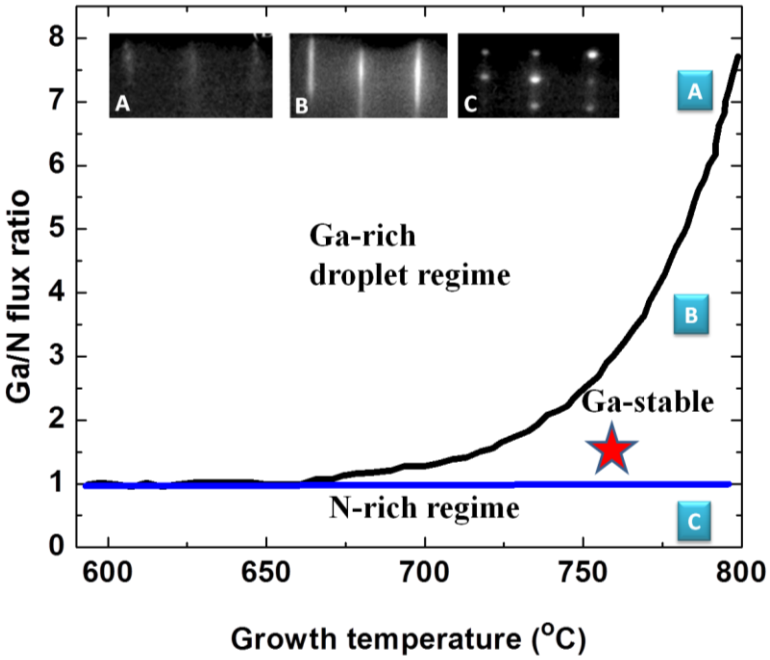

Figure 4.2 *shows plot of Ga-flux (active N-flux is kept constant) versus GaN growth temperature (rescaled from Reference. [184]). Star mark in figure shows growth conditions used to GaN layer over AlN template. Inset shows RHEED pattern corresponding to each growth regime*

On increasing to high flux results in the transition into the Ga droplet regime as shown in **Figure 4.2**. Under Ga-stable regime (Ga/N>1) at high temperature leads to atomically smooth terraces and the growth window becomes narrower and narrower until it ceases completely, since no room is left for adjustment of the Ga flux to attain the desired bilayer growth regime. A miniscule increase of the Ga flux leads to Ga droplet formation, whereas, a very small decrease of the Ga-flux results in N-rich growth with a rough plateau-valley sample surface morphology as an outcome. Ga-rich or droplet regime (Ga/N≫1) leads to large Ga droplets on GaN film surface (very low intensity streaky RHEED pattern **A**). Here, the incoming Ga flux is so high that Ga starts to accumulate which eventually leads to droplet formation because the flux of desorbing Ga cannot match the amount of Ga arriving at the surface. The RHEED pattern becomes very diffuse and of a very low intensity. Thus RHEED provides a convenient and good monitor to detect Ga rich growth conditions, in-situ during growth.

High quality GaN layer is grown on an atomically clean (0001)Al_2O_3 substrate, on which 1–2 monolayers AlN is precisely grown at 810℃. On smooth AlN template, GaN layer of thickness ≈1.3 μm is grown at 760℃. This temperature is at the higher end of GaN growth, because at ≈800℃ GaN starts dissociating, resulting in lower growth rates and rough surface morphologies. The forward plasma power was set at 375 W and Ga K-cell temperature 1060℃ (Ga BEP∼10^{-6} Torr), Al K-cell temperature 1370℃, and the N_2 flow rate was set to 4.5 sccm (∼10^{-5} Torr) which corresponds to a metal-stable or bilayer growth condition. The flux was also determined from the scanning electron microscopical thickness measurements from cross sections of thick GaN layers grown under Ga-rich conditions. Under these conditions all excess uncreated Ga desorbs from the growing surface at typical growth temperatures and thus the growth rate is limited by the active N flux. Analogously, the Al and Ga flux in terms of growth rates are determined from thickness measurements of AlN and GaN layers grown under N-rich conditions. The beam equivalent pressure of Ga and Al was also calibrated to the Ga and Al flux in terms of growth rate by measuring the thickness of films grown under N-stable conditions. In the following, all fluxes will be given as equivalent GaN growth rates in nm/min (assuming that the respective element limits the growth rate).

The nucleation of AlN on (0001)Al_2O_3 occurs through the formation of 2D layers. The zeroth and first order bulk streaks observed in RHEED pattern in **Figure 4.3** are indicated by white arrows. During growth and after growth of GaN film on a smooth AlN template, RHEED patterns are observed along [1$\bar{1}$00] and [11$\bar{2}$0] (**shown in Figure 4.3**) remain streaky with faint kikuchi lines and crossings, an evidence of a smooth and compact surface layer. This indicates that growth of GaN layer proceeded in a layer by layer growth mode (Frank Van der Merwe or 2D growth).

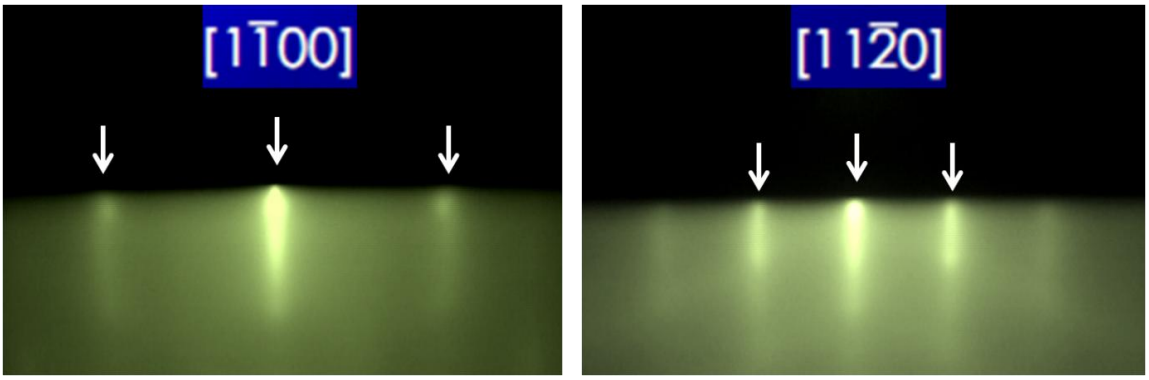

Figure 4.3 *RHEED pattern of GaN film acquired along* [1$\bar{1}$00] *and* [11$\bar{2}$0] *azimuth, zeroth and first order bulk streaks are indicated by white arrows.*

A 2θ–ω XRD pattern shown in **Figure 4.4(a)** of an undoped GaN film has peaks at 2θ= 41.6° and 91.5° that correponds to (0006) and (00 12) reflection from the sapphire substrate. And peaks at 2θ= 34.5°, 72.5° and 126.5° are indexed as (0002), (0004) and (0006) of the wurtzite GaN. For high crystalline epitaxial GaN films, the main tool for characterizing the structural and quality of the prepared films is the rocking curve measurement. Two types of rocking curves (**Figure 4.4b**) have been obtained: normal rocking curve measurement (ω-scan) and triple axis rocking curves have been obtained curve measurement (ω/2θ-scan). The normal rocking curve (ω-scan) is the change in the diffracted beam intensity due to the change in the incident angle θ(°). The triple axis rocking curve (ω/2θ-scan) is the change in the diffracted beam intensity due to the change in the θ-2 θ coupled together. The full width at half maximum (FWHM) of the normal rocking curve (ω-scan) refers to the elongation of the reciprocal space distribution [one

plane of the unit cell (hkl)] in the horizontal direction, while triple axis rocking curve (ω/2θ-scan) refer to elongation of the reciprocal space distribution [one plane of the unit cell (hkl) in the vertical direction.The elongation of the reciprocal lattice in vertical direction (ω/2θ-scan) is 108 arc sec and in horizontal direction (ω-scan) is also 108 arc sec. Thus, this equal and narrower elongation in both horizontal and vertical directions is an indicator of the high crystalline quality of the film. From symmetric reflections (0002) and (0004) crystal plane the estimated lattice constant is 5.175Å which is closer to the bulk lattice constant along c-axis.

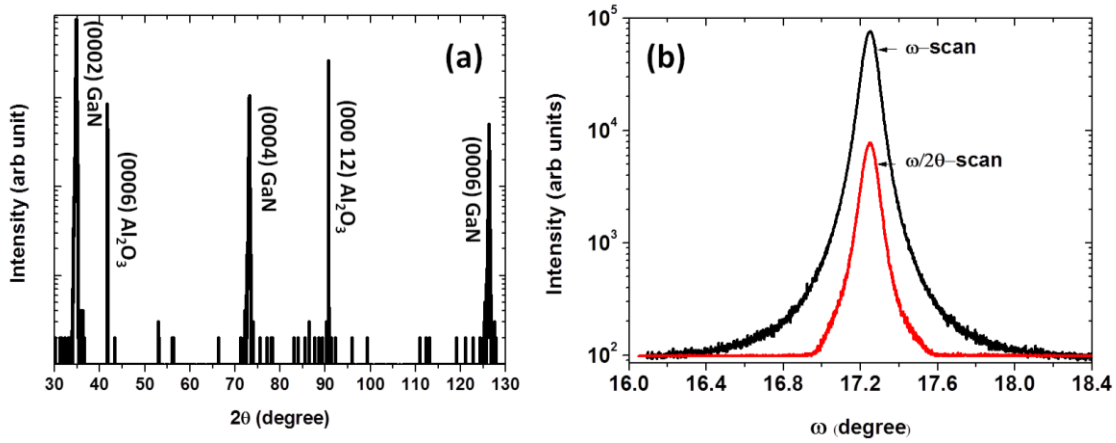

Figure 4.4 (a) *shows 2θ–ω XRD pattern,* ***(b)*** *rocking curves (ω-scan and ω/2θ-scan) along (0002) reflection of undoped GaN film.*

Figure 4.5 shows the RT absorption spectra of our undoped GaN film. The optical energy gap, E_g, is generally determined from Tauc's expression for direct band gap semiconductor by a linear extrapolation of the plot of $(\alpha h\nu)^2$ versus hν to the energy axis. The physical basis of Tauc's expression is the assumption of parabolic energy bands, an energy-dependent momentum matrix element and a relaxation of momentum conservation. **Figure 4.5 (a)** shows room temperature absorption spectrum reported by Maruska et al[188] which was the first accurate measure of GaN direct band gap energy ≈3.39 eV. **Figure 4.5(b)** show the oscillations in the plot of α versus hν, the absorption spectrum of the high quality undoped GaN film grown in our lab yields a band gap energy ≈ 3.4 eV, and thus confirms good optical quality of GaN film.

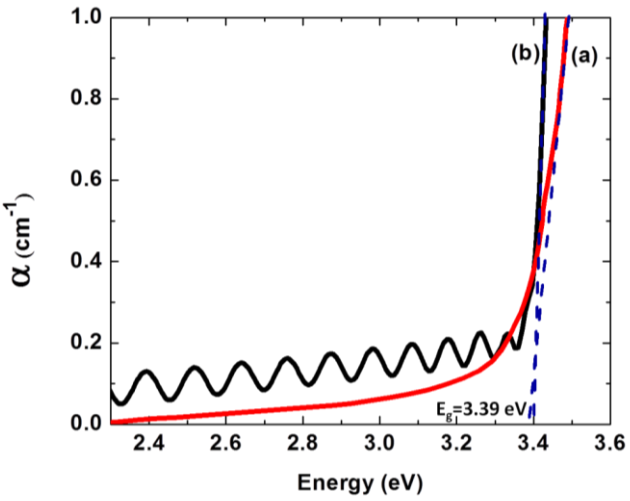

Figure 4.5 *(a) room-temperature absorption spectrum of bulk GaN (absorption coefficient α) reproduced from reference* [188]**,** *(b) absorption spectrum of GaN film grown over AlN layer on c-plane sapphire, in our study.*

Scanning electron microscopy (SEM) in combination with atomic force microscope (AFM) was used to characterize sample topological surface morphologies. **Figure 4.6(a)** shows SEM image, while **Figure 4.6(b)** the AFM micrograph of a GaN sample over a 5×5 μm^2 area (acquired at different region of the film). The peak-to-valley (P-V) roughness is ≈7 nm and the root-mean-square (RMS) roughness is ≈1 nm. The density of pit or dark spot seen in AFM and FESEM images is ~ 10^8 cm^{-2} which correspond to the threading dislocation density of the formed GaN film. The surface of the film grown within the intermediate Ga-stable regime has large areas of uniform and flat surface between pits, while the pits have irregular, faceted edges.

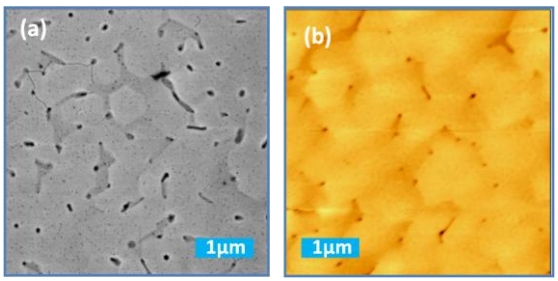

Figure 4.5 *(a) plan view FESEM image (b) AFM micrograph of undoped GaN film acquired over scan area of 5×5 μm^2.*

4.2 n- and p-type doping of GaN film

The fabrication of electrically driven semiconductor devices requires doping, and in most cases, both p-type and n-type doping is necessary. For GaN-based structures, which have a unique application potential in the ultra-violet to green spectral region, Mg and Si are by far the most commonly used p-type and n-type dopants, respectively. However, when doping GaN with Mg or Si, several challenges are encountered. The incorporation of Si into GaN films grown on sapphire (0001) substrates leads to a reduction of compressive strain, but if Si concentrations exceed $\sim 10^{18}$ cm^{-3} it lead to tensile strain. Also, an increasing density and variety of dislocations have been reported with increasing Si doping[189]. However, not only the dopant concentration, but also the thickness of the Si doped layer plays an important role for the defect density[190]. It has been proposed that Si induced tensile strain causes the formation of dislocations. Moreover, the stacking-fault energy has been shown to be reduced for increasing Si concentration. Another mechanism for strain relief has been reported for relatively thick and highly Si doped layers, where extended cracks with $<1\bar{1}00>$ sidewalls occur and can extend from the surface down to the sapphire substrate. In addition to these effects of Si doping on the microstructure, the surface morphology is also affected. A major problem in p-doping of GaN is the large activation energy of about 200 meV that leads to a free charge carrier density of only 1% of the Mg atom concentration at room temperature[191]. Therefore, large Mg concentrations are required in order to achieve moderate p-type conductivity. For large Mg concentrations, however, high densities of extended defects have been reported, such as Mg induced pyramidal defects, extended facetted defects, and nanotubes[192]. A common building blocks of all these defects is given by inversion domain boundaries where Mg is agglomerated, leading to a decrease of the hole concentration. It has been proposed that such defects arise from Mg surface segregation and they form as soon as a the local Mg concentration near the surface exceeds a certain threshold concentration[193].

4.2.1 Silicon doping of GaN film grown on AlN buffer layer

The Ga-polishing or Ga flash-off procedure described in the following is always performed before initiating the growth of not only GaN, but of any (Al, Ga, In)N layer grown on any substrate. This procedure effectively removes residual sub-oxides from the substrate surface. The plasma is kept off during the procedure and no nitrogen is flowing. The Ga effusion cell temperature is set to the temperature (1060℃) nominally used during growth. The Si effusion cell temperature is set to the temperature (1200℃) during growth of Si doped GaN. At 600℃, Ga is deposited for 1 minute onto the substrate and dissolves sub-oxides there. The reaction products and the excess Ga are concurrently desorbed by heating the substrate up to 800℃. The Ga shutter is opened again for 1 minute at 760℃ during the warm upto 800℃ thereby initiating a second Ga-polishing cycle. After after reaching 800℃ the substrate is cooled to the desired growth temperature of 760℃ in the case of 2D-GaN film growth, which marks the end of the Ga desorption procedure. After *in situ* polishing of 1.3 µm thick GaN film, growth of Si doped GaN is performed at substrate temperature of 760℃, by opening simultaneously Ga, N and Si shutters. To obtain 0.5µm thick Si doped GaN layer, growth is done for one and a half hour.

RHEED is used to monitor *in-situ* the entire growth sequence and pattern acquired during and after growth of Si doped GaN layer doping along [11$\bar{2}$0], (**Figure 4.7**) remains streaky with faint kikuchi lines and crossings, an evidence of a smooth and compact surface layer. The zeroth and first order bulk streaks are indicated by white arrows which is an indication of layer by layer growth mode.

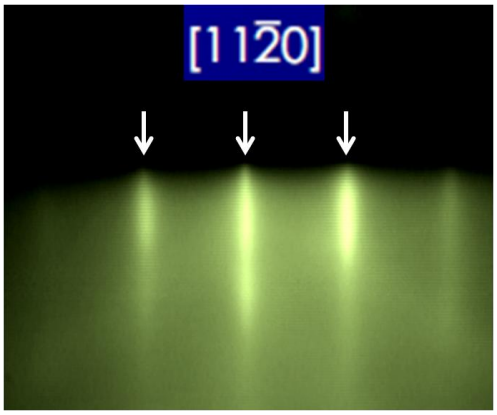

Figure 4.7 *RHEED pattern of GaN film acquired along* [11$\bar{2}$0] *azimuth, zeroth and first order bulk streaks are indicated by white arrows.*

The surface morphology is shown in **Figure 4.8(a)** which is a plan view of the FESEM image and **Figure 4.8(b)** is an AFM micrograph of a GaN sample over a 2.5×2.5 μm^2 area. The peak-to-valley (P-V) roughness is ≈17 nm and the root-mean-square (RMS) roughness is ≈3.6 nm. The density of pit or dark spot seen in AFM and FESEM images is calculated to be ~1.2 $\times 10^9$ cm^{-2}. This increase in defect density can be attributed to the result of Si doping. The surface of the film has extended cracks with <1$\bar{1}$00> sidewalls which seems to extend from the surface down to the sapphire substrate. These observations suggest a small amount of tensile stress is developed in the films at this Si flux.

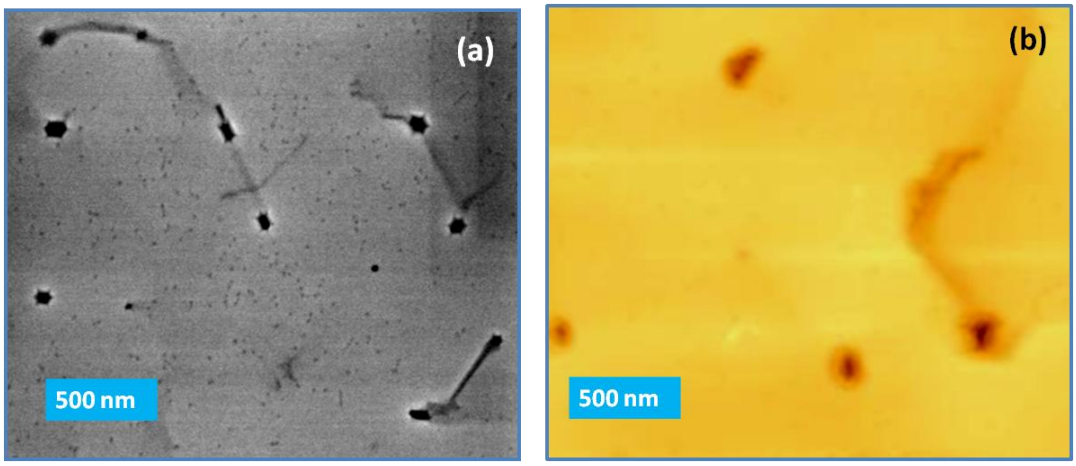

Figure 4.8 *(a) plan view FESEM image (b) AFM micrograph of Si doped GaN film acquired over scan area of 2.5×2.5 μm^2.*

The structural property of the films is measured as 2θ–ω XRD pattern as shown in **Figure 4.9** of an Si doped GaN film, peaks at 2θ= 41.6° and 91.5° correponds to (0006) and (00 12) reflection from the sapphire substrate, and peaks at 2θ= 34.5°, 72.5° and 126.5° are indexed as (0002), (0004) and (0006) of the wurtzite GaN film. The elongation of the reciprocal lattice in vertical direction (ω/2θ-scan) is 569 arc sec and in horizontal direction (ω-scan) is 640 arc sec. The elongation in horizontal direction is more than in vertical directions indicates an increase in threading screw dislocations in Si doped GaN film, as also seen in the FESEM and AFM micrograph **Figure 4.8**.

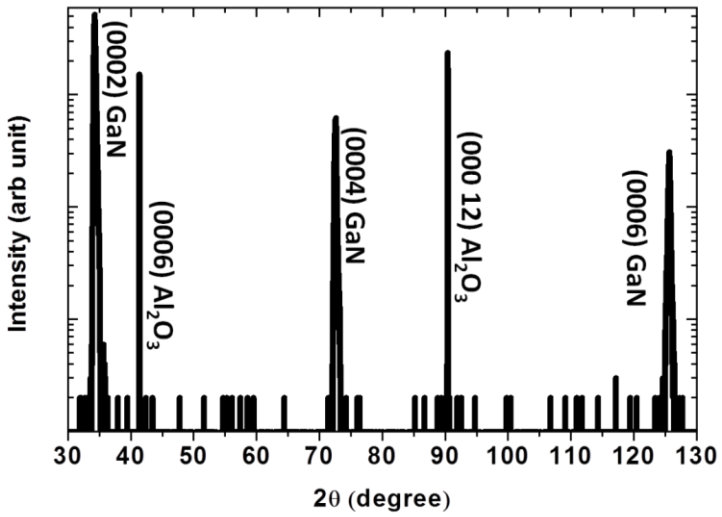

Figure 4.9 *shows a 2θ–ω XRD pattern of a Si doped GaN film.*

The carrier density and mobility of an Si doped GaN film is determined by Hall measurement in van der Pauw geometry is listed in **Table 4.I** at room temperature and 77K. Negative sign of carrier concentration confirms n-type doping.

Temperature	Carrier conc. (cm^{-3})	Mobility (cm^{-2}/Vs)	Sheet conc. (cm^{-2})
300K	-2.72×10^{17}	492	-4.35×10^{13}
77K	-8.82×10^{16}	550	-1.42×10^{13}

Table 4.I *Shows carrier and sheet concentration of Si doped GaN film and its mobility at room temperature and 77K.*

4.2.2 Magnesium doping of GaN film grown on AlN buffer layer

After *in situ* polishing of 1.3 µm thick GaN films, growth of Mg doped GaN layer is performed at substrate temperature of 760℃, by opening simultaneously Ga(1060℃), N and Mg (350℃), shutters. To obtain 0.5µm thick Mg doped GaN layer, growth is done for one and a half hour.

RHEED is used to monitor entire growth sequence and pattern acquired during and after growth of Mg doped GaN layer doping along [$11\bar{2}0$], (**Shown is Figure 4.10**) is

streaky with an envelope of spots elongated along vertical direction which is evidence of a compact surface layer with slight roughness (evidence in AFM image).

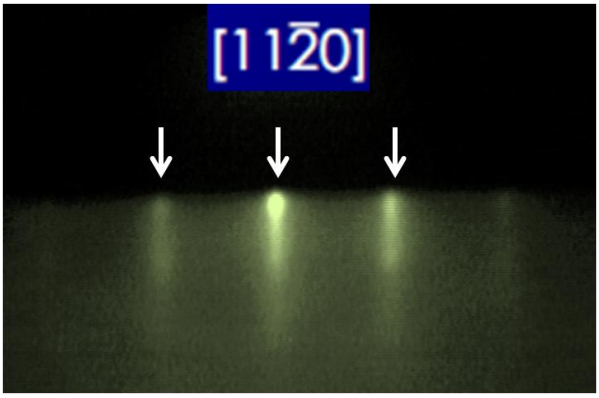

Figure 4.10 *RHEED pattern of Mg doped GaN film acquired along [11$\bar{2}$0] azimuth, zeroth and first order bulk streaks are indicated by white arrows.*

The electrical property of the p-doped film grown are measured as the carrier density and mobility of an Mg doped GaN film which is determined by Hall measurement in van der Pauw geometry and are listed in **Table 4.II** at room temperature and 77K. Positive sign of carrier concentration confirms p-type doping.

Temperature	Carrier conc. (cm^{-3})	Mobility (cm^{-2}/Vs)	Sheet conc. (cm^{-2})
300K	$9.04x10^{18}$	1.0	$4.52x10^{14}$
77K	$6.91x10^{15}$	12.0	$3.45x10^{11}$

Table 4.II *Shows carrier and sheet concentration of Mg doped GaN film and its mobility at room temperature and 77K.*

The structural property of the films grown is obtained by 2θ–ω XRD pattern shown in **Figure 4.11** of an Mg-doped GaN film, peaks at 2θ=41.6° and 91.5° corresponds to (0006) and (00 12) reflection from the sapphire substrate, and peaks at 2θ= 34.5°, 72.5° and 126.5° are indexed as (0002), (0004) and (0006) of the wurtzite GaN. The elongation of the reciprocal lattice in vertical direction (ω/2θ-scan) is 504 arc sec and in horizontal direction (ω-scan) is 580 arc sec. The larger elongation in the horizontal direction than in the vertical direction manifest the increase in threading screw

dislocations in Mg doped GaN film, as seen in the surface morphology images in **Figure 4.12**.

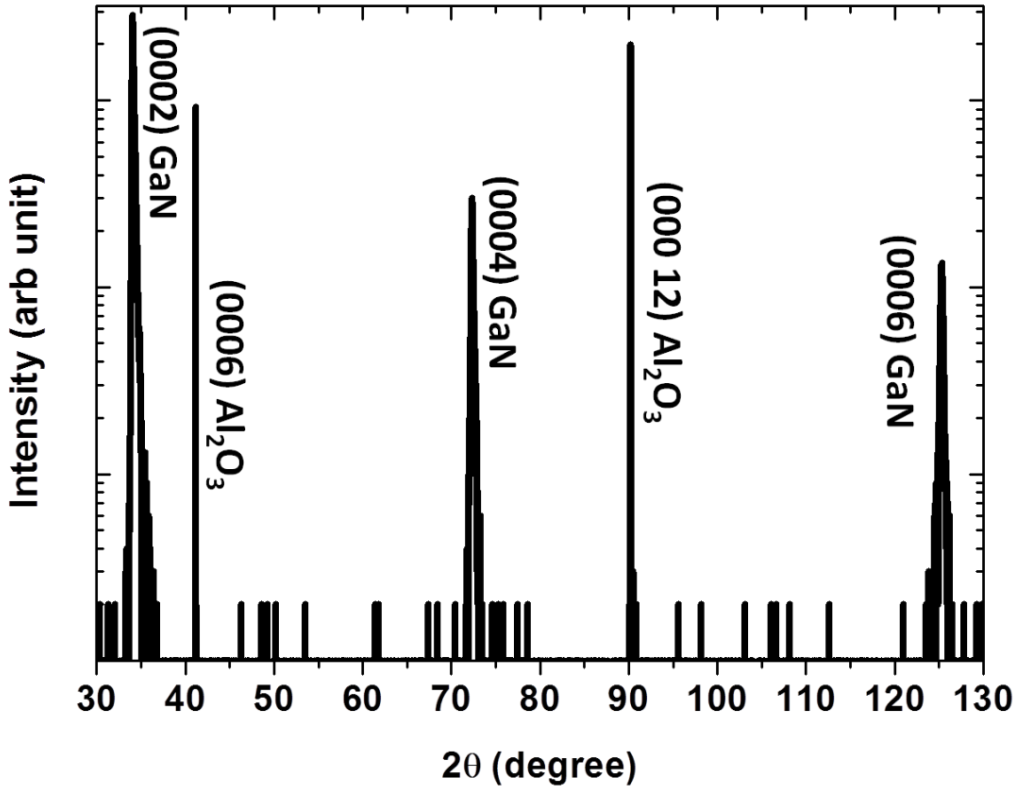

Figure 4.11 *shows a typical 2θ–ω XRD pattern of a Mg doped GaN film*.

The surface morphology of the p-doped films is shown in **Figure 4.12(a)** is a plan view FESEM image and **Figure 4.12(b)** is an AFM micrograph of a Mg doped GaN film over a 2.5×2.5 μm^2 area. The peak-to-valley (P-V) roughness is ≈47 nm and the root-mean-square (RMS) roughness is ≈5.9 nm. The density of pit or dark spot seen in AFM and FESEM images is ~1×10^{10} cm^{-2}, this increase in defect density is a result of Mg doping. The high densities of extended defects reported in literature, induced by Mg doping are pyramidal defects, extended facetted defects, and nanotubes. And major concerns are inversion domains boundaries where Mg generally gets agglomerated. The figures clearly show the extended defects both in density and configuration.

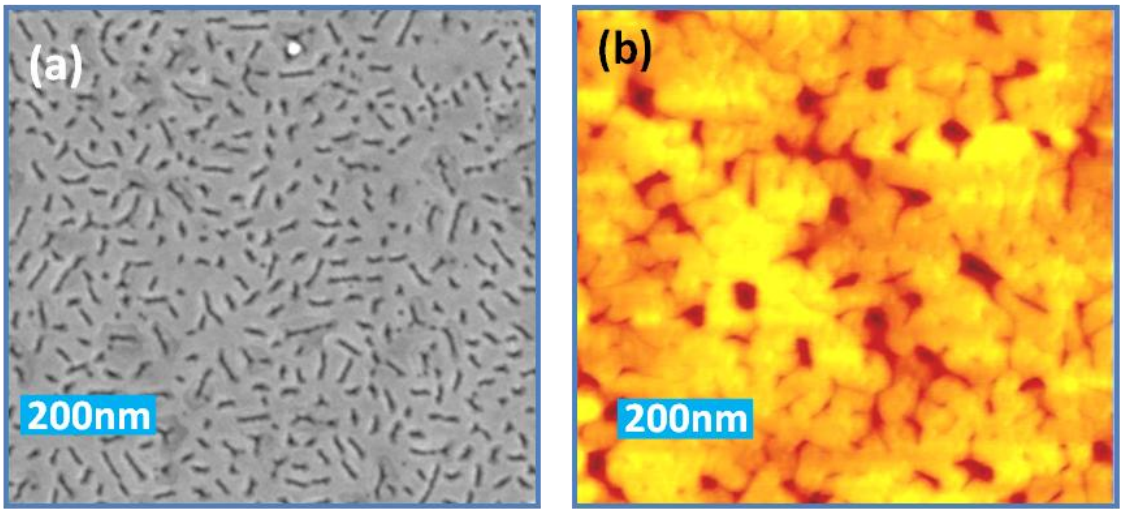

Figure 4.12 *(a) plan view FESEM image (b) AFM micrograph of Si doped GaN film acquired over scan area of 1×1 μm^2.*

4.3 Formation of High Electron Mobility Transistor (HEMT) structures

After accomplishing decent doping methods of GaN films, we now attempt the formation of the HEMT structure and characterizing it by several complementary tools.

The large energy band gap differences [E_G (GaN):3.4eV:E_G(AlN):6.2eV], high electron velocities (~10^7 cms^{-1}) and high thermal and chemical stability attracts III-Nitrides system for fabricating Gallium Nitride (GaN) based devices for high power and frequency. GaN/AlGaN high electron mobility transistor (HEMT) is the fastest transistor suitable for microwave and millimetre wave applications in modern communication systems. This heterostructure has unique high density two dimension electron gas (2DEG) formed at heterointerface due to steep spike-shaped quantumwell at the heterojuntion, where there is large conduction-band offset as well as large discontinuity in the piezoelectric and spontaneous polarization. 2DEG results in high transconductance and a high bandgap value facilitates operation at high temperatures and large voltage swings necessary for high temperature/high power transistors. From the technological point of view, the main factor limiting the performance of the high power optoelectronic and

electronic devices is the presence of different types of dislocations, mainly due to the growth of GaN on foreign substrates with a large lattice mismatch such as sapphire or SiC. AlGaN/GaN based high electron mobility transistors (HEMTs) are commonly grown on sapphire or SiC substrates. But the structure grown on sapphire with GaN buffers is important to provide a high buffer resistivity for proper channel pinch-off and low losses in the device at high frequencies. In 1991, Nakamura et al reported the then highest mobility of GaN film at room-temperature and liquid nitrogen temperature μ_n = ≈600 $cm^2 V^{-1} s^{-1}$ and μ_n = ≈1500 $cm^2 V^{-1} s^{-1}$ at carrier concentrations of n=4 $\times 10^{16}$ cm^{-3} and n = 8 × $l0^{15}$ cm^{-3}. In 1991 Khan et al have shown enhancement in mobility by fabricating heterostructure of AlGaN/GaN grown on sapphire substrate. The enhanced mobility reported by Khan et al of AIGaN/GaN heterostructure with 500 *Å* $Al_{0.09} Ga_{0.91} N$ cap layer was μ_n = 620 $cm^2 V^{-1} s^{-1}$ at room temperature and μ_n = 1600 $cm^2 V^{-1} s^{-1}$ at 77 K. The peak mobility, μ_n = 2626 $V^{-1} s^{-1}$ at 77 K, was realized in a 2000 *Å* GaN film grown on sapphire using an AIN buffer layer and capped with a 1000 *Å* $Al_{0.2}Ga_{0.8}N$ layer. This enhancement in mobility of GaN layer is attributed to increased interface conduction resulting from the presence of a 2D electron gas at the heterostructure interface and the thickness of either GaN of AlGaN layer.

Properties of two-dimensional electron gas (2DEG) in GaN/AlGaN interface are currently intensively studied due to the great impact of GaN based devices for electronic applications. It was already shown that due to the piezoelectric doping mechanism, the concentration of electrons in 2DEG is controlled by the thickness and Al content of AlGaN layer grown on Ga-polarity side. A very high electron concentration of 2DEG, n_{2D} ~10^{13} cm^{-2} and mobility, μ_{2D}≈1000–2000cm^2/(V s) at the room temperature (RT), makes GaN/AlGaN heterostructures to be very promising for high power and high frequency transistors. But theoretically it is predicted that optical phonons scattering mechanism limit room temperature mobility ≈2000 cm^2/(V s). Hence heterostructure needs to be modified to enhance mobility beyond theoretical limit, recently resistive GaN buffer layers are used to grow heterostructures with enhanced mobility. Although undoped high resistivity GaN buffers can be grown by different techniques it is challenging to do so

reproducibly. It is easier to achieve the high resistivity by doping GaN with deep level impurities, Fe impurity, which highly resistive GaN(Fe) layers and these Fe doped layers have the Fermi level pinned near E_c=(0.5–0.6 eV). Even if one grows an unintentionally doped GaN (UID GaN) layer on top of the Fe doped film, the resistivity of this composite buffer can still be high. This is desirable to avoid a high concentration of deep traps in or near the transistor channel region. The buffers can be made highly resistive which makes AlGaN/GaN(Fe) HEMTs prepared by MBE attractive in terms of achieving high transconductance and minimizing parasitic channel modulation due to traps in the buffer. But the low Fe concentration in MBE UID GaN films grown on top of Fe doped layers is open for debate due to the nature of compensation in the undoped part of the buffers.

Experimental growth conditions

Heterostructure structures are grown in an ultra high vacuum ($1x10^{-10}$Torr) Plasma Assisted Molecular Beam Epitaxy (PAMBE) system. Two structures are grown with and without GaN(Fe) buffer layer. The schematic cross-sections of these heterostructures are shown in **Figure4.13**. The heterostructures shown in **Figure4.13(a)** consists of thin layer of AlN over 2 inch c-plane sapphire substrate, 1 μm thick unintentional doped (UID) GaN layer, and 2 nm cap layer of UID GaN over 20nm thick layer of $Al_{0.2}Ga_{0.8}N$**.** Heterostructure shown in **Figure4.13 (b)** has an extra layer of Fe doped 0.5μm thick layer of GaN sandwiched between 1μm thick unintentional doped (UID) GaN layer and 20nm thick layer of $Al_{0.2}Ga_{0.8}N$ (TDI Semi-insulating GaN:Fe templates is Fe doped layer on AlN)**.** During growth of these heterostructures Al and Ga mole fraction is determined by Atomic Absorption spectrometer, (ACCUFLUX SVTA, USA). *In-situ* RHEED reveals surface cleanness, epitaxy and growth modes, while morphology is probed *ex-situ* by Atomic Force Microscope (AFM) and structural property of the sample is studied by high-resolution x-ray diffraction (HRXRD) using a Bruker D8 Discover diffraction system.The electrical properties are investigated by Hall measurement utilizing In contacts in Van der paw geometry.

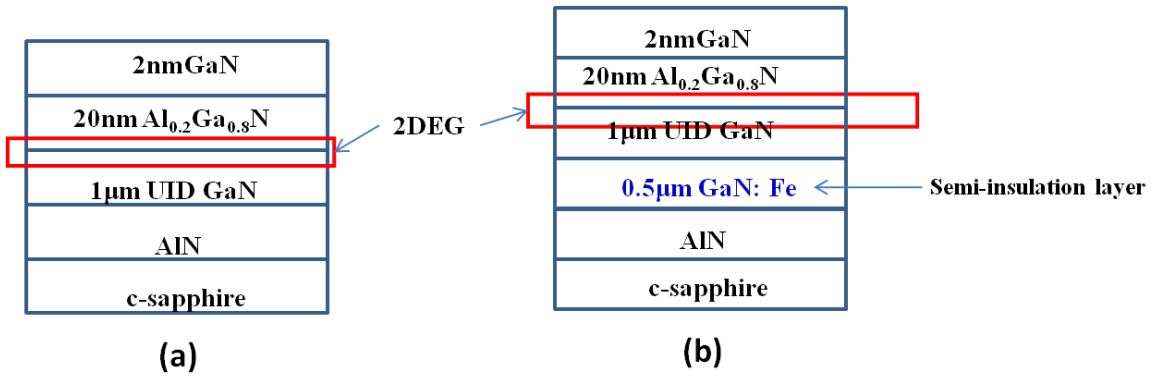

Figure 4.13 *Schematic cross section of the HEMT heterostructure (UID-unintentionally doped) (a) represent heterostructure without GaN(Fe) layer and (b) with GaN(Fe) layer. Interface between AlGaN/GaN is marked as 2 dimensional electron gas (2DEG).*

RHEED patterns observed along [11$\bar{2}$0] is shown in **Figure4.14** for both heterostructure (a) and (b) after completion of growth. Both streaky patterns with faint kikuchi lines and crossings, is an evidence of a smooth and compact surface layer. The zeroth and first order bulk streaks are indicated by white arrows. This indicates that growth of GaN layer proceeded in a layer by layer growth mode (Frank Van der Merwe or 2D growth).

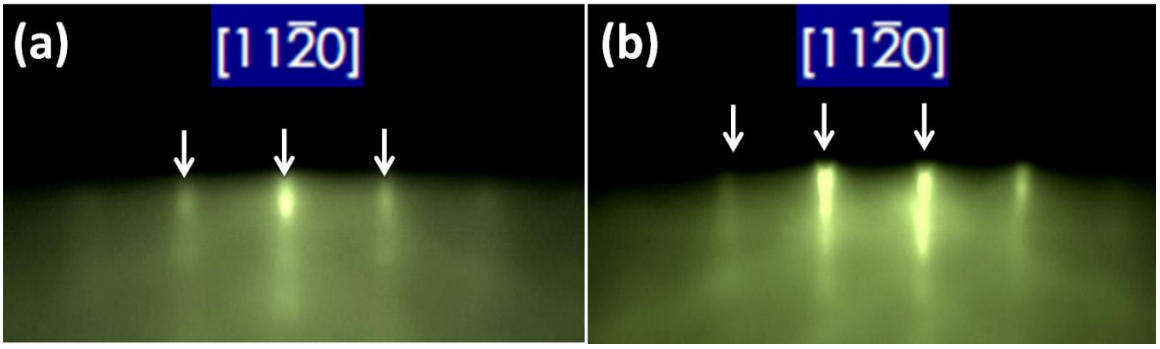

Figure 4.14 *RHEED pattern of GaN film acquired along [11$\bar{2}$0] azimuth, zeroth and first order bulk streaks are indicated by white arrows.*

Surface morphology of the structures grown, are studied by AFM in **Figure4.15**. The appearance of the surface is caused by spiral growth hillocks. These hillocks are composed of monolayer high steps and terraces that form around mixed dislocations.

Figure4.15.(a) shows AFM image of heterostructure (**Figure 4.13b**) whose root mean square roughness is measured to be ≈0.7nm with pits or dislocation density of ~10^9cm^{-2}. Images of nanopipes or nanopillar formed due to open-core or closed-core dislocations shown in **Figure4.15.(b)** and **15(c)**, respectively.

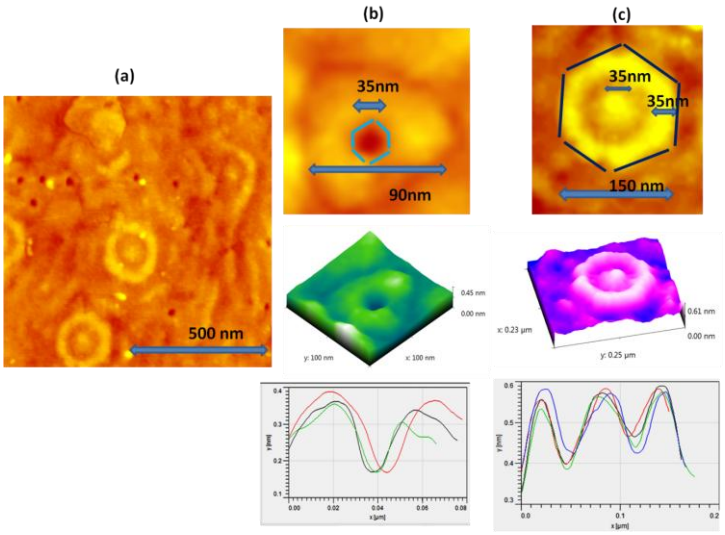

Figure4.15.(a) AFM image shows morphology of heterostructure (b), and (b, c) are the images of hexagonal hillocks apex and holes, respectively.

Surface morphology of heterostructure (**Figure 4.15b**) consists of hillocks with steps, holes, and flat (0001) surface. The outer diameter of these hexagonal hillocks is ≈2μm (observed from an AFM image of area 8x8μm^2) with average height ≈35nm from the flattest lowermost level, these hillocks seems to be bounded by a concentric set of $\{1\bar{1}00\}$ steps which appears to from closed loops and flatter region of these hexagonal features is along (0001) plane. Surface area scan of size 1x1μm^2 imaged by AFM is shown in **Figure4.15.(a)** the measured density of holes is ~2x10^7cm^{-2} and of spiral growth features (with hexagonal boundary) is ~3x10^8cm^{-2}. AFM image of one of these holes or dark spots is shown in **Figure4.15.(b),** its diameter is 35nm, with hexagonal periphery circumscribed by a triangular feature of height 0.2nm measured by line scan across the image. The dimensions of these holes are similar to an open-core screw dislocation which are typically formed due to more than two steps (height of individual

step ≈0.5c, c=0.52 nm) generated at the initial stages of GaN film growth. Qian et al [194] have shown that radius of nanopipes from 3-50nm by using high resolution Scanning Force Microscope (SFM). **Figure4.15 (c)** shows AFM image of the apex of hillock, it has smaller hexagonal hillocks of diameter ≈150nm of height ≈1nm. The line profile across image of hexagonal hillock shows that its height is ≈0.2nm and they appear like cater (a signatory of open-core screw dislocation reported by Qian[194]) concentric to smaller mound at the centre, these hexagonal hillocks also seems to be bounded by $\{1\bar{1}00\}$ plane along $<11\bar{2}0>$ capped by (0001) plane. The central mound is of diameter ≈35nm, height ≈2nm can be a closed core screw dislocations formed due to bunching of steps formed in spiral growth (which is beyond AFM resolution), and these were earlier reported by Transmission electron microscope (TEM) studies of MBE grown GaN films.

A 2θ–ω HRXRD pattern shown in **Figure4.16.(a)** of HEMT heterostructures, peaks at 2θ= 41.6° correponds to (0006) reflection from the sapphire substrate. And peaks at 2θ= 34.5°, 35.2° and 35.8° are indexed as (0002) reflections from wurtzite GaN, AlGaN and AlN. The elongation of the reciprocal lattice in vertical direction (ω/2θ-scan) is 543 arc and in horizontal direction is 180 arc sec.

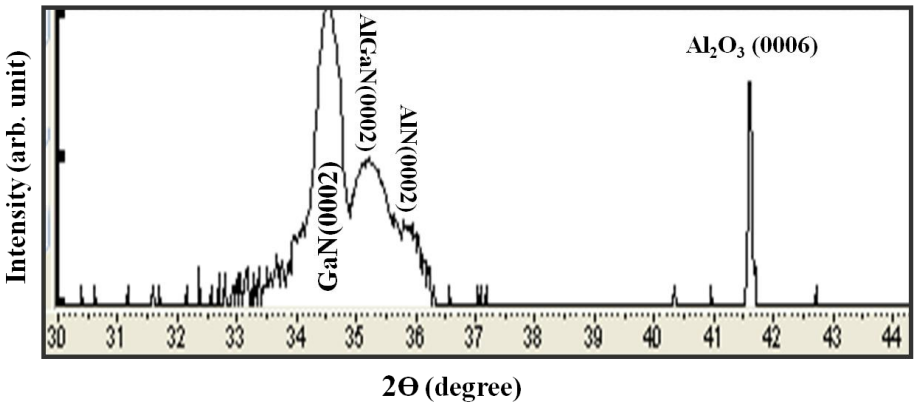

Figure 4.16 *High resolution X-ray diffraction pattern of heterostructures **(a) and (b).***

To confirm the lattice matching of AlGaN and GaN layer RSM is best tool. The thickness of GaN cap layer, AlGaN layer and Al, Ga compositions in AlGaN layer is determined by HRXRD in conjunction with simulations of the profiles. X-Ray reciprocal space mapping (RSM) of heterostructure around an asymmetric reflection is a powerful

tool to investigate the in-plane and out-of-plane lattice constants, and thus to simultaneously investigate the strain state as well as the exact alloy composition of the layers. **Figure4.17** depicts the HRXRD mapping in [105] direction of a heterostructure**.** Previously, the sample has been aligned on GaN layer, allowing correct determination of the strain in GaN and AlGaN layers. Two different GaN related peaks are observed: one corresponds to the almost fully relaxed GaN buffer layer that is grown on the substrate; the other is a pseudomorphically grown strained AlGaN layer on top of GaN layer. On theoretically fitting experimental data by LEPTOS software shows in-plane (lateral) strain ε_{xx}=1.198% and out-of-plane (normal) strain of ε_{zz}= -0.646% for AlGaN layer. The AlGaN layer is fully lattice matched on the GaN (a_{GaN}=0.31891, a_{AlGaN}=0.31891; c_{GaN}=0.51855,c_{AlGaN}=0.50500), hence no relaxation in the top layer observed.

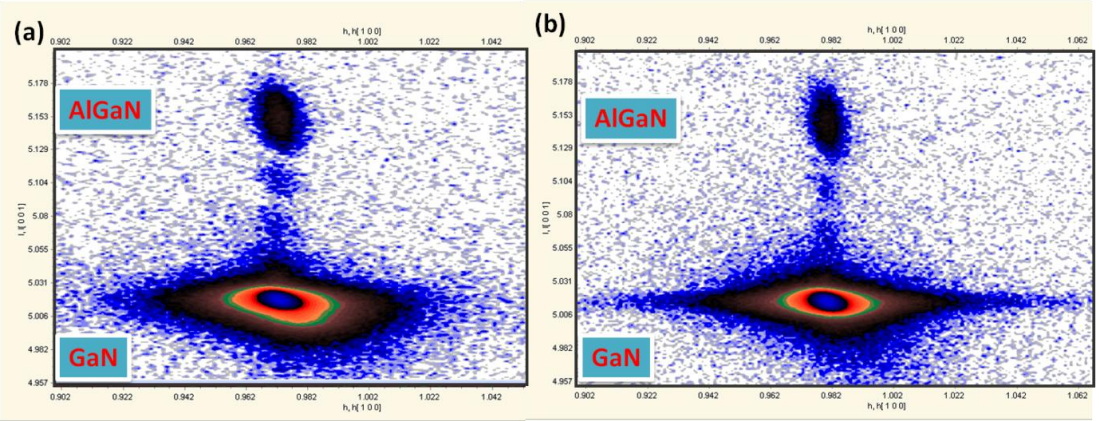

Figure 4.17 ***(a)*** *Reciprocal space map (RSM) of heterostructure (a), (b) RSM of heterostructure (b) mapped in mapping in [10$\bar{1}$5] direction.*

The thickness of the GaN layer and AlGaN layer is determined by simulating experimentally observed X-Ray reflectivity curve by LEPTOS (**Figure4.18**), the mole fraction of Ga=0.8 and Al=0.2, which matches well with observation made by atomic absorption spectroscopy. The calculated roughness of 0.4738 nm is observed for the AlGaN/GaN interface. And fringes seen in X-ray reflectivity curves gives an indication of sharp interface, four of small overlapping fringes on top of a single fringe indicate that the thickness ratio between GaN and AlGaN layer is 1: 5 (i.e. GaN cap layer 4 nm and AlGaN layer 20nm thick).

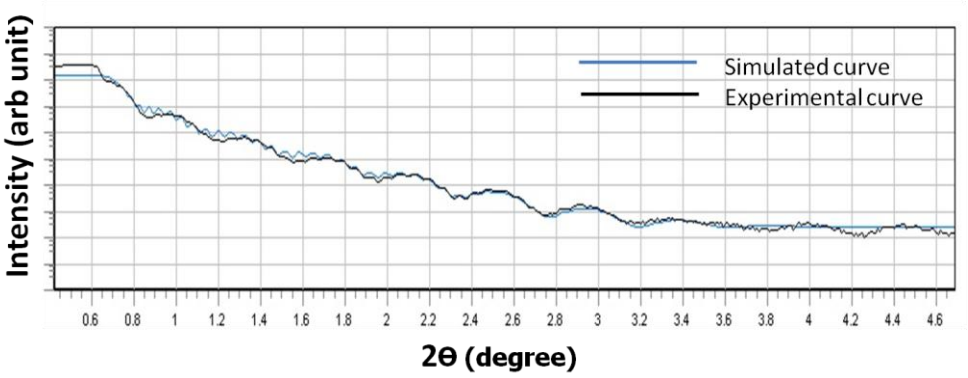

Figure 4.18 *X-Ray reflectivity curve (XRR) of heterostructures (black curve is an experimental curve and blue curve is simulated curve)*

We have used Van der Pauw Hall measurement to determine the carrier density and mobility of a given sample (details discussed in Chapter 3). An AlGaN/GaN single-channel HEMT with the AlGaN thickness of 20 nm (denoted as heterostructure **(a)**) has a Hall density of $1.4\times10^{13}cm^{-2}$ and a Hall mobility of 1300 cm^2/Vs at room temperature and 3200 cm^2/Vs at 77K. Another sample with similar structure with an extra GaN(Fe) layer (denoted as heterostructure **(b)**) sandwiched between UID and AlN layer has a Hall density of 1.2×10^{13} cm^{-2} and a Hall mobility of 1650 cm^2/Vs at room temperature and Hall mobility of 5000 cm^2/V-s at 77K.

300K		
	Sheet conc. (cm^{-2})	**Mobility (cm^2/Vs)**
Heterostructure (a)	**1.4×10^{13}**	**1300**
Heterostructure (b)	**1.2×10^{13}**	**1650**
77K		
Heterostructure (a)	**1.4×10^{13}**	**3200**
Heterostructure (b)	**1.2×10^{13}**	**5000**

Table 4.III *Shows carrier and sheet concentration and its mobility of heterostructure (Figure 12a, b) at room temperature and 77K.*

Summary

The high quality of the films growth is manifested by a narrow FWHM of ≈108 arc sec of the (0002) reflection in XRD studies, threading dislocation density by AFM of ~10^{8} cm^{-2}, mobility ≈500cm^{2}/Vs and 1cm^{2}/Vs carrier concentration of ~10^{17} cm^{-3} and 10^{19} cm^{-3} for Si doped and Mg doped films, respectively. A AlGaN/GaN high electron mobility transistors (HEMTs) structure is formed, with mobility of ≈1650 and ≈5000 cm^{2}/Vs at 300K and 77K respectively, and a sheet carrier concentration of ~$10^{13}$$cm^{-2}$.

Chapter 5

Growth of nanowall, nanocolumns, and 2D film on bare c-plane sapphire

5. Growth of nanowall, nanocolumn, and 2D film on bare c-plane sapphire

5.1 Introduction

Group III-nitride devices are typically grown on sapphire substrates due to their isostructure and suitable electronic and optical properties and absence of piezoelectricity**.** Finding a suitable substrate for growth of III-Nitride heterostructures has remained a challenge, though sapphire (Al_2O_3) is being extensively used now. However, 13.8% lattice mismatch causes enormous strain in the GaN overlayer that relaxes by forming ~10^{10} threading dislocations per cm^2, that are perpendicular to the substrate surface which have edge, screw and mixed characters. These act as scattering centres for electron and photon transport and consequently are detrimental to device efficiency and performance. Though several processes such as Epitaxial Lateral Overlayer Growth (ELOG), pendoepitaxy, buffer layers and domain/lattice matching epitaxy have made strides, the novel approach is to form defect controlled nanostructures, especially nanorods and nanowalls with tunable microstructure, aspect ratio that can provide additional degrees of manipulation for charge confinement, strain engineering and surface morphology.

The major challenge is to understand and tailor-make nanostructure assembly to generate ordered epitaxial structures with desired properties. The freedom to tune size of these nanostructures is an added advantage to synchronize them with the size of active regions of devices. Nanorods usually are being grown either by lithographic methods that involve expensive process steps or by the use of metal catalysts in the vapour-liquid-solid (VLS) method, in which remnant metals can act as performance barriers in applications. Spontaneous formation of epitaxially ordered 1-D (1-dimension) and 2-D (2-dimension) nanostructures such as nanowires and nanowalls are desirable since they do not involve extra process steps such as forming buffer layers, employing catalysts or lithography. Catalyst assisted growth yield nanocolumns that are random in orientation, due to lack of epitaxy and hamper device performance by alloying with Ga and being an undesirous

remnant in the system. Recently, there have been reports of spontaneous formation of GaN nanorods on both sapphire and silicon, but these studies consider it inevitable to involve a prior surface nitridation followed by growth of an AlN buffer layer and thus do not directly relate to the epitaxial relationship with the substrate. There are few reports on the spontaneous formation of GaN nanostructures on bare c-plane sapphire. The mechanism of anisotropic growth to form spontaneous nanostructures is not understood yet, which is eventually essential to be able to control their alignment, epitaxy and defects.

We present in this Chapter experimental results that demonstrate the formation of a high density (~10^8 cm^{-2}) of c-oriented GaN nanocolumns and a hexagonal nanowall network grown on bare c-plane sapphire by sheer control of growth parameters, without involving lithography, catalysts, buffer layers or even nitridation. The structural and optical properties of the different morphological forms are discussed.

5.2 Experimental methods: *Nitrogen rich condition*

A consolidated plot based on the review by Calleja et al [135] of GaN growth rate versus Ga flux for different various growth temperatures at a fixed N_2 flux is shown in **Figure 5.1**, Ga flux is measured Beam Equivalent Pressure (BEP) and curves (a−c). Since the early report by Yoshizawa et al[195] on the formation of GaN nanowires/ nanocolumns/ nanorods by PA-MBE, under Ga-rich condition at 800℃ on AlN/Al_2O_3(0001), various other groups have reported formation of GaN nanowires on silicon substrate by MBE. The growth conditions identified by Calleja et al[196] to form high quality GaN films and nanowires on a Si(111), Si(001) and AlN/Si(111) substrate are reproduced as curves (a−c). Curve (a), (b) and (c) corresponds to growth temperature 770℃, 720℃ and 660℃, respectively. The encircled region encompassing curves (a−c) is the N-rich condition found by Calleja et al to from GaN nanowires on bare Si(111), AlN/Si(111) and GaN buffer/Al_2O_3(0001). Shown as point (d), is the N-rich growth condition employed by Bertness et al [143], to spontaneously form GaN nanowires by PA-MBE, in N-rich conditions similar to Calleja et al in terms of Ga BEP but their growth temperature range

is (810−830℃), hence they observed a lower growth rate. Recently, Fernandez-Garrido et al [197] have succinctly compiled a growth diagram for the formation of GaN nanowires on bare Si(111) by PAMBE and suggested that nanowire formation occur only in a substrate temperature range (740−830℃), compact GaN layer forms below 740℃ growth temperature and no GaN growth take place above 830℃. This nanowire growth regime agrees well with Bertness et al [198] growth conditions as well as of other research groups. Arrows marked on curves (a−c) shows saturation regime, beyond which Ga droplet formation take place and below these saturation points GaN growth proceed in a layer by layer growth mode in the linear part of curves (a−c). The reported N_2 flux or flow rate (which is generally kept constant) leads to disagreement between Ga-rich or N-rich conditions employed in nanowire growth. This discrepancy in N_2 flux may be due to N_2 flow rates employed, which can differ due to variation in system design, plasma source geometry and pumping configurations (discussed in chapter 3) etc. Variation in active N_2 species in plasma has also been investigated by Bertness et al [199]).

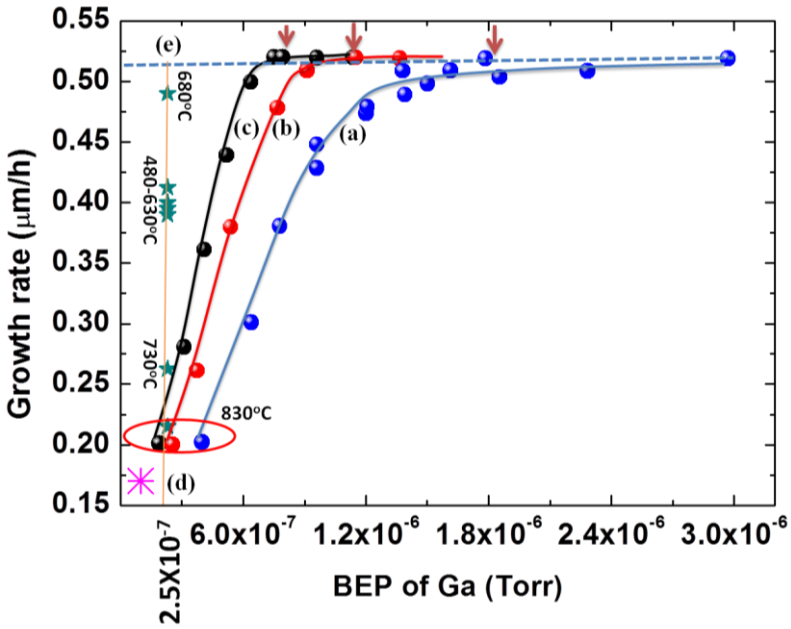

Figure 5.1 *Consolidated growth diagram for the formation of GaN nanowires, growth conditions proposed by Calleja et el (shows as curve (a−c)) and Bertness et al (shown as star mark (d)) are adapted from references [135]. Points marked as star along the line (e) is the condition employed in this study.*

Points marked as star in **Figure 5.1** along the line (e) correspond to growth condition employed in our study reported here to grow GaN films on bare c-plane sapphire [157-158]. At a fixed N/Ga BEP ratio of 100 GaN films are grown in the temperature range 480-880℃. N/Ga BEP ratio =100, calculated by taking Ga BEP=2.5×10^{-7}Torr and N_2 BEP =2.5×10^{-5}Torr (nitrogen pressure used during growth correspond to a flow rate of 4.5 sccm). The forward plasma power of 375W and reflected plasma power <10W is maintained constant for the entire growth time of 2 hours. For convenience the III/V ratio in the system for each experiment is measured by considering the ratio of the Beam Equivalent Pressure (BEP)[184]of Ga and Nitrogen as indicated by a line-of-sight Bayard-Alpert Gauge. We have considered BEP (Beam Equivalent Pressure) ratio as a measure of N/Ga flux ratio, since nitrogen flow rate reported by various groups can lead to disagreement in growth condition. The effusion cell held at 1000℃ provides the Ga molecular beam onto a rotating 3" Al_2O_3 c-plane substrate, held at different temperatures varying from 450 to 850℃ and the Ga flux from $2.86\times10^{14}cm^{-2}s^{-1}$ to $4.84\times10^{14}cm^{-2}s^{-1}$ by changing the temperature of the effusion cell, and the nitrogen flow rate is controlled from 2 sccm to 8 sccm by a precision mass flow controller. A typical GaN film deposited at 700℃, at 4.5 sccm and Ga source at 1000℃, had a growth rate of 0.3μm per hour as calibrated by a Quartz crystal (QC) thickness monitor, Accuflux and SEM cross-section studies. The morphology and structure analysis is done by high resolution FESEM and high resolution X-ray Diffraction. Cathodoluminescence (CL) measurement is done *in situ* at room temperature, with electron energy from 0 to 5 keV and photodetector with a resolution of 0.1 nm. Raman spectra are acquired at room temperature in the backscattering geometry of all GaN films. While the laser output power was set at 20 mW with an excitation wavelength of 514.5 nm. The focused beam size was approximately 2 μm, accumulation time was 10 sec, and a CCD detector was employed. By controlling the slit width and CCD pixel size the intensity of Raman signals is optimized. Raman peaks of sapphire substrate were visible along with wurtzite GaN mode, since GaN films are transparent to 513−531nm wavelength of green laser. The X-ray photoelectron spectroscopy is used for quantitative estimation of the surface composition of the GaN film in an Omicron system. Generally both Al Kα (1486.6 eV) and Mg Kα (1253.6 eV)

X-ray radiations are used for the quantitative measurements of GaN surface, since the Ga LNN Auger series overlaps with C 1s, O 1s XPS lines for Mg Kα source and N 1s , Ga 3s XPS lines for Al Kα source. In this study Al Kα source is employed for acquiring N1s core level spectra with constant pass energy of 20eV and step size of 0.1 eV. The charging effect induces 1−6 eV shift toward higher binding energies, therefore all core level spectra are referenced to the adventitious carbon peak at 284.6 eV. For extracting detailed information on the GaN stoichiometry and polarity, N1s core level spectra were de-convoluted into Gaussian components to identify the elemental chemical states. The relative elemental composition is estimated by measuring the area under the core level of four Gaussian peaks fitted with a suitable background subtraction.

5.3 Morphological evolution of GaN film in temperature range 480−630℃.

To understand role of kinetics in the growth of GaN film on c-plane Al_2O_3, we have looked into its morphological as well as the structural evolution, as a function of substrate temperature, which is varied from 480−630℃ in steps of 50°. **Figure 5.2** shows representative FESEM plan view images along with corresponding fast Fourier transform (FFT) of SEM image and corresponding RHEED pattern with incident electron beam azimuth along $[2\bar{1}\bar{1}0]$ direction, grown at different substrate temperatures. **Figure 5.2(*a*1)** is for the film grown at 480℃ which shows a surface network structure of tri-branched, nanowalls oriented along in-plane $<10\bar{1}0>$ and $<11\bar{2}0>$ directions, with an average branch length of 100nm, forming hexagonal feature surrounding the $\sim 5\times10^{10}$ voids per cm^2. On performing Fast Fourier Transform (FFT) on FESEM image of this film a weak 3-fold symmetry is realized as seen in **Figure 5.2(*a*2)**. The RHEED pattern shown in **Figure 5.2(*a*3)** acquired at 30^0 from the $[10\bar{1}0]$ direction is spotty, due to the transmission of electrons through the 3D grown thin nanowalls. The c/a ratio of distances between the centre of the RHEED spots in vertical and horizontal direction measured by line scans, is ≈1.63 (discussed in Chapter 3) shows that the GaN has wurtzite structure with $[0001]_{Al_2O_3}//[0001)]_{GaN}$, in the minimal mismatch configuration of $[10\bar{1}0]_{Al_2O_3}//$

$[11\bar{2}0]_{GaN}$ epitaxy. Also each of the spots is observed to be anisotropic with an aspect ratio of ≈2.1 along the horizontal $[1\bar{1}00]$ and vertical [0001] directions suggesting a small degree of misalignment of these walls oriented along $<11\bar{2}0>$ and $<10\bar{1}0>$ direction (or narrowing of the wedge shaped walls, as will be discussed later). **Figure 5.2(b1)** is for a film grown at 530℃ shows a surface network structure similar to 480℃ film, with an average branch length of ≈130nm, forming hexagonal feature surrounding the $\sim 3.5\times10^{10}$ voids per cm^2. On performing Fast Fourier Transform (FFT) on FESEM image of this film also a weak 3-fold symmetry is realized as seen in **Figure 5.2(b2)**. The c/a ratio of distances between the RHEED spots in vertical and horizontal direction is ≈1.63, again corresponds to the wurtzite structure. Each of the spots is also anisotropic with an aspect ratio of ≈2.4 along the horizontal $[1\bar{1}00]$ and vertical [0001] directions suggesting a small degree of misalignment in comparison to 480℃ pattern. The RHEED pattern shown in **Figure 5.2(b3)** is spotty due to transmission of electrons through thin nanowalls.

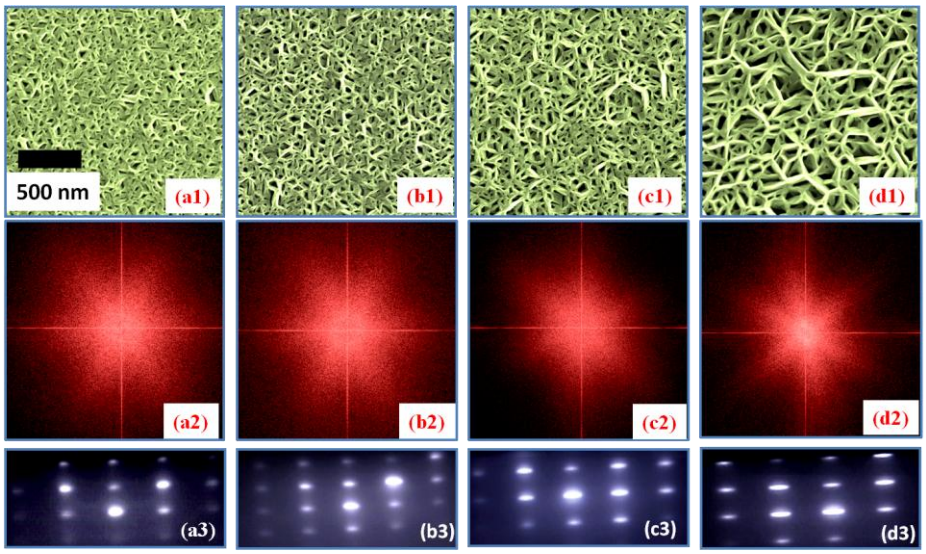

Figure 5.2*(a1−d1)* *are plan view FESEM images (all are of same magnification) with their corresponding RHEED pattern* ***(a3−d3)*** *(along the $[2\bar{1}\bar{1}0]$ zone axis) and fast Fourier transform (FFT)* ***(a2−d2)*** *of the GaN films grown on c-plane Al_2O_3 at 480^0C, 530^0C, 580^0C, and 630^0C.*

Figure 5.2(c1) is for a film grown at 580℃ shows a surface network structure similar to 480℃ and 530℃ films, with an average branch length ≈230nm, forming hexagonal feature surrounding the $\sim 2.5\times10^{10}$ voids per cm^2. Fast Fourier Transform

(FFT) on FESEM image (**Figure 5.2c2**) of this film interestingly shows a 3-fold symmetry with rotation of 30° with respect to that observed in the 480^0C and 530℃ cases, though it is relatively more diffuse. The RHEED pattern shown in **Figure 5.2(c3)** is again spotty due to transmission of electrons through thin nanowalls. The c/a ratio of distances between the RHEED spots in vertical and horizontal direction is ≈1.63 characteristic of wurtzite form. Also each of the spots is observed to be anisotropic with an aspect ratio of ≈2.9 along the horizontal [$1\bar{1}00$] and vertical [0001] directions, suggesting a higher degree of misalignment or increased steepness of the wedge shaped walls in comparison to 530℃ pattern. **Figure 5.2(d1)** is FESEM image of a film grown at 630℃ which shows a surface network structure with larger hexagonal network features. On close observation, which will be discussed later, these larger networks supercells that encompass smaller hexagonal cells at lower temperatures. The average wall length is ≈325nm, forming hexagonal feature surrounding the voids. Fast Fourier Transform (FFT) of FESEM image (**Figure 5.2(d2**) shows 3-fold symmetry with no rotation with respect to 580℃ case but rotated w.r.t. the 480 and 530 ℃ images. The streaks are sharper than the 580℃ the case suggesting higher ordering of nanowalls. RHEED pattern shown in **Figure 5.2(d3)** is again spotty due to transmission of electrons through the thin nanowalls. The c/a ratio of distances between the RHEED spots in vertical and horizontal direction is ≈1.63, and each of the spots is anisotropic with an aspect ratio of ≈3.7 along the horizontal [$1\bar{1}00$] and vertical [0001] directions suggesting a higher degree of misalignment (or apex narrowing) in comparison to the 580℃ pattern.

The density of voids measured (by counting) from the plan view FESEM images and the density of screw dislocation estimated from FWHM of rocking curve along (0002) reflection (discussed in details in Section 5.6) for GaN films grown in the temperature range 480−630 ℃ is plotted in **Figure 5.3**. The density of voids monotonically decreases from $4.8-1.0\times10^{10}$ cm^{-2}, and corresponding density of screw dislocation decreases from 1.5×10^{10} to 7.6×10^{9} cm^{-2} with an increase in growth temperature from 480 to 630℃ showing that the dislocation density depends on Ga adatom diffusion. The overlap of trends of density of voids and screw dislocation suggest

that the open voids amidst tri-branched nanowall networks are open screw dislocations. This suggests that smaller cells saturate in growth, and then only supercells grow, as seen in the SEM images.

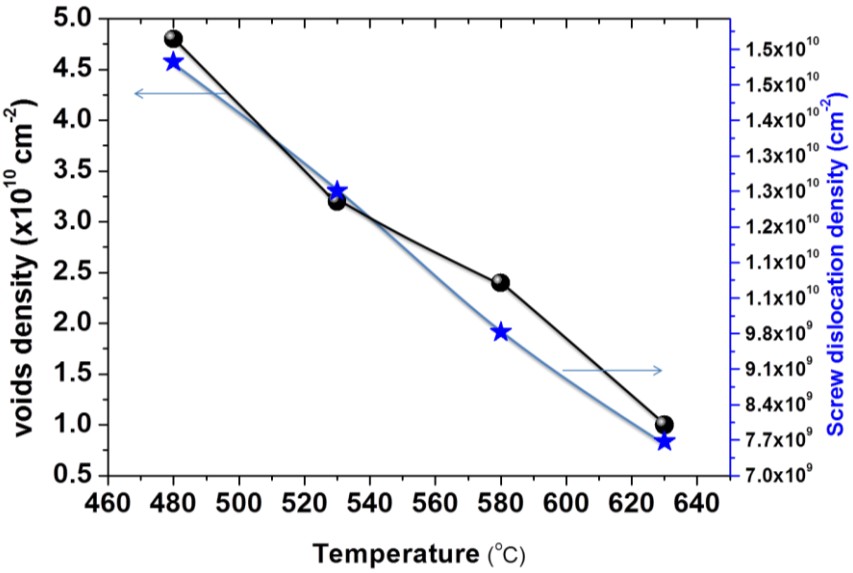

Figure 5.3 *plot of variation in density of voids and screw dislocation density versus temperature*

To provide deeper insight into a tri-branched nanowall network structure, we have obtained a typical high resolution FESEM images for the film grown at 630℃ shown in **Figure 5.4(a−d)**. **Figure 5.4(a)** is acquired at 30° tilt. The white dashed lines superimposed on the image are guiding lines on the larger supercells (height ≈900nm) show that these are fairly well formed hexagons and these circumscribe smaller cells that appear to be of various polygonal shape. Each larger hexagonal supercell encompasses smaller cells, and also the larger ones start forming after the smaller cells stop growing in height which is also evident in **Figure 5.4(b),** which also contains the angle subtended by the walls at the apex. These are obtained by line profile analysis performed over the plan view FESEM images, and the average thickness of these films determined from cross-section SEM image. Thicknesses of the films increase from 0.8−1μm with an increase in growth temperature of these films. The approximate angle between the inclined faces and base of nanowalls vary with growth temperatures. The angle 72° corresponds to crystallographic s-plane $(10\bar{1}1)$, and angle 57° to r-plane $(\bar{1}102)$ planes. In 480℃ case,

dominance of s-plane is observed which decreases with increase in growth temperature with weak shoulder of r-plane observed at low temperature begin to dominate at higher temperature. Thus, in the 630℃ case, combination of m-plane ($10\bar{1}0$), s-plane and r-plane is observed. Image J software is used to measure colour contrast threshold analysis over a plan view images suggest that each films has tri or bilayer deep cavities (voids). In case of 480℃, the film appear to have triple-layer cavity structure whose length varies from 0.07−0.14μm, and in 630℃ case film has bi-layer cavity structure of length varies from 0.13−0.25 μm. But the depth information is limited by the depth contrast from FESEM images, so this may not be accurate for deeper region, and thus the argument is qualitative at best.

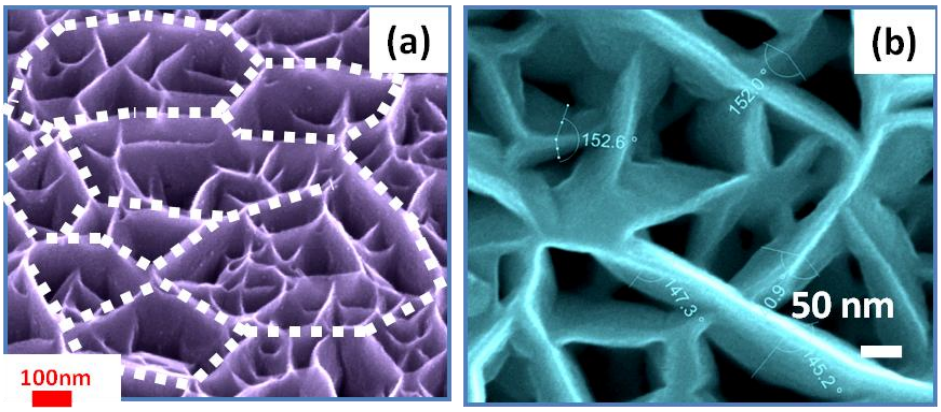

Figure 5.4 *shows high resolution FESEM image of film grown at 630℃ (a) image taken at 30° tilt (white dashed lines are guide to larger size voids), (b) is a plan view.*

5.4 Morphological evolution of GaN film in temperature from 730−880℃.

Figure 5.5(a−d) are plan view FESEM images along with their corresponding RHEED pattern of the films grown at 730−880℃. We will discuss the 650 and 680℃ temperature range later. At higher temperatures the film morphology is entirely different from the GaN nanowall network seen for 480−630℃ temperature range. The films are thinner, compact and flattened and the voids are replaced by a high density of threading dislocations. **Figure 5.5**(*a*1 and b1) shows a morphology that is similar to the typical

MBE grown at BEP V/III ratio <25 in literature [200], suggesting that at higher temperatures the rapid Ga adatom diffusion is faster than the nitridation probability. RHEED spots observed in **Figure 5.5*a*2, b2** at 730 and 780℃ are circular with no anisotropy in spot dimensions, manifesting large and aligned domains both vertically and horizontally, but the film is still rough enough to yield the spotty transmission RHEED pattern. The roughness of films measured by AFM measurement was ≈4nm. The 830℃ and 880℃ films (**5.5 c1, d1**) are made of fewer threading dislocations visible on the film surface, but have mounds developed on top of the films with few holes. The RHEED pattern (**5.5 c2, d2**) is streaky in the <0001> with an overlap of spots which tends to become triangular in shape, manifesting the faceting of the rough surface. The evolution of streaks in RHHED pattern along the [0001] direction indicates that the film is tending towards a 2D morphology. As seen in **Figure 5.8,** the XRD of these films show c-oriented wurtzite structure, but the FWHM of the (0002) peak decreases with increasing temperature, characteristic of compaction of the film at higher temperatures.

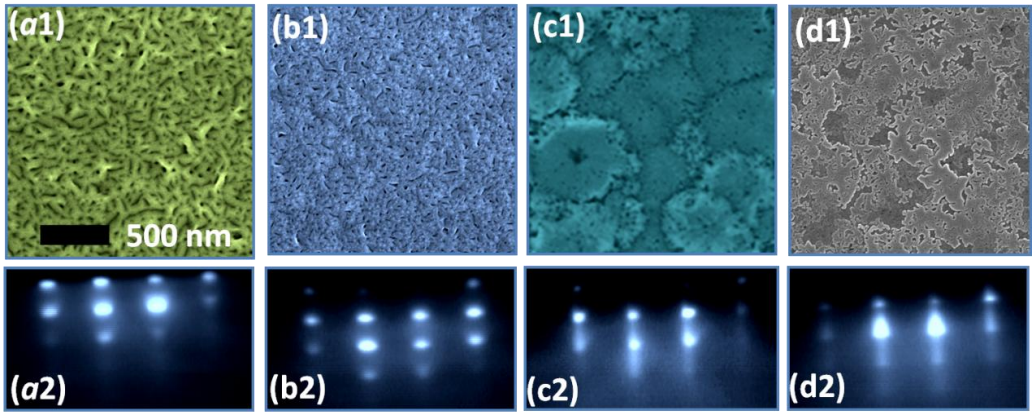

Figure 5.5 ***(a1−d1)*** *are plan view FESEM images with their corresponding RHEED pattern* ***(a2−d2)*** *(acquired along the [2$\bar{1}\bar{1}$0] zone axis) of the GaN films grown on c-plane Al_2O_3 at 730℃, 780℃, 830℃, and 880℃.*

Figure 5.6(a) is a cross-section FESEM image of GaN film grown at 830 ℃ with triangular pyramidal structures of height ≈100nm, on top of a compact 200nm layer. **Figure 5.6(b)** is an top surface FESEM image of GaN film grown at 880 ℃ acquired at a tilt angle of 30° with respect to basal plane (0001). The mounds appear like pillars ≈100nm wide grown over a compact GaN film. The films with mounds over compact

films, suggest that initially a compact layer grows in layer by layer growth mode upto a thickness ≈200nm in case of 830 ℃ film and ≈100nm in case of 880 ℃ film. Thus, beyond this critical thickness the growth proceeds as island growth, since the strain developed in GaN layer at the interface at these high temperatures, get relaxed, and mound like island structures form.

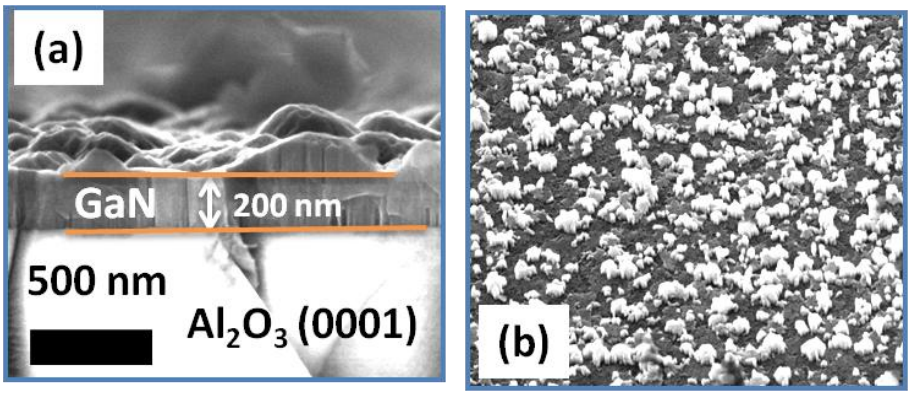

Figure 5.6 *(a) Cross-sectional view FESEM image of 830℃ and (b) tilt view image of 880℃ of the GaN films grown on c-plane Al_2O_3.*

5.5 Morphology of GaN film grown ≈680℃.

Figure 5.7(a) is an FESEM image of film grown at 680℃ acquired at a tilt of 30° with respect to basal plane (0001) shows GaN nanocolumns amidst nanowalls matrix network and RHEED pattern acquired along $[2\bar{1}\bar{1}0]$ zone axis is shown inset of **Figure 5.7(a)**, RHEED spots show an anisotropy ratio of ≈1.7 elongated in the $[1\bar{1}00]$ direction which is lesser than that of the film grown at 480℃. **Figure 5.7(b)** is the surface morphology of a 1μm thick film, which shows the emergence of a 140 nm hexagonal shaped nanocolumn in the GaN nanowall matrix. This shows clearly that the nanocolumns originate at the film-substrate interface and grow in the voids between the nanowall network. Initially with increasing coverage, the nanowalls grow upto a certain thickness, after which we see the growth of nanocolumns while the nanowall extent does not change further. The hexagonal shapes of the columns suggest m-plane side wall facets perpendicular to c-

plane of the wurtzite GaN nanocolumns [134]. **Figure 5.7(c)** shows the cross section FESEM image after growing 4.0 μm thick GaN, where we can visualize the nanowall matrix and the nanocolumns of about 400nm diameter and with a density of $\approx 1\times10^{8}$, as counted and averaged over several FESEM images (1μm x1 μm).

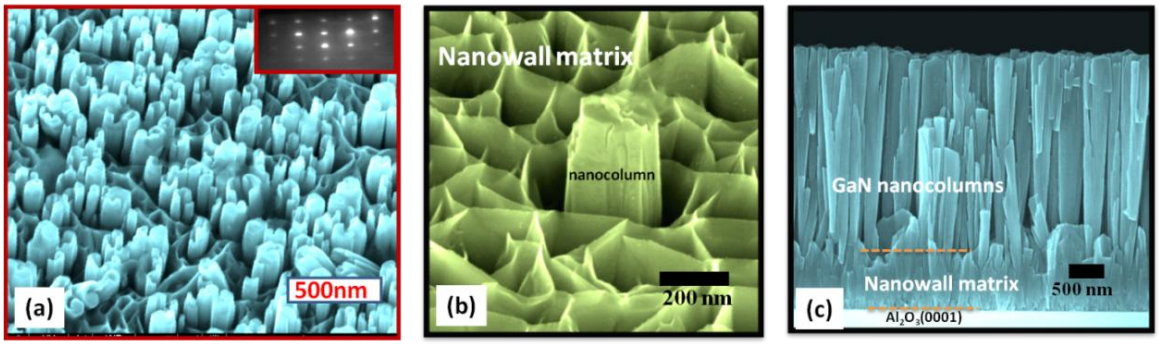

Figure 5.7. *(a) FESEM images acquired at 30° tilt of the GaN films grown on c-plane Al_2O_3 at 680^0C and inset show a RHEED pattern (along the [$2\bar{1}\bar{1}0$] zone axis), (b) is a high resolution plan view FESEM image of nanostructures acquired at 30° tilt with the surface normal for 0.6μm thickness and (c) cross-sectional view FESEM image of 4.0μm GaN nanocolumns.*

The nanocolumns of height ≈4μm appear protruding outward from a matrix layer of height ≈ 300nm. These nanocolumns originate at the film-substrate interface and grow in the voids between the nanowall network. After a critical height of the formation of walls, the nanorods grow at the cost of the walls, since the nanocolumns height increases while that of the network matrix height remains constant at ≈ 300nm. The GaN nanocolumns are c-oriented wurtzite, self aligned and hexagonally faceted with m-plane walls and bound by the nanowall honeycomb matrix, as will be shown by XRD results in addition to the RHEED with continued growth, the nanocolumn develop very high aspect rations, as shown in **Figure 5.7(c)**, where the columns are > 3μm long.

5.6 Structural and optical properties of GaN films grown on bare c-plane sapphire in temperature range 480-880℃.

Figure 5.8 (a) shows representative XRD 2Θ-ω pattern for all GaN films have peaks at 2θ= 34.54°, 72.8°, which correspond to symmetric reflection at the (0002) and (0004)

planes of GaN, and peaks at 2θ= 42.68°, 91.40° which are from symmetric reflections (0006) and (000 12) planes of (0001) Al_2O_3. In-plane φ scans were acquired by rotating samples around its surface-normal direction to investigate the in-plane alignment of the GaN film. The φ scan pattern shown as inset in **Figure 5.8 (b)** of the $(10\bar{1}5)$ plane of all GaN films shows six diffraction peaks from the $(10\bar{1}5)$ plane at 60° intervals, confirming the hexagonal wurtzite structure of the films. Hence all films are uniphase and wurtzite single crystals with their c-plane parallel to the substrate surface, similar to the surface structure observed by RHEED.

The X-ray ω-scan rocking curve is a direct measure of threading dislocation density and type. The structural quality of the films grown in the substrate temperature range of 480−880℃ is determined by the FWHM of rocking curves (ω-scan) and the thickness of the films is obtained from the cross-section FESEM image. In **Figure 5.8(b)**, y-axis shows the variation in full width at half-maximum (FWHM) as a function of substrate temperature of the (0002) reflection. The FWHM of the (0002) peak is observed to decrease from ≈70 arc min at 480℃ to ≈15 arc min to 880℃, with a flat region from 630 to 780℃ growth temperatures. To observe quantity of material incorporated into GaN films grown for fixed growth time of 2 hours at a constant incident Ga and N_2* flux (N/Ga BEP ratio 100) and different substrate temperatures, we plot the film thickness, obtained by cross-section FESEM images, on the alternate y-axis of **Figure 5.8(b)**.

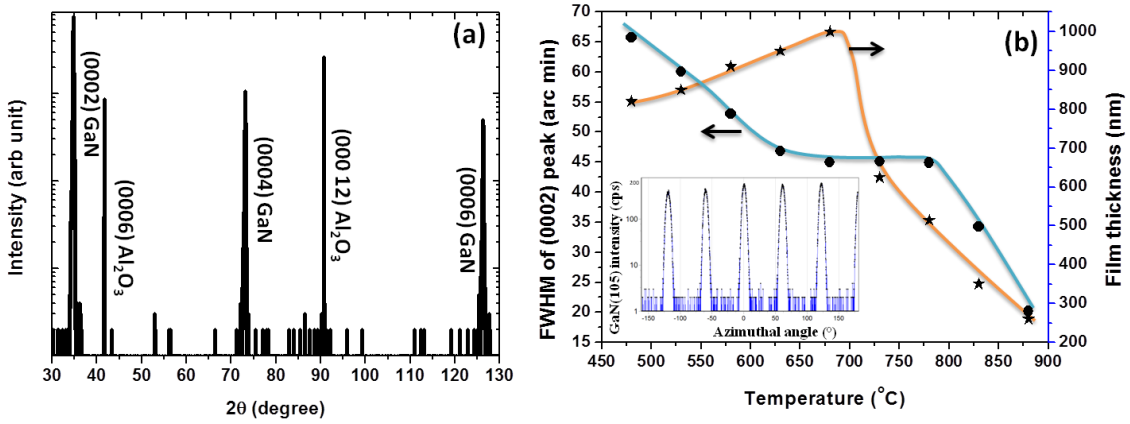

Figure 5.8 ***(a)*** *shows representative 2θ-ω XRD pattern and (**b**) plots of FWHM of the rocking curve along (0002) GaN reflection and GaN film thickness verses temperature. Inset shows representative azimuthal angle dependence (φ scan) of the intensity of GaN $(10\bar{1}5)$ plane.*

In temperature range of 480℃ to 680℃, the thickness of the film increases from ≈0.8−1μm, though the flux rate remains same. In this regime, the FWHM decreases linearly from ≈65−45 arc mins, which suggests a decrease in defect density. In temperature range 680℃ to 780℃, we observe a steep fall in film thickness from ≈1−0.5μm, but the FWHM remains constant, suggesting that the GaN film has reached its maximum compaction. At these higher temperatures, this can be attributed to higher diffusion lengths of Ga adatoms before they get nitrided, leading to the formation of flat films. However, at temperatures > 780℃, reduction in sticking coefficient of the impinging Ga or N species and dissociation of GaN prior to incorporation into the GaN film lead to thinner films of thickness < 0.5μm.

Types of threading dislocations present in GaN films can be screw, edge and mixed, which manifest in X-ray rocking curves. The FWHM of ω-scan for symmetric reflection (0002), (0004), and (0006) provide information of threading screw dislocation and for asymmetric reflections (10$\bar{1}$1), (10$\bar{1}$2), (10$\bar{1}$3), (10$\bar{1}$4), (10$\bar{1}$5) etc of edge dislocation density [201-202]. The screw dislocation density D_{screw} can be estimated from the following equation.

$$D_{screw}=\frac{\beta^2_{[hk\bar{i}\,l]}}{9\,b^2_{screw}} \quad \text{where h=k=0, and l}\neq 0 \quad \text{..... (5.1)}$$

Where β is the FWHM of ω-scan rocking curve, b is the magnitude of Burgers vector (b_{screw}=0.5185 nm). The simple ω-scan measurement along symmetric reflection is performed along (0002) reflection. Using equation (**5.1**) D_{screw} is calculated from the FWHM of rocking curve along (0002) reflection for GaN films grown in substrate temperature range 480℃ to 880℃. **Figure 5.9** shows a plot of screw dislocation density versus growth temperature. With increase in temperature density of screw dislocation per cm^2 (D_{screw}) decreases monotonically with increase in temperature range 480−630℃ and 780−880℃, but it remains almost constant in range 630−780℃. The density of screw component is highest in film grown at 480℃ and least in film grown at 880℃. Thus, relatively density of edge dislocation will be least in film grown at 480℃ and maximum in film grown at 880℃. Plateau region in the curve from 680℃ −780℃ suggests that the

density of threading dislocations remain constant for films grown in this temperature range. Epitaxial thin films having a large lattice mismatch with their substrate invariably form highly imperfect epitaxial layers with mosaic crystal structure of slightly disoriented sub-grains with respect to each other and the underlying substrate. The mosaic structure results due to line up of threading dislocation to form a network of low-angle grain boundaries. The mosaic structure is usually characterized by its x-ray rocking curve on a reflection normal to surface. Srikant et. al.[203] suggested that the tilt describes their out-plane rotation of the mosaic blocks. For (0001)-oriented GaN epitaxial layers, the tilt is related to the density of the screw-type treading dislocations with b=<0001>. Because of the character of the threading dislocations in GaN layers, the mean tilt angle was almost linearly depend on the (0002) FWHM, which can be measured directly using x-ray diffraction. Thus, the curves in **Figure 5.8(b)** and **5.9** suggest that the mean tilt angle which is directly proportional to the density of screw dislocation decreases with increase in temperature upto 630℃, and remain constant from 630−780℃, and decreases beyond 780℃. This can happen if void density remains same, but the growth of supercells hides information from the smaller cells. This will be discussed again later in this Chapter.

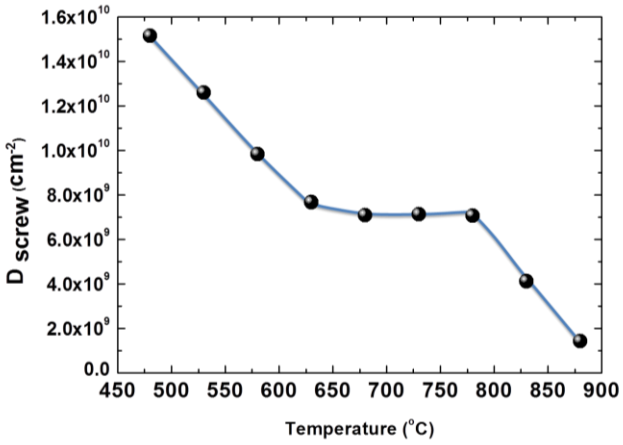

Figure 5.9 *plot of screw dislocation density D_{screw} versus substrate temperature.*

The study of the optical property by CL measurements at room temperature for each growth is consolidated in **Figure 5.10**. In a representative CL spectrum (**Figure 5.10a**) the emission peak centered at 365.2nm (3.40 eV) is attributed to the band-edge

luminescence (BEL) [204]. The peak positions (along y-axis) and FWHM (along alternate y-axis) for BEL of CL spectrum of the GaN films grown at temperatures from 480^{0}C to 880^{0}C are shown in **Figure 5.10(b)**. The band-edge transition energy is ≈3.43 eV for the film grown at 480^{0}C film, which increases to ≈3.53eV for films grown at 630^{0}C. For temperatures > 630^{0}C, transition energy decreases and almost attain the bulk values of 3.40 eV beyond 730^{0}C substrate temperature. Along the y-axis, the FWHM of the CL follows the trend similar to the plot of film thickness versus temperature shown in **Figure 5.8(b).** We attribute this variation in position of BEL peak positions and FWHM to the reduction of defects and strain in the GaN film.

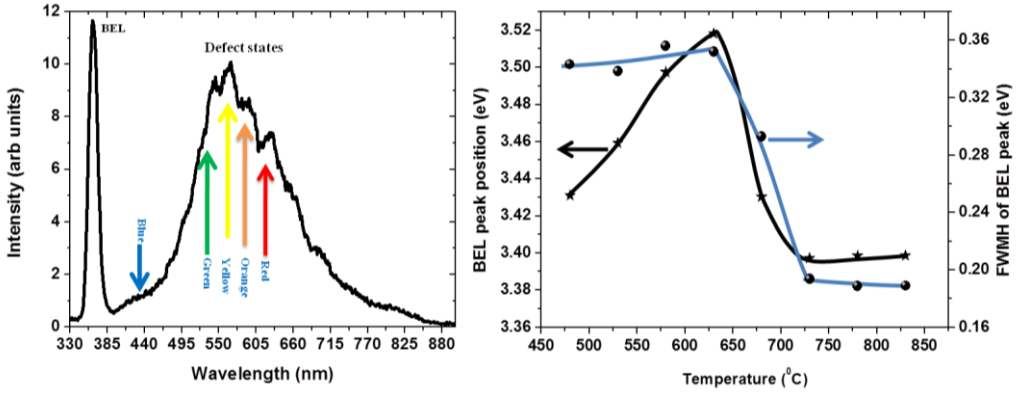

Figure 5.10 ***(a)*** *shows typical CL spectra and* ***(b)*** *is a plot of CL spectrum FWHM and BEL peak position versus temperatures*.

The intensity variation of XRD rocking curve along (0002) and CL band edge luminescence (BEL) shows similar trends with variation in growth temperature. The intensity of the CL emission is an important parameter to evaluate the quality of the material [205]. The plot of CL BEL peak intensity versus FWHM of rocking curve along (0002) reflection is a good indicator of CL intensity dependence on screw dislocation density[206]. **Figure 5.11(a)** shows a strong correlation between the CL intensity of BEL and the densities of screw-type dislocations, described by rocking curve FWHM along (0002) reflection. The intensities of the BEL of CL spectrum decreases with decrease in FWHM of rocking curve along (0002) reflection for films grown beyond 680℃, thus screw dislocation density decreases with increase in temperature greater than 680℃. At temperatures below 680℃ the intensity of the BEL of CL spectrum increases with

decrease in FWHM of rocking curve along (0002) refection when temperature is increased from 480−680℃, suggesting decrease in screw dislocation density. It is known that the energy bandgap of a semiconductor is affected by the residual stress in film. A tensile stress will result in a decrease of energy band gap while a compressive stress cause an increase of the band gap. According to Zhao et al[207], the bandgap of GaN film at room temperature can be expressed in terms of biaxial stress σ_{xx} as linear relation (5.2)

E_g=3.43+0.211σ_{xx} (eV) .....(5.2)

where E_g is the BEL peak position, alternately,

σ_{xx} = (BEL peak position − 3.42) (in meV)/21.2, where 1.5nm ≈ 14meV

The BEL peak positions (along y-axis) and biaxial stress (along alternate y-axis) of the GaN films grown at temperatures from 480℃ to 880℃ are shown in **Figure 5.11(b)**. The band-edge transition energy is ≈3.43 eV (σ_{xx}= 0.12 GPa) for the film grown at 480℃, which increases to ≈3.53eV (σ_{xx}= 4.24 GPa) for films grown at 630^{0}C, suggest increase in biaxial compressive stress. Beyond 630^{0}C biaxial stress changes into tensile stress. For 680℃ film the in-plane biaxial stress in minimum (σ_{xx}= 0.08 GPa), this signifies that film is more relaxed relative to other films. For temperatures beyond 680℃, transition energy decreases further so that σ_{xx}=−1.42 GPa.

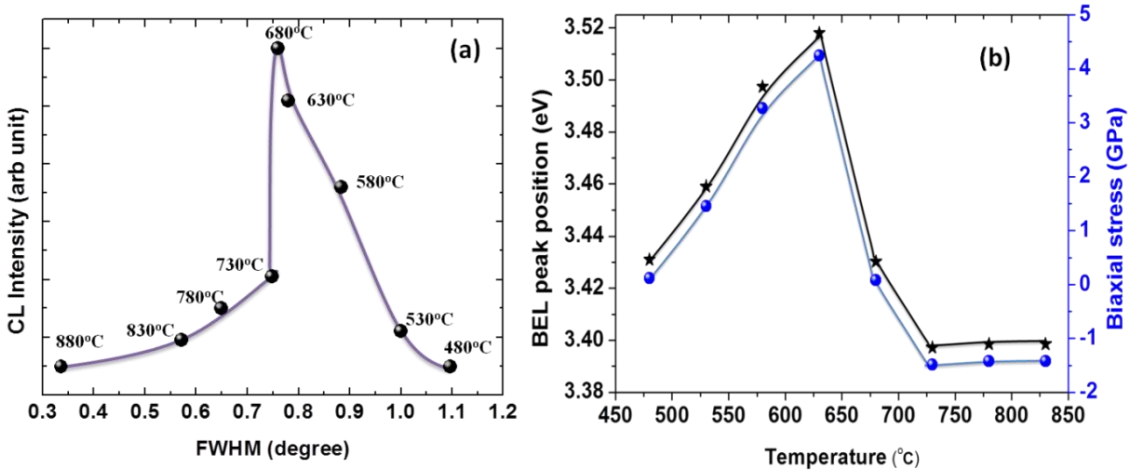

Figure 5.11(a) *Plot of CL intensities of band edge luminescence (BEL peak) versus FWHM of rocking curve along (0002) symmetric reflection, Figure **5.5(b)** BEL peak positions (along y-axis) and biaxial stress (along alternate y-axis) of the GaN films grown at temperatures from 480℃ to 880℃.*

The luminescent band as represented by the BEL peak position plot versus residual stress in GaN films grown at 480℃ to 880℃ is shown in **Figure 5.12**. This implies that as growth temperature is increase from 480−680℃, the in-plane compressive stress in the films increases and beyond 680℃ it tends to becomes in-plane tensile stress.

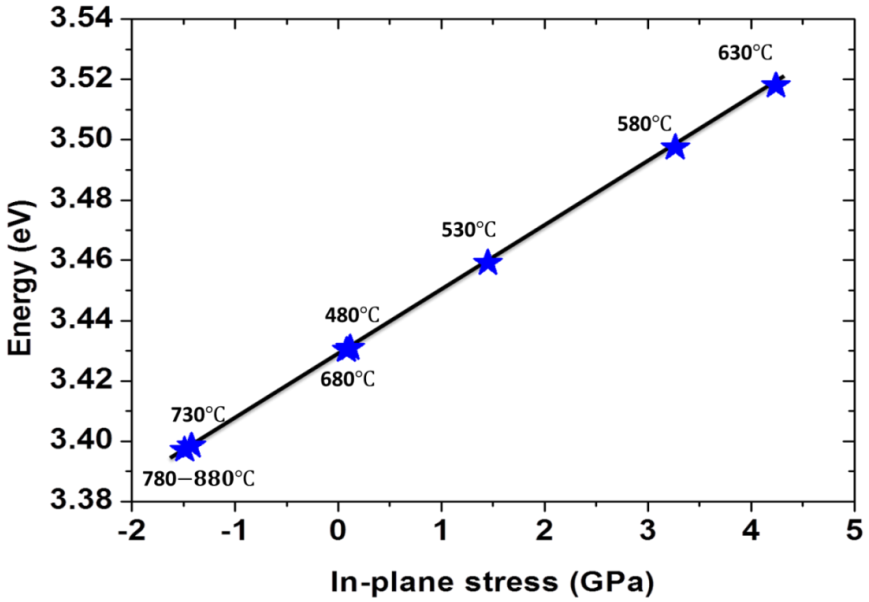

Figure 5.12 *shows the luminescent band as represented by the BEL peak position versus residual stress in GaN films grown at 480℃ to 880℃.*

Raman spectroscopy is well established as a non-destructive and relatively rapid method to determine the averaged values of residual strain. According to the Raman selection rules, only $E_2^{(1)}$(high), $E_2^{(2)}$(low), and A_1(LO) modes are observed with the backscattering z(x,x)$\bar{z}$ geometry for wurtzite GaN. **Figure 5.13(a)** shows the typical Raman spectra obtained, showing peaks at 559, 568 and 735 cm^{-1} which corresponds to E_1(TO), E_2(high) and A_1(LO). The Raman shift of the GaN E_2(high) mode has been reported by several groups (**REF**), and the reported values vary in the relatively large range of 565 to 572 cm^{-1}, reflecting differences in the residual strain in the epilayer after growth, suggesting high sensitivity of the technique. The reported shifts of the E_2(high) mode for freestanding GaN samples, show the relatively wide range 566−568 cm^{-1}, suggesting that freestanding GaN films grown by HVPE techniques usually contain high

defect densities due to relaxation of hydrostatic stress [208]. The E_2(high) mode of strain-free GaN is known to be at 567.6 cm^{-1}at room temperature [209]. **Figure 5.13(b)** shows variation in position of E_2(high) mode on left y-axis and on alternate y-axis relative shift ($\Delta\omega$) with respect to strain-free GaN versus growth temperature. The position of Raman E_2(high) mode for films grown at 480℃ and 530℃ is ≈570 cm^{-1} with a shift $\Delta\omega \approx 3.5 cm^{-1}$. But with increase in growth temperature form 530℃ to 680℃ the E_2(high) mode position shifts from ≈570 to 568 cm^{-1}, and shift $\Delta\omega$ decrease from ≈3.5 to 1.3 cm^{-1}. For growth temperature beyond 680℃ position of E_2(high) mode again shift toward higher wave number, as growth temperature increased from 680℃ to 880℃, E_2(high) mode position increases from ≈568 to 579 cm^{-1}, with increase in shift $\Delta\omega$ from ≈1.5 to 4.1 cm^{-1} is observed. Thus, the minimum residual strain is observed in case of film grown at 680℃, slightly higher than the bulk value. Since strain in GaN films affects the wavelength of the E_2 mode and its replicates, the location of E_2 peaks is used to determine the amount of strain in a film. Raman system if set up in Stokes mode, the relative shift in E_2 mode towards lower (higher) wave number is due to compressive (tensile) stress in the film with respect to bulk GaN. This suggests that as growth temperature is increased from 480-680℃ the in-plane compressive stress in the film decreases and beyond 680℃ in-plane tensile stress is observed.

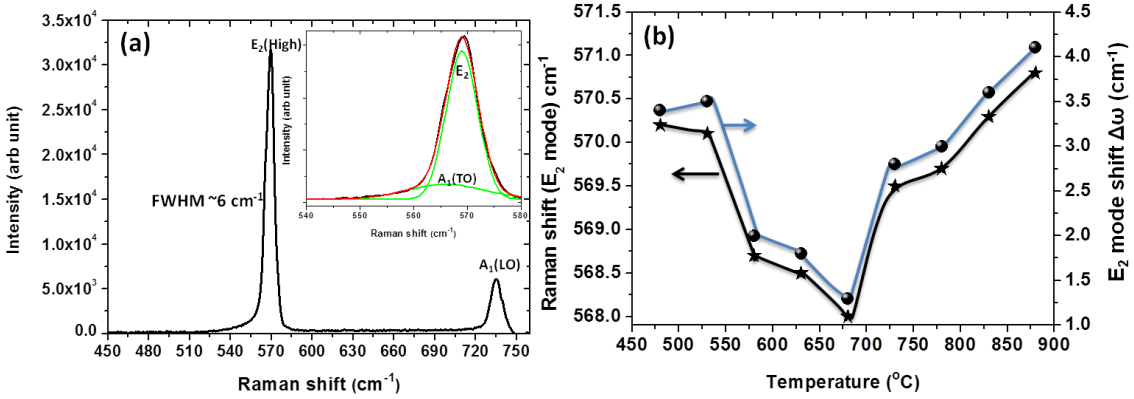

Figure 5.13(a) *shows a typical Raman spectra and inset shows magnified deconvoluted E_2(high) peak,* ***(b)*** *is a plot of variation in position of E_2(High) Raman mode and shift in E_2(High) ($\Delta\omega$) with respect to strain free GaN versus temperature. The Position of E_2(High) mode of strain-free GaN on sapphire substrate ≈567.6 cm^{-1}at room temperature.*

Figure 5.14 is plot of variation in hydrostatic and biaxial tensile stress in GaN films grown in temperature range 480 and 880℃. It is well known that a biaxial stress of 1 GPa shifts the E_2(high) Raman mode by ≈2.7±0.3cm^{-1}, and a hydrostatic stress of 1GPa shifts it by ≈4.17cm^{-1} with respect to strain-free bulk GaN. The deviation frequency of a given phonon mode γ under symmetry-conserving stress can be expressed in terms of biaxial stress σ_{xx} (in linear approximation) [210-211]. The relation between the frequency shift Δω (cm^{-1}) of E_2 (high) mode and biaxial stress σ_{xx} (GPa) can be expressed as $\Delta\omega_\gamma = K_\gamma\ \sigma_{xx}$, where K_γ is constant whose value is between 2.7 to 4.3, as reported in literature[208,210,212]. For all GaN films grown in temperature range 480-880℃, the position of E_2 (high) mode is above 567.6 cm^{-1}. Thus Δω is positive, and signifies tensile stress in the films. In case of GaN films grown at 480, 530, 830 and 880℃ shift in E_2 Raman mode 0.29cm^{-1} <Δω <0.36 cm^{-1} suggests hydrostatic tensile stress and for 630, 680, 730 and 780℃ shift in E_2 Raman mode 0.78cm^{-1} <Δω <0.96 cm^{-1} suggests biaxial tensile stress. Hydrostatic stress ≈ 0.3GPa in GaN film grown in the range 480 to 530℃, and increases to ≈ 0.3−0.35 GPa measured in films grown at 830 and 880℃. Biaxial stress of ≈0.8GPa is measured for GaN film grown at 480 and 530℃, increases to ≈ 0.8−1.0 GPa for films grown at 830 and 880℃.

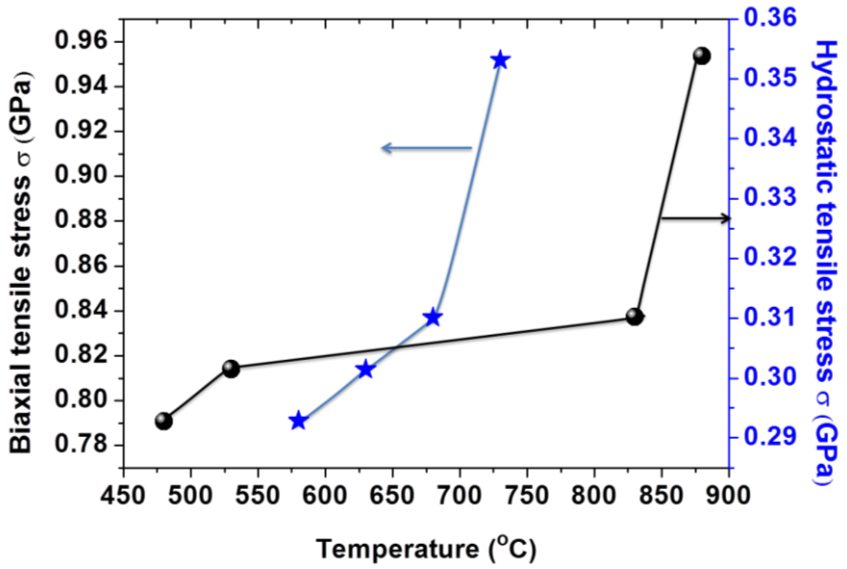

Figure 5.14 *Biaxial and Hydrostatic stress variation in GaN films versus temperature*

X-ray photoelectron spectroscopy (XPS) typically probes a few monolayers below films surface thus enabling us to extract information on N or Ga surface richness, quantitative estimation of the elemental composition and stoichiometery of GaN films [213-214]. X-ray photoelectron spectroscopy (XPS) measurements are performed for GaN films grown in temperature range 480−880℃. In **Figure 5.15(a)**, core N_{1s} level spectra of 480℃, 680℃, and 880℃ films are shown along which is deconvoluted into four Gaussian peaks labelled as P1, P2, P3, P4. Peaks P1, P2 correspond to the N(1S) at binding energies ≈397.0 eV (FWHM=2.0 eV), ≈395.0 eV (FWHM= 1.9 eV), respectively. Peaks P3, P4 corresponds to Ga $L_2M_{45}M_{45}$ Auger line at binding energies of ≈393.0 eV (FWHM=1.8 eV), ≈391.0 eV (FWHM=1.8 eV), respectively. In **Figure 5.15(b)**, ratio of percentage area under the peaks P1 and P3 are plotted on y-axis and on alternate y-axis ratio of percentage area under the peaks P2 and P4 is plotted versus growth temperature. In the case of film grown at 480℃, the ratio of percentage area is maximum and decreases monotonically with an increase in substrate temperature. Thus, GaN film grown at 480℃ is more nitrogen rich (N terminated) relative to film grown at 880℃, and film grown at 880℃ is gallium rich (Ga terminated).

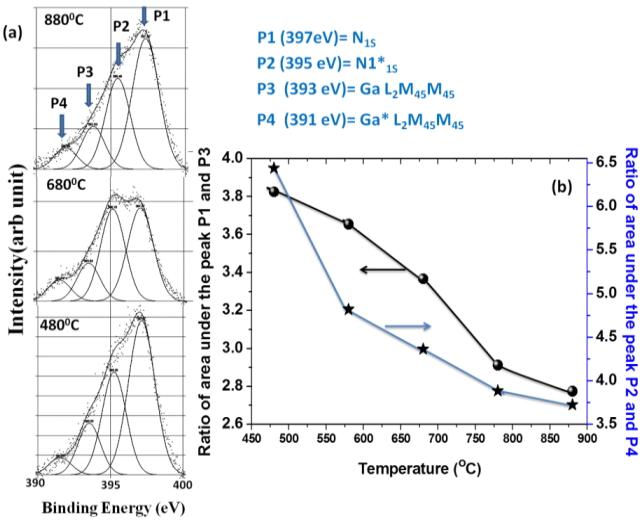

Figure 5.15*(a)* *core level peak of N(1S) spectra of GaN films grown at substrate temperature 480, 680 and 880*℃*, plot* ***(b)*** *on y-axis show ratio of area under the peak P1 and P3 and on the alternate y-axis ratio of area under the peak P2 and P4 versus substrate temperature 480 to 880*℃.

In **Figure 5.16** we show the photoelectron emission close to the valence band. **Figure 5.16(a)** shows valence band XPS spectra of GaN films grown at temperature 480−880℃. Peak A2 is mainly related to Ga(4s)−N(2p) bonding state (≈ 3eV) and peak A1 correspond to Ga(4p)−N(2p) (≈7eV). Figure 5.**16(b)** shows plot of ($E_{VBM}-E_F$) on y-axis and the ratio of area under peak A2 and A1 on alternate y-axis, versus growth temperature, were $E_{VBM}-E_F$ is a difference in energy between VBM (valence band maxima) and E_F(Fermi level). In literature, Fermi level E_F is referenced at 0 eV in all density of state calculations for GaN. The ($E_{VBM}-E_F$) in case of 480℃ is ≈1.5 eV which increases to ≈1.85eV for 880℃ film. In between 580 to 680℃ it is ≈1.7 eV. The ratio of areas under the peak A2 and peak A1 increases upto 580℃ and then decreases with increase in temperature.

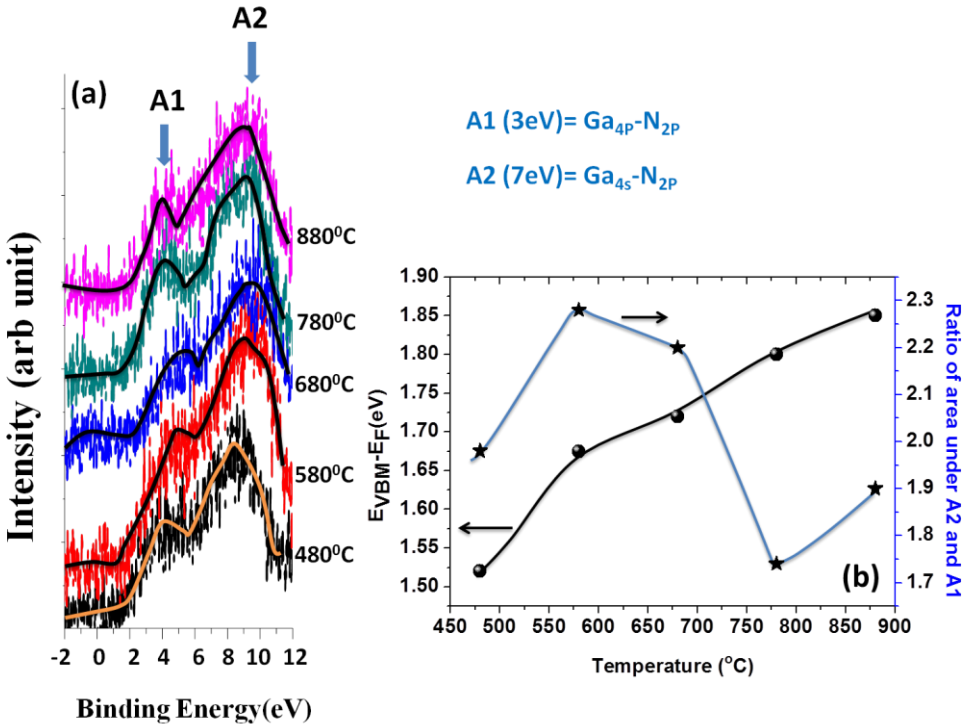

Figure 5.16 ***(a)*** *shows valence band spectra,* ***(b)*** *is a plots of E_{VBM}-E_F (E_F and E_{VB} represent energy at Fermi level and valence band maxima) on y-axis and on alternate y-axis ratio of area under the peak A_2 and A_1 (Peak A_1 and A_2 corresponds to Ga_{4p}-N_{2p} and Ga_{4s}-N_{2p}) of films grown at 480, 580, 680, 780, and 880℃.*

Until now we have discussed morphology, structural and optical properties of GaN films grown in the temperature range of 480−880℃, in steps of 50℃ where we observed that structural and optical properties alter on both sides of 680℃ this growth temperature. The FWHM of rocking curve acquired at (0002) reflection or the density of screw dislocations remains similar in this temperature range. Also the FWHM of BEL peak and its position in CL spectrum shows sudden transition on both alternate sides of this temperature range. Raman measurement shows that in temperature range 680-780℃ films have biaxial stress and beyond this range stress is hydrostatic. XPS measurements show that on the alternate side of this range film surface is either N-rich to Ga-rich surface. This variation in Ga-, N-rich surface of films grown in nitrogen rich conditions suggest that films are transforming from 3D growth mode as expected in N-rich condition to 2D growth mode in Ga-rich condition. Thus we decided to discuss entire temperature range 480−880℃ into three parts (480−630℃, 630−730℃ and 730−880℃) to extract information of surface structure and morphology of these films.

5.7 Effect of nitrogen flux on the formation of GaN nanocolumns on c-plane sapphire

We now perform experiments to study the effect of nitrogen flux on the growth of GaN films, while the substrate temperature is kept at 680℃ and Ga flux of 3.86×10^{14} atoms cm^{-2} s^{-1}. Plan view FESEM images of the surface morphology of GaN thin films formed at nitrogen flow rate of 2, 4.5, 6 and 8 sccm are shown in **Figure 5.17** a, b, c and d, respectively. It can be clearly seen that **Figure 5.17** a, c and d, show a 2-D network of GaN made up of nanowalls which have a 3-fold symmetry as realized by performing Fast Fourier Transform (FFT) on these images shown below each image. The images also show that these tri-branched network comprising of wedge shaped GaN nanowalls of thickness of ≈150 nm at the bottom tapering to ≈10 nm at the (apex) and are oriented in-plane along the $<11\bar{2}0>$ and $<10\bar{1}0>$ crystallographic directions. These walls circumscribe micro-cavities (voids) of density ~$10^9 cm^{-2}$, suggesting that the voids can be open screw dislocations[201]. For higher flux rates of 6 and 8 sccm, the network

morphology is seen to change with increase in the nanowall length and width. Line scans across the widths of the nanowalls formed, in these FESEM images, reveal that they have triangular features with an average angle φ ≈72, 45 and 22° with the (0001) plane normal for different N_2 flow rates and are included in the respective micrographs. **Figure 5.17(b)** shows plan view FESEM image of GaN film formed at the intermediate nitrogen flux of 4.5 sccm, in which we see that amidst the nanowall network, hexagonal nanocolumns of diameters of ≈150nm protrude out of the voids. The density of these hexagonal nanocolumn features is approximately ~ 10^9 cm^{-2} and are ≈1μm long for this 2 hour growth (corresponding to 0.6μm for a flat film) as measured from the cross-sectional FESEM images. As mentioned earlier, the line scans across the nanowall of **Figure 5.17(b)** show that the sides of the 2D nanowalls formed are the $\{\bar{1}102\}$ r-plane making an angle φ≈57° with the normal to the (0001) plane. It is known that the r-plane has lower sticking coefficient for Ga adatoms[134]. The side walls of the hexagonal faceted nanocolumns are seen to be m-planes $\{10\bar{1}0\}$ which also have a very low sticking coefficient for Ga adatoms. The mechanism that is possibly underlying these observations will be discussed in the next Chapter.

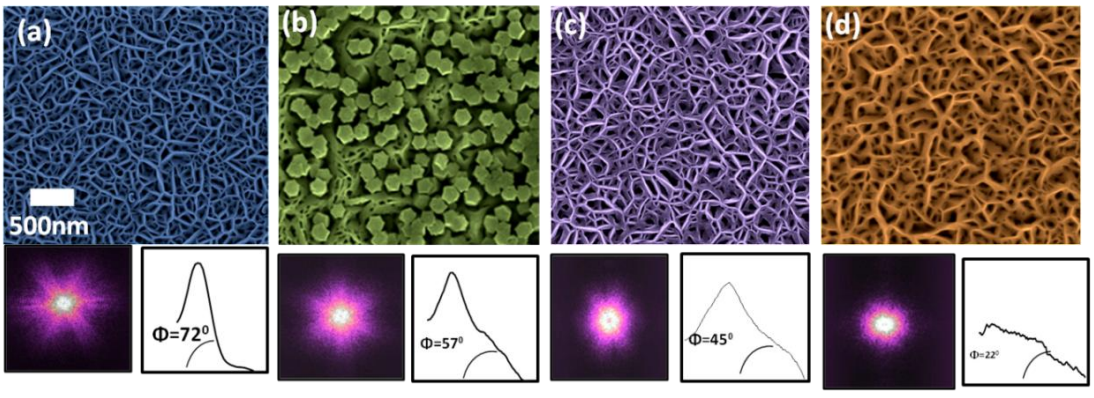

Figure 5.17 *show FESEM plan view images of GaN Nanowall Network grown at 2, 6 and 8 sccm nitrogen flow rate and of nanocolumns grown at 4.5 sccm nitrogen flow rate on bare c-plane sapphire. Φthe angle between the inclined faces of nanowalls with respect to (0001) plane is shown in each image.*

The monotonic decrease in angles with an increase in nitrogen flux suggest that with increasing nitrogen flux rates the widths of the nanowalls increase and the tapering

decreases (**Figure 5.18a**). The angle φ(72) of the nanowalls formed at 2 sccm shows that it is the s plane (10$\bar{1}$1), and the angle φ(57) of the remnant nanowalls seen alongwith the nanocolumns corresponds to the r plane ($\bar{1}$102) planes (**Figure 5.18b**). At higher nitrogen flux, the Ga adatoms diffuse only shorter lengths before they are nitrided by the active nitrogen plasma[215]. Under these conditions average diffusion lengths of Ga adatoms is small. With increase in nitrogen flux rates the increased diffusion barrier results in the lateral growth of the walls, making them wider at the cost of their height, and thus the reduction in the nanowall angle (φ).

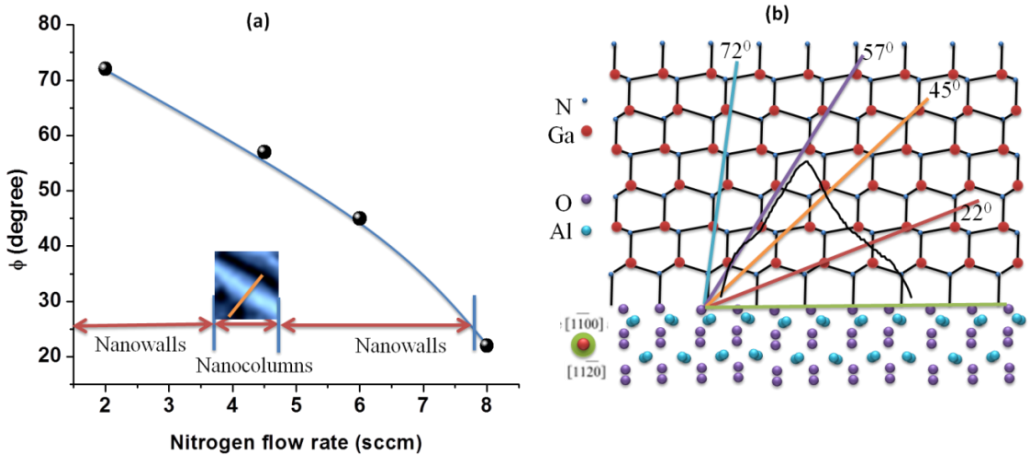

Figure 5.18 *(a) plot of Φ the angle between the inclined faces of nanowalls with respect to (0001) plane versus nitrogen flow rate, (b) Planes corresponding to angle Φ on ball and stick model also a line profile of a solitary nanowall seen in 4.5 sccm case films.*

A representative XRD 2Θ-ω pattern for GaN thin films for both the nanowall network (2 sccm) and nanocolumn (4.5 sccm) phases is shown in **Figure 5.19**. The pattern shows prominent peaks at 2θ=34.54°, 72.8° and 126.3° , which are identified as reflections from (0002), (0004) and (0006) planes of wurtzite GaN. Peaks at 2θ= 41.6°, 90.8° are indexed as reflections from respective (0006), (000 12) planes of the sapphire substrate[16]. Absence of reflections from other phases or disoriented grains confirms that the nanowalls and nanocolumns are made of high quality single crystalline, c-oriented wurtzite GaN. Inset of **Figure 5.19** shows the characteristic RHEED pattern recorded

along the {11$\bar{2}$0} azimuth observed for GaN films grown at nitrogen flow rates 4.5, and 6 sccm. The distance between RHEED spots in these characteristic transmission pattern through nanostructures, in lateral and vertical direction is 1.89 which is equal to 2a*/√3c* ratio (a*=2Π/a, c*=2Π/c) implying that the c/a ratio is 1.63, confirming the c-oriented wurtzite structures of these nanowalls and nanocolumns[169]. The spots in the 6 sccm case show elongation along [1$\bar{1}$00] direction, which can be attributed to the misorientation of the GaN nanowalls. However, the RHEED spots of the nanocolumn phase show less anisotropic spots. It is evident that the remnant nanowall network contributes to the spot elongation, while nanorods result in sharp circular spots.

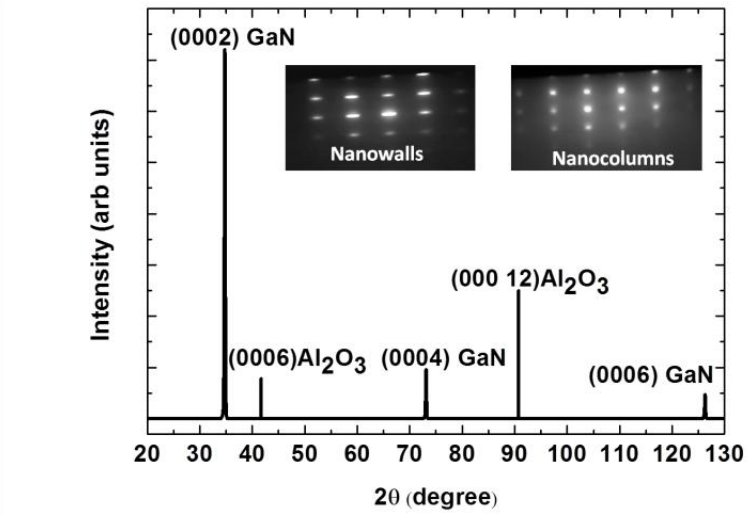

Figure 5.19 *shows typical 2Θ-ω XRD pattern of wurtzite GaN nanowall and nanorods. Inset shows representative RHEED pattern of nanowall and nanorods.*

To study the optical properties of these nitrogen flux dependent phases, Cathodoluminescence spectra are acquired *in situ* at room temperature by a 5kV incident electron beam for different nitrogen flow rates, and are shown in **Figure 5.20**. Wurtzite GaN yields a band-edge luminescence at 3.40eV and defect peaks in the range of 1.40−2.80 eV[204]. The spectra show that the band-edge emission and defect related peaks slowly rise with increasing nitrogen flux from 2.0 to 8.0 sccm, for all nanowall network phases. However, for the 4.5 sccm nanocolumn phase the band-edge emission is very intense and the defect related features are diminished. The inset of **Figure 5.20** shows the

quality of emission versus nitrogen flux, with its y-axis being the intensity ratio R of band-edge emission at 3.4 eV to defect luminescence measured at 2.0 eV as a function of nitrogen flux along y-axis. The overall intensity of the CL and the ratio R increases from 0.4 to 0.8 with increase in nitrogen flux rates 2.0, 6.0 and 8.0 sccm for all the nanowall phases, indicating a slight decrease in defect states. However, for the 4.5 sccm nanocolumn phase the ratio R increases sharply and yields highest intensity among all flux rates studied, not only due to enhanced band-edge emission at 3.40 eV, but also due to negligible defect emission. The FWHM of the CL band edge emission is also narrower (0.2eV) than that in the nanowall phase (0.6eV). This clearly suggests that the nanowall network consists of defects states but the nanocolumn phase has excellent crystallinity and high optical quality

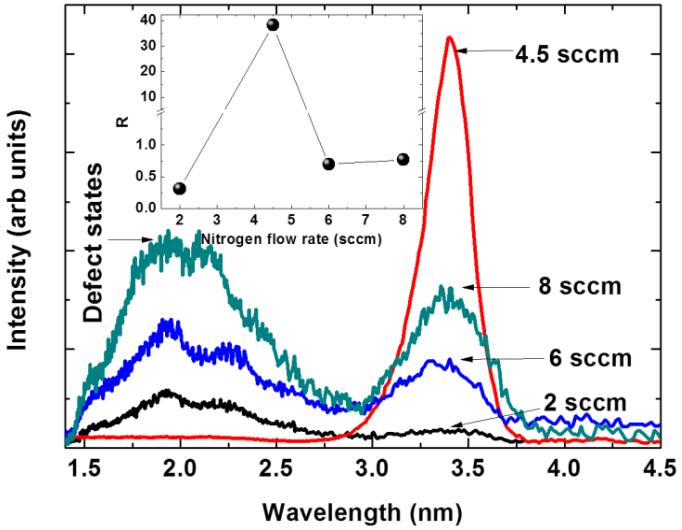

Figure 5.20. *Cathodoluminescence spectrum of the GaN nanowall network grown at 2, 6 and 8 sccm nitrogen flow rate and nanocolumns grown at nitrogen flow rate 4.5 sccm. Inset show plot of ratio R versus nitrogen flux.*

Information on the stress state and epitaxial quality is obtained using Raman spectroscopy. **Figure 5.21** shows a representative room temperature Raman spectrum acquired in backscattering geometry on GaN films grown at 2.0, 4.5, 6.0 and 8.0 sccm nitrogen flow rate. The spectra are dominated by strong E_2 (high) phonon ≈568 cm^{-1} and a weak A_1(LO) phonon ≈734 cm^{-1}, which is in agreement with Raman selection rules for wurtzite GaN. In addition, weak forbidden phonon A_1(TO) mode ≈533 cm^{-1} and E_1(TO)

mode ≈559 cm^{-1} are apparent, and two weaker bands near 654.2 and 736.6 cm^{-1} can be seen if deconvoluted by multi Lorenztian fitting. The A_1(TO) line is most likely seen due to right angle scattering which is observed if the incident light enters the nanocolumns or nanowall side faces. In case film grown at 4.5sccm the spectrum shows strong higher intense E_2 (high) line along with forbidden weaker A_1(TO) and A_1(LO) lines. The narrow linewidth of the E_2 (high) phonon, for nanocolumns is ≈8 cm^{-1}, is comparable to that of high quality epitaxial GaN, confirming high crystalline quality. Asymmetry in E_2 (high) line toward lower wave number is due to an overlap of weak E_1(TO) mode which may be attributed to deviation from true backscattering geometry. Raman Spectrum of 2.0, 6.0 and 8.0 sccm films also show strong E_2 (high) line with line width of ≈12cm^{-1} and with lesser asymmetry toward lower wave number in comparison to 4.5sccm film. Asymmetry in E_2 (high) line is attributed to weak features related to forbidden A_1(TO) and E_1(TO) modes, A_1(TO) mode might arise from the side face of nanowalls and E_1(TO) modes are observed due to crystal lattice disorder. A wide band ~665cm^{-1} is present in the high-energy part of Raman spectra in case of 4.5 and 6sccm films. And weakening of line in case of 2 and 8 sccm films at 665cm^{-1} implies reduction in free electron concentrations.

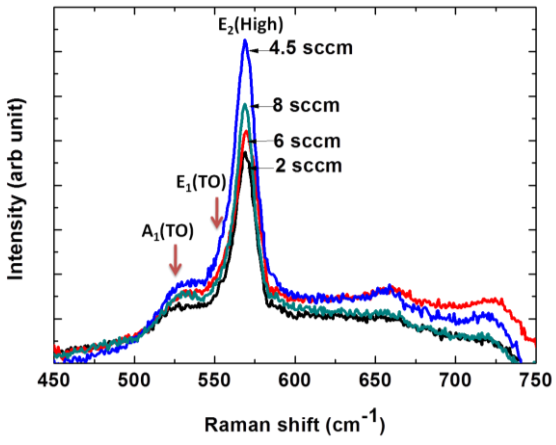

Figure 5.21: *Raman spectrum acquired at room temperature in backscattering geometry of GaN films grown at 2, 4.5, 6, and 8 sccm nitrogen flow rate at a substrate temperature of 680*℃ *and fixed Ga flux.*

As compared to the Raman spectrum of 2, 6 and 8 sccm films, a large increase in the scattering efficiency is clearly observed from the nanocolumnar 4.5 sccm film. An

increase in the scattering signal is due to the more efficient coupling of the scattered radiation due to surface nanostructuring. The well known Raman shifts for hydrostatic pressure is ≈4.17 cm^{-1}/GPa and biaxial stress is 2.7±0.3 cm^{-1}/GPa. Raman spectra obtained from nanocolumnar film grown at 4.5 sccm has E_2 line at 568 cm^{-1} which has a shift of Δω ≈1.8 cm^{-1} with respect to 566.2 cm^{-1} line of stress free GaN sample. Raman shift Δω < 3 cm^{-1} corresponds to biaxial tensile stress, thus GaN nanocolumns has biaxial tensile stress of 0.6 GPa. For films grown at 2, 6 and 8 sccm has Raman shift Δω ≈2.8 cm^{-1} which corresponds to ~1 GPa. Blue shift of the E_2(high) line may be due to increase in free electron concentration or due to enhanced compressive stress.

5.8 Effect of Gallium flux on the formation of GaN nanocolumns

We now concentrate on the role of Ga flux on the kinetics of GaN film growth. These are performed by maintaining the growth temperature at 680℃ and N_2 flow rate of 4.5sccm constant and Ga flux is varied from $2.86\times10^{14}cm^{-2}s^{-1}$ to $4.84\times10^{14}cm^{-2}s^{-1}$. **Figure 5.22** (a), (b) and (c) shows FESEM images and representative RHEED patterns (acquired along [11$\bar{2}$0] azimuth) of GaN films grown at N/Ga BEP ratio of 200, 100, and 25 at substrate temperature of 680℃.

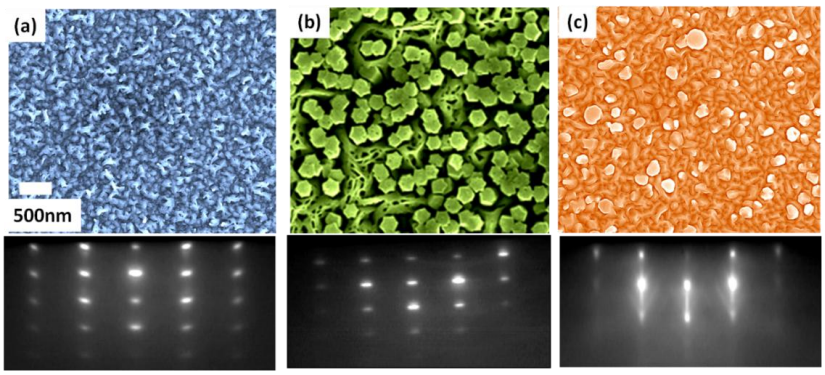

Figure 5.22 *FESEM images and representative RHEED patterns (acquired along [11$\bar{2}$0] azimuth) of GaN films grown at N/Ga BEP ratio of 200, 100, and 25 at substrate temperature of 680*℃.

The N/Ga BEP ratio is varied by changing the Ga effusion cell temperature from 940℃ to 1060℃. **Figure 5.22(a)** shows GaN film with granular morphology at N/Ga

BEP ratio of 200. Due to rough surface structure, spotty transmission pattern is observed with an overlap over faint vertical streaks. **Figure 5.22(b)** shows that the GaN nanocolumns are seen amidst nanowall network structure at N/Ga BEP ratio 100. Spotty RHEED pattern indicate a 3D diffraction, which is from the surface of high aspect ratio structures. **Figure 5.22(c)** at higher Ga flux where the N/Ga BEP ratio is 25, the RHEED pattern suggests that large sized terraces are formed on the film surface.

Figure 5.23 shows the result obtained from HRXRD observations. **Figure 5.23(a)** shows the rocking curve obtained for these representative Ga fluxes. On y-axis of **Figure 5.23(b)**, the growth rate of GaN films and on alternate y-axis full width at half-maximum (FWHM) of rocking curve along (0002) reflection is plotted versus variation in N/Ga BEP ratio along the x-axis. The FWHM of the (0002) peak is observed to decrease from ≈1.4° at N/Ga BEP ratio of 200 to ≈ 0.4° at N/Ga BEP ratio of 25 at growth temperature of 680℃. If we attribute the FWHM to the strain in the film, the curve indicates that the crystalline quality of GaN films improves significantly due to reduction in the strain, with decrease in N/Ga BEP ratio. With an increase in N/Ga BEP ratio, growth rate of GaN film decreases because of reduction in Ga adatoms at fixed nitrogen flux.

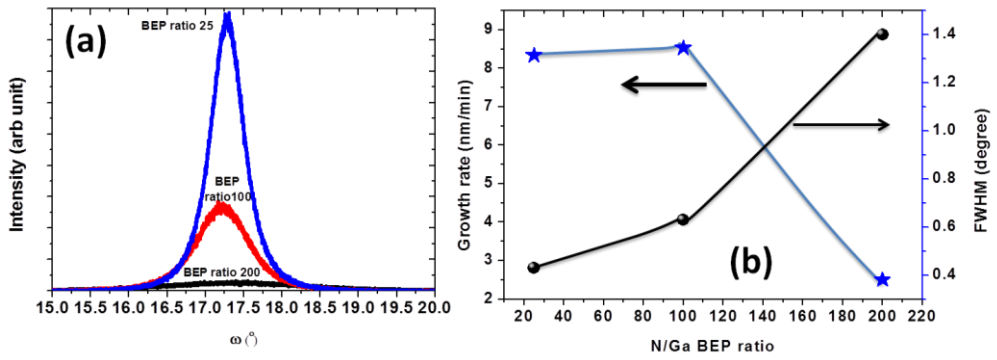

Figure 5.23 ***(a)*** *rocking curves for films grown at BEP ratio 25−200 obtained by varying Ga flux at 680℃ and N_2 flux 4.5sccm, (b) plot of growth rate and FWHM of rocking curve along (0002) reflection versus N/Ga BEP ratio.*

Figure 5.24 shows emission properties in PL spectra of GaN films grown at N/Ga BEP ratio of 25, 100 and 200 obtained by varying the Ga flux while keeping N_2 flux and

temperature constant at 4.5 sccm and 680℃. The GaN films with nanocolumn structures (BEP ratio 100) show a strong band-edge emission at ≈363.1 nm (3.42eV) and very low intensity defect related features in the 450 to 850 nm range with a band edge luminescence (BEL) to yellow luminescence (YL) ratio 23. However, for the film grown at BEP ratio of 25 the PL ratio between the intensity of band-edge peak at 364.1nm (≈ 3.41 eV) to yellow luminescence at 552.4nm (2.25eV), is 0.9. The PL ratio between the intensity of band-edge peak at 365.1nm (≈ 3.40 eV) to yellow luminescence at 552.4nm (2.25eV), for GaN film grown at BEP ratio 200 is 2.4. The FWHM of band-edge peak at 364.1nm (≈ 3.41 eV), is 4 nm (32 meV), suggesting that though the film grown at BEP ratio 25 is compact and it has a high density of threading dislocations, resulting in a strong defect related emission.

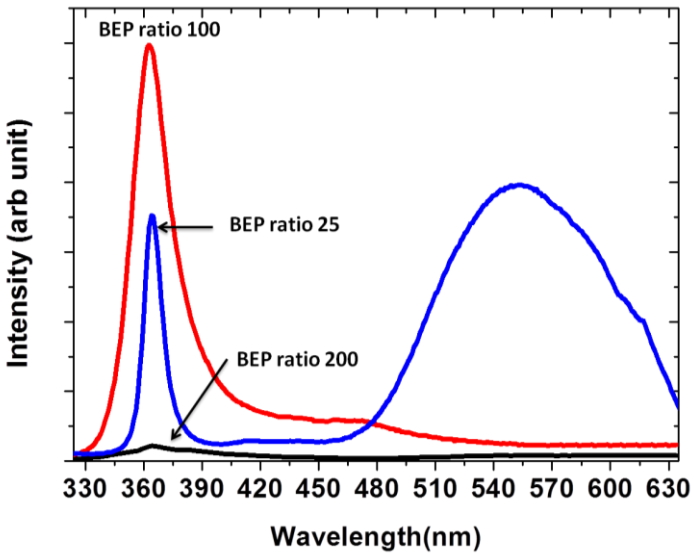

Figure 5.24 *Photoluminescence spectra of GaN films grown at N//Ga BEP ratio 25, 100 and 200.*

The PL ratio of band edge to the defect emission intensity seen for growth that shows nanocolumns in FESEM images is 23 which is twenty four times that of flat film grown at BEP ratio 25, and 10 time more than film grown at BEP ratio 200, showing high optical quality. It is known that the PL band-edge transition energy will shift to a higher (lower) energy as the compressive (tensile) stress in GaN films increases. Since in our

observations the band-edge transition energy for the film with nanocolumnar structure shift towards higher energy with respect to film grown at BEP ratio 25, suggest compressive stress in film grown at BEP ratio 100. But the band-edge transition energy of GaN film grown at BEP ratio 200 shifts toward lower energy with film grown at BEP ratio 25, suggest the possible presence of tensile stress in the films. Now we perform Raman studies to measure stress in the films

Figure 5.25 shows the room temperature Raman spectra acquired in backscattering geometry of GaN films grown at N/Ga BEP ratio 25, 100, 200 at substrate temperature 680℃**.** The Raman spectra are dominated by strong E_2 (high) line and weak lines of A_1(TO), A_1(LO), E_1(TO) and A_1(LO). The Raman spectra of film grown at N/Ga BEP ratio 100, shows intense E_2 (High) line along with forbidden weaker A_1(TO) and A_1(LO) lines. The narrow linewidth of the E_2 (High) phonon, for nanocolumns is $\approx 8cm^{-1}$, which is comparable to high quality epitaxial GaN. On deconvoluting E_2 (High) line with multiple Lorentzian fitting, other peaks at lower wave number corresponding to E_1(TO) mode are observed due to deviation from true backscattering geometry.

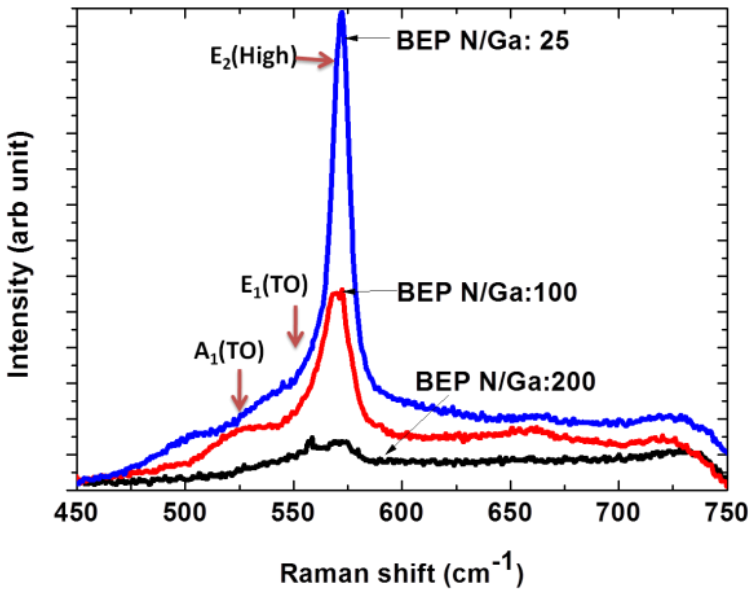

Figure 5.25 *Raman spectrum acquired at room temperature in backscattering geometry of GaN films grown at N/Ga BEP ratio 25, 100 and 200 at fixed nitrogen flow rate 4.5 sccm and substrate temperature of 680℃ .*

The Raman spectra of film grown at N/Ga BEP ratio 25 show strong symmetric line E_2 (High) of line width of ≈6 cm^{-1}. Raman spectrum of N/Ga BEP ratio 200 has broader E_2(high) mode and absence of other modes suggesting inferior quality film, since the thickness of this film is ≈250nm, and thus the spectra is dominated by intense substrate signal. Raman spectra obtained from film grown at N/Ga BEP raio 100 has E_2 line at 568 cm^{-1} which has a shift of $\Delta\omega$ ≈1.8 cm^{-1} with respect to 566.2 cm^{-1} line of stress free GaN sample, and the biaxial tensile stress is estimated to be 0.6 GPa is observed. For films grown at N/Ga BEP ratio 25, the Raman shift $\Delta\omega$ is ≈1 cm^{-1} which corresponds to ≈0.33 GPa. And in case of N/Ga BEP ratio 200 Raman shift $\Delta\omega = -10$ cm^{-1} which corresponds biaxial compressive stress of ≈3.3 GPa.

5.9 Parametric criticality on the formation of GaN nanocolumns: consolidated

In the previous sections we have observed that the morphology and properties of GaN films grown under different growth parametric conditions such as substrate temperature, nitrogen flow rate and gallium flux rates, which are different but reproducible. **Figure 5.26** consolidates the morphological images obtained by FESEM plan view micrographs for growth of GaN on Al_2O_3(0001) at different growth parameters. As indicated by the arrows, three pathways of varying a) substrate temperature, b) Ga flux and c) N_2 flux are depicted in the figure, and each of these stages is represented by the respective N/Ga BEP ratio. In the first case the substrate temperature is varied from 450℃ to 850℃ in steps of 50℃ but the figure consists of representative images obtained from samples grown at 630℃, 680℃ and 730℃, where the BEP ratio is 100 in each case. For temperatures below 680℃, a honeycomb structured nanowall network is observed, promoting 3D nucleation at the steps of edge dislocations and the strain relaxes to form a hexagonal GaN nanowall network, surrounding a void region. The walls are seen to be about 150nm at the bottom, tapering to 10 nm at their apex. The network structure grows with larger hexagons incorporating the smaller ones, as coverage increases. The dimension of nanowalls increases as deposition temperature rises from 480℃ to 650℃.

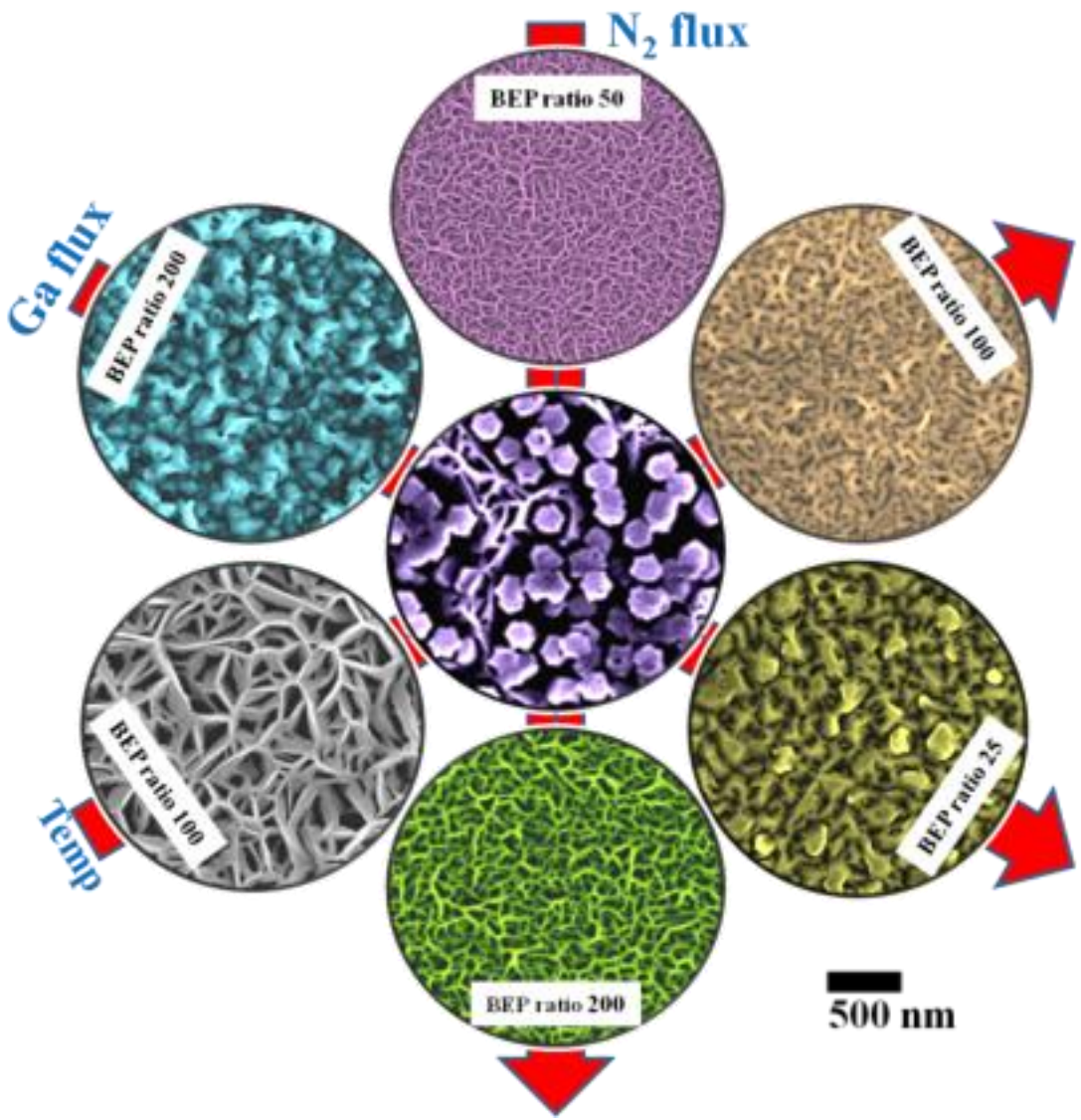

Figure 5.26: *Plan view FESEM images of 0.6μm GaN films grown in three pathways depicted by arrows with respective BEP ratios. Variation in substrate temperature is marked as temp, nitrogen flux is marked as N_2 flux and gallium flux is marked as Ga flux.*

For temperatures greater than 700℃, though the BEP ratio is still 100, the film morphology becomes flat with a high threading dislocation density (~10^{10}/cm^2) due to increased Ga diffusion and reduction in the nitrogen sticking probability. However, in-between these temperatures at around 680℃, we see the emergence of GaN hexagonal nanocolumns from within the network structure. After a critical coverage, the walls stop growing further and the growth of the nanocolumns alone persist for higher coverages.

The Ga flux dependent experiments for GaN film grown at substrate temperature of 680℃ are performed as Ga flux is varied from $2.86\times10^{14}cm^{-2}s^{-1}$ to $4.84\times10^{14}cm^{-2}s^{-1}$, at a constant N_2 flow rate of 4.5 sccm, by varying the temperatures of the Ga effusion cell. At lower Ga flux, BEP ratio of 200, GaN film forms with mound like granular features of around 200nm.

At higher Ga flux where the N/Ga BEP ratio is 25, we see evidence of Ga metal droplets. It may be noted that there is no formation of GaN nanowall network structure, except in the intermediate case of Ga BEP of 2.3×10^{-7} Torr, where columnar growth amidst the network is observed. The next set of experiments involved variation of N_2 flux by changing the N_2 flow rates (2sccm, 4.5sccm and 8sccm), varying the BEP ratio from 50 to 200 while the Ga flux was kept constant at $3.85\times10^{14}\ cm^{-2}\ s^{-1}$. In cases of 2sccm and 8sccm, we clearly see the hexagonal nanowall network formation, where the dimensions of the nanowalls increase with the nitrogen flow rate. However, at a flow rate of 4.5 sccm, we again see the emergence of GaN nanocolumns. The study, consolidated in **Figure 5.26** with representative FESEM images clearly shows the definitive role of the kinetics of film formation on the morphology and consequently on film properties of the GaN films. It is very clear that the nanocolumns form only in a very narrow growth parametric window. This formation of nanocolumns on bare sapphire without pre-treatment or use of catalysts, appears to have eluded researchers due to narrowness of the parametric window region it is observed in, and the high nitrogen rich conditions required.

Chapter 6

Properties and mechanism of GaN nanowall and nanocolumn formation

6. Properties and mechanism of nanowall and nanocolumn formation

The external efficiency and reliability of light emitting devices[216] are known to be sensitive to the type and density of extended defects[217]. As discussed earlier, group III-nitride films when deposited on sapphire substrate exhibits dislocation density ~$10^{10}cm^{-2}$, due to poor matching of lattice parameter and thermal expansion coefficient. The threading dislocations can be pure edge type forming low angle "twist" boundaries or nanopipes of radii 3.5−50 nm which thread through the entire film. The dislocations which thread though entire film upto the surfaces are observed as pinned steps, spiral hillocks, nanopipes, nanotrenches and surface depressions (V defects).[182] The interface roughening caused due to pinned steps reduces the carrier mobility in quantum heterostructures. In quantum wells thickness variation occurs due to spiral hillocks which cause variation in surface height, causing luminescence linewidth broadening. The fluctuation in composition of group III-nitride alloys and dopant concentrations is observed due to increase in planar step density near the centre of each growth spiral and their stepped structure. To improve performance of nitride base quantum heterostructures control of these surface features is essential. Many growth techniques such as epitaxial lateral overlayer growth (ELOG),[218] pendeoepitaxy,[219] lattice or domain matching epitaxy [220] etc have been tried to reduce dislocation mediated surface structures. The alternative method tried to overcome dislocations is to form one-dimensional (1D) nanomaterials such as nanowires (NWs), nanorods (NRs), and nanotubes (NTs).[74,221] There are only a few reports that show dislocations as origin to the formation of 1D nanomaterials. Morin et al[222] have proposed that axial screw dislocation provides self-perpetuating steps which enable 1D crystal growth and they demonstrate that screw dislocation drives growth in NWs and NTs of PbS [112]and ZnO[223]. Recently Cherns et al [113] has proposed that the spiral growth of the partial atomic step joins emerging dislocations to control GaN nanorods grown on AlN/(0001)Al_2O_3 template. As shown in the previous chapters, at high nitrogen proportion (BEP≈100) in MBE growth, there are interesting GaN nanostructure

formations in the temperature range 630 to 730℃. In this section we observe the coverage dependent morphological changes for three substrate temperatures. We demonstrate direct evidence of dislocation mediated surface morphologies leading to nanowall network and nanorod formation as per BCF theory predictions[110].

6.1 Coverage and temperature dependence study of GaN thin film growth on c-plane sapphire.

In chapter 5 and 6 we have discussed growth of GaN film in nitrogen rich condition, in growth temperature range of 630 to 730℃, aligned, c-oriented, wurtzite GaN nanostrucutres are formed on a bare c-plane sapphire. The precise parametric controlled growth by PAMBE can reveal the underlying growth mechanism that may be involved, amidst competitive processes such as Ga accommodation, adatom diffusion, reaction with nitrogen plasma, etc. To elaborate on the competitiveness among growth processes involved in nanocolumnar growth we vary growth time (coverage) and substrate temperature. The criticality of coverage and substrate temperature on the formation mechanism of GaN is discussed in detail below. In this study N/Ga BEP ratio 100 (Ga flux rate≈ 2.86×10^{14} atoms cm^{-2} s^{-1} and nitrogen flow rate ≈4.5sccm) is used and substrate temperature is varied from 630 to 680℃ and GaN films are grown for 120, 240 and 480 minutes at each temperature, and the surface morphology and structure of these nanostructures and probed. The nominal thickness of flat film grown for 120 min at temperature above 700℃ is ≈ 0.4μm but the films grown below 700℃ not flat hence we have used deposition time as a measure of coverage.

Figure 6.1 show a consolidated morphological evolution of GaN films grown on Al_2O_3(0001) at various substrate temperatures at three different coverage. **Figure 6.1**(a), (b) and (c) are SEM images of GaN films grown at substrate temperature 630℃ for 120, 240 and 480 min, respectively obtained at the same spatial resolution. GaN film grown for 120 min (**Figure 6.1a**) has a honeycomb structured tri-branched network with ≈70nm arms which comprises of GaN nanowalls around dark voids regions (≈30nm width)

oriented in-plane along crystallographic directions <11$\bar{2}$0> and <10$\bar{1}$0> and out-plane along [0001]. These voids are similar to nanopipes that have propagated trough the entire film along [0001] with increasing widths, as those reported by Qian et al[194]. The line profile along the arm of a tri-branched network show that the walls are wedge shaped with side face inclined along 72° with respect to c-plane (0001), corresponding to s-plane along (10$\bar{1}$1). The morphology of GaN film grown for 240 min (**Figure 6.1b**) is tri-branched network structure, with few star like features of size≈150nm amidst voids of size≈250nm. The smaller voids of size 24−45 nm are observed at the junction of a few tri-branches. The lower-most layer in this case has voids of size ≈120nm surrounded by ≈140nm long arms of tri-branched structure. The topmost layer has tri-branch structure of arms length ≈500nm with voids of size, ≈450 nm, but the voids in topmost layer circumscribe smaller voids. It appears that the longer arms of the walls in the topmost layers are formed due to merger of smaller arms of lower layer aligned along either <11$\bar{2}$0> or <10$\bar{1}$0>. In comparison to the lower coverage 120min film it has larger sized voids amidst tri-branched networks with reduced density. The arms of tri-branches surrounding triangular structure observed between the largest voids are wedge shaped with side faces inclined along 56° which corresponds to the r-plane. Film grown for 480 min (**Figure 6.1c**) has incomplete star shapes (porous) 1D-structures of size ≈600nm protruding out of voids of size ≈1μm amidst the tri-branched nanowall network.

Figure 6.1 (d), (e) and (f) represent images of GaN films grown at substrate temperature 650℃ for 120, 240 and 480 min, respectively. GaN film grown at 650℃ for 120min (**Figure 6.1d**) has a honeycomb structured nanowall network similar to **Figure 6.1(a)**, but smaller in size. From some of these voids star shaped nanocolumn of size ≈110nm emerge outward in the c-direction. In some regions we observe the coalescence of the nanocolumns, and thus merging several nano-voids together. Also, the density of the nanocolumns is much higher than at 120 min coverage. The hexagonal nanocolumns are observed to be of two types: Type I are oriented along in-plane <11$\bar{2}$0> and Type II are along <10$\bar{1}$0> directions. At higher coverage of 240 min (**Figure 6.1e**) are the hexagonal nanocolumns of size ≈150−250 nm are seen whose density is higher than 120

min coverage. Upon careful observation, on the top (c-plane) surface of each of these nanocolumns, a dark spot of size ≈30nm is observed. Around these nanocolumns, the line scans of the tri-branched network arms shows that they are wedge shaped with side faces inclined along 56° which corresponds to r-plane ($1\bar{1}02$). At 480 min growth time the surface morphology of film consists of a high density of closely packed nanocolumns of diameter 370−700nm with no trace of network (**Figure 6.1f**) in the plan view. The nanocolumns now have flat terraces along c-plane (0001), but still few nanocolumns with surface depression of size 100nm are visible. The shape of nanocolumns upon coalescence with columns in the vicinity, appears irregular.

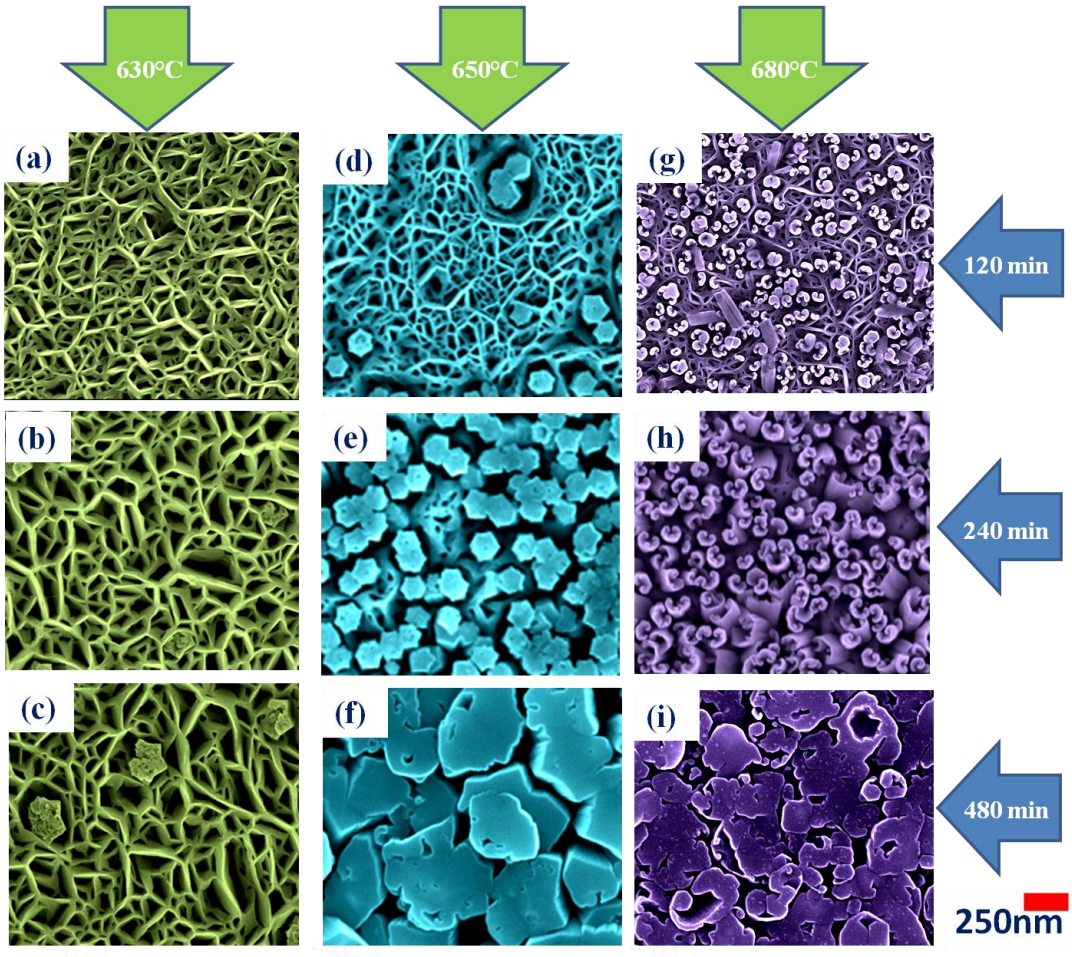

Figure 6.1*(a−i)* *shows morphologies of GaN films grown on Al_2O_3(0001) at substrate temperatures 630℃, 650℃ and 680℃ at coverage 120, 240 and 480 min, respectively.*

Figure 6.1(g), (h) and (i) represents images of GaN films grown at substrate temperature 680℃ for 120, 240 and 480 min, respectively. GaN film grown for 120 min (**Figure 6.1g**) has protruding nanostructures amidst honeycomb tri-branched network. The morphology of these nanostructures is similar to that discussed in the previous section. The branches of these tri-branched nanowall network are oriented in-plane along crystallographic directions <11$\bar{2}$0> and <10$\bar{1}$0> and out-plane along [0001]. Tri-branched network have bi-modal voids with smaller lower layer voids of size ≈15 nm, surrounded by tri-branched network of length ≈50nm, and larger features with tri-branches of arms ≈70−300nm circumscribing voids of size ≈200−400nm. 1-D nanocolumns of different sizes (≈50−100nm) and shapes are visible in this image. Some rods are lying horizontally on the c-plane, suggesting that some of the larger rods, due to mechanical instability, might have up-rooted from the substrate, and are lying on top during sample preparation. These rods show uniformity in diameter along the length of the rod. It is also interesting to note the top view shape of these nanorods which are different from the star-shape faceted ones observed at 630℃ and 650℃. Since most of the rods are C-shaped (embryo like). The morphology of GaN film grown for 240 min coverage consist of nanocolumnar structure of size 100−300nm with no tri-branched network observed at lower coverage (**Figure 6.1h**) in the top views. The size distribution of these nanocolumns varies due to their shape: if nanocolumns have single curvature then size is ≈150nm, but if several bunch together, their size becomes ≈300nm. The morphology of GaN film grown for 480 min coverage consist of nanocolumnar structure of irregular cross-section with size range of 150−400nm (**Figure 6.1i**).

6.2 Comparison of optical and structural properties of nanowalls and nanocolumns

So the new and distinct morphological features formed spontaneously without any buffer layers or catalysts are (a) nanowall network (630℃, 120min), (b) nanocolumns (650℃, 240min) and (c) flat 2D films (above 680℃, 480min). **Figure 6.2** shows surface

structure in the RHEED pattern that correspond to representative nanowall network (**Figure 6.1a**), nanocolumns (**Figure 6.1e**) and flat layer (**Figure 6.1i**) configurations. RHEED pattern (A) obtained with e-beam shining in the $[11\bar{2}0]$ direction shows spotty pattern characteristic of electron transmission through rough surfaces of the nanowalls and the in-plane axes follow the epitaxial relation $[11\bar{2}0]_{GaN}$ // $[10\bar{1}0]_{sapphire}$. Viewing from the $<11\bar{2}0>$ and $<1\bar{1}00>$ projections, the lattice periodicities observed by RHEED shows axial ordering, and the c/a ratio is 1.63. This ratio shows that the GaN films epitaxially grow with wurtzite crystal structure with c-axis perpendicular to the substrate surface[169]. The shapes of the spots in the RHEED pattern for the nanowalls show an anisotropic elongation in the $[1\bar{1}00]$ direction, which can be attributed to the thinness of the apex and misalignment of the nanowalls which form an irregular hexagonal honeycomb network,[224] as discussed earlier. The RHEED pattern for the case when nanocolumns are formed also show an anisotropy but with a smaller aspect ratio. However, when the flat films are formed (e.g. above 680℃, 4.5sccm), the spots are circular. By using Atomic force Microscope (AFM), the root mean square (rms) roughness of ≈4nm was measured by AFM for the film grown above 680℃ showing a compact 2D film with a high density of threading dislocations. However, the film is still rough enough to obtain transmission pattern in RHEED. At higher temperatures, when the surface roughness is reduced due to longer adatom diffusion, we begin to see streaks along the [0001] direction, characteristic of 2D film growth.

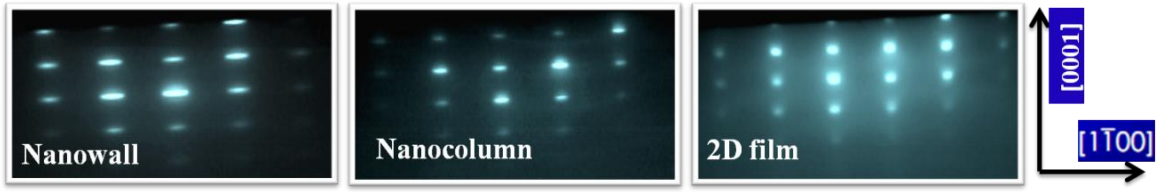

Figure 6.2 *RHEED pattern acquired along $[11\bar{2}0]$ azimuth for nanowall network (120min, 630℃), nanocolumns (240 min, 650℃) and 2D films (480 min, above 680℃)*

The CL spectrum in **Figure 6.3**, obtained at 5kV for the GaN nanowall network structures shows a strong band-edge emission at 355.8 nm (3.49eV) and low intensity defect feature in the 450 to 850 nm range. The CL ratio between the intensity of band-

edge to yellow luminescence at 565.4nm (2.21eV), for the nanowall network is 20. The intensity of these defects varies with network dimensions, but the qualitative nature of spectra remains the same. The strong band-edge emission shows that the GaN formed is stoichiometric and of high structural quality, despite the presence of a large void density. The CL of the flat film shows a significant decrease in the band edge emission, and also an increase in the defect peaks in the wavelength range 450−850nm.[134,204]

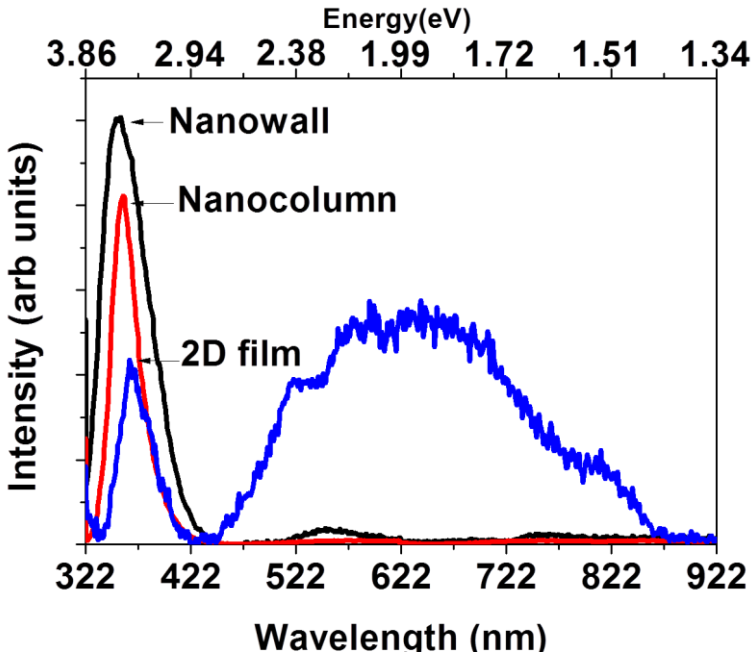

Figure 6.3 *Cathodoluminescence spectrum for nanowall network, nanocolumns and 2D films.*

The FWHM of band-edge peak at 364.1nm (≈ 3.41 eV), is 29.1nm (232.92 meV) and CL ratio is 1, suggesting that though the film grown above 680℃ has a compact and flat morphology, the threading dislocations lead to an increased extended defect state related emission. The CL spectra of the case when nanocolumns are formed is similar to that of the nanowall network, with a strong band edge emission at 363.1 nm (3.42 eV) and almost no defect related emission. The CL ratio of band edge to the defect emission intensity nanocolumns is 80 which is nearly four times that of nanowall network, showing high optical quality. CL spectra also show that the band-edge transition energy for the flat film is 364.1nm (3.41 eV), blue shifts to 358.9 nm (3.46eV) for the thin nanowall

network, and the FWHM of the CL peak for the flat film is 24.4nm (195.20 meV), which is about half that of the value obtained from the nanowall network 43.6nm (348.70 meV). The nanowalls are ≈150nm thick at the bottom and taper to ≈10nm on top. The blue shift and high intensity of emission can be attributed to the electron confinement effects at the apex of the walls. However, we also observe a broadening in FWHM of the CL spectrum, which may be related to misalignment of nanowalls, or due to the electron confinement in the narrow region of the nanowalls, which is seen as anisotropy in RHEED spots along [$1\bar{1}00$] direction.

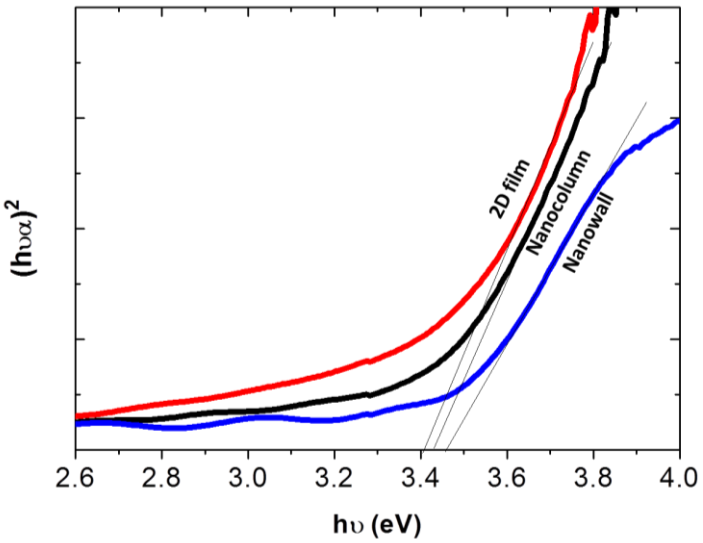

Figure 6.4 *Change in the optical energy gap for GaN nanowalls and nanocolumns.*

UV-VIS absorption studies were carried out on these samples in a Perkin Elmer system in transmission mode. The optical energy gap, Eg, was determined from Tauc's expression for direct band gap semiconductor by a linear extrapolation of the plot of $(\alpha h\nu)^2$ versus hν to the energy axis. The physical basis of Tauc's expression is the assumption of parabolic energy bands, an energy-dependent momentum matrix element and a relaxation of momentum conservation[225]. **Figure 6.4** show the variation in the plot of $(\alpha h\nu)^2$ versus hν (Tauc's plot) for GaN nanowalls and nanocolumns. It was found that the calculated optical energy gap values were in the range between 3.15– 3.55 eV without any specific observable trend. The optical energy gap for 2D film is ≈3.41 eV,

nanocolumn is ≈3.42 eV and for nanowall is ≈3.49 eV. Thus, blue shift is observed for the nanowall network manifesting the electron confinement in the narrow apex of the nanowalls which are about 10nm wide.

GaN with hexagonal wurtzite structure belongs to the C^4_{6v} space group .For $\vec{q}$=0 ($\vec{q}$ is a wave vector), group theory predicts eight sets of phonon modes: $2E_2$, $2A_1$, $2E_1$ and $2B_1$, of which both E_2 [(E_2 (high), E_2 (low)] one A_1(LO), one E_1(TO) and one E_1(LO) are Raman active and the B_1 modes are not[226]. The Raman spectrum of the GaN films in the nanowall, nanocolumn, and 2D film configuration are shown in **Figure 6.5.** Raman spectrum **6.5(a)** for the nanocolumns shows strong line E_2 (high) which is symmetry allowed in backscattering along the wurtzite c axis, and a weak symmetry forbidden A_1(TO), which is most likely seen due to right angle scattering occurring when the incident light enters the sidewalls of the nanocolumns. The narrow linewidth of the E_2 (High) phonon, for nanocolumns is ≈8 cm^{-1}, due to high quality epitaxial GaN [208]. Asymmetry in E_2 (high) peak shape towards lower wave number may be due to an overlap of weak E_1(TO) mode which may be attributed to deviation from true backscattering geometry. Raman Spectrum **6.5(b)** is from GaN nanowalls consists of a strong E_2 (high) line with line width of ≈12 cm^{-1} with an asymmetry towards lower wave number, attributed to weak features related to forbidden A_1(TO) and E_1(TO) modes. A_1(TO) mode can arise from the side face of nanowalls and E_1(TO) modes are observed to be due to crystal lattice disorder. Raman Spectrum **6.5(c)** is from GaN flat film consist of strong E_2 (high) line with line width of ≈10 cm^{-1}. The A_1 (TO) peak at 527.5 cm^{-1}, is 4.5 cm^{-1} below the A_1 (TO) peak expected for perfect GaN crystal. Peak around 518 cm^{-1} reflects the LO phonon-plasmon mode (LPP). The broad A_1 (TO) lines indicate the degeneration of LPP^- and A_1 (TO) peaks[227]. The LPP^- /A_1 (TO) peak is observed as a shoulder in the E_2 (high) peak. A wide band ≈665cm^{-1} is present in the high-energy part of Raman spectra, with A_1 character. The position of the strong E_2 (high) line is commonly used to determine stress in epitaxial GaN. Raman spectra obtained for nanocolumn that have the hexagonal structure have E_2(high) peak at 568 cm^{-1} where line position at 566.2 cm^{-1} is expected for stress free GaN sample. We attribute this increase in

the compressive stress to be responsible for the blue shift of Raman line, though it can be either due to enhanced compressive stress.

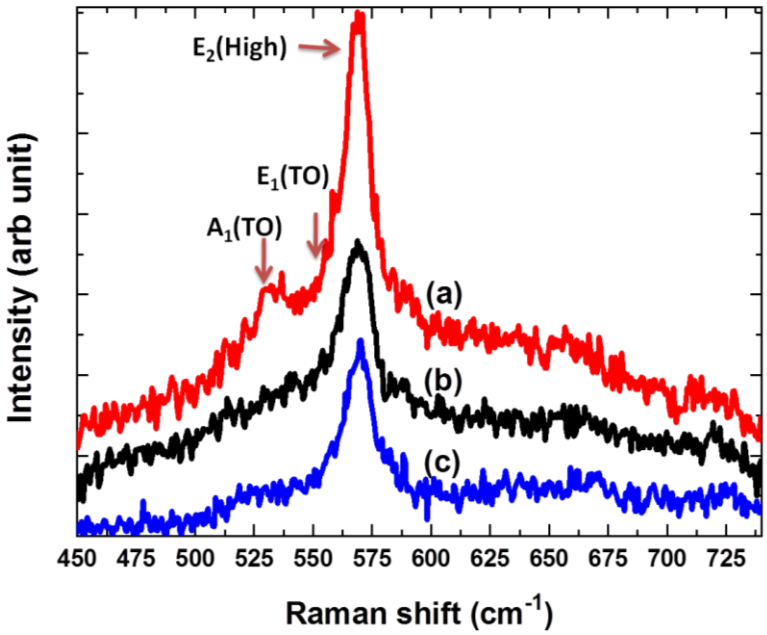

Figure 6.5 *Raman spectra acquired at room temperature in backscattering geometry of (a) nanocolumns, (b) nanowall matrix, and (c) flat layer of GaN.*

We have discussed properties of GaN film grown in three different morphologies till now and beyond this we look into growth mechanism of these interesting nanostructures.

6.3 Nanowall network details

In this section we look at the details of the interesting nanowall network morphology, at very early stages of growth, in an attempt to understand the underlying mechanism that leads to this phase.

To understand the mechanism of nanocolumn formation, a ≈150nm thick GaN films grown for 20min (corresponding to a flat film thickness of ≈ 80nm) under N/Ga BEP ratio 100 at 680℃ on a bare c-plane sapphire is discussed. **Figure 6.6(a)** is FESEM image of GaN film whose surface morphology consists of voids (≈20−30nm) surrounded by tri-branched walls of ≈30−40nm. The dark spots in the images are either surface depression

or V defects whose formation is shown schematically in **Figure 6.9(a),** and originate at screw dislocations. The straight arm of these tri-branched networks represents unbowed edge dislocation step. These tri-branched networks and surface voids can be collectively named as open screw dislocation that thread through the compact films, and open into voids for N rich conditions observed here. By using open source software Image J, binary image **6.6(b)** and edge threshold image **6.6(c)** of an FESEM image **6.6(a)** are generated. Binary image shown in **Figure 6.6(b)** clearly distinguishes tri-branched network from surface depressions, where white lines are edge dislocations steps and black region are surface depressions or voids or V defects. Edge threshold image shown in **Figure 6.6(c)** provides detailed insight into dislocation mediated surface structures. Tri-branched network has a tri-layer structure, the lowermost layer comprise of dark pin holes of diameter ≈10nm. These pinholes are observed at the junction of these tri-branched and can be nanopipes formed by screw dislocations. The mid-layer structure consists of tri-branched network of branch length ≈30nm, these branches circumscribe voids of diameter ≈25nm. The topmost layer consist of a tri-branch network structure of walls of length≈60 nm, which surround group of voids observed in the second layer. Thus, the topmost layer branch appears to be a superset of second layer branches aligned in similar directions.

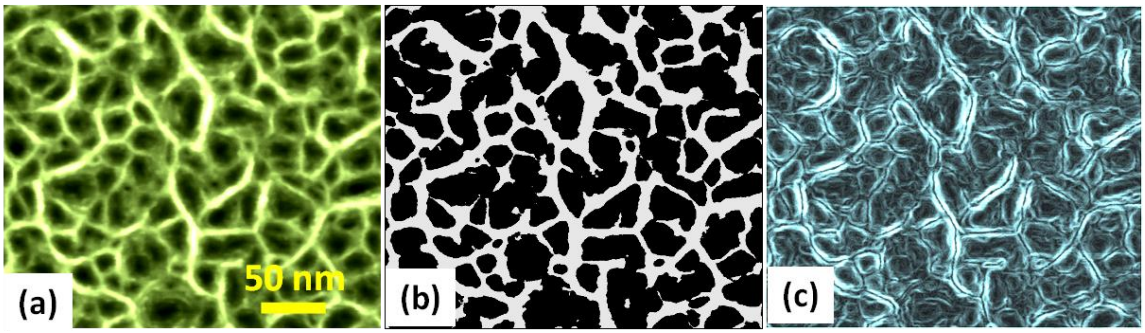

Figure 6.6*(a) FESEM image of GaN film grown at 680*℃ *on bare c-plane sapphire for 20 min under N/Ga BEP ratio 100, (b) binary image of (a), and (c) edge threshold image of (a).*

The in-plane orientation and shape of voids of tri-branched network observed in **Figure 6.6 (a)** is discussed in this section. The arms/branches of these tri-branched network are oriented either along <10$\bar{1}$0> or <11$\bar{2}$0> which show that they form along

edge dislocation. **Figure 6.7(a, b)** shows branches directed along <10$\bar{1}$0> and **6.7(a', b')** are branches directed along <11$\bar{2}$0>. The few possible permutation of tri-branched networks **(a, a', b, and b')** are shown as (I- VII). On closer observation of **Figure 6.6 (b),** the dark spots in the images correspond to polygonal shapes which are shown in **Figure 6.7(I-VII).**

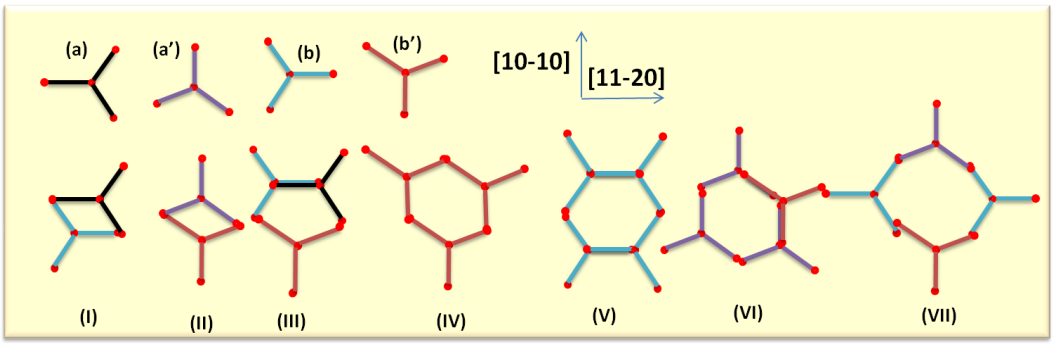

Figure 6.7*(a, a', b, b')* *are schematic representation of few permutation of tri-branched structures and* ***(I-VII)*** *polygonal shape of voids.*

Figure 6.8 shows several line profiles acquired the across arms of tri-branched network of **Figure 6.6(a).** The arms of these tri-branched networks are wedge shaped having triangular cross-sections as seen from line profiles with similar wedge angles. The side face of these triangular walls are along 56° which corresponds to r-plane (1$\bar{1}$02).

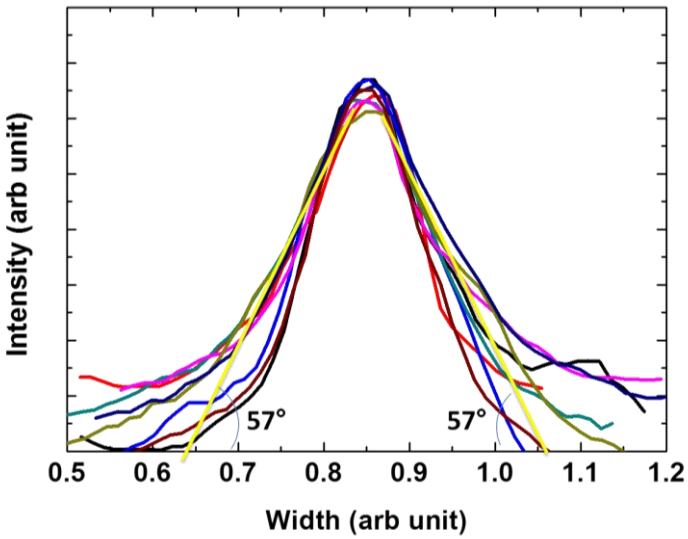

Figure 6.8 *line profiles across arms of tri-branched network of* ***Figure 6.6(a).***

As per earlier[228] prediction, the formation of surface depressions take place at the termination of film surface, due to strain-energy density associated with the dislocation. The line tension directed into the material can be considered as internal strain energy which may be balanced by tension directed out of the material due to surface energy. At equilibrium, depression is created as shown in **Figure 6.9** (a) in the crystal since the crystal surface must be pulled down due to internal force at the dislocation to balance the tangential surface tension along the free surfaces. **Figure 6.9(b)** is the high resolution FESEM image of film shown in **Figure 6.6(a)**, which clearly shows surface depressions at screw dislocation and edge dislocation steps surrounding nanopipes or nanotrenchs in **Figure 6.9(c).**

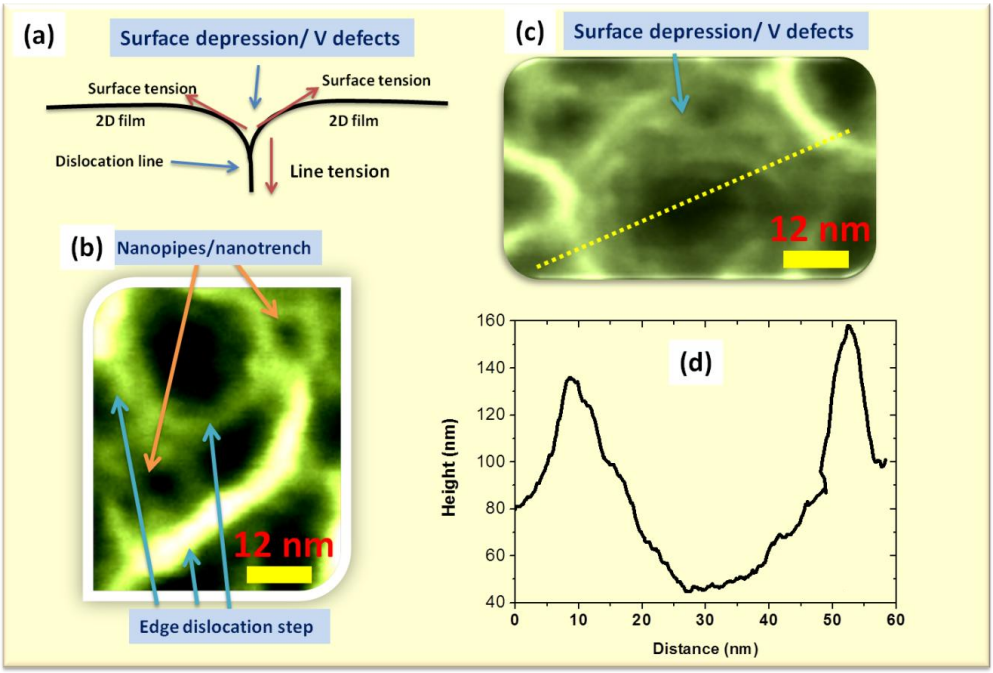

Figure 6.9(a) *schematic representation of a surface depression and force balance at the termination of a dislocation, (b) high resolution FESEM images of nanopipes/nanotrench and edge dislocation steps (c) surface depression or V-pits and (d) line profile along line drawn in (c).*

The smallest voids (nanotrenches) of diameter ≈6 nm which are in the range of nanopipe diameters of 5−25nm observed by Qian et al[194] hence these smaller voids can be associated to pure screw dislocations with elementary Burgers vector $\pm\mathbf{c}$ ($c=\frac{1}{3}[0003]$)

along <0001> directions of typical density ~10^9cm^{-2} and the larger voids (V pits or surface depressions) are of diameter ≈50 nm. Since the arms of tri-branched network are along <$10\bar{1}0$> directions, hence straight arm of tri-branched network of width in range 2−5 nm are nanowall and can be associated to pure edge dislocations lying along {$10\bar{1}0$} planes with an elementary Burgers vector $\pm$**a** (a=$\frac{1}{3}$[$11\bar{2}0$]) of typical edge dislocation density in range ~10^{10} cm^{-2}. It has been proposed by Qian et al[229], that the Burgers vector **c** is 62% larger than **a** and the elastic energy of screw is larger than edge dislocations. As a result of this, edge dislocations parallel to the c axis outnumbers the screw dislocations by an order of magnitude and nanopipes are never associated with edge dislocations. In this view, we propose that the branches of tri-branched networks obtained in this study are edge dislocations which surround the void which are open screw dislocations.

Nanotrench formation may be attributed to threading screw dislocations. According to Frank[230] dislocation with large Burger vector may lower its energy by emptying the highly strained core region. But to maintain equilibrium, the critical core radius r is

$$r = \frac{\mu b^2}{8\gamma\pi^2} \quad \text{.....(6.1)}$$

where μ is the shear modulus, **b** is the Burgers vector, and γ is the surface energy of the material. If we consider a case when **b** is along <0001> and its magnitude b=0.518nm (lattice constant along c axis), μ=C_{13} ~10^{11}N/m^2, and the family of planes surrounding open core {$10\bar{1}0$} which are pure edge dislocations.

The plot of surface energy γ versus diameter of core d will follow the trend shown in **Figure 6.10** which is a rectangular hyperbola, since $\gamma r = \frac{\mu b^2}{8\pi^2}$ = constant (for b=0.518nm). For core diameter d =0.34 nm the surface energy γ=1.89 J/m^2 and for d=100nm surface energy γ=0.006 J/m^2. Thus with an increase in core diameter of screw dislocation, surface energy decreases, hence screw dislocation formed with diameter

d=0.34 nm, open up by relaxing its surface energy. The open core screw dislocation diameter can become more that 0.34nm.

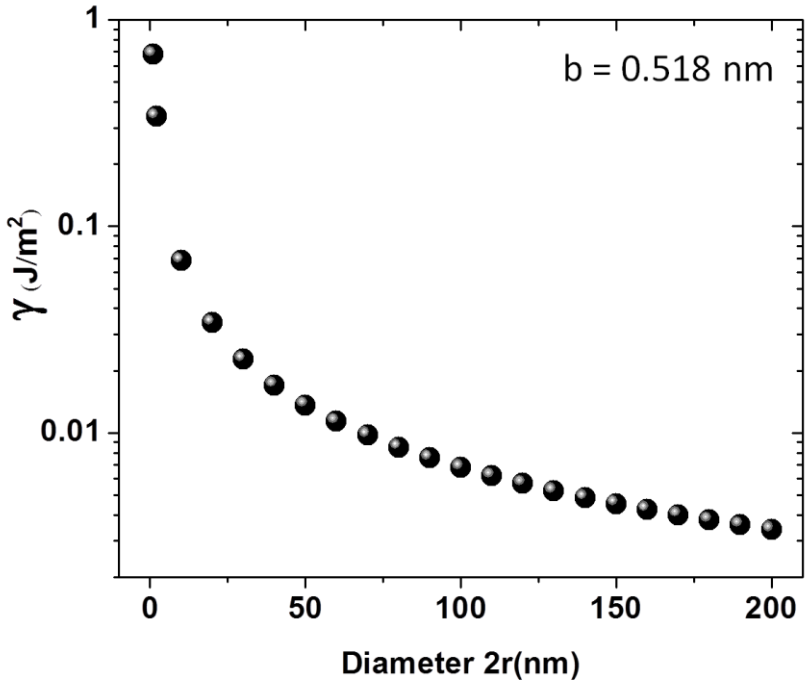

Figure 6.10 *Plot of (a) surface energy γ versus diameter d for fixed magnitude of Burger vector* ***b,*** *for nanopipe or nanotrench.*

6.4 Nanocolumn formation

After discussing nanowall network structure, we now attempt to understand the mechanism that leads to the observed growth morphology and shapes of nanocolumns grown under different growth conditions.

Under N-rich conditions used in this study, the Ga adatoms encounter more frequent N_2* species, with higher probability of reacting. Thus, both collision induced energy transfer and the reaction probability, reduce Ga diffusion length. Once the diffusion length is shorter, a statistical roughening of the surface can be expected, and the adatom might be trapped at sites not corresponding to thermodynamic equilibrium positions. Effective parameters average[110] over a large area including not only the clean surface but

also steps, impurities, dislocations, etc. Skierbiszewski et al[231] and Koblmuller et al have shown growth of GaN on c-plane (0001) under nitrogen-rich (N-rich) at temperature ≤ 750℃ results in rough surface morphology, because three dimensional (3D) growth mode is dominant[232-233], which results from very high diffusion barriers for Ga adatoms theoretically predicted by Zywietz[53]. In N-rich condition and temperature <750℃ results in heavily pitted surfaces, tilted columnar structures with a high density of stacking faults is shown by Tarsa et al[234]. Since the effective diffusion barrier is dominated by the process at the highest barrier, we expect the adatoms to encounter this at regions where the initial layers have formed a dislocation at the GaN/Al_2O_3 (0001) interface. As discussed earlier, heteroepitaxial growth of GaN on sapphire due to the large lattice mismatch, the initial few layers are strained pseudomorphic layers, which after a critical thickness gets strain relaxed by forming dislocations that promote 3D growth. Depending on the coverage and III/V ratio, the supersaturation at these misfit dislocations takes place, inducing nucleation centres that eventually grow into nanowalls and nanocolumns. When GaN is grown under extreme N-rich conditions (very high V/III ratio), stable nuclei will not coalesce because the arriving Ga adatoms will preferentially incorporate on their top, which have a tendency to grow in a columnar fashion (columnar grains)[135]. The diffusion retarded epitaxy process which dominates in N-rich condition is shown schematically in **Figure 6.11.**

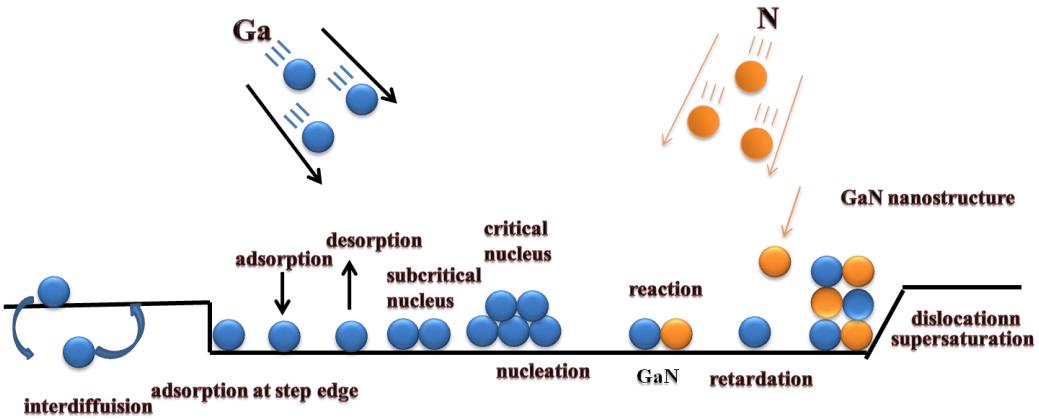

Figure 6.11 *Schematics of the surface processes occurring during growth of GaN nanocoloumns by PAMBE.*

The incoming Ga and N* atoms or molecules directed toward substrate surface remain unreacted until they reach the substrate and the high substrate temperature 300℃ enhances the chances of GaN formation. The presence of high concentration of N* retards diffusion of Ga adatoms thus, promoting an accumulation at the dislocation energy barriers. Once the Ga and N* species react to form GaN they become partially immobile or move together slowly and nucleate at the dislocation site. Further, growth is driven by the nature of dislocation site. If dislocation site is screw, atomic steps are formed above the surface resulting in spiral growth which propagates along [0001] direction, in case of edge site dislocation prefers to grow along $\{10\bar{1}0\}$ planes.

Figure 6.12 (a) represents FESEM image of GaN film grown on a bare c-plane sapphire by PAMBE for 120min (similar to the **Figure 6.1(g)**) under nitrogen rich condition (N/Ga BEP ratio 100), **(b)** cross-section view of film grown for 480min at 680℃ substrate temperature. The surface morphology consists of voids surrounded by tri-branched network and protruding GaN nanocolumns. The arms of these tri-branched networks are nanowalls and protruding structures amidst the nanowall network are either fully or partially formed nanorods. The formation mechanism of tri-branched networks structure has been discussed in previous section. In this section we will discuss the formation mechanism of GaN nanorods, and attempt to explain their different morphologies.

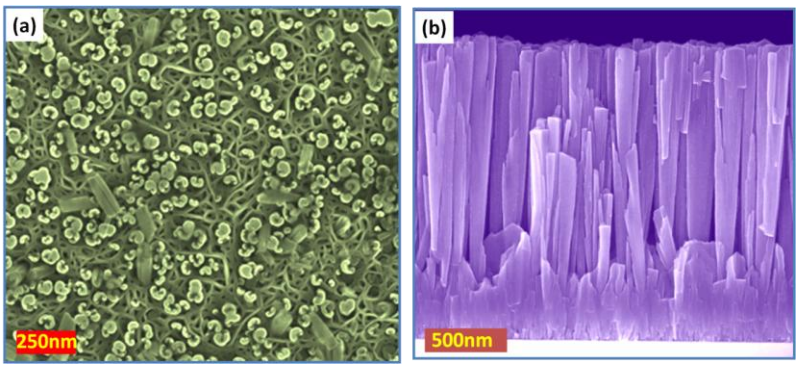

Figure 6.12: *(a) FESEM image of GaN film grown by PAMBE on bare c-plane sapphire for 120 min, (b) cross-section view of film grown for 480min at 680*℃ .

Figure 6.12(b) shows the cross section FESEM image after growing 4.0 μm thick GaN, where we can visualize the nanowall matrix and the nanocolumns with a density of $\approx 1\times10^{8}cm^{-1}$, as counted and averaged on several FESEM images (1μm×1μm). The GaN nanocolumns are c-oriented wurtzite, self aligned and hexagonally faceted with m-plane walls and bound by the nanowall honeycomb matrix. The shapes of the nanorods are essentially of two types i) hexagonal and ii) c-shaped (or embryo shaped). We shall discuss the origin of these shapes later in this Chapter. First we shall focus on the kinetics of nanorods growth.

Under high supersaturation, the linear dependence of nanowire length (l) versus reciprocal of diameter ($1/d$) is agreed in literature[100,235-236] for diffusion induced (DI) growth of nanowires which proposed by Ruth et al[237] and more recently supported by Debnath et al[116] for spontaneous growth of GaN NWs on Si(111) substrate. Thus, most of the kinetic growth models in literature obey equation (6.2), where C_1 and C_2 are constants.

$$l = C_1\left(1+\frac{C_2}{d}\right) \quad \text{.....(6.2)}$$

C_1 is related to the thickness of a compact layer and C_2 is related to the DI growth. Johansson et al[121] in their theoretical calculation suggested that $C_2 = 2\delta$, where $\delta(=\sqrt{D\tau})$, D is surface diffusion coefficient, and τ is time of stay for an adatom on the surface before adsorption or desorption. The diffusion length along the side of NW and the growth time of thinner wires is limited by the diffusion process on NW sidewalls. In case $l > \delta$, the atoms condensed at the base of NW will not reach the tip of NWs. More recently Dubrovskii et al[238] suggested that l varies linearly with $1/d^2$ for vapour-solid process and Chen et al[239] proposed that the NW prefer to grow axially via VLS mechanism. All growth models suggest existence of critical NW radius, above which NW thickens. More recently Dubrovskii et al[240] addressed NW sidewall nucleation issue, where NW diameter was considered as function of distance from the substrate surface and total NW length which is applicable for conically shaped NW which can be obtained under lower growth temperatures. More recently Plante et al[243] elaborated model initiated by Tchernycheva et

al[240], have suggest a model based on step flow mediated growth mechanism for an isolated NW (neglecting effect of neighbouring NWs excluding competition for adatoms and shadowing).

We argue now that the anisotropic growth of GaN nanocolumns along [0001] direction on bare c-plane sapphire is driven by axial screw dislocations. Since the formation mechanism appear to be different from diffusion induced mechanism, as the expression (6.2) suggests that $l \times d$=constant *(*l=length and d=diameter of NWs) which is for rectangular hyperbola (curve shown as broken line in **Figure 6.13**) observed in diffusion induced case does not converge here. Thus, we now compare experimentally determined growth kinetics with those predicted using fundamental BCF and LBL crystal growth theories[47,110]. BCF theory predicts a dislocation-growth rate (R_{axial}) linearly dependent on supersaturation where C is the rate constant C and σ is supersaturation.

$$R_{axial} = \dot{l} = C\sigma \quad \text{.....(6.3)}$$

Where layer-by-layer (LBL) growth has an exponential growth rate (R_{radial})

$$R_{radial} = \dot{d} = J_o L^2 \beta \propto e^{-\frac{g_n}{kT}} L^2 \beta \quad \text{.....(6.4)}$$

where J_o is the rate of 2D nucleation, L is the length of the facet (assuming a square growth facet), b is the step height, k is Boltzmanns constant, T is the temperature, and g_n is the energy barrier to 2D nucleation, which is inversely proportional to supersaturation. According to equation (6.3) and (6.4), LBL growth requires the formation of 2D nuclei by overcoming the energy barrier g_n, but dislocation growth has no such barrier because of self-perpetuating growth steps. Thus, at low supersaturation condition dislocation growth dominates and supersaturation above the critical supersaturation of forming 2D nuclei is expected to overtake dislocation growth. If only axial dislocations are observed, LBL growth accounts for radial growth (broadening) exclusively, and the barrier to 2D nucleation on the side walls heavily impact the aspect ratio. In low supersaturation condition when Ga and N* adatoms react together to form GaN nucleus, depending on the type and number of nucleation, 1D anisotropic growth of nanocolumns is expected.

But the shape of rods depend on the competition between growth rate both axial (R_{axial}) and radial (R_{radial}). As from **Figure 6.13**, the diameter versus length plot of nanocolumns is almost linear up to growth time of 120min, and beyond 120 min it still remains linear with only a change in gradient ($m = \frac{\Delta d}{\Delta l}$). The gradient of curve upto 120 min is ~220 and beyond 120 min it is ≈ 80. After 60 minute growth the nanowalls attain r-plane configuration and stop growing. Thus, growth rate till 120min coverage depends on Ga adatoms which are funnelled via wedge shaped nanowalls and direct impingement. Linear dependence of faster growth rate suggests strong dependence on dislocation driven growth R_{radial} ($R_{radial} \gg R_{axial}$). Beyond 120 min coverage (b−c) growth rate become slower, since contribution of diffusing Ga adatoms along side walls of nanowalls become lesser with increasing coverage. Now only directly impinged Ga adatoms of those lying within Ga diffusion length, diffuse back to the terrace of nanocolumns contribute to growth rate. Here R_{radial} and R_{axial} seems to contribute equally for anisotropic growth. This supports the BCF theory argument that if the rate of advance of a step is independent of its orientation the growing spiral will form a low cone, but it will tend to form a nanorod when the rate of advance depends on the orientation.

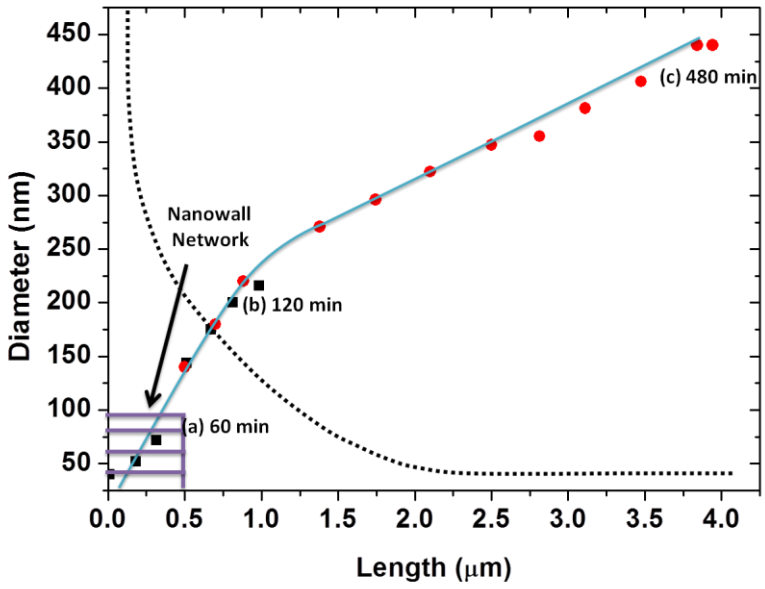

Figure 6.13 *shows plot of nanocolumnar growth rate versus length of nanorods. The rectangular hyperbola shown as broken line represent, the l*d=constant.*

For anisotropic spontaneously formation of GaN nanowires it has been argued by Debnath et al[116] that axial dominates over radial growth rate due to Ga adatom diffusion on the nanowire lateral surface towards the tip. But recent theoretical predictions by Lymperakis[147] suggested that for Ga adatoms exhibit smaller diffusion barrier along c-axis for a-plane surface and larger diffusion barrier along c-axis on m-plane surface. Thus, sticking coefficient of Ga adatom for c-plane (0001) > m-plane $(10\bar{1}0)$ > r-plane $(1\bar{1}02)$, in line with the Berntess et al[134] argument, that the c-oriented growth is promoted by larger nucleation and incorporation on nanowire terrace with respect to the corresponding rates on the side facets. The diffusion induced growth model along with inclusion of sticking coefficient and diffusion of Ga adatom on side facets and supersaturation at nucleation sites, is necessary for a comprehensive growth.

To provide more details on the underlying mechanism of nanorods formation, the plan view high resolution SEM image of isolated nanocolumns grown at 630℃, 650℃, and 680℃ for 480 min coverage (≈ 2.5μm thickness equivalent for flat film) are shown in **Figure 6.14 a, b and c**. The defected surface of the c-plane top of the nanocolumns formed at 630℃ (**Figure 14a**) is due to voids of sizes in the range ≈50−100nm, surrounded by tri-branched network, these star shaped nanocolumns have more than six sides. The other unformed sides suggest that they evolved from one of the arms of tri-branch attached to cavity, which is evident in structures formed at lower coverage 240min grown film. The voids of size ≈100nm with non-hexagonal shape surround structures similar to C-shaped structure with of size ≈38nm. The voids of size ≈52−72nm with regular polygonal shape, are surface depressions created due to nanopipes beneath them. Smaller hexagonal dark spots of size distribution 5−18nm are nanopipes reported by Quain et al. The surface morphology of nanocolumns formed in case of 650℃ is star or rosette shaped (**Figure6.14b**) is smoother than 630℃. The cross-section of these nanocolumns appear hexagonal when observed in low resolution SEM images (**Figure 6.1f**) which implied that the topmost surface should be along (0001) plane and sidewalls along $(10\bar{1}0)$. But in higher resolution images **6.14(a) and (b)** superimposed yellow coloured hexagons can circumscribe these structures, but red coloured stars when

enveloped on these structures give better representation. Thus, the enveloping regular dodecagon over two triangles rotated with respect to each other by 30° is a better overlap of nanocolumn shape. Both the triangle bounded by a-planes {11$\bar{2}$0} but the sides of one triangles are along <11$\bar{2}$0> direction and other triangle along <10$\bar{1}$0>.

The SEM image of nanocolumn in case of 680℃ (**Figure 6.14c**) is acquired at slight tilt of sample surface. The nanocolumn surface morphology appears like a hexagon and the hexagonal faces are along m planes {10$\bar{1}$0} and topmost surface is definitely along c-plane (0001). This suggests that the a-planes {11$\bar{2}$0} surface observed in case nanocolumns formed at 630℃ and 650℃ tends toward m planes {10$\bar{1}$0} which may be because the energy of formation of a-plane is higher than m-plane. The nanorod is more compact but still has the remnant defect spiralling through, as seen at the 4 O'clock position. Hence, surface morphology discussion of films grown in proximity of 680℃ for 480 min suggest that the mechanism of growth for 630℃, 650℃ and 680℃, are similar, but the compaction increases at higher temperatures, due to the expulsion of defects and approach towards equilibrium crystal shape bounded by {10$\bar{1}$0} planes.

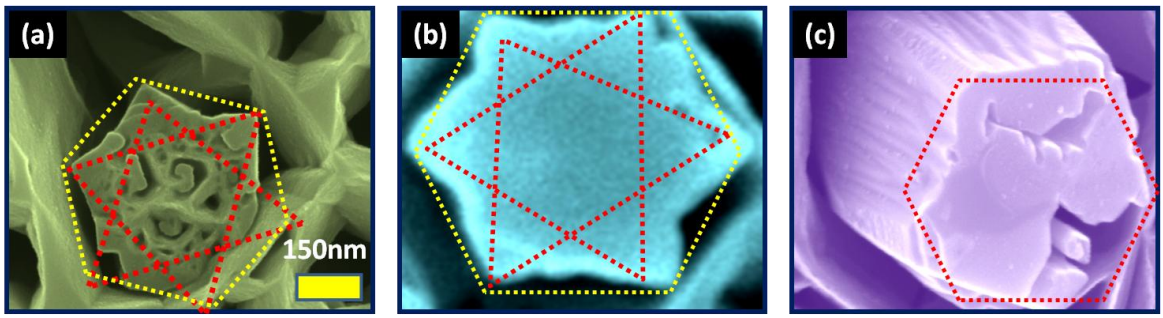

Figure 6.14 ***(a–c)*** *are high resolution plan view SEM images of a nanocolumns formed at 630*℃, *650*℃, 680℃ *for 480 min coverage.*

To show that the formation mechanism of nanocolumns is driven by spiralling step of screw dislocation, we performed AFM measurement on the surface of the nanocolumns formed in 650℃ case. **Figure 6.15 (a)** is an AFM image of nanocolumns seen in GaN film grown at 650℃ and 480min coverage, **Figure 6.15 (b)** is a line profile acquired across line seen on nanocolumn surface. The cross-section of nanocolumn

appears hexagonal with diameter ≈500nm. The line profile across the terrace of nanocolumns suggests a step spiralling step of height ≈100nm.

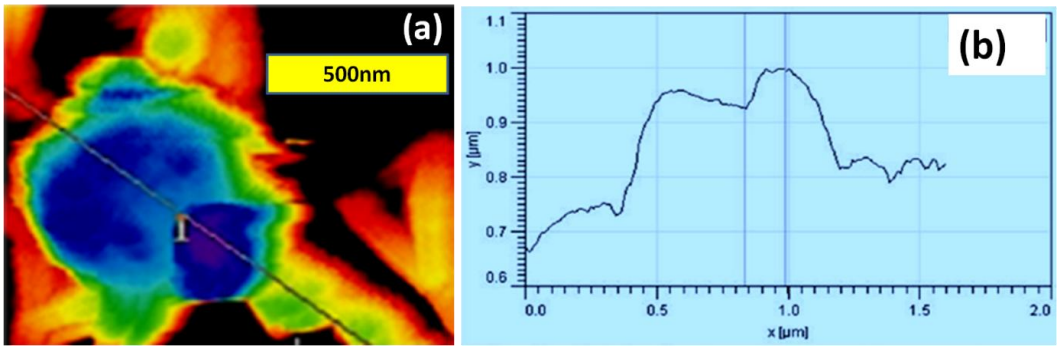

Figure 6.15 ***(a)*** *AFM image of nanocolumn observed in GaN film grown at 650℃ for 480min, (b) line profile taken along line shown over the nanocolumn surface.*

Frank et al[230] proposed that the growth of crystals under low supersaturation are imperfect due to termination of screw dislocations in the surface, which will provide the steps required for growth, preventing two-dimensional nucleation. In case of screw dislocation, emergence of a component of displacement vector normal to the crystal face in observed and under a supersaturated environment, the step due to a dislocation winds itself in a spiral in such a way that a single screw dislocation sends out successive turns of steps in growing crystal as shown in **Figure 6.16**.

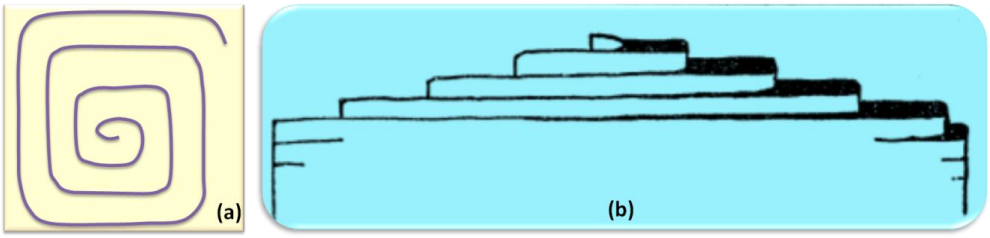

Figure 6.16 (a) top view, (b) side view of *growth pyramid formed due to single screw dislocation.*

6.5 Growth at dislocations

First described by Burton, Cabrera, and Frank[110] in the 1950s, crystals can grow via the propagation of self-perpetuating spiral step edges provided by screw dislocations

intersecting the surface[110] this BCF theory predicted the macroscopic rate laws that describe the rate at which a crystal face will grow via a dislocation mechanism. But due to limitations of imaging techniques at that time, there were few experimental observations to prove their predictions. With the advent of high resolution microscopes such as AFM, STM, and SEM, there are a few experimental observations of dislocation mediated growth in the literature.[184,234,241-243] Frank [230] predicted that a pinned step must form when a threading dislocation with a screw component intersects the free surface of a crystal. Screw dislocation will cause a surface displacement equal to the component of the Burgers vector normal to the surface. This displacement is manifested in steps connecting two dislocation terminations of opposite sign (**Figure. 6.17a**). On an atomically smooth surface, the pinned step is created from the dislocation slip plane, the ends of the step is fixed at mixed dislocation. The pinned step elongates when steps bow out from the dislocation fixed at ends. Due to bowing, the curvature of the step line at dislocation increases and as a result, the energy of the system increases. According to BCF prediction this increase in energy slows the step motion near the dislocation and ultimately limits the radius of curvature of the pinned step line to

$R_c = \gamma a / [kT \ln(P/P_o)]$, ...(6.5)

where γ is the step energy per molecule, a is the monolayer height, k is the Boltzmann constant, T is the temperature, P is the actual vapor pressure, and P_o is the equilibrium vapour pressure of the material. In BCF theory only heterogeneous thermodynamic condition is considered, thus Heying et al [242] have generalized equation (6.5) by introducing thermodynamic conditions involved in growth of GaN film. The proposed generalized form is

$R_c = -\gamma_s \omega / \Delta G$ ..... (6.6)

where γ_s is the surface energy/unit surface of the step edge, ω is the volume per mole of GaN in the crystal, and $\Delta G = -[kT \ln(P/P_o)]$. ΔG is the change in Gibbs free energy/mole for a system going from pressure P to pressure P_o.

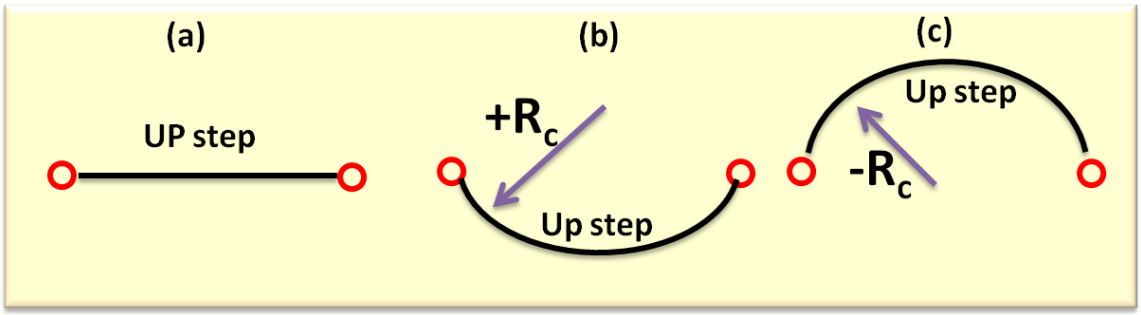

Figure 6.17 *The schematic representation of a pinned monolayer step between two dislocation terminations of opposite sign under (a) equilibrium (b) positive driving force and (c) negative driving force conditions observed in a top view of film.*

Heying et al have also replaced $kT \ln(P/P_o)$ term by ΔG to make it a more general driving force for the growth associated with a change in either the pressure or temperature for any thermodynamic system. As ΔG tends to 1 ($P \approx P_o$), the surface is in equilibrium with surrounding and the step will be a straight line, when ΔG is negative ($P > P_o$), the drive to grow is positive and the step will bow out (**Figure 6.17b**) to form nanorods. When the ΔG is positive ($P < P_o$), sublimation will occur from the step edge and the step line curvature will become negative (**Figure 6.17c**), and tends to form the open screw dislocations.

In light of above discussion we tried to probe into the morphology of C-shaped structures observed in **Figure 6.12(a).** The higher resolution images shown in **Figure 6.18(a−f)** of GaN nanostructures protruding outward from a tri-branched network observed in **Figure 6.12(a)**. A mixed case of straight (≈330nm) and bowed steps (≈68nm) are seen together at one extreme of a straight pinned step in **Figure 6.18(a).** Instead of other straight arms or pinning point, a bowed step shares a similar pinning point (dark spot of diameter ≈16nm) with straight step. The distance between pinning point is ≈32nm and radius of curvature≈24nm for a bowed step. **Figure 6.18(b)** is a solitary bowed step (≈86nm) with unclear pinning points appears at a separation of ≈ 50nm and radius of curvature ≈32nm. The absence of pinning points is due to tightening of spiralling bowing step around the pinning centres observable at this resolution. **Figure 6.18(c)** has a near hexagonal tubular structure with five complete and one incomplete side. On closer observation it appears to have three bowed steps similar to **Figure**

6.18(b), with six pinning centres. The separation between the pinning sites ≈50nm for two larger bowed steps (radius of curvature ≈40nm) and ≈30nm for the smaller bowed steps (radius of curvature ≈24nm). The hexagonal tubular structure has inner core diameter (2r) ≈86nm and outer core diameter (2R) ≈150 nm whereas the ratio r/R =0.57. Darker depression at the centre of this tubular structure appears like a hollow cone. Consider *x*=distance between pinning points and r=radius of curvature. **Figure 6.18(d)** is a clearer observation of a bowed step (r ≈32nm) with pinning ends as dark spots (diameter ≈10nm), and similar to **6.18(b**) its ends of step is curled around pining centres *x* ≈70 nm. **Figure 6.18(e)** on close observation appears as a combination of two bowed steps, larger bowed step similar to 6.**18(d)** and smaller bowed step similar to 6.**18(a).** It also appears like a single bowed step with separation between pinning point's *x*≈92nm and r≈78nm. **Figure 6.18(f)** has a pair of bowed structures, which can merge to form structures that appear as nanotubes.

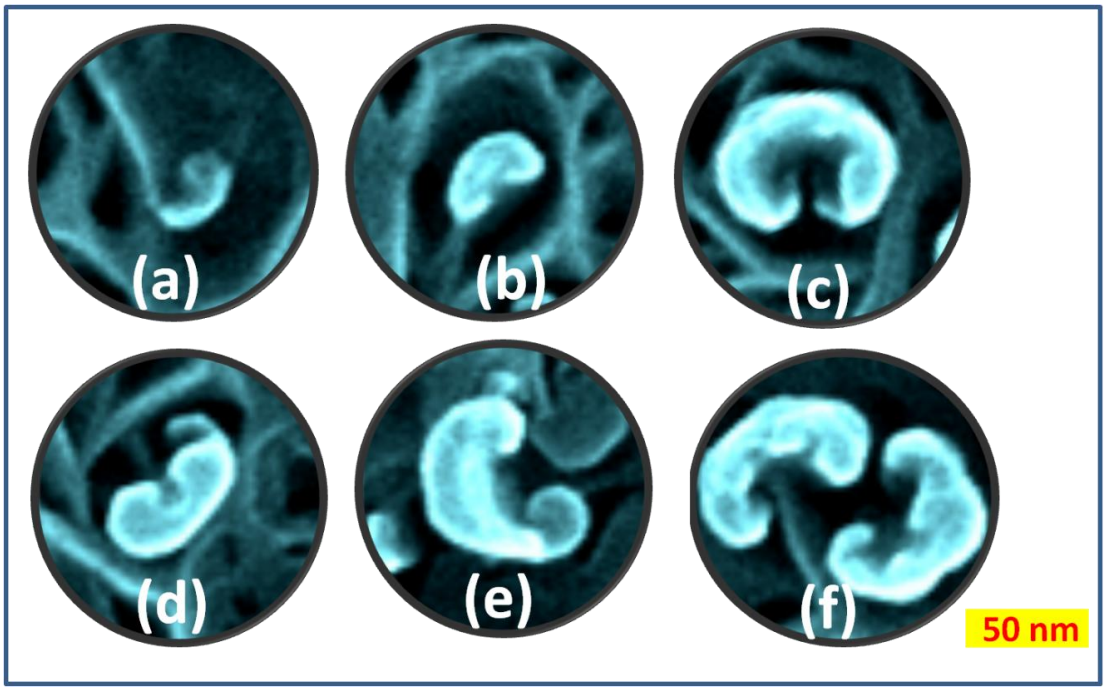

Figure 6.18(a–f) *are high resolution images of GaN nanostructures observed amidst nanowall network in Figure 10(a).*

If the step is due to a right and left handed pair of dislocations, they will send out closed loops (**Figure 6.19)** provided their distance apart is greater than the diameter of a critical nucleus. In both cases the dislocations will form pyramids and the concentration of step lines will be large and independent of the number of dislocations. With an addition of new layers on growth spirals, the direction of the dislocation remains perpendicular to the surface, since this will usually minimize the elastic energy.

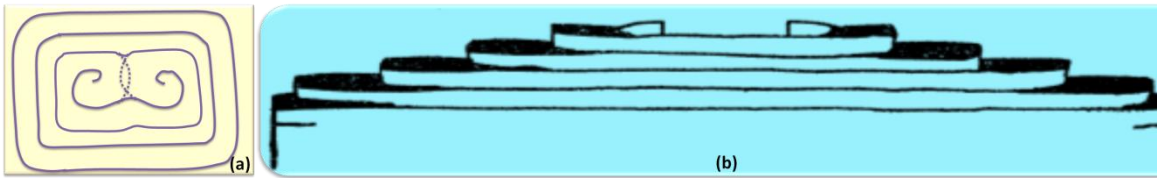

Figure 6.19 (a) top view, (b) side view of *growth pyramid formed due to a pair of screw dislocation in growing crystal.*

In GaN films spiral growth hillocks are formed due to lateral growth of pinned steps with a small critical radius of curvature. When pinned step bow out from the dislocation it winds into a spiral centered on the mixed dislocation. The tightness of the spiral or the rate of advance of the pinned step around the dislocation falls to zero when the critical curvature at the centre of spiral is reached. The spiral rotates with a stationary shape the growth of pinned step goes on despite zero tightness of the spiral. The resulting hillock is formed from the spiral ramp created by the terrace associated with the pinned step.

The C-shaped structure matches neither with **Figure 6.16** nor **6.19,** and hence cannot be explained only from the Frank spiral growth mechanism. In next section we try to understand these morphology more sequentially to understand their spontaneous evolution

Frank Read Source

Frank-Read (F-R) source is a well known mechanism for dislocation generation, which can be characterized as a localized source. A dislocation segment lying on a slip plane when gets pinned at its ends by nodes of the dislocation network or by changing onto another plane where it is not mobile, is sketched in the left panel of **Figure 6.20**.

Under suitable stress, the mobile segments move though different stages marked **(a−e).** This localized source can operate repeatedly to emit a greater number of dislocations on the same slip plane. **Figure 6.20** shows the different stages of the F-R source, along with our images obtained at the different stages of nanorods formation. The striking similarity qualitatively suggests that a F-R source may be underlying the formation of these nanorods in a narrow growth parametric windows, as shown earlier.

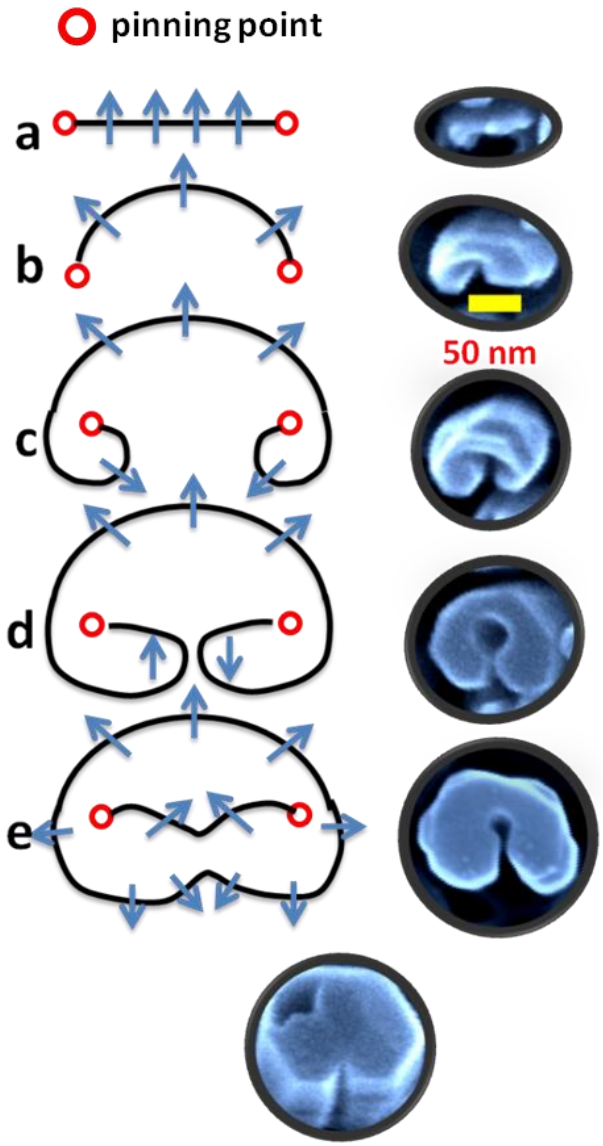

Figure 6.20 *Schematic representation of various stages of Frank-Read source shows as (a−e) and correspondingly SEM image of each stage shown alongside.*

Figure 6.20 shows a schematic representation of various dislocation looping stages along with respective high resolution instantaneous snapshot FESEM images (acquired at 10° tilt), providing a direct evidence of the role of Frank-Read Source in GaN nanostructure formation. **(a)** is an initial stage of Frank Read source where a straight step which gets pinned by a pair of threading dislocations **(b)** is a second stage where a pinned straight step gets bowed into an arc due to the negative driving forces. This is a critical stage where the bowing step tends to attain a semi-circular equilibrium. This bowing of step will continue past the semi-circular equilibrium state, (radius r_c) beyond which curling of step around the pinning centres will take place, as seen in **(c).** Figure **(d)** is a penultimate stage when the bowed step which curls around pining points approach toward each other, while the walls thicken, leading to the final stage **(e)** when bowing steps coalesce and the oppositely directed Burger vectors cancel each other. In this case the bowed step curls around pining points and approach toward each other. The final stage is a solid hexagonal shaped rod of diameter ≈100nm, tending toward an equilibrium crystal shape.

Growth model for the spontaneous formation of GaN nanocolumns on bare c-plane sapphire

The schematic of a growth model proposed in this work for GaN nanocolumn formation on bare c-plane sapphire is shown in **Figure 6.21**. In chapter 5, we have discussed GaN films grown for 120 min, when the growth temperature is increased from 480−630℃ at BEP ratio 100, the side face on nanowalls tends toward r-plane. Similarly at growth temperature 680℃, the side face of nanowalls tends toward r-plane with decrease in nitrogen flux from 8−4 sccm (or BEP ratio 200−100). In Chapter 6 we have shown that at growth temperature 680℃ and growth time 20 min, the side face of nanowalls is r-plane. The variation in growth temperature and nitrogen flux drive convergence of the side walls planes of nanowall network toward r-plane which with low sticking coefficient for Ga adatoms. The mechanism involved in the formation of nanocolumns for films grown for 480min coverage at 630℃, is driven by the size, shape and apex incline plane of the nanowalls surrounding the voids.

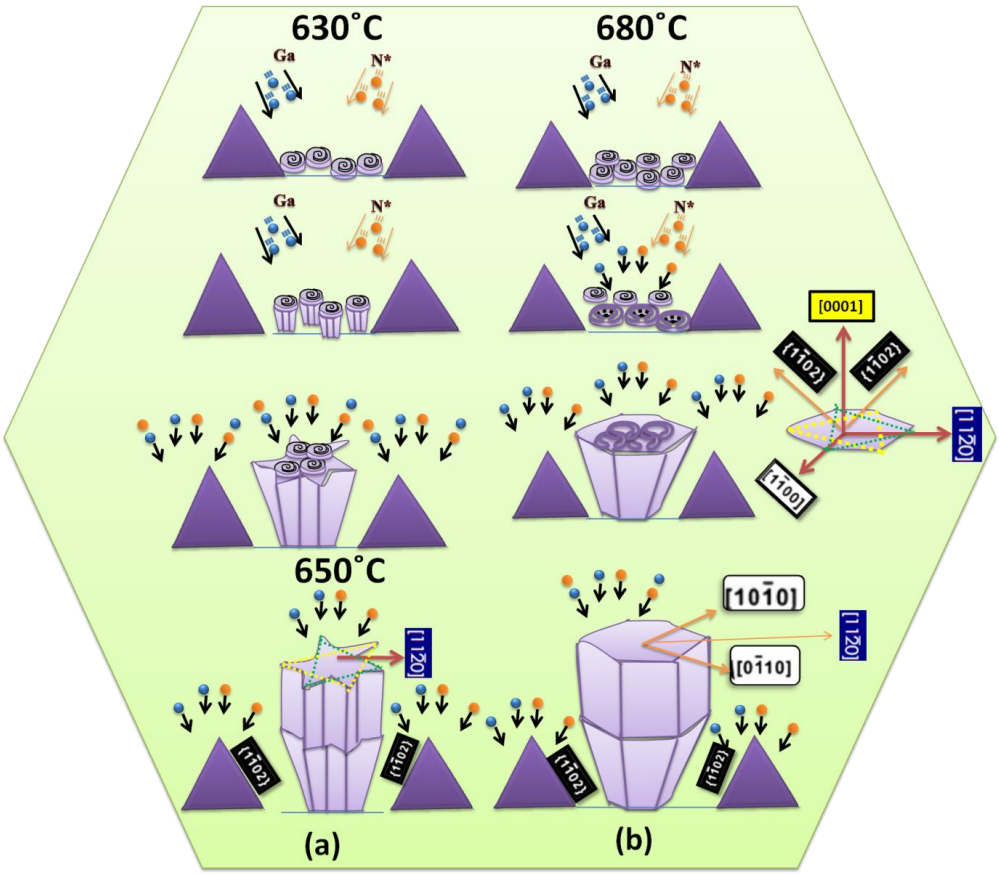

Figure 6.21 *schematic representation of formation mechanism of GaN nanocolumn on bare c-plane sapphire.*

The size of voids formed amidst tri-branched 2-D networks increases and their density decreases with increase in coverage. Hexagonal nanowall network ceases to grow after 2μm thickness for 630℃ and 0.5 μm for 650℃ and 680℃ films. Line scans performed over individual nanowalls surrounding nanocolumn observed in a plan view image of 630℃, 480min coverage and 650℃ , 680℃ films grown at 120 min coverage, suggested that these nanowalls are wedge shaped at their apex and the incline plane is along r-plane ($\bar{1}102$). The nanowalls cease to grow once they attain r-plane plane, since the sticking coefficient of Ga adatoms on r-plane is small. Thus, the Ga adatoms are funnelled into open void (with bowed step of screw dislocation as nucleation site) causing supersaturation in the voids, resulting in nucleation of the nanocolumns at the screw dislocations. The low sticking coefficient of Ga on the m-plane of the columns, enable

them to diffuse on these sidewalls of the nanocolumns to reach the [0001] c-plane tip of the nanocolumns, causing an anisotropic 1-D growth of GaN. As a result nucleation of GaN nanocolumns begins at these voids which are strongly dependent on the nucleation sites. If the nucleation site has screw dislocation steps (**Figure 6.21a**), then in this case Frank spiral growth mechanism will result in nanocolumns formation observed at substrate temperature 630℃ and 650℃. If nucleation occurs at a single screw steps pinned at two sites (**Figure 6.21b**), provided the distance between the pinning sites is greater than the radius of curvature of the spiralling bowed step, then Frank-Read source mechanism will result in nanocolumns observed at substrate temperature 680℃. Immediately after the initial nucleation at screw dislocation sites, anisotropic growth of nanocolumn proceeds along [0001] direction. The growth of nanowalls stops as soon as they attain r-plane, but they will begin to feed Ga adatom into open voids due to their lower sticking coefficient of Ga adatoms on m-plane side face of nanocolumns, and enable them to diffuse along the sides of the nanocolumns to reach the [0001] c-plane tip. When height of nanocolumns become higher that the nanowalls the adatom diffusing along the m-plane side wall will not diffuse up to the terrace of nanocolumns instead they will desorbs back into chamber. Hence now growth rate of nanocolumns will be governed by only Ga adatoms impinging directly on the tip and those diffusing along m-plane side facets toward the tip. The higher sticking coefficient of c-plane is evident from the surface of GaN nanocolumns grown at 680℃ for 480 minutes. GaN crystals (which are not Ga droplets) are seen on nanocolumn tip which is the most favourable c-plane of wurtzite GaN.

Conclusions

We have shown that the straight edge dislocation steps act as diffusion barriers, consequently enhancing the probability of nucleating GaN at these dislocation steps as nanowalls. The strained GaN films formed at the straight step of edge dislocations relax in the 3-fold symmetric network pattern. When the apex GaN nanowalls attain r-plane they cease to grow and the nanocolumns that also receive adatoms from direct impingement, grow at a faster rate along the c-direction.

Chapter 7

GaN nanorods on low index silicon substrates and nanowires on c-plane sapphire

7. GaN nanorods on low index silicon substrates and nanowires on c-plane sapphire

One of the challenging issues is the achievement of a reliable integration of optoelectronic devices with complementary metal oxide semiconductor (CMOS) technology in real integrated circuits. However, Si (001) substrate is preferred from a technological point of view because Si (001) is widely used in silicon mainstream technology, but deposition of GaN on this surface is challenging due to difference in crystallographic surface structures (hexagonal GaN and diamond cubic Si(001)). III-nitride devices have been realized on Si(111) at temperatures compatible with Si technology, either by molecular beam epitaxy (MBE) or metal organic vapour phase epitaxy, but still, it is plagued by lattice and thermal mismatches that generate a very high density of undesirable extended defects in the compact layers[26,217]. Though sophisticated approaches like buffer layer engineering[244-245], domain matching epitaxy (DME)[246], pendeoepitaxy[247-248] and heteroepitaxial growth yielded promising results, no commercial solutions are available because of the complexity, unreliability, high cost, and thermal incompatibility. Few reports on growth of GaN compact films on Si(001) aimed either to obtain pure cubic phase GaN[249] or wurtzite GaN avoiding cubic inclusions by means of complex buffer structures[250]. None of the attempts were able to achieve high quality, defect-free, single crystal structure layers, neither cubic nor wurtzite. Biphasic mixture of cubic and hexagonal GaN formation on Si(001) is reported in literature, with few reports on monophase growth of hexagonal GaN film is also observed by two-step growth methods, where low temperature buffer layer of crystalline GaN, AlN, γ-Al_2O_3, β-Si_3N_4 and amorphous Si or Si_xN_y layer is grown prior to high temperature growth of GaN or by self nitridation[251-252].

III-nitride nanocolumns formation on Si(111) and (0001)Al_2O_3 are known to accommodate the lattice mismatch at the heterointerface through a dense network of dislocations that end at the nanocolumn free surface[31,253]. Once relaxation takes place, the nanocolumns grow by keeping its own lattice parameter, a fact that is helped by the

nanocolumns high free-surface-to-volume ratio. As a consequence, nanocolumns form without strain and are dislocation-free. Cerutti et al [254] reported for the first time, formation of strain-free, defect-free, single crystalline wurtzite GaN nanocolumns on Si(001) by PAMBE. Since then, there are a few reports on the formation of GaN nanocolumns on Si(001) [31,255]. Strain relaxed wurtzite GaN nanowires on bare Si(111) and Si(001) substrates are reported, where epitaxial constraints due epitaxial relation between film and substrate or surface reconstructions effect are eluded. In literature, various mechanisms for the formation of GaN nanowires on Si(111) substrate were surveyed in detail in **Chapter 2,** but the mechanism of spontaneous growth, structure and role of intermediate layer and orientation of GaN nanorods is still in debate. A detailed mechanism for the formation of wurtzite GaN nanowires on diamond cubic Si(001) is yet to be reported. We demonstrate here the growth of high quality GaN wurtzite nanorods on a bare Si(001)2×1 surface by plasma-assisted molecular beam epitaxy, and dwell on the probable mechanism involved.

7.1 Growth of GaN nanorods on Si(001)

A Si(001) substrate which is thermally annealed in the preparation chamber for one hour and transferred to growth chamber where removal of native SiO_2 layer is done by repeated flash heating at 850℃. Atomically clean stable Si(001)-2×1 reconstructed surface is seen by RHEED before growing ≈0.7μm GaN layer at 700℃ , under nitrogen rich conditions (N/Ga BEP ratio 100). GaN film is characterized by field emission scanning electron microscopy (FESEM) and room temperature cathodoluminescence (CL) and X-ray diffraction (XRD). **Figure 7.1** shows RHEED pattern acquired *in-situ* along <11$\bar{2}$0> direction for (a) clean Si(001)-2×1, and (b) GaN on clean Si(001)-2×1. The streaky RHEED pattern **Figure 7.1(a)** of Si(001) with faint crisscross streaks (Kikuchi lines) suggest cleanliness of Si(001) surface with 2×1 reconstruction, with no native SiO_2. RHEED image **Figure 7.1(b)** for GaN grown on clean Si(001)-2×1 shows diffraction spots elongated along the ring-like pattern, manifests the polycrystalline (or disordered) nature of the GaN overlayer. Though not sharp, spotty pattern suggests 3D

surface roughness of GaN overlayer on Si(001)-2×1 substrate. Elongation of diffraction spots along circular arc has angular spread in RHEED spots of about 30° indicating disordered orientation of structures. Tilt and 3D roughness can explain angular spread is shown schematically below **Figure 7.1(b).**

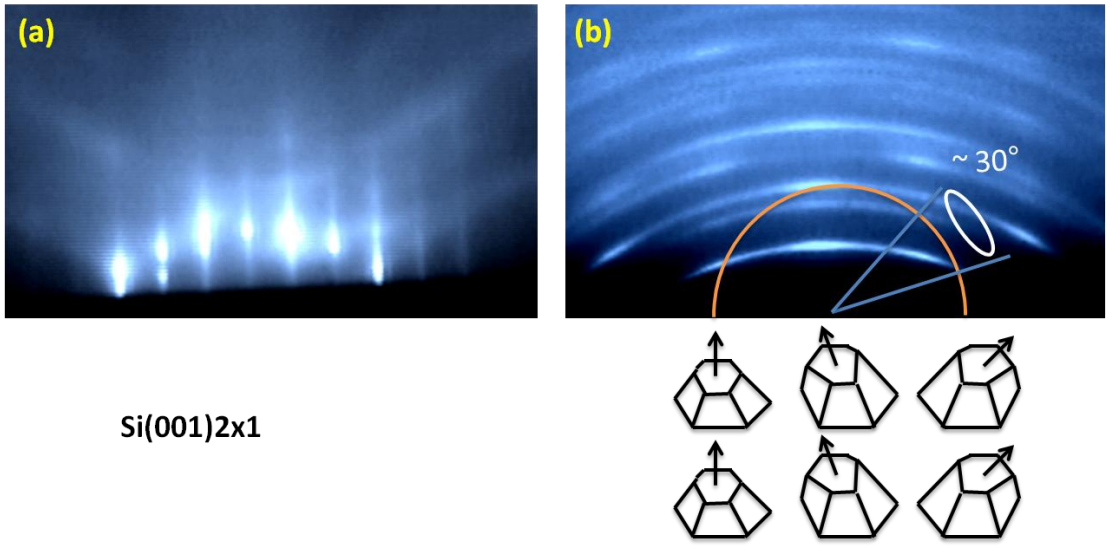

Figure 7.1 *RHEED pattern acquired along <11$\bar{2}$0> direction for (a) clean Si(001)-2×1, and (b) GaN overlayer grown on clean Si(001)-2×1 with schematic of tilted 3D structures beneath.*

To decipher surface morphology and surface structure, high resolution scanning electron microscopy is performed. **Figure 7.2** (a) is a plan view (b) cross-sectional view SEM images and inset of (a) shows higher resolution SEM image. The figure (a) shows GaN nanorods (NRs) of various shapes and alignment on the clean Si(001)-2×1. Few of these NRs are solid but most of them appear as tubes with central depressions and some with c-shape structure, as shown in the inset of **Figure 7.2(a).** GaN NRs grown are aligned along surface normal direction [0001] and with few of them deviating from it, and have density ~5.5x10^9/cm^2 and diameter in the range ≈50−100 nm. NRs are highly dense and are c-oriented since 1D anisotropic growth of wurtzite GaN prefers [0001] direction. Inset of **Figure 7.2(a)** provides a clearer view of solid NRs (size ≈100nm) with hexagonal cross-section with their terrace along (0001) c-plane with {10$\bar{1}$0} m-plane side facets, but most have a central depression which appears to be bounded by {10$\bar{1}$1} s-plane or r-plane {1$\bar{1}$02} facets. Other partially formed c-shaped tubular structures of

diameter ≈50nm are three sided semi-hexagonal features surrounded by {10$\bar{1}$0} m-planes. **Figure 7.2(b)** is a cross-sectional view of NRs showing a height range of 500−700 nm. Many nanorods appear to be oriented normal to the substrate surface, but several seem to deviate from the [0001] direction by 10−30°. The maximum tilt observed is 30° from the substrate normal which agrees well with the angular spread of RHEED spots determined by RHEED pattern shown in **Figure 7.2b**.

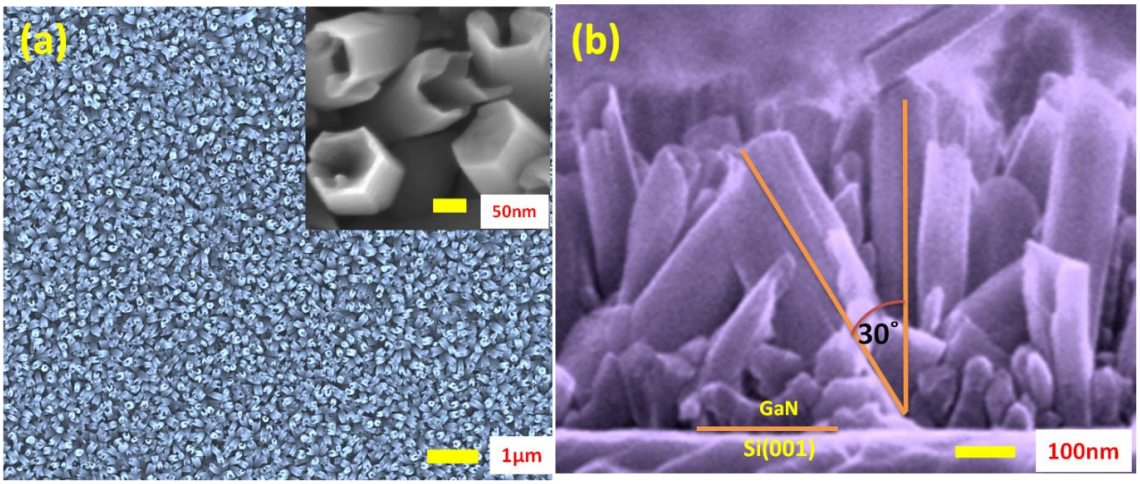

Figure 7.2 *(a) plan (b) cross-sectional view SEM images of GaN overlayer grown on Si(001)-2 × 1 and inset of figure (a) shows high resolution plan view SEM image.*

The powder XRD (PXRD) patterns are acquired on sample (a) continuous rotation (b) no rotation and (c) when turned by 90° with respect to position (b) is shown in **Figure 7.3**. Typical pattern exhibit diffraction peaks located at 2θ=32.4, 34.5, 36.8, 48.1, 57.7, 63.4, 67.7, 69.1, 70.6 are attribute to (10$\bar{1}$0), (0002), (10$\bar{1}$1), (10$\bar{1}$2), (11$\bar{2}$0), (10$\bar{1}$3), (2000), (11$\bar{2}$3), (20$\bar{2}$1). In XRD pattern of GaN NRs three dominant diffraction peaks are observed at 2θ=32.4, 34.5 and 36.8, which are characteristic of the GaN (10$\bar{1}$0), (0002) and (10$\bar{1}$1) peaks, respectively. From these symmetric and asymmetric reflections of hexagonal wurtzite structure, the observed lattice constants are a=0.318 nm and c= 0.518 nm. The dominant peaks at 2θ=69.4, 48.3 and 32.8 are due to reflections from Si (400), (220) and (002) and the other reflections (11$\bar{2}$0) and (10$\bar{1}$3) of GaN are overlapped with silicon reflections. When a pattern is acquired with no rotation shown as (b), diffraction from silicon (002) peak vanishes and GaN (11$\bar{2}$0) appears, but when the sample is rotated

by 90° with respect to position (b), diffraction from GaN (11$\bar{2}$0) plane disappears. Since for hexagonal wurtzite crystals planes of GaN (1$\bar{1}$00) and (11$\bar{2}$0) are at 90° rotation to each other, this observation confirms that GaN NRs are wurtzite and are tilted upto 30° from the [0001] direction.

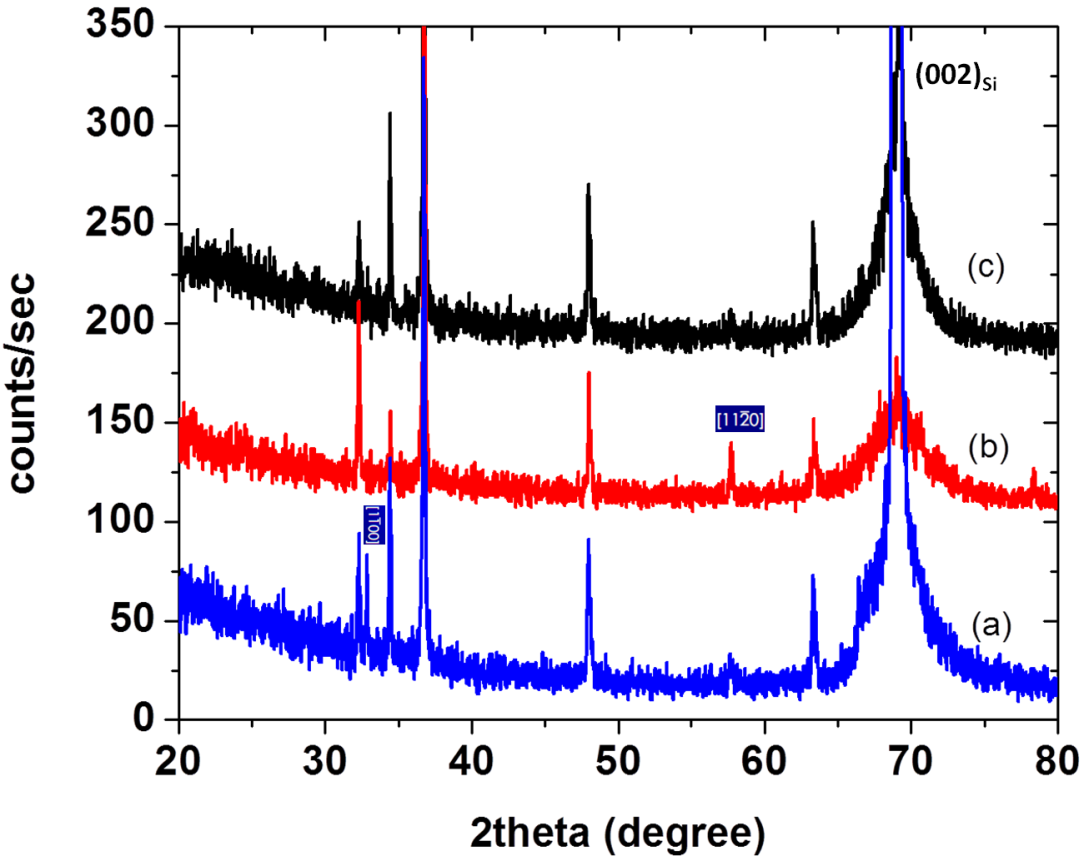

Figure 7.3 *PXRD patterns acquired with sample (a) rotation (b) no rotation and (c) when turned by 90° with respect to position (b).*

CL spectrum is acquired at room temperature of the samples to study the optical properties of the GaN nanorods formed. **Figure 7.4** shows CL spectra with a strong band-edge emission at ≈364.8nm (3.4eV) with full width at half maximum (FWHM) ≈15.0 nm (120.0meV). Negligible yellow or other defect luminescence ≈550.0nm(2.2eV) demonstrates that the GaN nanorods are also of very good optical qaulity. The band-edge position of GaN NRs agrees well with the band-edge emission from a bulk GaN is

≈364.5(3.4eV) at room temperature suggests relaxed, complete strain free wurtzite GaN. The broad width of the band-edge emission 120.0 meV(15.0 nm) can be attributed to the tilt in nanorods, due to anisotropic emission from different planes exposed to the detector.

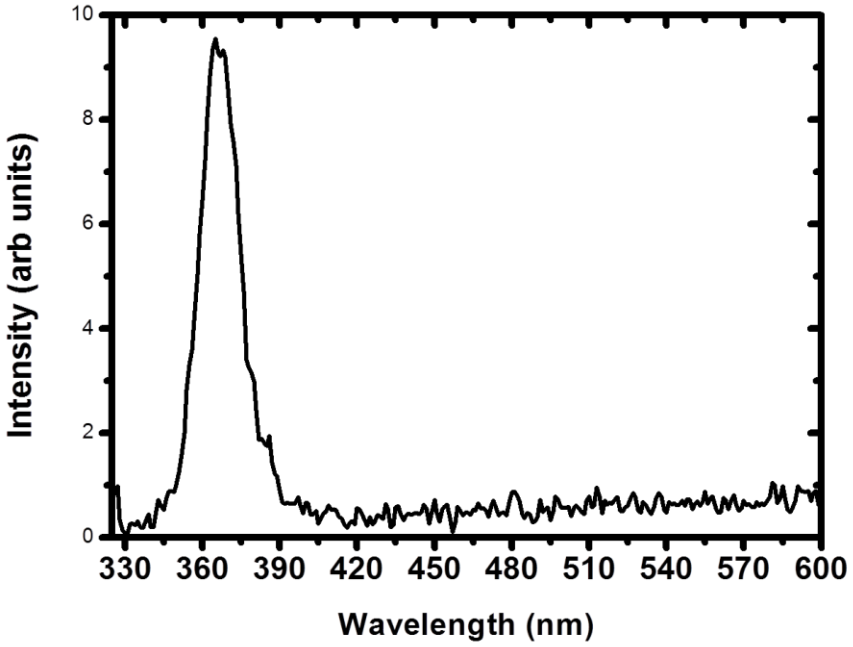

Figure 7.4 *shows CL spectra of GaN NTs/NRs grown on Si(001) at room temperature.*

7.2 Superstructure of self-aligned hexagonal nanorods of GaN on nitride Si(111) surface

We have also studied the growth of GaN on clean Si(111) surface. The experimental procedure is similar to that used for Si(001).

In late 1990s research groups from Sophia University, Tokyo[256] and Universidad Politecnica, Madrid[135] has reported the spontaneous formation of GaN nanowires on silicon by PAMBE. Later numerous groups have reported growth morphology, model, phase diagram, mechanism (which is reviewed in detail in Chapter 2). The most commonly used substrate for the spontaneous formation of GaN nanowire is Si(111). To

prevent intermixing between Ga and Si and to increase the uniformity of the nanowire during nucleation process and, thin AlN buffer layer is commonly used by various groups. Bertness et al[257] and Largeau et al[258] have shown that GaN NWs predominantly align azimuthally to the underlying Si (GaN <11$\bar{2}$0>// Si<1$\bar{1}$0>). Recently Chen et. al [169] reported formation of GaN nanowires on Si(111) substrate by PAMBE over single crystalline β-Si_3N_4(0001)/Si(111) by nitridation to avoid intermixing of Ga with silicon and amorphous interlayer of Si_xN_y layer which is generally observed due to self nitridation of silicon substrate during growth of GaN on Si(111) under nitrogen rich condition. The use of silicon nitride as an intermediate layer could be an alternate solution, because of its process compatibility to MBE and its ability to form the requisite template for initial nucleation of strain relaxed crystalline GaN nanostructure growth. Details of the effect of the chemical surface modification on defect induced emission, N-diffusion, orientation of nanorods, etc., are yet to be resolved due to lack of systematic studies. Thus, the mechanisms have only been widely speculated in literature, and have led to controversial inferences regarding the use of intermediate layers.

In this section, we address the critical role of single crystalline and amorphous nature of intermediate silicon nitride layer on GaN nanorod (NR) growth *in-situ* in a PA-MBE system on Si(111). Our results demonstrate that there is no need of AlN buffer layers for the formation of high quality GaN NRs and that the method of nitridation of Si(111) substrate determines the nature of the nanorod assembly. We also employ the simple and reliable Fast Fourier Transformation (FFT) method[259] to determine the shape, size and orientation of the GaN nanorods. We show that wurtzite nanorods are c-oriented and are hexagonal both in shape and in their superstructural organization, when grown on the the crystalline phase of silicon nitride intermediate layer.

After sample degassing and cleaning by standard RCA procedure, combinations of substrate temperatures and N* plasma exposure have been carried out in PA-MBE system. Optimal conditions for the formation of amorphous and crystalline silicon nitride intermediate layer on Si(111) surface are determined by RHEED and XPS. Correlating the structure by Reflection High Energy Electron Diffraction (RHEED) and performing

deconvolution studies of the Si(2p) and N(1s) X-ray Photoelectron Spectroscopy (XPS) core levels, we find that at 850^{o}C, 8 minutes of nitridation yields a crystalline interface, while 60 minutes of nitridation results in an amorphous phase. We have determined quantitative XPS (results not shown here) that the amorphous silicon nitride is sub-stoichiometric, while the crystalline phase is in the form of Si_3N_4. To identify the role of the nature of silicon nitride intermediate layer on the quality of GaN films grown on them, we have performed GaN growth on the following surfaces, in different sets of experiments: a) clean Si(111)-7x7, b) amorphous Si_xN_y/Si(111)-7×7 and c) crystalline Si_3N_4(0001)/Si(111) 7×7. All the GaN growths are performed by PA-MBE at 4.5sscm N_2 flow rate and substrate temperature of 750^{o}C. The samples have been characterized *in-situ* by RHEED and *ex-situ* by Field Emission Scanning Electron Microscopy (FESEM), X-ray Diffraction (XRD) and Photoluminescence (PL). The Fourier analysis was performed by taking FFT of Field Emission Scanning Electron Microscopy (FESEM) images based on the work of Fujita et al, in Ref [259]. In the resulting Fourier space image, each point (pixel) represents a particular frequency contained in the real space image. The frequencies are essentially 1/a; a is the distance in real space. As in **Figure 7.6(d),** we have a dominant scattering peak corresponding to characteristic length scale which is essentially the nearest rod to rod distance in the FESEM image. By computing mean rod to void length ratio along horizontal and vertical directions we extract the mean rod size.

Figure 7.5 consists of plan-view FESEM images, where (a), (b) and (c) correspond to GaN grown on clean Si(111)-7×7, amorphous Si_xN_y/Si(111)-7×7 and single crystalline Si_3N_4(0001)/Si(111)-7×7, respectively. The figure shows the formation of GaN nanorods (NR) in all the three cases, with different shapes, sizes and alignment. We also notice in these three images that though several rods are solid, most of them appear as tubes with central depressions unlike the morphology of GaN nanorods on Si(001). The GaN NRs grown on Si(111)-7×7 and amorphous Si_xN_y/Si(111)-7×7 [**Figure 7.5(a,b)**] are not aligned and are tilted along different directions, with the tilt relatively less in case of rods grown on clean Si surface. The size distribution of GaN

NRs on clean silicon is from 60 to 130 nm with density ≈$9.03\times10^{8}cm^{-2}$ and for GaN NRs on amorphous silicon nitride the size distribution is from 45−100nm with density ≈$1.9\times10^{9}cm^{-2}$. The GaN NRs grown on crystalline Si_3N_4(0001)/Si(111)-7×7 are highly dense and are well-aligned perpendicular to the substrate and thus are all c-oriented, as shown in **Figure 7.5(c)**. The line scans yield a rod-density of ~$3.38\times10^{9}/cm^{2}$ and average size of 160 nm for GaN grown on crystalline silicon nitride.

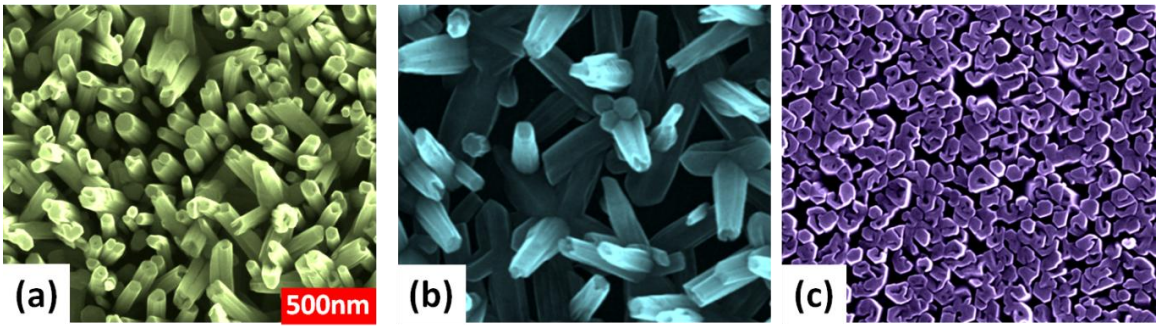

Figure 7.5 *FESEM images, where (a), (b) and (c) corresponds to GaN NR growth clean Si(111)-7×7, amorphous Si_xN_y/Si(111)-7×7 and single crystalline Si_3N_4(0001)/Si(111)-7×7, respectively.*

We have carried out the Fourier analysis of the FESEM images[260] to identify the symmetry and length-scale relevant to morphological details. The reciprocal space images of the respective FESEM images in **Figure 7.5 (a−c)** are shown in **Figure 7.6**(a−c), images (a) and (b) are almost featureless in reflecting no particular dominant shape of the rods. Fourier analysis of GaN NRs grown on crystalline Si_3N_4(0001)/Si(111)-7×7 shows a dominant six-fold symmetry, a characteristic of regular hexagon shaped rods shown in **Figure 7.6(c).** Though the nanorods shown don't appear to be perfectly uniform in shape and size, we estimate a reliable value of their size by using statistical analysis of the FFT image of **Figure 7.6(c).** First, we examine an intensity profile of the FFT image along horizontal and vertical lines passing through the centre of the image (see **Figure 7.6d**), removing the intensity corresponding to the central pixel (that represent the average value of the whole image) as it is unusually higher than that of other pixels. Since the image is represented with real values, its FFT is symmetric about the zero-frequency (see the curves in **Figure 7.6(d**). Coarse-graining the data (solid line) corresponding to intensity profile (dashed line) average length-scales determined from the horizontal and vertical

intensity profiles are 263 nm and 222 nm respectively. Secondly, we extract the average size of the rods by representing the images in binary form with rods as white and voids as black regions. The average ratios of the length of the region occupied by rods to that occupied by the voids along horizontal and vertical directions are 2.04 and 2.08, respectively. The average size of the nanorods thus estimated is 163 nm close to the visually estimated value of 160 nm. The FFT image also contains information about the symmetry of the stacking of the nanorods, which is extracted by adjustment of contrast at longer length scales (central portion of the FFT image)

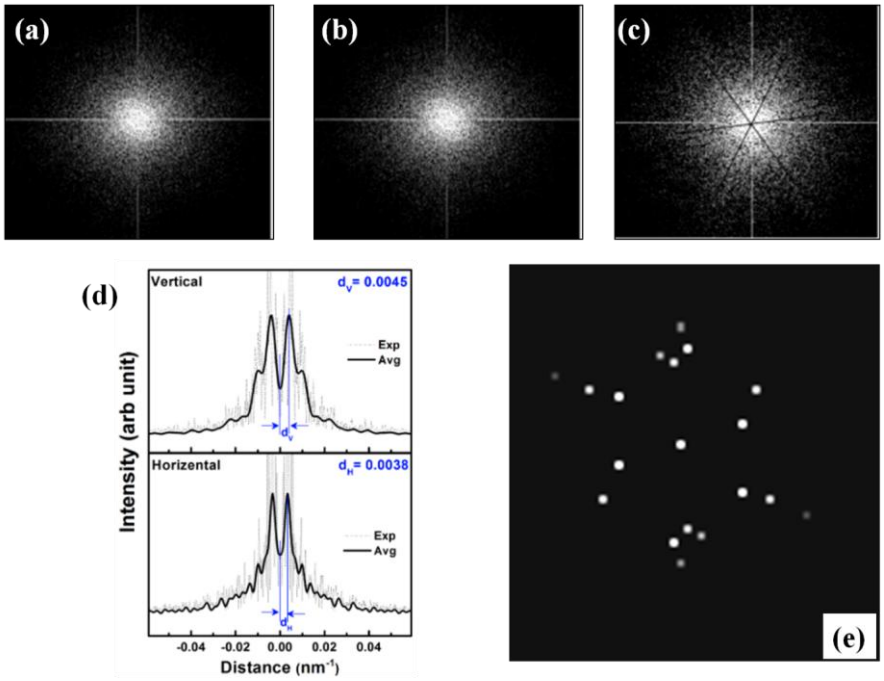

Figure 7.6 *FFT images, where (a), (b) and (c) corresponds to GaN NR growth on clean Si(111)-7×7, amorphous Si_xN_y/Si(111)-7×7 and single crystalline Si_3N_4(0001)/Si(111)-7×7, respectively, (d) shows the line scan for the size measurements, and (e) corresponds to FFT image after appropriate thresholding of the FFT image (c),*

Figure 7.6(e). We find that the arrangement of rods has hexagonal symmetry, with epitaxial stacking of rods in a 2D hexagonal lattice**.** Upon further examination, we see that there is a 20^o rotation between the hexagonal features at the two length scales (shape and arrangement). Thus, **Figure 7.6(e)** corresponds to a hexagonal superstructure

of hexagonal rods with a rotational mismatch, showing an epitaxial relationship of rods with the substrate properties.

Figure 7.7 shows *in-situ* RHEED pattern taken in the [11$\bar{2}$0] direction after the growth, where (a), (b) and (c) correspond to GaN grown on clean Si(111)-7×7, amorphous Si_xN_y/Si(111)-7×7 and single crystalline Si_3N_4(0001)/Si(111)-7×7, respectively. RHEED images for GaN grown on clean Si(111)-7×7 and amorphous Si_xN_y/Si(111)-7×7 show elongation of the diffraction spots along the ring-like pattern, that manifests the disordered nature of the GaN overlayer. Elongation of diffraction spots along circular arc suggest that GaN NRs are tilted from the [0001] direction. The angular spread in case of RHEED spots along circular arc with respect to (0,0) reflection in case of GaN NRs grown on Si(111)7×7, amorphous Si_xN_y/Si(111) 7×7 and single crystalline Si_3N_4(0001)/Si(111)7×7 surface is ~15°, ~30° and < 5° respectively.

The RHEED spots become sharp, intense and circular for GaN deposited on crystalline Si_3N_4(0001)/Si(111)-7×7, as shown in **Figure 7.7(c)**, where the spotty pattern is characteristic of electron transmission through the 3D features. The ratio of lateral to vertical spot distances is ≈1.9 (= c/a ratio ≈ 1.63), which shows that nanorods have wurtzite structure, and the diffraction spot intensity is highest for GaN grown on crystalline Si_3N_4(0001)/Si(111)-7×7. Overall, the RHEED pattern shows that of the three cases, only GaN grown on crystalline silicon nitride are c-oriented and normal to the substrate.

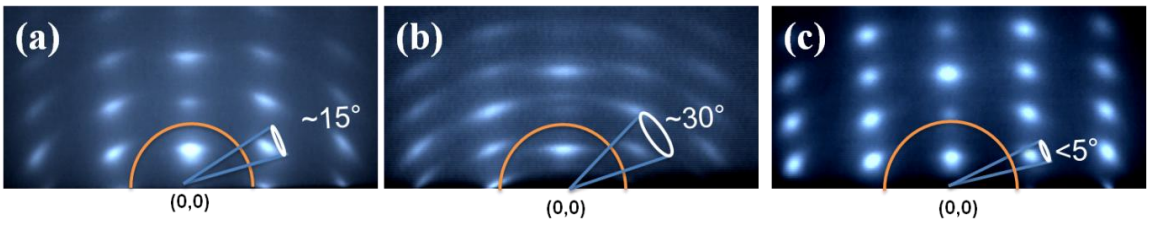

Figure 7.7 *RHEED pattern after GaN growth, where (a), (b) and (c) correspond to GaN growth on clean clean Si(111)-7×7, amorphous Si_xN_y/Si(111)-7×7 and single crystalline Si_3N_4(0001)/Si(111)-7×7, respectively.*

After confirming the dependence of the morphological aspects of GaN nanorod formation on nitrided Si(111) surface we examine their atomic structure by XRD, whose

results are shown in **Figure 7.8**. In the θ-2θ XRD pattern, where (a), (b) and (c) correspond to GaN NR grown on clean Si(111)-7×7, amorphous Si_xN_y/Si(111)-7×7 and single crystalline Si_3N_4(0001)/Si(111)-7×7, respectively.

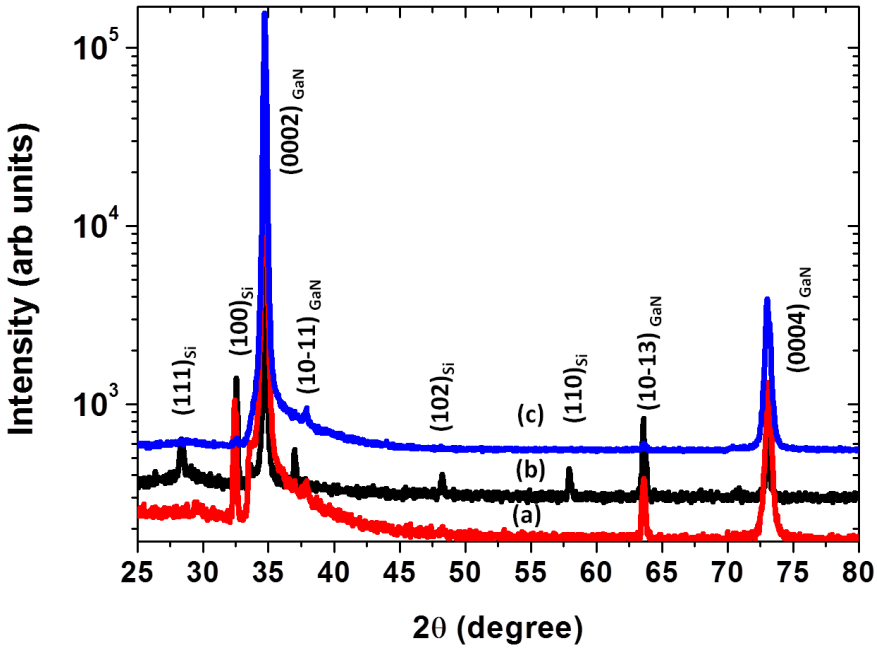

Figure 7.8: *XRD 2θ scan for GaN films grown on (a) clean Si(111)-7×7, (b) amorphous Si_xN_y/Si(111)-7×7 and (c) crystalline Si_3N_4(0001)/Si(111)-7×7, respectively.*

Figure 7.8 shows characteristic reflections of GaN along with the [(10$\bar{1}$0), (0002), (10$\bar{1}$3) and (0004)] for the Si(111) surface and [(111), (100), (002), (101), (102), (110) (103) and (004)] reflection for amorphous Si_xN_y/Si(111)-7×7, showing that GaN NRs grown on clean Si(111)-7×7and on amorphous Si_xN_y/Si(111)-7×7 are disordered in nature, manifesting reflections from multiple planes. This suggests that GaN NRs grown on clean Si(111)-7×7and on amorphous Si_xN_y/Si(111)-7×7 are tilted with respect to [0001] direction, thereby exposing other planes of wurtzite GaN. The θ-2θ scan for GaN NR grown on crystalline Si_3N_4(0001)/Si(111)-7×7 shows the presence of intense (0002) and (0004) related peaks. The high structural quality of GaN nanorods formed on crystalline Si_3N_4 is testified by the XRD observations.

Mechanism for tilt in GaN nanorods on Si(001) and Si(111)

N-rich conditions can be achieved by increasing V/III BEP ratio, or by increasing the deposition temperature which results in a higher Ga desorption. Calleja et al[135] has reviewed growth of group III-nitride nanocolumns or nanowires on bare Si(111) and (001) in N-rich condition by PAMBE and have shown that most of the group III-nitride nanocolumns on bare silicon substrates are well aligned, but not completely normal to the substrate. Other groups[116,169,261] have argued that the in-homogeneity in thickness and partially amorphous or crystalline structure of SiN layer is the reason for random orientation of nanorods. They have also reported that SiN layer is formed due to self nitridation of silicon surface since N atoms have strong affinity for Si atoms. The interface of GaN nanocolumns grown over Si(111) or Si(001) probed by high resolution transmission electron microscopy (HRTEM) revealed that an intermediate SiN layer thickness is ≈2nm [262]. It is also shown that due to the presence of SiN layer, GaN nanocolumns follow in-plane axial epitaxial relation between $< 2\bar{1}\bar{1}0 >_{GaN}$ and $[\bar{1}10]_{Si}$ ($< 1\bar{1}00 >_{GaN}$ and $[11\bar{2}]_{Si}$)[100,169,253]. Guha et al [263] have shown that randomness in GaN nanocolumns orientation is due to amorphous SiO_2/Si(111). Hans Luth et al[138,264] by HRTEM has probed the intermediate layer, is typically observed between GaN nanowire (NWs) and silicon substrate[136]. This intermediate layer is amorphous SiN (in agreement with Calleja group) formed due to self nitridation with a thin GaN wetting layer between GaN NWs and SiN. By electron energy loss spectroscopy (EELS) studies they showed the absence of SiO_2 layer due to oxidation. Stocia et al [136] suggested that in the early stages of GaN NWs growth on silicon substrate, in nitrogen rich condition, there will be high surface density of Si and N adatoms which can increase the probability of the SiN chemical reaction since the bond energy Si-N (4.5eV) is greater than GaN (2.2eV). Small GaN crystalline clusters formed on top of the amorphous SiN layer may act as seed or nucleation centre for NWs. Also the morphologic defects of the surface resulting from *in-situ* annealing and interface layer formation are suggested to be the reason for small inclinations of NWs and the critical diameter of GaN cluster is ≈7nm which is the seed for NWs nucleation of diameter ≈10−15nm.

Wang et al[265] have shown by scanning tunnelling microscopy(STM) that β-Si_3N_4(0001)/Si(111)-7×7 are truncated triangular islands. And recent reports from Chen et al[169] have shown that GaN nanorods grown on intentionally formed single crystalline β-Si_3N_4(0001)/Si(111)-7×7 surface by nitridation, are fully relaxed and epitaxially oriented both in vertical [0001] direction and on the growth plane[169]. They also proposed on the basis of TEM observation of GaN nanocrystals grown on β-Si_3N_4(0001)/Si(111)-7×7 that truncated triangular pyramids can form via VW growth mode on GaN on β-Si_3N_4(0001) by PAMBE. **Figure 7.9** is a schematic of the top face of truncated triangular pyramid (tetragonal island) and (I-III) are the side face of pyramids whose cross-section across the terrace (0001) and edge of terrace of pyramids (grown with basal plane parallel to silicon surface) along directions <1$\bar{1}$00> and (IV-VI) are cross-sectional views of pyramids (with basal plane tilted by few degree from the silicon surface) taken across the terrace (0001) and edge of pyramids along directions <1$\bar{1}$00>.

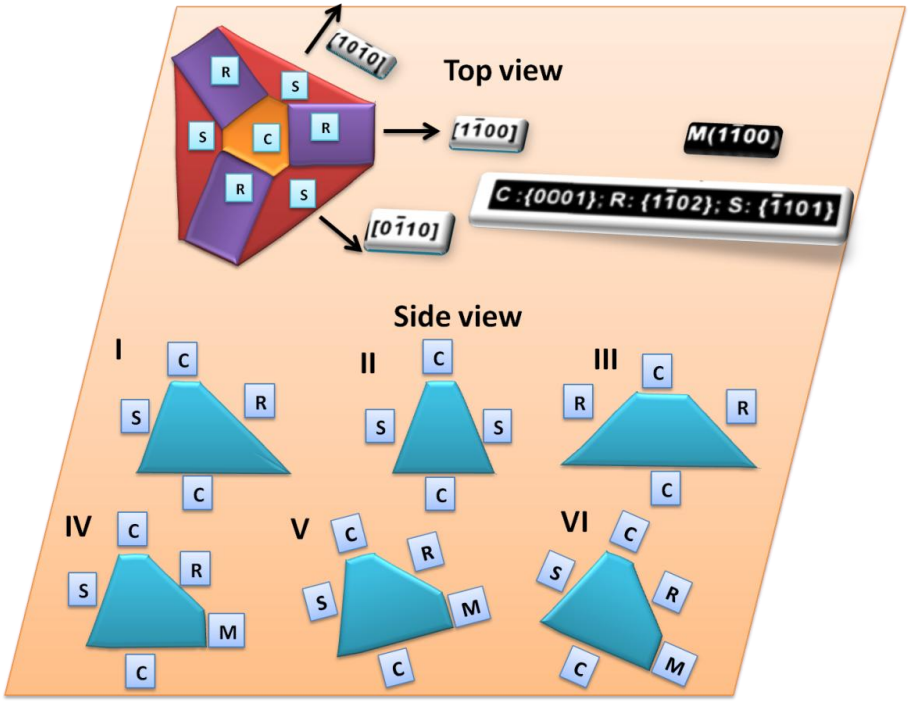

Figure 7.9 *Schematic of top view of tetragonal island (truncated triangular pyramid), (I-III) are cross-sectional view of pyramids across the terrace and edge terrace of pyramids (0001) plane directions <1$\bar{1}$00> aand (IV-VI) are cross-sectional view of tilted pyramids across the terrace and edge terrace of pyramids (0001) plane directions <1$\bar{1}$00>.*

On the basis of observations and assuming truncated pyramids of SiN we propose that tilt in GaN nanorods grown on Si(001)2×1 depends on the basal plane alignment of GaN nanocrystal seed. It is known that the preferential direction for 1D anisotropic growth GaN is along c-directions, since the sticking coefficient of c-plane > m-plane > r-plane > s-plane. Hence, the probability of GaN nanorods formation on side faces of tetragonal GaN nanocrystals is lesser. If the basal plane of tetragonal GaN nanocrystals is parallel to substrate surface then GaN nanorods will grow normal to the surface. If the basal plane of GaN nanocrystals is tilted by angle θ with respect to silicon surface, then GaN nanorods will be tilted accordingly. If bunch of multi-directional GaN nanorods is observed on silicon substrate then it may be due to group of one or more than one nanocrystal grown nearer to each other with tilt. Second possibility may be due to anisotropic growth on m-,r-, s- planes of tetragonal GaN nanocrystals.

Frank-spiral growth and Frank Read sources:

One-dimensional (1D) line imperfections in crystal structure resulting from missing or irregularly positioned atoms are dislocations. Frank (1949)[230] postulated that underlying screw dislocation may result as unending source of steps on crystal surface. Since the core of dislocation is fixed, hence adsorbed adatoms in vapour or liquid phase will attach to the step, the step winds around the core which produces spiral-shaped step pattern on the surface of crystal. Recently Hannon et al[266], reported that if crystal grows via a screw dislocation intersecting silicon surface, then on Si(111) surface classic spiral pattern predicted by Burton, Cabrera, and Frank (BCF)[110] in 1951 are observed. As discussed in Chapter 6, in nitrogen rich conditions of growth of GaN by MBE, due to retarded diffusion of metal adatoms and reaction with the nitrogen plasma species, nanorods are formed. It is speculated that these rods with hexagonal m-plane faceted walls have low sticking coefficient and thus promote diffusion of Ga adatoms to the top of the rod (c-plane) which, along with the arrival Ga flux, cause the anisotropic 1D growth. The nanostructures in GaN on sapphire are already shown to spontaneously form (without any pre-treatment) due to super-saturation and nucleation around screw

dislocations formed at the initial stages of growth. In view of this knowledge, we can make some qualitative inferences for the present GaN/Si_xN_y/Si(111) system. On careful observation, we see that most of the nanorods are not actually solid hexagons but are tubular in shape and have a central depression. This also suggests that the rods are nucleated at screw dislocations, and undergo spiral 1-D growth. In case of bare Si and amorphous Si_xN_y, the dislocations can thread in random orientations and thus resulting in the un-aligned nature of the rods on the two surfaces. However, on the crystalline Si_3N_4 the screw dislocations have the burgers vectors direction parallel to the c-orientation of the wurtzite GaN and consequently, the emanating rods are all c-oriented and highly dense.

In case of Si(001) surface more complicated step motion are observed by Hannon et el[266] which are not fully described in dislocation-mediated crystal growth surfaces predictions of BCF. The difference in structures on Si(111) and Si(001) surface may be due to the atomic structure of Si(111) and Si(001). Surface dangling bonds on the surface of bulk terminated Si(001) rebond to form dimer pairs which align to form rows along the <110> directions of the crystal. These highly anisotropic atomic structures elastically strain the silicon crystal in a direction parallel to the dimer row and will result in different energy of the surface compared to that when it is strained perpendicular to the row. On Si(001) surface where a step of size equal to the silicon lattice parameter, a double step can dissociate into two single-height atomic steps, due to diamond crystal structure of low index (001) silicon surface is shown in **Figure 7.10.**

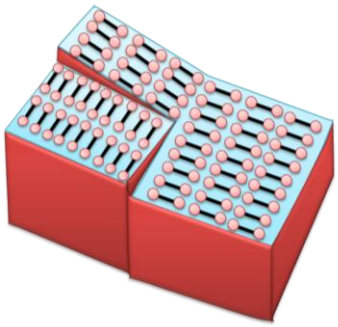

Figure 7.10 schematic *model of Si(001) surface showing the two single-height atomic steps that emanate from the dislocation core and the dimer rows. The dimer (two pink balls with black stick) rows orientation changes on crossing a step.*

Unlike double-height steps, the orientation of the dimer rows changes by 90° across the step. Hence formation of GaN nanorods evolve from a dislocation mediated surface structures formed due to annealing of Si(001) substrate to obtain 2×1 reconstructions. The steps on Si(001) substrate similar to that observed by Hannon et al [266] may have lead to frozen spiralling screw steps on the surface, and may have acted as nucleation sites for the evolution of GaN nanorods on Si(001).

A schematic representation of intermediate looping stages of Frank-Read source under shear stress corresponding to high resolution plan view FESEM images of GaN film grown on Si(001)-2×1 shown in **Figure 7.11**. The SEM images shown alongside are the instantaneous snapshots of the schematically represented various stages of Frank-Read source, and provides direct observation of Frank Read Source as underlying mechanism in GaN nanorods formation grown on Si(001)-2×1.

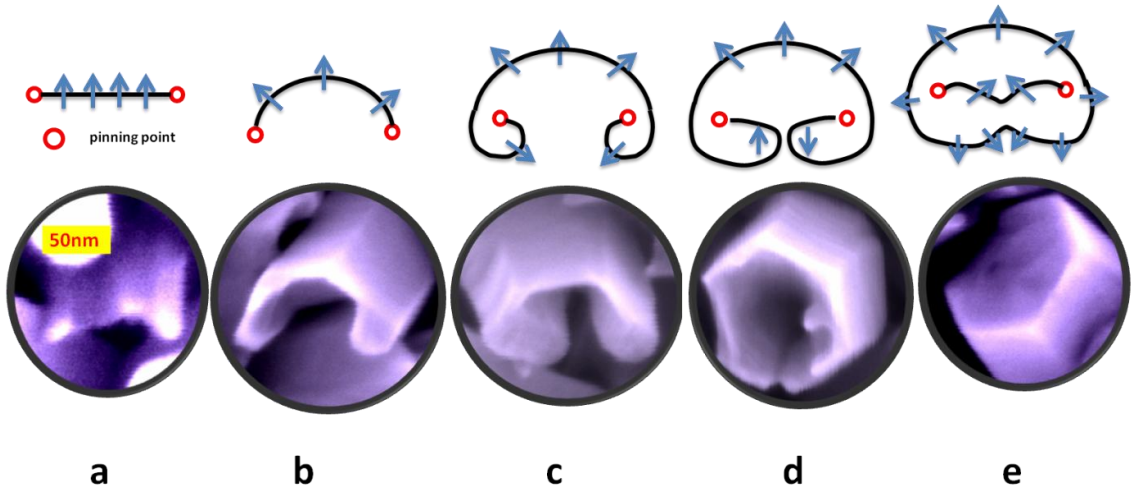

Figure 7.11 *Schematic representation of various intermediate stages of Frank-Read source shown as (a−e) and correspondingly high resolution of FESEM image of each stage shown alongside.*

Figure 7.11(a) is an initial stage of Frank Read source where a straight step (length=*x*) which gets pinned by a pair of threading dislocations. **Figure 7.11(b)** is a second stage where a pinned straight step gets bows into an arc due to positive or negative driving forces ($x = 2\times$ r, r is radius of curvature of an arc) is a critical stage where bowing step attain semi-circular equilibrium. As per Frank-Read suggestion bowing of step will

continue until dislocation passes semi-circular equilibrium state, beyond which curling of step around pinning centre will take place. **Figure 7.11(c)** is a third stage of bowing step where r increases beyond r_c ($r > r_c$). At this stage the bowing step curls around the pinning site and around pining sites. **Figure 7.11(d)** is a penultimate stage when the bowed step curls around pining points approach toward each other, the radius of curvature of bowing step around pining sites. **Figure 7.11(e)** the final stage when bowing steps coalesce and the oppositely directed Burger vectors cancel each other due to opposite nature. In this case the bowed step curls around pining points and approach toward each other and a new straight step similar to the initial stage (**Figure 7.11a**) and part of older bowing steps continues to moves outward. The final stage is represented as solid hexagonal shaped rod of diameter≈100nm.

7.3 ELOG on nanowall network and GaN nanowire formation by dewetting

We have seen that the lattice mismatch between GaN and Al_2O_3 and Silicon results in formation of dislocations as the strain relaxation route. However, the dislocations form nucleation sites for 1-D GaN nanorods growth, specifically. The lattice mismatch between GaN film and (0001) Al_2O_3 substrate cause enormous strain in film which relaxes by generating ~10^5 cm^{-1} basal stacking-fault (BSFs) densities and ~10^{10} cm^{-2} threading dislocations densities (TDDs), which are perpendicular to the substrate surface having edge, screw and mixed characters [267]. Epitaxial layer overgrowth (ELOG) technique has shown promising results by reducing TTDs from ~10^{10} to 10^6 cm^{-2} in a wing region of GaN overlayer [218]. But still TDDs remain high in the seed layer which is almost one-fourth of the entire layer and the wing region consist of rotated grains upto 1° resulting in grain boundary defects and stacking faults. In ELOG, seed of micrometer sized columns of GaN (restricted to masking and etching resolution) is used to grow continuous lateral overlayer. Process complexities in ELO techniques have restricted development of devices based on ELO buffers. Hence, necessity of growing mask less seed columns for ELO has generated common interest among researchers, [268] and a novel

nano-ELOG technique is introduced in which a continuous layer is grown over seed columns of diameter and spacing in range ≈20−100 nm which is about two orders of magnitude lesser than conventional ELOG and have shown reduction in TDs by two to three order of magnitude [269]. The earliest reports on GaN epitaxial lateral overlayer (ELO) growth using template of GaN nanocolumns (≈100nm diameter with ≈50nm gap space) grown by PAMBE on AlN/Al_2O_3(0001) by Kusakabe et. al.[270], and by Piquette et al [271] GaN mesh like microstructure (≈10nm mesh width with ≈100nm voids diameter) on AlN/Al_2O_3(0001). As a follow up more recent reports by Bougrioua et al.[272] formed GaN nanowires (≈10nm) grown over Si(111) and AlN/Si(111), Chern et al [273] had GaN nanowires (≈20−50 nm) on AlN/Al_2O_3(0001) template and others have shown GaN overlayer of TDDs ~10^8 cm^{-2}. The overlayer grown by these groups is either by MBE (in a Ga-rich condition) or by MOCVD on GaN nanostructure templates. Cherns et al [274], has summarized GaN nano-ELOG growth along with their detailed microstructure investigation of the continuous GaN overlayers and proposed change in polarity as the key factor for the growth of continuous GaN overlayer nanowires or nanocolumns. Qiming et el [275] have proposed Nanowire-templated lateral epitaxial growth (NTLEG) technique and grown suspended coalesced non-polar GaN film of TDDs~$10^9 cm^{-2}$ and BSFs density~$10^5 cm^{-1}$ of a-plane on r-plane sapphire. The quality of overlayer grown on nanowires template depends on the alignment, structural quality and aspect ratio of nanowires. It is shown by theoretical studies that the nanowire geometry prevents the propagation of threading dislocations in the core of nanowires, since the free surface at the sidewalls permits elastic relaxation of the strain [276]. Thus, dislocations are expected to be confined at the interface between nanowire and the substrate or bend to the sidewalls at the bottom of the nanowires[74]. Spontaneously formed GaN nanowires by PAMBE are generally free of strain generated due to mismatch between the substrate and nanowires, which gets relieved via formation of screw dislocations perpendicular to the (0001) planes[135]. By rigorous complex TEM studies, Cherns et al[113] has shown that screw dislocations can thread through GaN nanowires grown over thin AlN layer on c-plane sapphire substrate. Forming small wire diameter structures allow ease of dislocation glide

within the c-plane result in annihilation of the dislocations at the nanowire surface, leaving the crystal to grow defect-free [90].

To mitigate TDDs and BSFs in GaN nanowires, we have attempted a novel process, motivated by the nano-ELOG and spontaneous catalyst free nanowire growth in a single growth run. Typically in nano-ELOG method GaN overlayer is grown in Ga-rich condition by PAMBE (or by MOCVD) over nanowires grown in N-rich condition (or nanowires formed by photolithography on GaN film), but here we use our nanowall network as the base template for the required morphology. In this study growth is performed under nitrogen rich condition (BEP ratio ≈100) in four different steps, in the first step GaN nanowall network is grown at 630℃ on bare c-plane sapphire substrate followed by forming GaN overlayer at 400℃ over a template of GaN nanowall network. In the third step amorphous GaN layer grown at 200℃ over the 400℃ grown GaN overlayer, and finally the 3-step structure is annealed at 750℃ in ~10^{-10} Torr vacuum, to form 1-D nanowires. Thickness of the entire structure and individual stages is determined from cross-sectional FESEM image. Initially 0.5μm thick single crystalline GaN film grown for first 60 min at 630℃ which is followed by a 0.8 μm thick GaN layer grown at 400℃ for the next 100mins. In third step ≈0.2−0.3 μm thick amorphous GaN layer is grown for another 40 min at 200℃. In final fourth step amorphous GaN layer is annealed in growth chamber (base pressure ~10^{-10} Torr) by ramping at 20℃/min rate to 700℃ and kept for 60 minutes.

The cross-sectional view FESEM image of the first step of 4-step GaN structure and corresponding RHEED pattern (acquired along [$11\bar{2}0$] incident electron beam azimuth) is shown alongside in **Figure 7.12a**. Cross-section FESEM image shows porous columnar structures well separated by 20−50 nm wide voids and aligned along [0001] direction normal to the substrate. The plan view morphology of GaN film grown at 630℃ for first 60 min, has surface network structure that is composed of nanowalls which are tri-branched, oriented along <$11\bar{2}0$> and <$1\bar{1}00$> directions, with average width < 10nm and length of <100nm. As described earlier, the hexagonal nanowalls surrounding the 10^{10} voids per cm^2 are formed due to nucleation of Ga adatoms around the open screw dislocations. For the first 5 minutes of growth, the RHEED pattern was streaky (similar to clean sapphire), which suggests that GaN layers has grown as 2D flat layers on the sapphire substrate. Up to a coverage of 0.1μm intensity, the pattern diminishes partially

and recovers back again. Faint streaks were observed upto 15 minutes beyond which RHEED pattern transforms to a bright spotty pattern which remains spotty till 60 min (2D to 3D transition). The spots in the pattern suggest that the grown film has grown in 3D mode with a surface roughness < 20 nm measured by AFM, sufficient enough to allow electrons to transmit though 3D structures. The transformation of RHEED pattern from streaks to spots indicates that threading dislocations assist nucleation form 3D structures, as discussed in Chapter V and VI. The spots circumscribed within the rectangular box which is drawn over a representative RHEED pattern (acquired in step 1) are circular with aspect ratio unity, whereas spots outside the box show slight spread in horizontal direction. The observed lattice periodicities in $<11\bar{2}0>$ and $<1\bar{1}00>$ projections are c and $c/2$ which is in agreement with the axial ordering where as in plane ordering is a and $a/\sqrt{3}$. The ratio of spacing between RHEED spots in horizontal and vertical direction is $2a^*/\sqrt{3}c^* \approx 1.89$ for pattern viewed along $[11\bar{2}0]$ and is $2a^*/2c^* \approx 1.63$ for RHEED pattern viewed along $[1\bar{1}00]$ (where $a^*=2\pi/a$ and $c^*=2\pi/c$). Thus from both $<11\bar{2}0>$ and $<1\bar{1}00>$ azimuths, the equivalent c/a ratio is 1.63. This corresponds to bulk lattice parameters of wurtzite GaN, hence columnar GaN film is single crystalline, c-oriented and wurtzite.

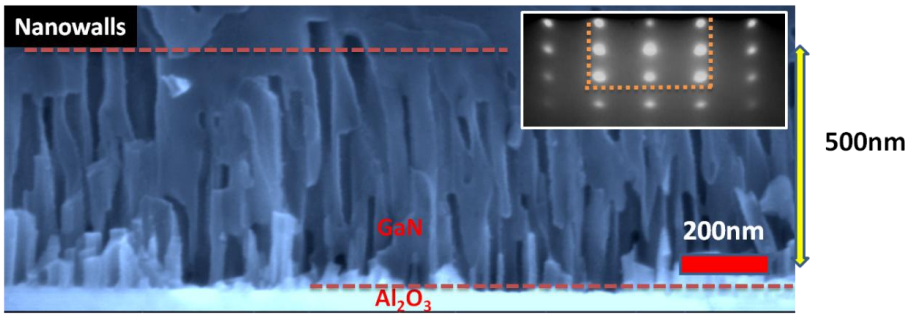

Figure 7.12a *cross-section FESEM image of first step of four steps GaN structure and RHEED patterns acquired along $[11\bar{2}0]$ incident electron beam azimuth.*

To probe interface of nanowall and c-plane sapphire substrate high resolution transmission electron microscopy (HRTEM) is performed. HRTEM micrograph of GaN nanowall and $Al_2O_3(0001)$ interface is shown on the extreme left of **Figure 7.12b**, in centre Fast Fourier Transform (FFT) and on extreme right Inverse Fast Fourier Transform

(IFFT) images of GaN nanowall, $Al_2O_3(0001)$ and their interface. The IFFT image of interface shows locally a matching of GaN and sapphire by the formation of an almost coherent array of misfit dislocations. Seven $\{2\bar{1}\bar{1}0\}$ GaN units fitting eight $\{01\bar{1}0\}$ sapphire planes at the early stages of the growth. The corresponding FFT image confirms the alignment of $\{2\bar{1}\bar{1}0\}$ and $\{01\bar{1}0\}$ planes.

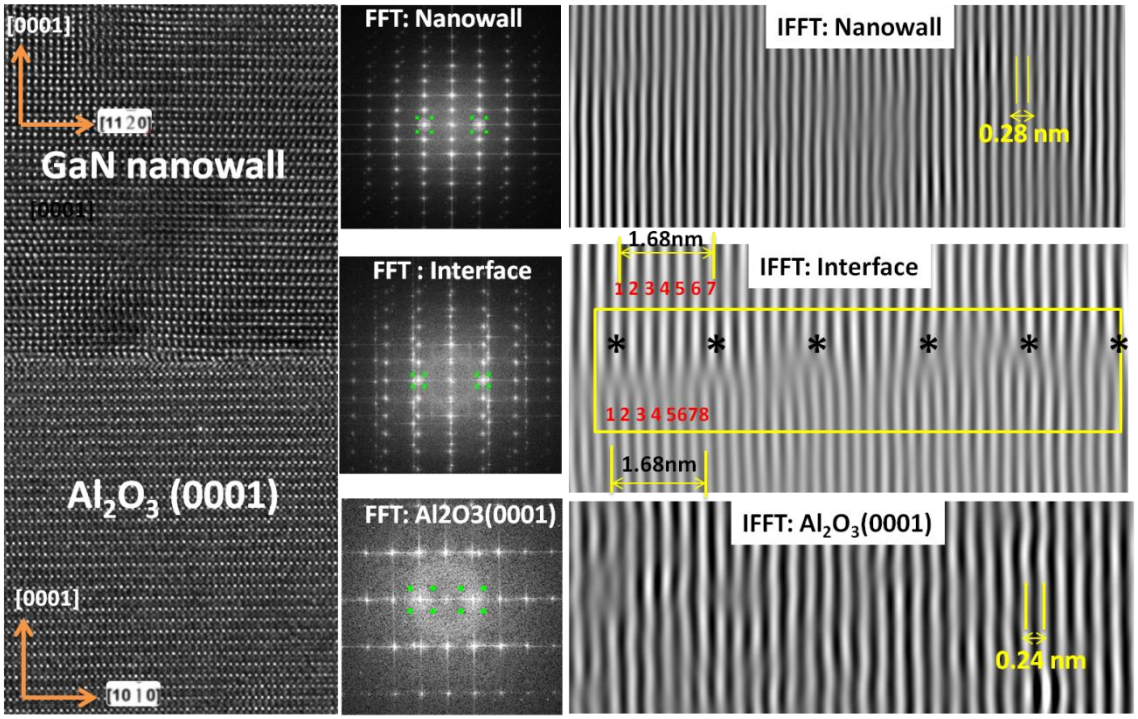

Figure 7.12b *shows high resolution TEM images of GaN nanowall and $Al_2O_3(0001)$ interface with corresponding Fast Fourier Transform (FFT) and Inverse Fast Fourier Transform (IFFT) images*

The c plane of GaN rotates by 30° in the basal plane of sapphire, which leads to alignment of ½$(30\bar{3}0)$ planes of sapphire with $(2\bar{1}\bar{1}0)$ planes or *a* planes of GaN. Thus, domain matching of sapphire planes (having $a_{sapphire}/\sqrt{3}$) with *a* planes of GaN. By alternating the domains, there is almost a perfect matching a $6\times a_{GaN}$ (3.186Å) ≈ $7\times a_{sapphire}/\sqrt{3}$ (2.7512). From these planar spacing the calculated strain −11.8% is equivalent to 7/8 planar matching suggested by Nararyan et al[246]. This array of dislocations, with the Burgers vector in the basal plane, releases − 11.8% of the mismatch

between sapphire and GaN. The TDs result from the residual strain of − 2.1%. The strain reduces to about − 0.2%, measured at the surface for a 1 μm thick GaN layer.

Cross-section view FESEM image of the step 2 of this method is shown in **Figure 7.13(a).** The film grown from 60 to 160 min is compact, without voids or columnar feature. Corresponding RHEED pattern shown inset is a 2×1 streaky pattern which indicates that the film is single crystalline, wurtzite, compact and flat with a surface roughness less than 1nm. **Figure 7.13(b)** is a high resolution cross-section FESEM image acquired of region cleaved across the compact zone to expose film grown at 400℃ (step 2). It reveals a flat nature of the layer with few voids, which may be local strain relaxation features or might have formed due to generation of grain boundaries caused due to island coalescence. Vertical GaN nanowalls arrays formed in step 1 served as a strain-relief template for the lateral growth of low-dislocation density GaN film. Lateral growth of GaN film grown over nanowall network on top of void space might have prevented reformation of threading dislocation in the GaN overlayer.

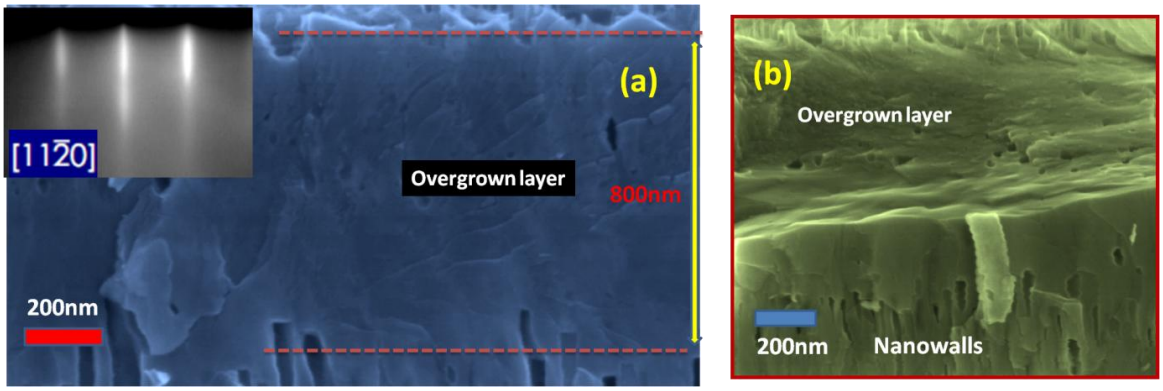

Figure 7.13 (a) *cross-section FESEM image of second step of four steps GaN structure and RHEED patterns acquired along [11$\bar{2}$0] incident electron beam azimuth, (b) plan view FESEM image acquired at 60° tilt with respect to surface normal.*

To reveal detailed microstructure, high resolution TEM image is acquired at the junction of GaN nanowall and 2D-film is shown in **Figure 7.14**.The magnified image of the nanowall, interface and the 2D film are shown on left side in **Figure 7.14.** HRTEM image shows that that the nanowall region is devoid of defects and the 2D film is devoid of dislocations and no features related to any type of defects are observed. Formation of

2D GaN layer over nanowall network seems to have generated stacking faults at the junction of nanowall and 2D films as visible in the central region.

Beyond 160 min, RHEED spots tend to become elongated along faint circular arcs which gets further reduce to just faint circular arcs around 200 min growth time. After 200min, the growth is stopped and sample is cooled from growth to room temperature, when the RHEED pattern turned completely darker. The envelope of circular arc over spots is an indication of polycrystallinity of the film and just arcs correspond to an amorphous film. The amorphous GaN layer is annealed in the growth chamber by ramping at 20℃/min rate to 700℃. During this annealing duration no change in RHEED pattern is seen and it remain dark. Finally as the temperature is raised to 770℃ and kept for 60 minutes, darker RHEED pattern transform to a spotty pattern, suggesting evolution of single crystalline 3D features.

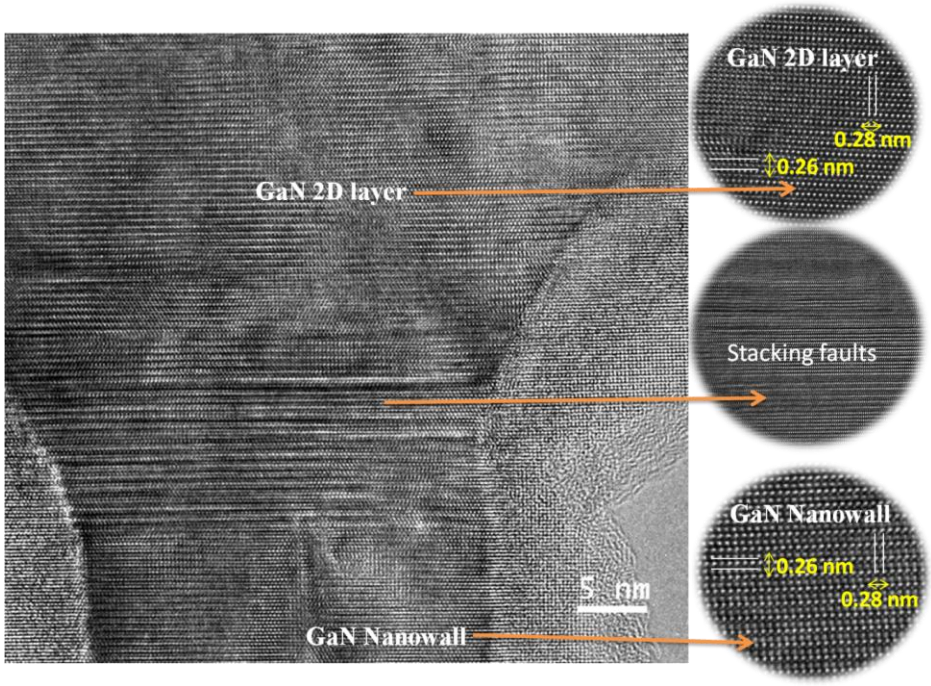

Figure 7.14 *shows high resolution TEM images of GaN nanowall formed in the first stage and 2D-film formed in the second stage. On right side are high-resolution images of nanowall, nanowall and 2D film interface, and 2D film is shown.*

Figure 7.15 shows the FESEM images of the topmost region with well separated 1D-nanowires over the films surface with few darker regions (seen in tilt view FESEM

image shown on bottom right panel). These voids indicate that dislocations may have threaded through the entire length of the flat layer. Few nanowires are seen to be mechanically unstable and are tilted, bent or uprooted during the mechanical sample cleavage procedure due to their thinness. Cross-sectional view of FESEM image shows thin nanowires on of < 30nm top of the film limited by the resolution of FESEM.

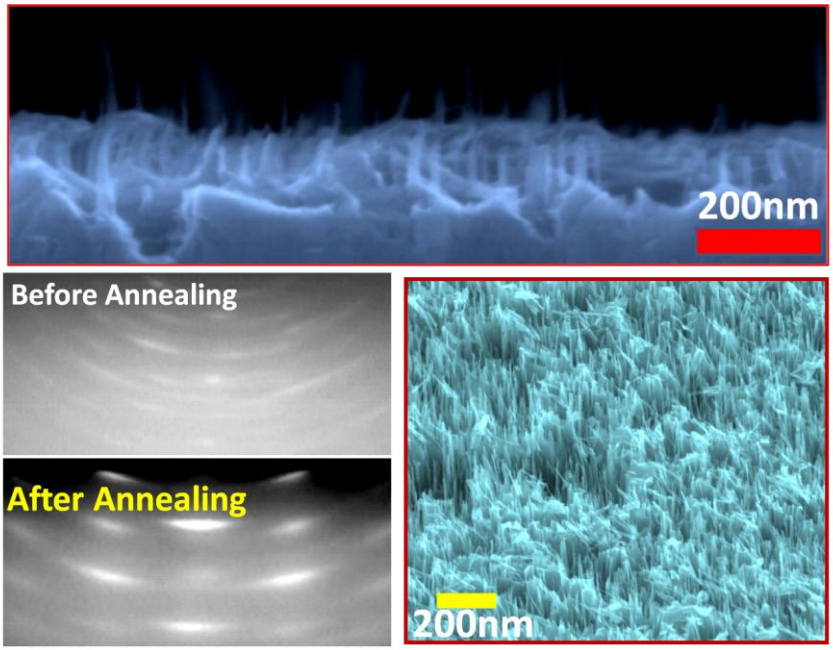

Figure 7.15 *shows cross-section FESEM image of the fourth step of four steps GaN structure and on bottom left panel RHEED patterns acquired before and after fourth stage, along [11$\bar{2}$0] incident electron beam azimuth, and on the bottom right panel plan view FESEM image acquired at 60° tilt with respect to surface normal.*

RHEED pattern acquired in [11$\bar{2}$0] azimuth before and after annealing are shown on the bottom left panel of **Figure 7.15.** RHHED pattern acquired before annealing shows polycrystalline nature of the film and pattern acquired after annealing shows spots with an anisotropic spread along faint arcs as an envelope. Anisotropy in spots is due to tilt in nanowires from [0001] direction and c/a ratio ~1.63 suggests single crystalline and wurtzite structure of nanowires that are c-oriented.

XSEM imaging is done to decipher information on nanowires which are formed on annealing of amorphous layer. XSEM image (**Figure 7.16)** shows average length of nanowires ≈350nm and average diameter ≈30nm. These dimensions measured by

FESEM were not reliable since aspect ratios of these 1D nanowhiskers was varying during imaging probably due to local charging effects.

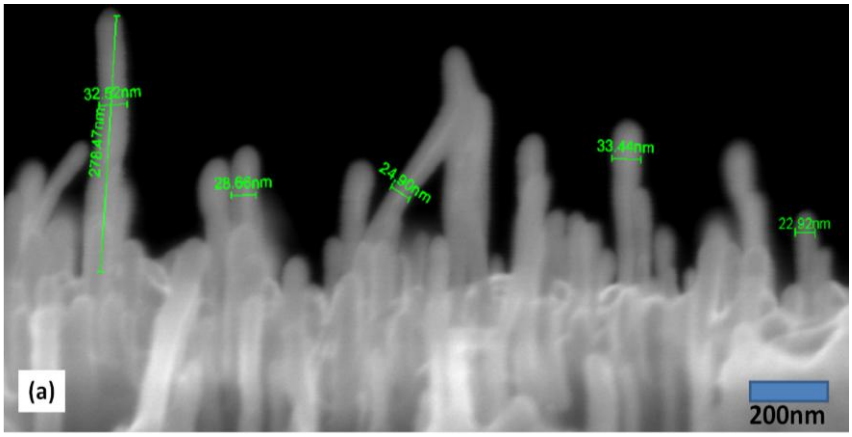

Figure 7.16 *high resolution cross-section view FESEM image of nanowires*

Hence, the nanowires were removed by lightly scraping them off from the topmost layer and then after light sonicating in alcohol dispersed on a TEM grid for imaging. **Figure 7.17(a)** is a low resolution TEM image of the top of a group of 1-D nanowires, and **Figure 7.17(b)** is the image of a solitary nanowire. The aspect ratio of these nanowires is ≈25 and an average length ≈250nm and diameter ≈10nm, determined from TEM image of a single wire (also can be called whisker).

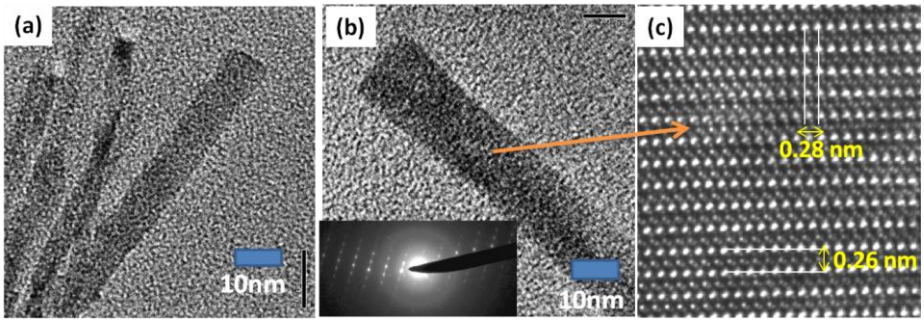

Figure 7.17 *(a−b) TEM image of nanowires and (c) HRTEM image of single nanowire.*

Inset of **Figure 7.17(b)**, show selective area electron diffraction (SAED) pattern of a single nanowhisker with the c/a ratio of 1.63, calculated from the separation between spots in horizontal and vertical direction (similarly by RHEED pattern) corresponding to

wurtzite GaN. A single nanowire has darker linear contrast on its surface, which may be due to edge of hexagonal nanowire. **Figure 17(c)** is an ultra-high resolution TEM image acquired at the centre of an individual nanowires which confirms that the nanowires are defect free, single crystalline and wurtzite (measured c=0.514nm and a=0.312nm from the atomic spacing).

Conclusions

In conclusion, it is evident from the data presented in this Chapter that the epitaxy and orientation of GaN formation can be controlled by appropriate modification of the Si(111) and sapphire substrate. The screw dislocations that originate at the interface appear to act as nucleation centres for m-walled hexagonal GaN growth. GaN nanorod growth on bare Si(111) and Si(001) and amorphous silicon nitride intermediate layer yield mis-oriented alignment of the 1D structures. However, a crystalline Si_3N_4 template formed on Si(111) by nitridation, leads to highly dense hexagonal shaped wurtzite nanorods that are well-aligned (c-oriented) with a 20^o rotation with the superstructure organization with hexagonal stacking. Resulting GaN nanorods show high quality single-crystalline phase and optical emission properties. We have also demonstrated formation of single crystalline GaN nanowires on GaN layer grown in nitrogen-rich condition. Four stages of GaN growth is performed to obtain high crystalline quality GaN nanowires over high quality GaN layer. The initial layer is grown such that defect free nanowalls are formed. This is used as a template to mitigate misfit and threading dislocations generated at the interface of GaN layer and c-plane sapphire substrate. The topmost layer of the film is formed by annealing the threading dislocation free 2D GaN layer. Due to de-wetting of this layer, defect free 1-D nanowires of <10nm which are c-oriented were formed. We propose this as a novel method of forming dislocation free non-catalytic growth of ordered and oriented GaN nanowires by PA-MBE, in a single growth.

Chapter 8

Summary and conclusions

8. Summary and Conclusions:

The most important issue of not being able to use III-nitrides to their full potential, is the non-availability of compatible substrates[277]. Among the ones available, c-plane sapphire and silicon have shown viability, but still are plagued by significant lattice and thermal expansion coefficient mismatches that induce defects in the structures[9]. Contemporary research involves finding surface treatments and modifications, and formation of nanostructures (such as nanorods), in an attempt to enhance device performance[26,31,216]. This dissertation presents an investigation of growth and characterization of Gallium Nitride films and nanostructures on single crystalline substrates by Plasma Assisted Molecular Beam Epitaxy. The work involves synthesis of GaN films in growth parametric space, followed by characterization using complementary techniques. It provides an insight into the role of growth parameters on the mechanisms underlying the formation of GaN nanowires, nanorods, nanocolumns and compact 2D films, and relate their structural and optical properties. The work provides the first evidence for the surface-treatment-free and catalyst-free growth of GaN nanowires, nanorods, nanocolumns on Si(001), Si(111) and Al_2O_3(0001) which are shown to be self-organized, oriented and single crystalline[156-159]. This Chapter provide a summary of the work accomplished, highlights the main and novel results and identifies the future course this work need to proceed in.

Formation of HEMT structures on Al_2O_3(0001)

First, we form conventional 2D GaN films, fabricate a HEMT structure and characterize its performance. The heterostructures of AlGaN/GaN possesses attractive electronic and mechanical properties due to presence of a two-dimensional electron gas (2DEG) with carrier density $n_s \sim 10^{13}$ cm^{-2} in an undoped material at AlGaN/GaN interface[46,278-279]. If high two-dimensional carrier mobility can be achieved in AlGaN/GaN quantum wells (QWs) then high-power devices of record performance can be fabricated[280]. But despite high quality structural and electrical properties of High

electron mobility transistor (HEMT) structures they still possess threading dislocations which limit their actual performance[281-283]. Since the effect of interface defects (such as misfit dislocations, surface cracks, alloy reordering etc.) which generally originate due to relaxation of the strain energy accumulated in the AlGaN layer, will result in interface roughness. The interface roughness caused due to defects results in non-uniform charge distribution at interface, which contributes to the room temperature mobility drop at high electron concentration via scattering mechanism. The threading dislocations originated in the GaN side of the heterostructure typically pierce QWs also negatively influence room temperature mobility due to extrinsic scattering mechanism[284]. Thus, the challenge to obtain HEMT structures with room temperature mobility larger than 1800cm^2/Vs, still remains.

To obtain HEMT structure, we have initially grown conventional GaN films over thin AlN buffer layers that were formed on Al_2O_3(0001) substrate. Both n- and p-type doping of these GaN films is performed, and their structural and electrical characterization manifested their relatively high quality. The XRD rocking curve measurement for (0002) reflection of these films shows narrow FWHM ≈ 80−100 arc sec and rms surface roughness determined by AFM measurement is < 1nm, showing smooth morphology and a pit density of threading dislocation of ~ $10^8 cm^{-2}$. The mobility and carrier concentrations of Si (Mg) doped film determined by Hall measurement are ≈ 500 cm^2/Vs, ~$10^{17} cm^{-3}$ (≈ 1 cm^2/Vs, ~$10^{19} cm^{-3}$), respectively. HEMT structure of sheet concentration ≈$1.4\times10^{13} cm^{-2}$ and a Hall mobility of ≈1300 cm^2/V-s at room temperature, and ≈3200 cm^2/V-s at 77K is formed over undoped GaN/AlN/Al_2O_3 template. Similar structure with an additional GaN(Fe) layer (charge compensated) sandwiched between unintentionally doped (UID) GaN and AlGaN layer shows sheet concentration of ≈1.2×10^{13} cm^{-2} and a Hall mobility of ≈1650 cm^2/V-s at room temperature and ≈5000 cm^2/V-s at 77K. Threading defects of edge, screw and mixed character are also seen in AlGaN/GaN heterostructure formed on GaN films grown over c-plane sapphire. Since isolated or organized screw dislocations as observed as columnar structures, nanopipes and inversion domains with density ~$10^{10} cm^{-2}$. And edge type dislocations appear as

isolated or organized in low-angle sub-grain boundaries, thus also result in columnar structures.

Formation on nanowalls and nanocolumns on c-plane sapphire

The formation of 1D and 2D nanostructures of GaN on Al_2O_3 substrates can circumvent the need for having dislocation free epitaxial films, due to strain relaxation, with the possibility of expelling defects over short distances[31]. The structures also provide a tunable handle due to electron and photon confinement, large surface area and control of surface defects[255]. There have been a few reports in literature on GaN nanorods formation, all of them involve lithography or surface preparation such as use of catalysts, buffer layers, etc[135]. This work demonstrates that epitaxial, aligned and single crystal GaN nanostructures can be formed spontaneously in certain growth conditions not only on silicon surfaces by PAMBE without use of any external catalyst but also on bare sapphire substrate[157-159,285]. Careful kinetically controlled growth studies on bare c-plane sapphire, have enabled us to modify surface diffusion and nitridation reactions to form an epitaxial hexagonal nanowall matrix and nanocolumns without catalyst or AlN buffer layers. We present here the results of the formation and characterization of GaN nanostructures in high nitrogen rich growth condition (N/Ga BEP ratio 100) and in a relatively low temperature growth regime (480-630°C). We observe the formation of dense GaN wedge-shaped hexagonal nanowall network and formation of films with a flat 2D morphology at higher temperatures (730-880°C), which transform into faceted mounds beyond 830°C. We observe the formation of GaN nanocolumns (150-200 nm diameters) amidst nanowall network at 680°C substrate temperature in a narrow growth parametric window. The nanostructures formed are observed to be self-assembled, c-oriented wurtzite films with high structural and optical quality. The nanowalls that form at ≈630℃ increase in height and thickness upto temperature 630℃ and then for temperature > 680℃ film transform into flat and compact layers by the thickening and merging of the nanowalls into each other, however comprising of a high density of dislocations that thread through the film thickness. The sharpness in the transition

temperature suggest the criticality of Ga diffusion and GaN formation at this temperature after which Ga desorption and GaN decomposition become dominant factors, influencing the growth morphology.

After identification of growth temperature for the formation of GaN nanocolumns at 680℃ in nitrogen rich condition we looked into the effect of variation in growth parameters (N_2 and Ga flux) at this growth temperature. A consolidated picture of a narrow parametric window by kinetic control to form nanostructures is identified by varying Ga flux ($2.86-4.84\times10^{14}cm^{-2}s^{-1}$), Nitrogen flow rate (2−8 sccm) and temperature (480−880°C), where a high density ($1\times10^{8}cm^{-2}$) 1-D nanocolumns of GaN is observed. The results clearly show the dominant role of kinetics in the nitrogen rich conditions that influence diffusion, supersaturation and reaction in determining epitaxial growth of nanostructures, which can be tuned to form crystalline and ordered nanowall network and nanocolumn assembly. The structure and optical properties of these nanostructures show that they are almost defect free with strong bandedge emission that also shows a size dependent blue-shift. This work is the first report of forming high density ($\sim10^{8}cm^{-2}$) of high quality c-oriented wurtzite GaN nanostructures on bare c-plane sapphire spontaneously. Thus, we demonstrate that by shear growth parametric kinetic control epitaxial nanostructure assemblies can be formed. This enables novel device formation with reduced process steps and enhanced performance for future applications.

Properties and mechanism of GaN nanowall and nanocolumns formation

After identifying parametric dependence on the formation of GaN nanocolumns we performed coverage dependent study in the substrate temperatures range 630−680℃ to understand the mechanism of nanostructure formation. After extensive study of the morphology, structural and optical properties[159] we infer a detailed mechanism that may be involved in the formation of oriented GaN nanocolumns and a hexagonal nanowall network on bare c-plane sapphire. The CL spectrum of nanocolumns is similar to that of the nanowall network, with a strong band edge emission at 363.1 nm (3.42 eV) and no defect related emission. The CL ratio of band edge to defect emission intensity for

nanocolumns is 80 which is nearly four times that of nanowall network, showing high optical quality. CL spectra also show that the band-edge transition energy blue shifts to 358.9 nm (3.46eV) for the thin nanowall network, and the FWHM of the CL peak for nanowall network is 43.6nm (348.70 meV). The nanowalls are wedge shaped being ≈150nm thick at the bottom and taper to <10nm on top. The blue shift and high intensity of emission can be attributed to the electron confinement effects at the apex of the walls. However, broadening in FWHM of the CL spectrum, may be related to misalignment of nanowalls, or due to the electron confinement in the varying width of the narrow region of the wedge-shaped nanowalls, which is also reflected as anisotropy in RHEED spot intensity along $[1\bar{1}00]$ direction. Raman spectrum of nanocolumns and nanowalls shows strong line E_2 (high) which is symmetry allowed in backscattering along the wurtzite c axis, and a weak symmetry forbidden A_1(TO), which is most likely seen due to right angle scattering occurring when the incident light enters the sidewalls of the nanocolumns. The narrow linewidth of the E_2 (high) phonon, for nanocolumns and nanowalls are ≈8 and ≈12 cm^{-1}, suggest high quality epitaxial GaN [208]. Raman spectra for nanocolumns and nanowalls have E_2 (high) peak at 568 cm^{-1} where line position at 566.2 cm^{-1} is expected for stress free GaN showing the reduced strain in these nanostructures.

The nanowall formation is identified to nucleate on edge dislocation as straight arms of tri-branches network, surrounding the advancing spiralling screw dislocation step driven by Frank mechanism as open screw dislocations. The formation of nanocolumns is driven by the size, shape and apex incline plane of the nanowalls surrounding the voids. The wedge shaped hexagonal nanowall network cease to grow when their inclined face attains r-plane $(\bar{1}102)$ configuration. This plane has a very low Ga adatom sticking coefficient compared to that of a-plane which forms the side walls of the nanostructures. Thus, the Ga adatoms are funnelled into the open void between the nanowall network causing supersaturation in the voids, resulting in the nucleation of the nanocolumns due to spiral growth on the screw dislocation. We observe that the number, density and type of nucleation sites govern the mechanism of nanocolumns formation. If the nucleation site is

a single screw dislocation step at 630℃ at a coverage ≈ 4μm and at 650℃ for a coverage of ≈1μm, rosette shaped nanocolumns are observed. At temperatures of 630℃ and 650℃, Frank mechanism dominates due to tightened spiralling screw steps propagating along [0001] direction in the pyramidal form. The study of axial and radial growth rate provides justification for dislocation driven growth of nanocolumns in our studies. If more than one nucleation sites are involved, with one or more screw steps and mixed or edge dislocations, then the formation of nanocolumns is driven by the Frank-Read source mechanism. We show various formation stages of Frank-Read growth at ≈1μm coverage at 680℃. At higher coverage of ≈4μm near hexagonal shaped nanocolumn formation. We provide visual, morphological evidence for the Frank-Read mill pinned by screw dislocation at the interface, as the basic mechanism underlying these low-dimensional structure formations. The dislocations are thus mitigated and result in defect free emission from these structures.

GaN nanorods on low index silicon substrates and nanowires on c-plane sapphire

After realizing the growth of GaN nanocolumns on bare c-plane sapphire, we looked into the effect of substrate type, surface modification etc on the formation of nanocolumns at N/Ga BEP ratio 100 on silicon substrate. Since in literature, various mechanisms for the formation of GaN nanowires on Si(111) substrate are proposed**,** but the mechanism of growth, structure and role of intermediate layer and orientation of GaN nanorods are still debated. We demonstrate spontaneous formation of ordered GaN 1-D nanostructures on Silicon (001) and (111) substrates and have shown that surface pre-modification of Si(111) by nitrogen plasma controls the nanostructure alignment. We have also addressed the crystallinity issue of SiN intermediate layer formed during growth of GaN nanowire on silicon substrates. Various groups attribute silicon surface roughening as pits, mounds and islands as nucleation centres for non-epitaxial nanorods formation. However, with careful experiments, we propose that tilt in GaN nanorods grown on bare Si(001)-2×1 and Si(111)-7×7 may depend on alignment of the SiN

nanocrystal seed formed at the interface, since the nanorods prefer to grow on (0001) c-plane which has a higher sticking coefficient. Flat SiN interface that is single crystalline results in aligned GaN nanorods on silicon substrates by the Frank mechanism at interfacial screw dislocations. GaN nanorod growth on bare Si(111), Si(001) and amorphous silicon nitride intermediate layer yield non-aligned, c-oriented 1D structures. The crystalline Si_3N_4 template formed on Si(111) by nitridation, leads to highly dense hexagonal shaped wurtzite nanorods that are well-aligned (c-oriented) with $\approx 20^o$ rotation with the superstructural organization. Resulting GaN nanorods show high quality single-crystalline phase and optical emission properties. After forming dislocation mediated nanostructures of GaN we attempt to form dislocation-free GaN nanowires. We initially grow the defect free nanowall network at high temperature ($\approx$ 630℃) and form a low temperature high crystalline quality GaN film ($\approx$ 400℃) that laterally overgrown on top of it. These temperatures are very low in comparison to the reported growth temperature ($\approx$ 730℃) for high quality 2D GaN film. This over layer is seen to become polycrystalline with no influence of threading dislocations that have terminated in the nanowalls. Annealing this system results in the formation of high density of very fine ($\approx$10nm) single crystal GaN c-oriented nanowires, which are defect free. We attribute this to a de-wetting phenomenon of the polycrystalline GaN overlayer to result in this high quality oriented nanowire formation.

Highlights:

We list here some significant results that have been obtained for the first time, in this thesis dissertation:

- Un-doped 2D-GaN films of TDs ~10^8 cm^{-2} are grown at substrate temperature 780℃ at N/Ga BEP ratio = 1, n and p type doping of GaN film with carrier concentrations of 2.72×10^{17} cm^{-3} and 1.04×10^{19} cm^{-3} is achieved comparable to the best in literature where the values are ~10^{17} and ~10^{20} cm^{-3}, respectively.

- High electron mobility transistor (HEMT) structure with high room temperature mobility of ≈1500 cm^{-2}/Vs and at 77K ≈5000 cm^{-2}/Vs is formed (values achieved in literature are ≈1700 cm^{-2}/Vs and at 77K ≈6000 cm^{-2}/Vs).

- Growth diagram for GaN nanocolumn, nanowalls, 2D film on bare c-plane sapphire without use of pre-treatment, buffer layer, catalyst is presented. Shown that a narrow growth parametric window is required for the spontaneous nanocolumn formation, without the use of buffer layer, surface treatment or catalysts.

- We propose that the nanowall formation on bare c-plane sapphire takes place via accumulation of Ga and N adatoms on edge dislocations which are along the periphery of open screw dislocations. The nanowalls formed are defect free crystals with high structural and optical quality, and large surface area.

- We propose a Frank-type mechanism for the formation of nanocolumns to be via open and closed screw dislocation mediated spiral growth. For dislocations pinned in proximity, we provide direct morphological evidence Frank Read Mill induced nanocolumnar growth for the first time.

- We demonstrate that amorphous and crystalline SiN layer formed as template, results in mis-aligned and aligned (and self assembled) GaN nanocolumns on Si(111) respectively. Nanotubes of GaN on Si(001) are observed to be formed on silicon without pre-nitridation.

- Using the defect free nanowall network as template, very high quality single crystal c-oriented GaN nanowires (<10nm) are formed by a novel de-wetting process.

Future Directions:

To control the aspect ratio, orientation and crystalline quality of nanocolumns, it is essential to develop and elaborate understanding the aspect of their nucleation and

growth. As a follow up, detailed study by RHEED can provide more valuable information on nucleation mechanisms. In order to deepen the understanding on self-induce nanocolumns and nanowalls formation on c-plane sapphire, investigation of the nucleation dependence of growth parameters can be the next step. Similarly, nucleation of self induced growth of GaN nanowires on (m-, c-, r- plane) sapphire and low and high index surfaces of silicon can be studied by RHEED, STM, XPS, HRTEM to identify the exact nature of the intermediate Si_xN_y layer. The morphology of this intermediate layer should be compared to the diameter, orientation and location of NWs forming on the intermediate layer. In present work, the optical properties of the nanocolumns and nanowalls have been investigated on ensembles. The broadening of the band-edge CL peaks put restrictions on the exact identification of the transitions in proximity to ≈ 3.42 eV characteristic to bulk GaN. Since there could be contribution from individual nanocolumns or nanowalls, this impediment could be overcome by the direct comparison of crystal defects with the optical properties by CL mapping, PL and HRTEM characterization of single nanowalls and nanocolumns, and compare with similar studies performed on InP and ZnO to bring the deep understanding on the radiative recombination's related to structural defects.

It is important for future experiments to un-reveal the mechanisms involved at the atomistic level, to evaluate the veracity of the proposals made in this thesis. Detailed surface science experiments using STM and photoemission, in the sub-monolayer regime complemented with density functional theory (DFT) and Monte Carlo calculations, are necessary to find the underlying mechanisms at initial stages of growth accurately. More interface studies using high resolution TEM are essential to look at lattice and domain matching schemes that govern the morphology dependence on growth conditions, in these systems. The defect properties of the nanowall network, nanocolumns and nanowires formed in these experiments also need to be probed in detail, to elucidate electron confinements, facet formation and self-assembly effects in electron and light emission. Spatially resolved Cathodoluminescence and field emission of these low dimensional structures can be very important in evaluating novel phenomena and applications, since

the dimensions of the nanostructures are smaller than the wavelength of the band-edge emission.

The investigations that have been carried out in this work provide only a modest part of the knowledge necessary to integrate NWs in functional devices. Therefore, extension of the above studies to the whole III-Nitride family as well as to the doping processes, are required to move toward photovoltaic applications covering the whole UV-IR range. The smooth sidewalls and systematic growth mode, under selective epitaxy processes, offer unique architecture for devices made from this technologically important material. Future systematic detailed study is expected to produce greater variety in heterostructures, parallel fabrication of large ensembles for device applications, and greater ability to measure key optical and electrical properties. To exploit these structures for futuristic devices, n and p- doping of these nanostructure systems and alloying with In for band-gap engineering can be an immediate follow-up. After optimizing parameters to accomplish these, simple devices such as HEMT, LED, Laser diodes and photovoltaic structures should be made from these structures. The strain and defect free nature of these systems and simplicity of processing is expected to provide a unique architecture for future devices that may show enhanced electrical and optical performance.

References

1. R. N. Hall, G. E. Fenner, J. D. Kingsley, T. J. Soltys, and R. O. Carlson, Physical Review Letters 9, 366 (1962).
2. J. N. Holonyak and S. F. Bevacqua, Applied Physics Letters 1, 82 (1962).
3. Schubert, E. F, Light Emitting Diodes, second edition (Cambridge University Press, Cambridge 2006).
4. J. I. Pankove, E. A. Miller, and J. E. Berkeyheiser, Journal of Luminescence 6, 54 (1973).
5. J. I. Pankove, E. A. Miller, and J. E. Berkeyheiser, Journal of Luminescence 5, 84 (1972).
6. H. Amano, N. Sawaki, I. Akasaki, and Y. Toyoda, Applied Physics Letters 48, 353 (1986).
7. H. Amano, I. Akasaki, T. Kozawa, K. Hiramatsu, N. Sawaki, K. Ikeda, and Y. Ishii, Journal of Luminescence 40–41, 121 (1988).
8. S. Nakamura and G. Fasol. The blue laser diode. Springer-Verlag`, Berlin Heidelberg`, New York`, 1997.
9. M. R. Krames, O. B. Shchekin, R. Mueller-Mach, G. O. Mueller, Z. Ling, G. Harbers, and M. G. Craford, Display Technology, Journal of 3, 160 (2007).
10. Y. B. Kwon, J. H. Je, P. Ruterana, and G. Nouet, Journal of Vacuum Science & Technology A: Vacuum, Surfaces, and Films 23, 1588 (2005).
11. M. A. Moram, C. S. Ghedia, D. V. S. Rao, J. S. Barnard, Y. Zhang, M. J. Kappers, and C. J. Humphreys, Journal of Applied Physics 106, 073513 (2009).
12. V. Narayanan, K. Lorenz, W. Kin, S. Mahajan, Appl. Phys. Lett. 78, 1544 (2001).
13. L. Liu and J. H. Edgar, Mater. Sci. Eng. 274, 1 (2002).
14. V. Lebedev, Journal of Applied Physics 108, 013515 (2010).
15. K. Barghout and J. Chaudhuri, Journal of Materials Science 39, 5817 (2004).
16. M. A. Moram and M. E. Vickers, Reports on Progress in Physics 72, 036502 (2009).
17. J. Kang and T. Ogawa, Applied Physics Letters 71, 2304 (1997).
18. C. J. Humphreys, Solid-State Lighting, MRS Bulletin 33, 459 (2008).
19. W. A. Brantley, O. G. Lorimor, P. D. Dapkus, S. E. Haszko, and R. H. Saul, Journal of Applied Physics 46, 2629 (1975).
20. F. Koyama, S. Kinoshita, and K. Iga, Applied Physics Letters 55, 221 (1989).
21. P. Bhattacharya, W. Guo, M. Zhang, J. Heo, A. Das, and M. Jankowski, Winter Topicals (WTM), 2011 IEEE, 23 (2011).

22. W. Guo, A. Banerjee, P. Bhattacharya, and B. S. Ooi, Applied Physics Letters 98, 193102 (2011).
23. W. Guo, M. Zhang, A. Banerjee, and P. Bhattacharya, Nano Letters 10, 3355 (2010).
24. F. Limbach, T.Gotschke, T.Stoica, R.Calarco, E. Sutter, J.Ciston, R. Cusco, L. Artus, S. Kremling, S. Hofling, L. Worschech, D. Grutzmacher, Journal of Applied Physics 109, 014309 (2011).
25. M.L. Kuo, Y.S. Kim, M.L. Hsieh, and S.Y. Lin, Nano Letters 11, 476 (2010).
26. H. P. T. Nguyen, S. Zhang, K. Cui, X. Han, and Z. Mi, Lasers and Electro-Optics (CLEO), 1, 2011.
27. N. Nepal, P. Frajtag, J. M. Zavada, N. A. El-Masry, and S. M. Bedair, physica status solidi (c) 8, 2354 (2011).
28. D. A. B. Miller, D. S. Chemla, T. C. Damen, A. C. Gossard, W. Wiegmann, T. H. Wood, and C. A. Burrus, Physical Review Letters 53, 2173 (1984).
29. S. F. Chichibu, A. Uedono, T. Onuma, B. A. Haskell, A. Chakraborty, T. Koyama, P. T. Fini, S. Keller, S. P. DenBaars, J. S. Speck, U. K. Mishra, S. Nakamura, S. Yamaguchi, S. Kamiyama, H. Amano, I. Akasaki, J. Han, and T. Sota, Nat Mater 5, 810 (2006).
30. A. Cantarero, A. Cros, N. Garro, M. I. Gómez-Gómez, A. García, M. M. de Lima, B. Daudin, A. Rizzi, C. Denker, and J. Malindretos, Annalen der Physik 523, 51 (2011).
31. K. A. Bertness, N. A. Sanford, and A. V. Davydov, Selected Topics in Quantum Electronics, IEEE Journal of 17, 847 (2011).
32. W. Guo, M. Zhang, P. Bhattacharya, and J. Heo, Nano Letters 11, 1434 (2011).
33. H. Sekiguchi, K. Kishino, and A. Kikuchi, Electron. Lett. 44, 151 (2008).
34. P.Kidd, J. Mater. Sci. Mater. Electron. 14, 541 (2003).
35. N. C. Gerhardt, M. Y. Li, H. Jahme, H. Hopfner, T. Ackemann, and M. R. Hofmann, Applied Physics Letters 99, 151107 (2011).
36. H. Sekiguchi, K. Kishino, and A. Kikuchi, Appl. Phys. Express 1, 124002 (2008).
37. E. F. Schubert, Y. H. Wang, A. Y. Cho, L. W. Tu, and G. J. Zydzik, Applied Physics Letters 60, 921 (1992).
38. P. A. Porta, M. Harries, and H. D. Summers, Applied Physics Letters 89, 121120 (2006).
39. C. Weisbuch, M. Nishioka, A. Ishikawa, and Y. Arakawa, Physical Review Letters 69, 3314 (1992).
40. A. Kavokin and B. Gil, Applied Physics Letters 72, 2880 (1998).

41. T. Tawara, H. Gotoh, T. Akasaka, N. Kobayashi, and T. Saitoh, Physical Review Letters 92, 256402 (2004).
42. A. K. Panda, D. Pavlidis, and E. Alekseev, Electron Devices, IEEE Transactions on 48, 820 (2001).
43. Y. Ando, Y. Okamoto, H. Miyamoto, T. Nakayama, T. Inoue, and M. Kuzuhara, Electron Device Letters, IEEE 24, 289 (2003).
44. M. A. Huque, S. A. Eliza, T. Rahman, H. F. Huq, and S. K. Islam, Solid-State Electronics 53, 341 (2009).
45. Rashmi, A. Kranti, S. Haldar, M. Gupta, and R. S. Gupta, Microwave Theory and Techniques, IEEE Transactions on 51, 607 (2003).
46. T. Palacios, A. Chakraborty, S. Rajan, C. Poblenz, S. Keller, S. P. DenBaars, J. S. Speck, and U. K. Mishra, Electron Device Letters, IEEE 26, 781 (2005).
47. J. A. Venables, G. D. T. Spiller, and M. Hanbucken, Reports on Progress in Physics 47, 399 (1984).
48. H Lüth. Solid Surfaces, Interfaces and Thin Films. Advanced Texts in Physics. Springer Verlag, 2001.
49. J. Tersoff and F. K. LeGoues, Physical Review Letters 72, 3570 (1994).
50. R. L. Schwoebel, Journal of Applied Physics 38, 1759 (1967).
51. J. Villain, J. Phys. I France 1, 19 (1991).
52. K.Oura, V.G. Lifshits, A.V. Saranin, A.A. Zotov, and M. Katayama. Surface Science: An Introduction, Advanced Texts in Physics, Springer-Verlag, 2003.
53. T. Zywietz, J. Neugebauer, and M. Scheffler, Applied Physics Letters 73, 487 (1998).
54. M. A. Sánchez-García, J. L. Pau, F. Naranjo, A. Jiménez, S. Fernández, J. Ristic, F. Calle, E. Calleja, and E. Muñoz, Materials Science and Engineering B 93, 189 (2002).
55. O. Zsebök, J. V. Thordson, Q. X. Zhao, and T. G. Andersson, Applied Surface Science 166, 423 (2000).
56. E. J. Tarsa, B. Heying, X. H. Wu, P. Fini, S. P. DenBaars, and J. S. Speck, Journal of Applied Physics 82, 5472 (1997).
57. J. A. Stroscio, and D. M. Eigler, Science 254, 1319 (1991).
58. R. X. Yan, D. Gargas, and P. D. Yang, Nat. Photonics 3, 569 (2009).
59. A. I. Hochbaum and P. D. Yang, Chem. Rev. 110, 527 (2010).
60. W. Lu and C. M. Lieber, Nat. Mater. 6, 841 (2007).

61. W. Kim, J. K. Ng, M. E. Kunitake, B. R. Conklin, and P. D. Yang, J. Am. Chem. Soc. 129, 7228 (2007).
62. R. S. Wagner and W. C. Ellis, Applied Physics Letters 4, 89 (1964).
63. R. S.Wagner, A.P.Levitt (Ed.), Whisker Technology(1970), p.47
64. R. Wagner and W. Ellis, Appl. Phys. Lett. 4, 89 (1964).
65. M. Yazawa, M. Koguchi, A. Muto, and K. Hiruma, Adv. Mater. 5, 577 (1993).
66. M. Yazawa, M. Koguchi, A. Muto, M. Ozawa, and K. Hiruma, Appl. Phys. Lett. 61, 2051 (1992).
67. K. Haraguchi, T. Katsuyama, and K. Hiruma, J. Appl. Phys. 75, 4220 (1994).
68. T. J. Trentler, K. M. Hickman, S. C. Goel, A. M. Viano, P. C. Gibbons, and W. E. Buhro, Science 270, 1791 (1995).
69. H. J. Dai, E. W. Wong, Y. Z. Lu, S. S. Fan, and C. M. Lieber, Nature 375, 769 (1995).
70. P. D. Yang and C. M. Lieber, Science 273, 1836 (1996).
71. Y. Cui and C. M. Lieber, Science 291, 851 (2001).
72. K. A. Dick, Progress in Crystal Growth and Characterization of Materials 54, 138 (2008).
73. A. I. Persson, M. W. Larsson, S. Stenstrom, B. J. Ohlsson, L. Samuelson, and L. R. Wallenberg, Nat Mater 3, 677 (2004).
74. Y. Xia, P. Yang, Y. Sun, Y. Wu, B. Mayers, B. Gates, Y. Yin, F. Kim, and H. Yan, Advanced Materials 15, 353 (2003).
75. S. N. Mohammad, The Journal of Chemical Physics 125, 094705 (2006).
76. A. I. Hochbaum, R. K. Chen, R. D. Delgado, W. J. Liang, E. C. Garnett, M. Najarian, A. Majumdar, and P. D. Yang, Nature 451, 163 (2008).
77. A. I. Boukai, Y. Bunimovich, J. Tahir-Kheli, J. K. Yu, W. A. Goddard, and J. R. Heath, Nature 451, 168 (2008).
78. B. Z. Tian, X. L. Zheng, T. J. Kempa, Y. Fang, N. F. Yu, G. H. Yu, J. L. Huang, and C. M. Lieber, Nature 449, 885 (2007).
79. E. Garnett and P. Yang, Nano Letters 10, 1082 (2010).
80. G. F. Zheng, F. Patolsky, Y. Cui, W. U. Wang, and C. M. Lieber, Nat. Biotechnol. 23, 1294 (2005).
81. J. Johnson, H. Choi, P. Yang, and R. Saykally, Nat. Mater. 1, 106 (2002).
82. E. Stern, J. F. Klemic, D. A. Routenberg, P. N. Wyrembak, D. B. Turner-Evans, A. D. Hamilton, D. A. LaVan, T. M. Fahmy, and M. A. Reed, Nature 445, 519 (2007).

83. M.T. Hill, Y. S. Oei, B. Smalbrugge, Y. Zhu, T. De Vries, P. J. Van Veldhoven, F. W. M. Van Otten, T. J. Eijkemans, J. P. Turkiewicz, H. De Waardt, E. J. Geluk, S. H. Kwon, Y. H. Lee, R. Notzel, and M. K. Smit, Nat. Photonics 1, 589 (2007).
84. F. A. Ponce and D. P. Bour, Nature, 386, 352 (1997).
85. X. F. Duan, Y. Huang, Y. Cui, J. F. Wang, and C. M. Lieber, Nature 409, 66 (2001).
86. Y. Huang, X. F. Duan, and C. M. Lieber, Small 1, 142 (2005).
87. E. D. Minot, F. Kelkensberg, M. van Kouwen, J. A. van Dam, L. P. Kouwenhoven, V. Zwiller, M. T. Borgstrom, O. Wunnicke, M. A. Verheijen, and E. P. A. M. Bakkers, Nano Lett. 7, 367 (2007).
88. F. Qian, Y. Li, S. Gradecak, D. Wang, C. J. Barrelet, and C. M. Lieber, Nano Lett. 4, 1975 (2004).
89. T. Mukai, IEEE J. Sel. Top. Quantum Electron. 8, 264 (2002).
90. B. A. Korgel, En*cyclopedia of Inorganic Chemistry (*John Wiley & Sons, Ltd, 2006).
91. M. Law, L. E. Greene, A. Radenovic, T. Kuykendall, J. Liphardt, and P. D. Yang, J. Phys. Chem. B 110, 22652 (2006).
92. B. Tian, X. Zheng, T. J. Kempa, Y. Fang, N. Yu, G. Yu, J. Huang, and C. M. Lieber, Nature 449, 885 (2007).
93. M. A. Green, Physica E 14, 65 (2002).
94. J. Johansson, B. A. Wacaser, K. A. Dick, and W. Seifert, Nanotechnology 17, S355 (2006).
95. B. A. Wacaser, K. A. Dick, J. Johansson, M. T. Borgström, K. Deppert, and L. Samuelson, Adv. Mater. 21, 153 (2009).
96. A. I. Persson, M. W. Larsson, S. Stenström, B. J. Ohlsson, L. Samuelson, and L. R. Wallenberg, Nat. Mater. 3, 677 (2004).
97. K. A. Dick, K. Deppert, M. W. Larsson, T. Martensson, W. Seifert, L. R. Wallenberg, and L. Samuelson, Nat. Mater. 3, 380 (2004).
98. S. Kodambaka, J. Tersoff, M. C. Reuter, and F. M. Ross, Science 316, 729 (2007).
99. E. Givargizov, J. Cryst. Growth 31, 20 (1975).
100. L.Schubert, P. Werner, N. D. Zakharov, G. Gerth, F. M. Kolb, L. Long, U. Gosele, and T. Y. Tan, Applied Physics Letters 84, 4968 (2004).
101. S. Kodambaka, J. Tersoff, M. C. Reuter, and F. M. Ross, Phys. Rev. Lett. 96, 096105 (2006).

102. G. A. Bootsma and H. J. Gassen, Journal of Crystal Growth 10, 223 (1971).
103. T. Martensson, C. P. T. Svensson, B. A. Wacaser, M. W. Larsson, W. Seifert, K. Deppert, A. Gustafsson, L. R. Wallenberg, and L. Samuelson, Nano Lett. 4, 1987 (2004).
104. M. T. Bjork, C. Thelander, A. E. Hansen, L. E. Jensen, M. W. Larsson, L. R. Wallenberg, and L. Samuelson, Nano Lett. 4, 1621 (2004).
105. J. E. Allen, E. R. Hemesath, D. E. Perea, J. L. Lensch-Falk, Z. Y. Li, F. Yin, M. H. Gass, P. Wang, A. L. Bleloch, R. E. Palmer, and L. J. Lauhon, Nat. Nanotechnol. 3, 168 (2008).
106. S. H. Oh, K. v. Benthem, S. I. Molina, A. Y. Borisevich, W. Luo, P. Werner, N. D. Zakharov, D. Kumar, S. T. Pantelides, and S. J. Pennycook, Nano Letters 8, 1016 (2008).
107. M. C. Putnam, M. A. Filler, B. M. Kayes, M. D. Kelzenberg, Y. Guan, N. S. Lewis, J. M. Eiler, and H. A. Atwater, Nano Letters 8, 3109 (2008).
108. M. Volmer and L. Estermann. Phys., 7, 13 (1921).
109. G. W. Sears. Acta Metallurgica, 1, 457 (1953).
110. W. K. Burton, N. Cabrera, and F. C. Frank, Philosophical Transactions of the Royal Society of London. Series A, Mathematical and Physical Sciences 243, 299 (1951).
111. G. W Sears. Acta Metallurgica`, 3`, 367 (1955).
112. M. J. Bierman, Y. K. A. Lau, A. V. Kvit, A. L. Schmitt, and S. Jin, Science 320, 1060 (2008).
113. D. Cherns, L. Meshi, I. Griffiths, S. Khongphetsak, S. V. Novikov, N. R. S. Farley, R. P. Campion, and C. T. Foxon, Applied Physics Letters 93, 111911 (2008).
114. J. M. Blakely and K. A. Jackson. J. Chem. Phys., 37, 428 (1962).
115. E. I. Givargizov. J. Cryst. Growth, 20, 217 (1973).
116. R. K. Debnath, R. Meijers, T. Richter, T. Stoica, R. Calarco, and H. Luth, Applied Physics Letters 90, 123117 (2007).
117. J. Johansson, L. S. Karlsson, C. Patrik T. Svensson, T. Martensson, B. A. Wacaser, K. Deppert, L. Samuelson, and W. Seifert, Nat Mater 5, 574 (2006).
118. V. G. Dubrovskii, N. V. Sibirev, G. E. Cirlin, I. P. Soshnikov, W. H. Chen, R. Larde, E. Cadel, P. Pareige, T. Xu, B. Grandidier, J. P. Nys, D. Stievenard, M. Moewe, L. C. Chuang, and C. Chang-Hasnain, Physical Review B 79, 205316 (2009).
119. V. G. Dubrovskii, N. V. Sibirev, G. E. Cirlin, J. C. Harmand, and V. M. Ustinov. Phys. Rev. E, 73, 021603 (2006).
120. R. L. Schwoebel. J. Appl. Phys., 38,1759 (1967).

121. J. Johansson, C. P. T. Svensson, T. Mårtensson, L. Samuelson, and W. Seifert, The Journal of Physical Chemistry B 109, 13567 (2005).
122. L. Geelhaar, C. Cheze, W. M. Weber, R. Averbeck, H. Riechert, T. Kehagias, P. Komninou, G. P. Dimitrakopulos, and T. Karakostas, Applied Physics Letters 91, 093113 (2007).
123. R. Songmuang, O. Landre, and B. Daudin, Applied Physics Letters 91, 251902 (2007).
124. C. Colombo, D. Spirkoska, M. Frimmer, G. Abstreiter, and A. Fontcuberta i Morral, Physical Review B 77, 155326 (2008).
125. J. Ristic, E. Calleja, S. Fernández-Garrido, L. Cerutti, A. Trampert, U. Jahn, and K. H. Ploog, Journal of Crystal Growth 310, 4035 (2008).
126. S. Guha, N. A. Bojarczuk, and D. W. Kisker, Applied Physics Letters 69, 2879 (1996).
127. H. D. Park, S. M. Prokes, M. E. Twigg, R. C. Cammarata, and A. C. Gaillot, Appl. Phys. Lett. 89, 223125 (2006).
128. H. D. Park and S. M. Prokes, Applied Physics Letters 90, 203104 (2007).
129. S. Guha, N. A. Bojarczuk, M. A. L. Johnson, and J. F. Schetzina, Applied Physics Letters 75, 463 (1999).
130. E. Calleja, M. Sánchez-Garcia, F. Sánchez, F. Calle, F. Naranjo, E. Muñoz, U. Jahn, and K. Ploog, Phys. Rev. B 62, 16826 (2000).
131. H. W. Seo, Q. Y. Chen, L. W. Tu, C. L. Hsiao, M. N. Iliev, and W. K. Chu, Physical Review B 71, 235314 (2005).
132. C. L. Hsiao, L. W. Tu, T. W. Chi, H. W. Seo, Q. Y. Chen, and W. K. Chu, J. Vac. Sci. Technol., B 24, 845 (2006).
133. E. A. Stach, P. J. Pauzauskie, T. Kuykendall, J. Goldberger, R. He, and P. Yang, Nano Letters 3, 867 (2003).
134. K. A. Bertness, A. Roshko, L. M. Mansfield, T. E. Harvey, and N. A. Sanford, Journal of Crystal Growth 310, 3154 (2008).
135. E. Calleja, J. Ristić, S. Fernández-Garrido, L. Cerutti, M. A. Sánchez-García, J. Grandal, A. Trampert, U. Jahn, G. Sánchez, A. Griol, and B. Sánchez, physica status solidi (b) 244, 2816 (2007).
136. T. Stoica, E. Sutter, R. J. Meijers, R. K. Debnath, R. Calarco, H. Luth, and D. Grutzmacher, Small 4, 751 (2008).

137. M. Tchernycheva, C. Sartel, G. Cirlin, L. Travers, G. Patriarche, J. Harmand, L. S. Dang, J. Renard, B. Gayral, L. Nevou, and F. Julien, Nanotechnology 18, 385306 (2007).
138. R. Meijers, T. Richter, R. Calarco, T. Stoica, H. P. Bochem, M. Marso, and H. Lüth, Journal of Crystal Growth 289, 381 (2006).
139. F. Furtmayr, M. Vielemeyer, M. Stutzmann, J. Arbiol, S. Estrade, F. Peiro, J. R. Morante, and M. Eickhoff, J. Appl. Phys. 104, 034309 (2008).
140. M. Yoshizawa, A. Kikuchi, M. Mori, N. Fujita, and K. Kishino. Jpn. J. Appl. Phys., 36, L459 (1997).
141. J. Ristić, E. Calleja, S. Fernández-Garrido, L. Cerutti, A. Trampert, U. Jahn, and K. H. Ploog, Journal of Crystal Growth 310, 4035 (2008).
142. R. Calarco, R. J. Meijers, R. K. Debnath, T. Stoica, E. Sutter, and H. Luth, Nano Lett. 7, 2248 (2007).
143. K. A. Bertness, A. Roshko, N. A. Sanford, J. M. Barker, and A. V. Davydov, Journal of Crystal Growth 287, 522 (2006).
144. R. Calarco, M. Marso, T. Richter, A. I. Aykanat, R. Meijers, A. V. D. Hart, T. Stoica, and H. Luth, Nano Letters 5, 981 (2005).
145. L. Lari, R. T. Murray, T. J. Bullough, P. R. Chalker, M. Gass, C. Chèze, L. Geelhaar, and H. Riechert, Physica E 40, 2457 (2008).
146. C. Chèze, L. Geelhaar, O. Brandt, W. Weber, H. Riechert, S. Münch, R. Rothemund, S. Reitzenstein, A. Forchel, T. Kehagias, P. Komninou, G. Dimitrakopulos, and T. Karakostas, Nano Research 3, 528 (2010).
147. L. Lymperakis and J. Neugebauer, Physical Review B 79, 241308 (2009).
148. C. T. Foxon, S. V. Novikov, J. L. Hall, R. P. Campion, D. Cherns, I. Griffiths, and S. Khongphetsak, Journal of Crystal Growth 311, 3423 (2009).
149. T. Stoica and R. Calarco, IEEE Journal of Selected Topics in Quantum Electronics 17, 859 (2011).
150. B. Andres de Luna, T. Maria, J. Gwenole, R. Lorenzo, J. François Henri, C. Shu-Ting, L. Yuan-Ting, T. Po-Han, and T. Li-Wei, Nanotechnology 21, 315201 (2010).
151. P. Deb, H. Kim, Y. Qin, R. Lahiji, M. Oliver, R. Reifenberger, and T. Sands, Nano Letters 6, 2893 (2006).
152. P. J. Pauzauskie, D. J. Sirbuly, and P. Yang, Phys. Rev. Lett. 96, 143903 (2006).

153. M. H. Huang, S. Mao, H. Feick, H. Yan, Y. Wu, H. Kind, E. Weber, R. Russo, and P. Yang, Science 292, 1897 (2001).
154. P. T. Blanchard, K. A. Bertness, T. E. Harvey, A. W. Sanders, N. A. Sanford, S. M. George, and D. Seghete, IEEE Transactions on Nanotechnology, PP, 1 (2011).
155. L. Myongjai, C. Jen-Hau, Y. C. Lee, D. Seghete, S. M. George, J. B. Schlager, K. Bertness, and N. A. Sanford, Electronics Componensts and Technology Conference (ECTC), 843, 2009.
156. M. Kesaria and S. M. Shivaprasad, Applied Physics Letters 99, 143105 (2011).
157. M. Kesaria, S. Shetty, and S. M. Shivaprasad, Journal of Crystal Growth 326, 191 (2011).
158. M. Kesaria, S. Shetty, P. I. Cohen, and S. M. Shivaprasad, Materials Research Bulletin 46, 1811 (2011).
159. M. Kesaria, S. Shetty, and S. M. Shivaprasad, Crystal Growth & Design 11, 4900 (2011).
160. A. John R, Surface Science 500, 189 (2002).
161. J. Heffernan, M. Kauer, S. E. Hooper, V. Bousquet, and K. Johnson, physica status solidi (a) 201, 2668 (2004).
162. M.A. Herman and H. Sitter. Molecular beam epitaxy- Fundamentals and current status,volume 24 of Crystal Research and Technology. Springer-Verlag Berlin-Heidelberg,1989.
163. J. Osaka, M. S. Kumar, H. Toyoda, T. Ishijima, H. Sugai, and T. Mizutani, Applied Physics Letters 90, 172114 (2007).
164. T. Araki, Y. Chiba, M. Nobata, Y. Nishioka, and Y. Nanishi, Journal of Crystal Growth 209, 368 (2000).
165. T. Kikuchi, A. S. Somintac, O. Ariyada, M. Wada, and T. Ohachi, Journal of Crystal Growth 292, 221 (2006).
166. E. Iliopoulos, A. Adikimenakis, E. Dimakis, K. Tsagaraki, G. Konstantinidis, and A. Georgakilas, Journal of Crystal Growth 278, 426 (2005).
167. A. Ichimiya and P. I. Cohen, "Reflection High-Energy Electron Diffraction", Cambridge University Press, 2004.
168. A. Y. Cho, Journal of Applied Physics 42, 2074 (1971).

169. H.Y. Chen, H.W. Lin, C.-H. Shen, and S. Gwo, Applied Physics Letters 89, 243105 (2006).
170. B.D. Cullity and S.R. Stock Elements of X-Ray Diffraction 3rd edn (Englewood Cliffs, NJ: Prentice-Hall) 2001.
171. U. Pietsch, V. Holy and Baumbach High Resolution X-Ray Scattering From Thin Films and Multilayers 2nd edn (New York: Springer) 2004.
172. Birkholz M`, Fewster P F and Genzel C, Thin Film Analysis by X-Ray Scattering (Weinheim: Wiley-VCH) 2006.
173. D. K. Bowen and B. K. Tanner High Resolution X-Ray Diffractometry and Topography (London: Taylor and Francis) 1998.
174. P. F. Fewster, X-Ray Scattering from Semiconductors 2nd edn (London: Imperial College Press) 2003.
175. P. Y. Yu and M. Cardona, Fundamentals of Semiconductor, Physics and Material Properties, Springer, Germany`, Ed. 3, 345-369, 2005.
176. E. F. Schubert, Light-Emitting Diodes, Cambridge University Press, Cambridge, UK`, Ed. 2, 2006.
177. J. Jimenez, Microprobe Characterizations of Optoelectronic Materials, Taylor and Francis Books, Inc., 2003.
178. B. G. Yacobi and D. B. Holt, Cathodoluminescence Microscopy of Inorganic Solids (Plenum`, New York`, 1990).
179. C. V. Raman. Indian Journal of Physics, 2, 387 (1928)
180. C. V. Raman. Nature, 121, 619 (1928).
181. L. van der Pauw, Philips Technical Review, 20, 220(1958); Philips Research Reports, 13, 1(1958).
182. B. Heying, E. J. Tarsa, C. R. Elsass, P. Fini, S. P. DenBaars, and J. S. Speck, Journal of Applied Physics 85, 6470 (1999).
183. G. Koblmueller, R. Averbeck, L. Geelhaar, H. Riechert, W. Hosler, and P. Pongratz, Journal of Applied Physics 93, 9591 (2003).
184. B. Heying, R. Averbeck, L. F. Chen, E. Haus, H. Riechert, and J. S. Speck, Journal of Applied Physics 88, 1855 (2000).
185. S. Strite and H. Morkoç, J. Vac. Sci. Technol. 10, 1237 (1992).
186. T. Nishida, N. Kobayashi, and T. Ban, Applied Physics Letters 82, 1 (2003).

187. J. R. Shealy, V. Kaper, V. Tilak, T. Prunty, J. A. Smart, B. Green, and L. F. Eastman, Journal of Physics: Condensed Matter 14, 3499 (2002).
188. H. P. Maruska and J. J. Tietjen, Applied Physics Letters 15, 327 (1969).
189. L. Romano, B. Krusor, R. Singh, and T. Moustakas, Journal of Electronic Materials 26, 285 (1997).
190. E. Calleja, M. A. Sánchez-García, F. Calle, F. B. Naranjo, E. Muñoz, U. Jahn, K. Ploog, J. Sánchez, J. M. Calleja, K. Saarinen, and P. Hautojärvi, Materials Science and Engineering B 82, 2 (2001).
191. S. Nakamura, Japan. J. Appl. Phys. 30, 1620 (1991).
192. L. T. Romano, M. Kneissl, J. E. Northrup, C. G. Van de Walle, and D. W. Treat, Applied Physics Letters 79, 2734 (2001).
193. M. Zhang, P. Bhattacharya, W. Guo, and A. Banerjee, Applied Physics Letters 96, 132103 (2010).
194. W. Qian, M. Skowronski, M. De Graef, K. Doverspike, L. B. Rowland, and D. K. Gaskill, Applied Physics Letters 66, 1252 (1995).
195. M. Yoshizawa, A. Kikuchi, M. Mori, N. Fujita, and K. Kishino, Japanese Journal of Applied Physics, Part 2: Letters 36, L459 (1997).
196. E. Calleja, M. Sanchez-Garcia, F. Sanchez, F. Calle, F. Naranjo, E. Munoz, S. Molina, A. Sanchez, F. Pacheco, and R. Garcia, J. Cryst. Growth 201, 296 (1999).
197. S. Fernandez-Garrido, J. Grandal, E. Calleja, M. A. Sanchez-Garcia, and D. Lopez-Romero, Journal of Applied Physics 106, 126102 (2009).
198. K. A. Bertness, A. Roshko, N. A. Sanford, J. M. Barker, and A. Davydov, J. Cryst. Growth 287, 522 (2006).
199. K. A. Bertness, A. Roshko, L. M. Mansfield, T. E. Harvey, and N. A. Sanford, J. Cryst. Growth 300, 94 (2007).
200. J.K. Tsai, I. Lo, K.L. Chuang, L.W. Tu, J.H. Huang, C.H. Hsieh, and K.Y. Hsieh, Journal of Applied Physics 95, 460 (2004).
201. T. Metzger, R. Höpler, E. Born, O. Ambacher, M. Stutzmann, R. Stömmer, M. Schuster, H. Göbel, S. Christiansen, M. Albrecht, and H. P. Strunk, Philosophical Magazine A 77, 1013 (1998).
202. H. Heinke, V. Kirchner, S. Einfeldt, and D. Hommel, Applied Physics Letters 77, 2145 (2000).

203. V. Srikant, J. S. Speck, and D. R. Clarke, Journal of Applied Physics 82, 4286 (1997).
204. M. A. Reshchikov and H. Morkoc, Journal of Applied Physics 97, 061301 (2005).
205. A. Toure, A. Bchetnia, T. A. Lafford, Z. Benzarti, I. Halidou, Z. Bougrioua, and B. E. Jani, physica status solidi (a) 205, 2042 (2008).
206. J. H. You and H. T. Johnson, Journal of Applied Physics 101, 023516 (2007).
207. D. G. Zhao, S. J. Xu, M. H. Xie, S. Y. Tong, and H. Yang, Applied Physics Letters 83, 677 (2003).
208. A. Hushur, J. Appl. Phys. 106, 054317 (2009).
209. C. Kisielowski, J. Krüger, S. Ruvimov, T. Suski, J. W. Ager, III, E. Jones, Z. Liliental-Weber, M. Rubin, E. R. Weber, M. D. Bremser, and R. F. Davis, Physical Review B 54, 17745 (1996).
210. J. M. Wagner and F. Bechstedt, Appl. Phys. Lett. 77, 346 (2000).
211. J. Gleize, M. A. Renucci, J. Frandon, E. Bellet-Amalric, and B. Daudin, Journal of Applied Physics 93, 2065 (2003).
212. L. Bergman, D. Alexson, P. L. Murphy, R. J. Nemanich, M. Dutta, M. A. Stroscio, C. Balkas, H. Shin, and R. F. Davis, Physical Review B 59, 12977 (1999).
213. B. Baur, G. Steinhoff, J. Hernando, O. Purrucker, M. Tanaka, B. Nickel, M. Stutzmann, and M. Eickhoff, Applied Physics Letters 87, 263901 (2005).
214. H. S. Craft, Appl. Phys. Lett. 98, 082110 (2011).
215. A. Georgakilas, S. Mikroulis, V. Cimalla, M. Zervos, A. Kostopoulos, P. Komninou, T. Kehagias, and T. Karakostas, physica status solidi (a) 188, 567 (2001).
216. Nanowires, Nanowhiskers, and green LED, III-Vs Review 19, 43 (2006).
217. M. T. Hardy, D. F. Feezell, S. P. DenBaars, and S. Nakamura, Materials Today 14, 408 (2011).
218. V. P. Beaumont and P. Gibart, Phys. Status Solidi 227, 1 (2001).
219. Z. Lin and et al., Applied Physics Letters 89, 024103 (2006).
220. Y. T. Moon, C. Liu, J. Xie, X. Ni, Y. Fu, H. Morkoc, L. Zhou, and D. J. Smith, Applied Physics Letters 89, 024103 (2006).
221. J. Narayan, Metallurgical and Materials Transactions B 36, 5 (2005).
222. E. Calleja, M. A. Sánchez-García, F. J. Sánchez, F. Calle, F. B. Naranjo, E. Muñoz, U. Jahn, and K. Ploog, Physical Review B 62, 16826 (2000).
223. S. A. Morin, M. J. Bierman, J. Tong, and S. Jin, Science 328, 476 (2010).

224. S. Jin, M. J. Bierman, and S. A. Morin, The Journal of Physical Chemistry Letters 1, 1472 (2010).
225. K. L. Averett, J. E. V. Nostrand, J. D. Albrecht, Y. S. Chen, and C. C. Yang, J. Vac. Sci. Technol., B 25, 964 (2007).
226. R. Dingle, D. D. Sell, S. E. Stokowski, P. J. Dean, and R. B. Zetterstrom, Physical Review B 3, 497 (1971).
227. H. Hiroshi, Journal of Physics: Condensed Matter 14, R967 (2002).
228. Y. D. Wang, S. J. Chua, S. Tripathy, M. S. Sander, P. Chen, and C. G. Fonstad, Applied Physics Letters 86, 071917 (2005).
229. F. C. Frank and J. H. van der Merwe, Proceedings of the Royal Society of London. Series A. Mathematical and Physical Sciences 198, 205 (1949).
230. W. Qian, G. S. Rohrer, M. Skowronski, K. Doverspike, L. B. Rowland, and D. K. Gaskill, Applied Physics Letters 67, 2284 (1995).
231. F. Frank, Acta Crystallographica 4, 497 (1951).
232. C. Skierbiszewski, K. Dybko, W. Knap, M. Siekacz, W. Krupczynski, G. Nowak, M. Bockowski, J. Lusakowski, Z. R. Wasilewski, D. Maude, T. Suski, and S. Porowski, Applied Physics Letters 86, 102106 (2005).
233. C. Skierbiszewski, M. Siekacz, P. Perlin, A. Feduniewicz-Żmuda, G. Cywiński, I. Grzegory, M. Leszczyński, Z. R. Wasilewski, and S. Porowski, Journal of Crystal Growth 305, 346 (2007).
234. G. Koblmuller, F. Wu, T. Mates, J. S. Speck, S. Fernandez-Garrido, and E. Calleja, Applied Physics Letters 91, 221905 (2007).
235. E. J. Tarsa, B. Heying, X. H. Wu, P. Fini, S. P. DenBaars, and J. S. Speck, Journal of Applied Physics 82, 5472 (1997).
236. M. C. Plante and R. R. LaPierre, Journal of Crystal Growth 286, 394 (2006).
237. V. Ruth and J. P. Hirth, The Journal of Chemical Physics 41, 3139 (1964).
238. V. G. Dubrovskii, G. E. Cirlin, I. P. Soshnikov, A. A. Tonkikh, N. V. Sibirev, Y. B. Samsonenko, and V. M. Ustinov, Physical Review B 71, 205325 (2005).
239. Z. Chen, C. B. Cao, and H. S. Zhu, Chemical Vapor Deposition 13, 527 (2007).
240. V. G. Dubrovskii, N. V. Sibirev, G. E. Cirlin, M. Tchernycheva, J. C. Harmand, and V. M. Ustinov, Physical Review E 77, 031606 (2008).

241. B. Heying, I. Smorchkova, C. Poblenz, C. Elsass, P. Fini, S. Den Baars, U. Mishra, and J. S. Speck, Applied Physics Letters 77, 2885 (2000).
242. B. Heying, E. J. Tarsa, C. R. Elsass, P. Fini, S. P. DenBaars, and J. S. Speck, Journal of Applied Physics 85, 6470 (1999).
243. A. R. Smith, R. M. Feenstra, D. W. Greve, J. Neugebauer, and J. E. Northrup, Physical Review Letters 79, 3934 (1997).
244. R. Ebel, M. Fehrer, S. Figge, S. Einfeldt, H. Selke, and D. Hommel, Journal of Crystal Growth 201-202, 433 (1999).
245. D. G. Zhao, D. S. Jiang, J. J. Zhu, Z. S. Liu, S. M. Zhang, H. Yang, and J. W. Liang, Journal of Crystal Growth 303, 414 (2007).
246. J. Narayan, Metallurgical and Materials Transactions A 36, 277 (2005).
247. K. Linthicum, T. Gehrke, D. Thomson, E. Carlson, P. Rajagopal, T. Smith, D. Batchelor, and R. Davis, Applied Physics Letters 75, 196 (1999).
248. P. Dogan, O. Brandt, C. Pfüller, J. Lähnemann, U. Jahn, C. Roder, A. Trampert, L. Geelhaar, and H. Riechert, Crystal Growth & Design 11, 4257 (2011).
249. B. Yang, O. Brandt, A. Trampert, B. Jenichen, and K. H. Ploog, Applied Surface Science 123–124, 1 (1998).
250. S. Joblot, F. Semond, Y. Cordier, P. Lorenzini, and J. Massies, Applied Physics Letters 87, 133505 (2005).
251. T. Ohachi, T. Kikuchi, Y. Ito, R. Takagi, M. Hogiri, K. Miyauchi, M. Wada, Y. Ohnishi, and K. Fujita, physica status solidi (c) 0, 2589 (2003).
252. I. W. Feng, X. K. Cao, J. Li, J. Y. Lin, H. X. Jiang, N. Sawaki, Y. Honda, T. Tanikawa, and J. M. Zavada, Applied Physics Letters 98, 081102 (2011).
253. K. Hestroffer, C. Leclere, C. Bougerol, H. Renevier, and B. Daudin, Physical Review B 84, 245302 (2011).
254. L. Cerutti, J. Ristic, S. Fernandez-Garrido, E. Calleja, A. Trampert, K. H. Ploog, S. Lazic, and J. M. Calleja, Applied Physics Letters 88, 213114 (2006).
255. L. Geelhaar, Che, x, C. ze, B. Jenichen, O. Brandt, Pfu, C. ller, Mu, S. nch, R. Rothemund, S. Reitzenstein, A. Forchel, T. Kehagias, P. Komninou, G. P. Dimitrakopulos, T. Karakostas, L. Lari, P. R. Chalker, M. H. Gass, and H. Riechert, IEEE Journal of Selected Topics in Quantum Electronics, 17, 878 (2011).
256. M. Yoshizawa, Kikuchi A, M. Mori, M. Fujita and K. Kishino, 36, L459 (1997).

257. K. A. Bertness, A. W. Sanders, D. M. Rourke, T. E. Harvey, A. Roshko, J. B. Schlager, and N. A. Sanford, Advanced Functional Materials 20, 2911 (2010).
258. E. Galopin, L. Largeau, G. Patriarche, L. Travers, F. Glas, and J. C. Harmand, Nanotechnology 22, 245606 (2011).
259. T. Fujita and M. W. Chen, Jpn. J. Appl. Phys. 47 (2008) 1161.
260. T. Fujita, L.H. Qian, K. Inoke, J. Erlebacher, and M.W. Chen, Applied Physics Letters 92, 251902 (2008).
261. C. L. Wu, L. J. Chou, and S. Gwo, Applied Physics Letters 85, 2071 (2004).
262. E. Calleja, M. A. Sánchez-García, F. J. Sánchez, F. Calle, F. B. Naranjo, E. Muñoz, S. I. Molina, A. M. Sánchez, F. J. Pacheco, and R. García, Journal of Crystal Growth 201-202, 296 (1999).
263. S. Guha, N. A. Bojarczuk, M. A. L. Johnson, and J. F. Schetzina, Applied Physics Letters 75, 463 (1999).
264. R. Calarco, M. Marso, T. Richter, A. I. Aykanat, R. Meijers, A. v.d. Hart, T. Stoica, and H. Lüth, Nano Letters 5, 981 (2005).
265. X. S. Wang, G. Zhai, J. Yang, L. Wang, Y. Hu, Z. Li, J. C. Tang, X. Wang, K. K. Fung, and N. Cue, Surface Science 494, 83 (2001).
266. J. B. Hannon, V. B. Shenoy, and K. W. Schwarz, Science 313, 1266 (2006).
267. V. Potin, P. Vermaut, P. Ruterana, and G. Nouet, Journal of Electronic Materials 27, 266 (1998).
268. P. Gibart and B. Beaumont, Proc. SPIE CR83, 112 (2002).
269. D. Cherns, L. Meshi, I. Griffiths, S. Khongphetsak, S. V. Novikov, N. Farley, R. P. Campion, and C. T. Foxon, Applied Physics Letters 92, 121902 (2008).
270. K. Kusakabe, A. Kikuchi, and K. Kishino, Jpn. J. Appl. Phys., Part 2 40, L192 (2001).
271. E. C. Piquette, P. M. Bridger, Z. Z. Bandic, and T. C. McGill, J.Vac.Sci. Technol. B. 17 (1999) 1241-1245.
272. Z. Bougrioua, P. Gibart, E. Calleja, U. Jahn, A. Trampert, J. Ristic, M. Utrera, and G. Nataf, Journal of Crystal Growth 309, 113 (2007).
273. D. Cherns, L. Meshi, I. Griffiths, S. Khongphetsak, S. V. Novikov, N. Farley, R. P. Campion, and C. T. Foxon, Applied Physics Letters 92, 121902 (2008).

274. D. Cherns, L. Meshi, I. Griffiths, S. Khongphetsak, S. V. Novikov, R. P. Campion, C. T. Foxon, C. Liu, P. Shields, and W. N. Wang, Journal of Physics: Conference Series 209, 012001 (2010).
275. Q. Li, Y. Lin, J. R. Creighton, J. J. Figiel, and G. T. Wang, Advanced Materials 21, 2416 (2009).
276. F. Glas, Physical Review B 74, 121302 (2006).
277. L. Liu and J. H. Edgar, Materials Science and Engineering: R: Reports 37, 61 (2002).
278. L. F. Eastman, V. Tilak, V. Kaper, J. Smart, R. Thompson, B. Green, J. R. Shealy, and T. Prunty, physica status solidi (a) 194, 433 (2002).283 physica status solidi (b), (2010).
279. R. Gutt, L. Kirste, T. Passow, M. Kunzer, K. Köhler, and J. Wagner, physica status solidi (b) 247, 1710 (2010).
280. Q. Diduck, Electronics Letters 45, 758 (2009).
281. J. W. P. Hsu, N. G. Weimann, M. J. Manfra, K. W. West, D. V. Lang, F. F. Schrey, O. Mitrofanov, and R. J. Molnar, Applied Physics Letters 83, 4559 (2003).
282. M. Tapajna, S. W. Kaun, M. H. Wong, F. Gao, T. Palacios, U. K. Mishra, J. S. Speck, and M. Kuball, Applied Physics Letters 99, 223501 (2011).
283. C. Hodges, N. Killat, S. W. Kaun, M. H. Wong, F. Gao, T. Palacios, U. K. Mishra, J. S. Speck, D. Wolverson, and M. Kuball, Applied Physics Letters 100, 112106 (2012).
284. F. A. Marino, N. Faralli, T. Palacios, D. K. Ferry, S. M. Goodnick, and M. Saraniti, Electron Devices, IEEE Transactions on 57, 353 (2010).

Papers published in international journals

1. Nitrogen flux induced GaN nanostructure nucleation at misfit dislocations on Al_2O_3, **Manoj Kesaira**, S. M. Shivaprasad, **Applied Physics Letters, 99 (2011) 143105-08.**

2. Evidence for dislocation induced spontaneous formation of GaN nanowalls and nanocolumns on bare c-plane sapphire. **Manoj Kesaria**, Satish Shetty, S. M. Shivaprasad, **Crystal Growth & Design, 11 (2011) 4900-03**

3. Transformation of c-oriented nanowall network to a flat morphology in GaN films on c- plane sapphire **Manoj Kesaria**, Satish Shetty, P. I. Cohen, S. M. Shivaprasad, **Materials Research Bulletin, 46 (2011) 1811-13.**

4. Spontaneous formation of GaN nanostructures by molecular beam epitaxy, **Manoj Kesaria**, Satish Shetty, S.M. Shivaprasad, **Journal of Crystal Growth, 326 (2011) 191-194.**

Papers Published in international Journals (Not included in Thesis)

5. Effect of Pb adatom flux rate on adlayer for Stranski-krastanov growth mode on Si(111)7x7 surface, **Manoj Kesaria**, Mahesh Kumar, Govind, S.M. Shivaprasad, **Applied surface science 356 (2009) 576-579.**

6. Role of substrate temperature in the pulsed laser deposition of zirconium oxide thin film, J. Mitra, G.J. Abraham, **Manoj Kesaria**, S. Bhal, A.Gupta, S.M. Sivaprasad, C.S. Viswanadham, U.D.Kulkarni, G.K.Dey, Materials Science Forum, 710 (2012) 757-761

Papers communicated to international journals

7. Direct evidence of Frank-Read source in dislocation induced spontaneous nanocolumn formation at the GaN/Al_2O_3 interface, **Manoj Kesaira**, P.I. Cohen, S. M. Shivaprasad **(communicated to Nano Letters)**

8. Formation of defect free c-oriented single crystalline GaN nanowires over GaN nanowall template formed by nano-ELOG technique, **Manoj Kesaira**, S.M. Shivaprasad **(communicated to Applied Physics Letters)**

9. A direct evidence of role of Frank and Frank Read mill on GaN nanowires formation on bare c-plane Si(001) by PAMBE, **Manoj Kesaria**, S. M. Shivaprasad (**communicated to Applied Physics Letters**)

10. Formation of HEMT structure on semi-insulating GaN(Fe) layer by PAMBE, **Manoj Kesaria**, S. M. Shivaprasad (**communicated to Journal of Crystal Growth**)